Contributions to the Study of Permanent Magnet Synchronous Machines with Nonoverlapping Windings

Teză destinată obţinerii
titlului ştiinţific de doctor
la
Universitatea ”Politehnica” din Timişoara
în domeniul
INGINERIE ELECTRICĂ
de către

Ing. Marcel TOPOR

Conducător ştiinţific: Prof.univ.dr.ing. Ion BOLDEA

Referenţi ştiinţifici: Prof.univ.dr.ing. Mircea RĂDULESCU
Prof.univ.dr. ing. Iulian BIROU
Conf.univ.dr.ing. Lucian TUTELEA

Ziua susţinerii tezei: 30 noiembrie 2011

Seriile Teze de doctorat ale UPT sunt:

1. Automatică
2. Chimie
3. Energetică
4. Ingineria Chimică
5. Inginerie Civilă
6. Inginerie Electrică
7. Inginerie Electronică şi Telecomunicaţii
8. Inginerie Industrială
9. Inginerie Mecanică
10. Ştiinţa Calculatoarelor
11. Ştiinţa şi Ingineria Materialelor

Universitatea ”Politehnica” din Timişoara a iniţiat seriile de mai sus în scopul diseminării expertizei, cunoştinţelor şi rezultatelor cercetărilor întreprinse în cadrul şcolii doctorale a universităţii. Seriile conţin, potrivit H.B.Ex.S Nr. 14 / 14.07.2006, tezele de doctorat susţinute în universitate începând cu 1 octombrie 2006.

Romania, 300159 Timişoara, Bd. Republicii 9,
tel. 0256 403823, fax. 0256 403221
e-mail: editura@edipol.upt.ro

Preface

This thesis is an outcome of research during my Ph.D. study at ”Politehnica” University of Timişoara. My work was supported, encouraged and inspired by a number of people, therefore, I would like to express my gratitude towards them.

I wish to express my deep gratitude to my supervisor Prof. dr. eng. Ion Boldea. His guidance, support and encouragement made this work possible. I would like to thank also Prof. Marignetti Fabrizio, Vincenzo Delli Colli, Roberto Di Stefano, Cancelliere Piergiacomo from Università degli Studi di Cassino for their support and for the fruitful discussions during my researching period in Cassino.

I wish also to express my gratitude for the professionalism and support to Ph.D. Do-Hyun Kang, Ph.D. Dae-Hyun Koo, Ph. D. Yon Chun from the Korea Electrotechnics Research Institute of Changwon, South Korea.

I want to thank all of those who contributed to my engineering formation and also to my colleagues from Intelligent Motion Control Laboratory at Faculty of Electrical Engineering, Timisoara, especially to Assoc. Prof. dr. eng. Lucian Tutelea.

I am also honored to express my gratitude to the distinguished Prof. dr. eng. Mircea Rădulescu and Prof. dr. eng. Iulian Birou from Technical University of Cluj for referencing of my work.

Finally, and most of all, I want to dedicate this to my beloved parents Emil and Aurelia, to my wife Diana and to her family for their support and understanding.

This thesis is dedicated to them.

Deva, 2011, October 18^{th}

Marcel Topor

Marcel, Topor

Contributions to the Study of Permanent Magnet Synchronous Machines with Nonoverlapping Windings

Teze de doctorat ale UPT, Seria 6 Nr. 24
Editura Politehnica, 2011,
285 pagini, 190 figuri, 15 tabele.

ISBN: 978-606-554-394-2
ISSN: 1842-7022

Cuvinte cheie: MSMP, înfăşurări fracţionare, reversare de flux

Rezumat

MSMPs cu înfăşurări fracţionare ($q<1$) au fost introduse recent în numeroase aplicaţii de la echipamente electrocasnice până la actuatoare electrice pentru automobile şi chiar generatoare eoliene de turaţii reduse. Pierderile scăzute în cupru (randament ridicat) şi reducerea dimensiunilor de gabarit ale maşinii odată cu reducerea costului maşinii sunt principalele merite ale acestor maşini în acţionări electrice cu turaţie variabilă performante. Această teză a fost concepută să aducă noi contribuţii interesante în proiectarea conceptuală, modelul dinamic şi analiza FEM a configuraţiilor noi de MSMP cu înfăşurări fracţionare. Pornind de la una din sintezele cele mai complete cu privire MSMP cu înfăsurări fracţionare cu câmp longitudinal şi transversal, radiale si axiale, cu magneţi permanenţi MP pe stator şi pe rotor, cu o bibliografie reprezentativă şi cu aprecierea corecta a meritelor şi a deficienţelor fiecărei din configuraţiile analizate, au fost realizate experimente pe trei prototipuri diferite de maşini sincrone cu magneţipermanenţi cu înfăsurări fracţionare cu confirmări acceptabile ale dezvoltarilor teoretice dar mai ales cu rezultate de căutare practică.

Contents

List of Figures

List of Tables

1 Introduction

PMSMs with non-overlapping concentrated windings have become a competitive alternative to PMSMs with distributed windings for certain applications. Non-overlapping concentrated windings are indeed attractive for several reasons. Besides the short end-windings a low cogging torque, good fault-tolerant capability and a high constant power speed range can be achieved.

Therefore, PMSMs with non-overlapping concentrated windings have recently been widely investigated by many researchers.The design of such PMSMs differs from the design of PMSMs with conventional distributed windings due to particularities and more complex winding. The goal of this chapter is to underline the particular design features of 1 phase and 3-phase PMSMs incorporating tooth concentrated windings.

Numerous applications require low speed electric drives with high torque density. For example, such a machine can be made in a smaller size to fit In addition, the machine tends to require less active material and can be made cheaper if manufacturing costs are in line with more conventional machines.

The formidable performance of high energy PM's allowed recently to look for direct drives for low speeds, in the hope that the low speed machine will have competitive (or better) overall torque at less total weight than the indirect drive which includes the high speed motor and the mechanical transmission.

By low speed we mean speeds below $150 rpm$ and torques of tens and hundreds Nm. At such speeds, the travelling field winding stator can not be built efficiently as the pole pitch tends to be below 30mm. Hence most low speed drive applications have been handled through indirect electric drives. That means that a high speed motor plus a high ratio mechanical transmission is still the dominant solution below 150 rpm or so. For indirect low speed drives the travelling field AC motors with vector (or direct torque) control is still the norm.

Finally the absence of backlash makes the precision position control much simpler with direct drives. As a travelling field winding stator is not feasible, unless the torque is in the thousands of Nm, to allow pole pitches above $60 mm$ or so, other machine configurations than induction have to be considered.

1.1 Thesis objectives

The present thesis is organized in seven chapters following the above presented objectives:

to investigate the use of fractional nonoverlapping windings in PMSM machines,

to develop two new fractional winding prototypes with flux reversal;

to evaluate the effect of fractional nonoverlapping windings in low speed axial flux PMSM machines;

to develop a new prototype of a dual rotor single stator axial flux machine for hybrid electric drives.

In the first chapter we present a review of new topologies of electric machines with improved torque density:

- Radial flux Permanent Magnet Machine;
- Axial flux with Circumferential Current PM Machine;
- Axial flux PM Machines;
- Transverse flux PM Machine;
- FRM flux reversal machine

In chapter 2 we use existing analytical models in order to evaluate some characteristics of PMSM with fractionary windings. The chapter presents a review of basic mathematical equations used to build analytical models of PMSMs. The analytical evaluation method has the advantage of being fast and very versatile being capable to analyze accurately a large number of radial PMSM topologies. Combined with the fact that the model is easy to be integrated in the form of a symbolic software computation program ie. Mathematica this can provide a useful tool in the design and optimization of radial flux PMSMs . The model presented is capable to provide a good estimate of the armature reaction field, back-emf and instantaneous torque produced by the 3-phase stator windings with fractional or integer slot per pole and per phase of iron-cored internal rotor.

The analytical model is used in order to investigate the armature reaction field, back-emf and instantaneous torque produced by the 3-phase stator build with fractional non-overlapping windings. The model it has been validated by numerical results in chapter 3. This chapter provide an implementation of the analytical model for giving a basis for comparative studies between existing permanent magnet (PM) machines (with distributed or fractional windings) and searching for new PM machines topologies or in optimization studies.

Chapter 3 presents some characteristics of low speed 72/68 slots/poles PMSG the performances are presented both by FEM and laboratory tests.

Chapter 4 is dedicated to the analysis of a linear non-overlapping flux reversal prototype developed in collaboration with Hanyang Univ., Seoul, South Korea. The chapter includes design specification, FEM analysis and dynamic simulation of the operating regimes. Also in chapter 4 is introduced another

possible application of non-overlapping winding PMSM, the radial flux reversal machine with flux concentration effect FRMFC. Despite the more complex mechanical structure the configuration shows at initial evaluation good characteristics being capable to compete with topologies like transverse flux machines. the chapter includes the design and finite element results.

Chapter 5 is focused on the analysis of two axial flux PMSM machines. A 18/16 configuration is analyzed an some measures in order to reduce the cogging torque is presented. A special direct drive axial flux PMSM (48/40 slots/poles) machines specially build for electric vehicles traction characterized by FEM and laboratory tests. Also a possible solution for control is given.

Chapter 6 presents a special designed system build on the topology of axial flux machines equipped with fractional windings for more compact HEV traction applications.

In chapter 7 the work is summarized and the conclusions, contributions and future perspectives are presented. Briefly the present work is focused on the following directions.

1. to present some important characteristics of fractional winding permanent magnet machines
2. to introduce two new configurations of flux reversal machines with design and finite element simulations.
3. to analyze and to provide some improvement of axial flux PSMS with fractional nonoverlapping windings
4. to present a new dual rotor PM axial flux configuration permanent magnet machine with application in HEV.

1.2 Motivation

1.2.1 New topologies of electric machines with improved torque density: a review

Large scale introduction of power electronics drives has been an enabling technology for a new class of electric machines with improved torque density – Converter Fed Machines (CFM's), such as:

- Brushless DC Machine;
- Switched reluctance Machine;
- Axial flux PM Machines;
- Transverse flux PM machine;
- Axial flux with Circumferential Current PM Machine;
- FRM (flux reversal machine);

The Transverse flux Machine, has been a popular topology for exploration of high torque density machines, such as a direct drive for ship propulsion [5], wind generators etc. The Claw Pole Machine [6] and the Axial flux Circumferential Current Machine [7] can also be regarded as the members of this machine family. In order to achieve high torque density, most of this new configurations machines must have three-dimensional working flux distributions (i.e. flux components must exist in all three dimensions), including all the machines mentioned above.

Comparison of the machines presented is very difficult. The machines are designed for different specifications using different methods [10]. For example, the total cost of the machines depends on the price of materials and on the complexity of construction. Also, the total design of a electric drive depends on the weight and the size of the machine. However, the design principles of the directly driven generators do not differ much from the ordinary one. They can be built in the same way as other electrical machines. Some comparisons of different machine topologies have been presented in literature.

1.3 Review of PM machines with nonoverlapping windings

We can use this term to represent a large class of electric machines. A non overlapping winding is a winding where a coil is not overlapping another coil under the same pole. This structure is met both for radial and axial flux machines. This is synonym with a machine having the number of slots per pole and phase q less than 0.5.

For radial flux machines the winding is called to be a concentric winding or single tooth coil. The winding could have a single winding in a single slot or there it could be a double layer.

For axial flux machines the winding could have different shapes like toroidal or gramme, ring shape [11].

The winding influence in the performances of the machine is obviously if only considering the copper losses and the influence of the windings in the no load voltage.

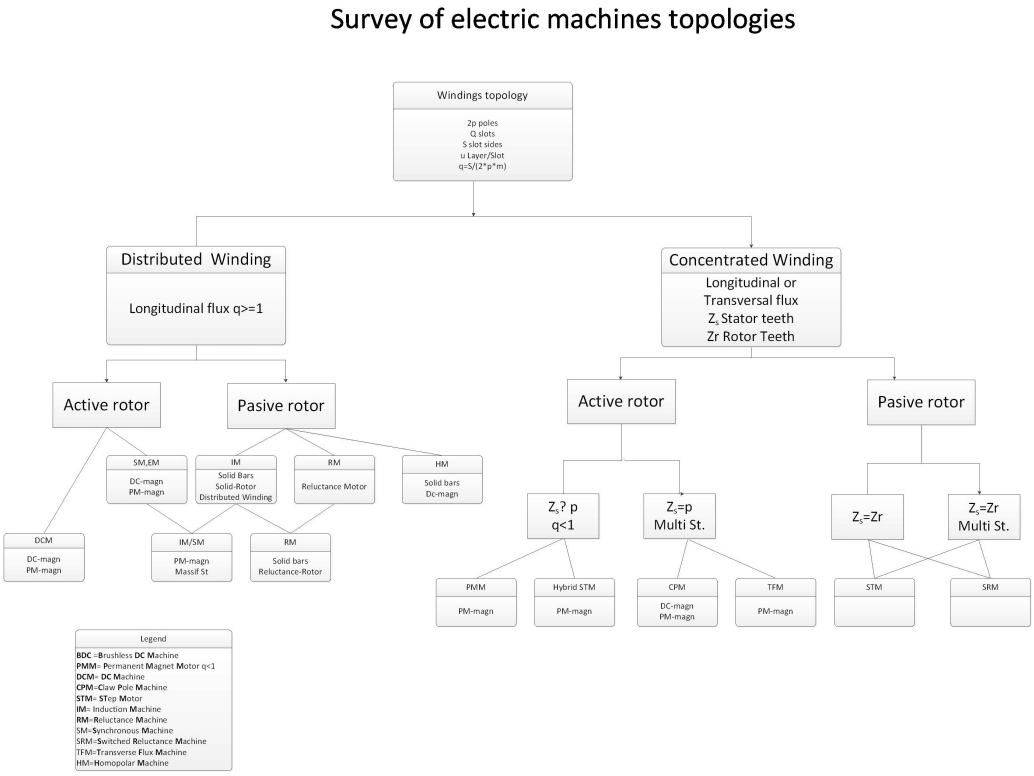

Figure 1.1: Winding based classification of machine topologies.

1.3.1 Radial Flux PM Machines with fractional nonoverlapping windings

The use of windings concentrated around the teeth offer obvious advantages for the electric machines with radial airgap. With such windings, the volume of copper used in the end-windings can be reduced in significant proportions, in particular if the axial length of the machine is small.

Furthermore, a significant reduction of the Joule losses is achieved, and the efficiency of the motor is improved when compared to more traditional structures with one slot per pole and per phase for example.

In the case of the three-phase machines, the concentrated winding is often associated and restricted to a winding with a short pitch of 120 electric

degrees, to a winding with performances reduced compared to the traditional structures. But there is a significant number of three-phase structures [12] which can support a concentrated winding Fig. 1.1 if the number of poles is increased. These structures present a fractional number of slots per pole and per phase $q < 0.5$.

The principal difficulty for the study of these machines lies in the determination of optimal winding configuration (poles slots) and in particular the order of the phases under each pole.

The three-phase machines which can be equipped with a concentrated winding have a number of slots per pole and per phase less than or equal to $\frac{1}{2}$.

$$q = \frac{Q_s}{2pm} \tag{1.1}$$

where Q_s is the number of slots, $2p$ is the number of pairs of poles and an m integer number which stands for the number of phases. In it is presented in detail the table of slots/poles combinations and corresponding winding factor.

The following table gives a list of the various structures where it is possible to obtain a balanced concentrated winding.

2p \ Qs	2	4	6	8	10	12	14	16	18	20	22	24
3	*1/2*	*1/4*		*1/8*	*1/10*		*1/14*	*1/16*		*1/20*	*1/22*	
	0.866	0.866		0.866	0.866		0.866	0.866		0.866	0.866	
6		*1/2*		*1/4*	*1/5*		*1/7*	*1/8*		*1/10*	*1/11*	
		0.866		0.866	0.866		0.866	0.866		0.866	0.866	
9			1/2	3/8	3/10	3/12	3/14	3/16		3/20	3/22	
			0.866	0.945	0.945	0.866	0.945	0.945		0.945	0.945	
12				1/2	2/5		2/7	1/4		1/5	2/11	
				0.866	**0.966**		**0.966**	**0.966**		0.866	0.966	
15					1/2		5/14	5/16		1/4	5/22	
					0.866		0.866	0.866		0.866	0.966	
18						1/2	3/7	3/8		3/10	3/11	1/4
						0.866	0.945	0.945		0.945	0.902	0.866
21							1/2	7/16		7/20	7/22	
							0.866	0.932		0.953	0.953	
24								*1/2*		*2/5*	*4/11*	
								0.866		0.966	0.957	

configurations with high winding factor

Figure 1.2: Winding factor table

In Fig. 1.2 the table of fundamental winding factors are presented. In this table, the winding coefficient of the fundamental component is used to characterize the performances of each structure.

1.3.2 The definition of the winding factor for Radial Flux Permanent Magnet Machines

The number of turns of the space harmonics of the winding distribution of a full pitch winding with one slot per pole and per phase is:

$$n_{sa}(\alpha_s) = \begin{cases} \frac{N}{p\beta_{so}} & \text{where } \frac{\pi}{2p} - \frac{\beta_{so}}{2} < \alpha_s < \frac{\pi}{2p} - \frac{\beta_{so}}{2} \\ -\frac{N}{p\beta_{so}} & \text{where } \frac{3\pi}{2p} - \frac{\beta_{so}}{2} < \alpha_s < \frac{3\pi}{2p} - \frac{\beta_{so}}{2} \\ 0 \text{ everywhere} & \text{else on } 0 < \alpha_s < 2\pi p \end{cases} \tag{1.2}$$

where β_{so} is the slot opening angle in mechanical radians;

$$n_{sa}(\alpha_s) = \sum_{k=1,2,3\ldots}^{\infty} \frac{1}{2} N_{s,k} \sin(pk\alpha_s) \tag{1.3}$$

where the Fourier coefficients of the winding distribution $\frac{1}{2}N_{s,k}$ are calculated as:

$$\frac{1}{2}N_{s,k} = \frac{2p}{2\pi}\int_0 n_{sa}(\alpha_s)\sin(pk\alpha_s)d\alpha_s = \frac{2N}{\pi}\sin(\frac{1}{2}k\pi)\frac{\sin(\frac{1}{2}pk\beta_{so})}{\frac{1}{2}pk\beta_{so}} \tag{1.4}$$

For a winding with infinitesimal slot openings the Fourier coefficients are:

$$\frac{1}{2}N'_{s,k} = \frac{2N}{\pi}\sin(\frac{1}{2}k\pi) \tag{1.5}$$

The winding factor $k_{w,k}$ is introduced as the ratio of $Q_{s,k}$ of a real distributed winding to $N'_{s,k}$ of a full pitch winding in infinitesimal slots.

$$k_{w,k} = \frac{\sin(\frac{1}{2}pk\beta_{so})}{\frac{1}{2}pk\beta_{so}} \tag{1.6}$$

Often a winding is distributed over several slots. the effect of this distribution is considered by the distribution factor :

$$k_{wdistribution,k} = \frac{\sin(\frac{k\pi}{6})}{q\sin(\frac{k\pi}{6})} \tag{1.7}$$

distribution factor;

frequently the windings are short pitched: the winding span is not a pole pitch. This effect is considered by the pitch factor or the chording factor $k_{chord,k}$:

$$k_{wchord,k} = \cos(1/2pk\beta_{chord}) \tag{1.8}$$

where β_{chord} is the chording angle in mechanical radians;

If the rotor and the stator are skewed with the respect to each other to reduce higher space harmonics or to reduce cogging torque. In permanent magnet machines the skew angle is often equal to the slot angle, because this way the cogging torque is eliminated. The effect of skewing on the Fourier coefficients of the winding distribution is considered by the skewing factor $k_{wskew,k}$:

$$k_{wskew,k} = \frac{\sin(\frac{1}{2}pk\beta_{skew})}{\frac{1}{2}pk\beta_{skew}} \tag{1.9}$$

where β_{skew} is the chording angle in mechanical radians;

Often the skew factor is not considered as part of the winding factor of the machine because is not present in the self inductance of the winding. Any way this is present in the mutual inductances of the between windings which are skewed with respect to each other. It is also present in the no load voltage of a permanent magnet machine if the magnets are skewed with respect to the stator.

The winding factor is the product of the various contributions.

$$k_{w,k} = k_{wskew,k} \cdot k_{wdistribution,k} \cdot k_{wchord,k} \tag{1.10}$$

The winding factor is the product of the distribution factor and the pitch factor:

$$k_{p,\nu} = k_{d,\nu} k_{p,\nu} \tag{1.11}$$

$$k_{dv} = \frac{\sin\left(\frac{\nu\pi}{2mp}\right)}{\frac{\nu\pi}{2mp}} \tag{1.12}$$

The pitch factor is equal to:

$$k_{p,\nu} = \sin\left(\frac{W}{\tau_p} \cdot \frac{\nu \cdot \pi}{2}\right) \leq 1 \tag{1.13}$$

where:

$-W$ is the coil width;

$-\tau_p$ pole pitch;

$-\nu$ harmonic number;

The harmonic number is given by:

$$\nu = \frac{2}{\mathrm{p}}(1 + \mathrm{m} \cdot \mathrm{g}) \tag{1.14}$$

p is the number of poles;m the number of phases $m = 3$;

For tooth wound windings the distribution factor is equal to unity and thus the winding factor can be modified only by the pitch factor.

In the case of a traditional machine with one slot per pole and per phase, the winding coefficient of the fundamental component is equal to one in the case of an armature where the slots are not skewed. The same coefficient is reduced to 0.955 when the slots are skewed as it presented in [22].

For nonoverlapping windings with $q = 0.5$ and $q = 0.25$ the value of the ordinal number are:

$$q = \frac{1}{4} \quad \nu = \frac{1}{2}; -1; 2, -\frac{5}{2}, \frac{7}{2}, -4, 5; \tag{1.15}$$

$$q = \frac{1}{2} \quad \nu = 1; -2; 4, -5, 7, -8, 10 \tag{1.16}$$

for $q = 0.25$ the winding design can produce a large number of subharmonics defined as ($\nu < 1, \nu \notin N$ or $\nu \in N_{even}$). the presence of subharmonics is undesirable. leading to undesirable forces, unintended torques, and losses, [1]. The production of harmonics is not limited to fundamental and subharmonics as stated in [22].

A advantage is that with an appropriate design the PM machine with concentrated windings can act as an electromechanical harmonic filter (the winding can suppress or add some harmonics [11]). The machine with its unique design can be used to cancel the most dominant current harmonics of the adjacent nonlinear load.

The performance of a machine is directly related to the value of this ratio for a sinusoidal current supply and also for a rectangular current supply.

According to [12] it is possible to design a machine with concentrated windings having an irregular distribution of slots by starting from an original machine with a fractional number of slots per pole and per phase. It is interesting because it is possible with these specific structures to directly minimize the cogging torque without skewing the slots [8]. Some coils can also be removed to maximize the winding coefficient of the fundamental component [8].

The three-phase structures with concentrated windings demonstrates improved performances of these machines compared to traditional machines with one slot per pole and per phase.

The performances of the machines with concentrated windings are higher than the performances of the traditional machines, because the minimization of both copper volume and Joule losses are reducing the manufacturing costs and improving the output characteristics.

Applications of concentrated winding machines in radial flux machines have prompted a number of significant problems which concern the design of both the machine and the power converter supplying the machine. Further advantages can be achieved from a suitable arrangement of the machine supply. In fact, the performance of such concentrated winding PM drives can be improved greatly in terms of average output torque if the machine is fed by means of current waveforms which allow full contribution of the machine back EMF waveform in producing torque [12], such as in the case of a supply arrangement using either full square-wave or trapezoidal current waveforms. Such an approach, however, requires a suitable power converter configuration, since a large harmonic current flows in the machine neutral resulting from star connection of the stator winding[11].

In chapter 3 we will investigate in detail the features of a 72/68 slots/poles radial flux permanent magnet machine.

1.4 Axial flux PM machines (AFPM)

Radial flux permanent magnet (RFPM) machines, for good reasons, have traditionally made up the majority of commercial PM machines for they offer good magnetic and electric loading and so provide very compact electromagnetic devices with high efficiency. The use of axial PM machines has increased

in recent years, applications such as motor/generators for Hybrid Electric Vehicles, Micro Turbines and Wind Turbines are all examples of where axial flux machines are employed [13].

In some applications (like in the case of HEV), the available space for the machine imposes a physical limit on the outside diameter and this becomes the main design driver. Consequently, in this study, the outer diameter of both the axial and radial flux machines is fixed.

The high compactness of AFPM machines compared with the conventional induction, DC and radial flux permanent magnet (RFPM) machines, provides a considerable reduction in volume and weight. Furthermore, AFPM machines present high efficiency due to the absence of rotor currents.

1.4.1 Topology description

The stator of the machine is usually built with a sheet of laminated iron wound in a spiral fashion (Fig. 1.3). The stator slots have subsequently been milled in order to create the slots.

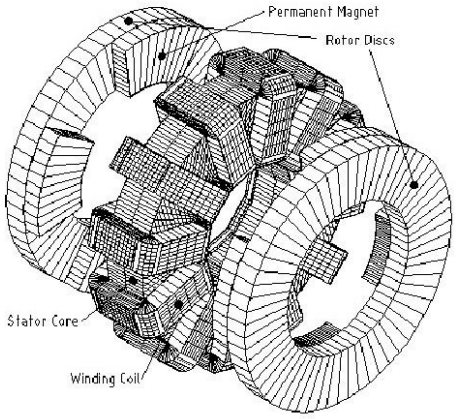

Figure 1.3: Three-dimensional sketch of the AFPM torus (slotless).

In chapter 6 we will further investigate two fractional Axial Flux PMSM with 18/16 and 48/40 slots/poles.

1.5 The PM Vernier machine

The Permanent Magnet Vernier Machine has the feature of high torque at low speed, and is thus suitable for direct drive applications. The high torque at low speed feature is based on the so called 'magnetic gearing effect,' which is also made use of in many types of stepper motors and various types of machines.

The stator has a toothed-pole structure (Fig. 1.4), which has windings in slots with a conventional overlapped configuration, and the rotor has surface

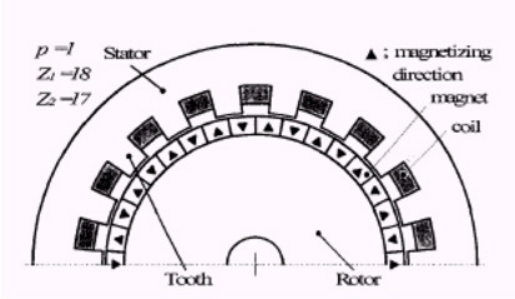

Figure 1.4: Half-cross-sectional view of a typical three phase SPMVM.

permanent-magnet poles. The stator and the rotor are constructed by steel laminations.

In this machine, there exists the following rule:

$$Z_2 = Z_1 - p \tag{1.17}$$

or

$$Z_2 = Z_1 + p \tag{1.18}$$

where p, Z_1, Z_2 and are the numbers of winding pole pairs, stator teeth, and rotor pole pairs, respectively. Due to this rule, a unique phenomenon appears, for a small movement of the rotor makes a large change of the flux, which results in a high torque. This phenomenon is called the "magnetic gearing effect."

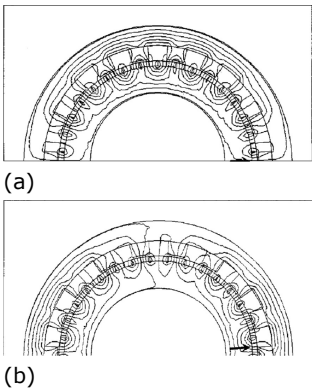

Figure 1.5: Flux distribution with the rotor position in an SPMVM.

This figure above shows the difference of the flux distribution with the rotor position in an SPMVM (surface mounted permanent magnets Vernier Machine). The parameters of the machine are $p = 1, Z_1 = 18$, and $Z_2 = 17$. The flux is due only to the permanent magnet, and between Fig. 1.5 a) and (b), there is a slight difference of the rotor positions, which corresponds to a

quarter of the stator tooth pitch. It is noted that the number of the pole pairs of the flux distribution equals the value of number of poles.

The steady torque is produced by synchronizing the coil magnetomotive force (MMF) to the flux rotation. It is also observable that the flux distribution changes 90 electrical degrees with the indicated difference of the rotor position.

The phases of the harmonics must be taken into account. The phases of the harmonics can be proven to make a critical difference in the torque production between the cases $Z_2 = Z_1 - p$ of and $Z_2 = Z_1 + p$;

There are several typical forms for each of the stator, the windings and the rotor, and most of the machines are considered as combinations of these forms.

The flux is due only to the permanent magnet, and between the two figures (a) and (b) there is a slight difference of the rotor positions, which corresponds to a quarter of the stator tooth pitch. It is noted that the number of the pole-pairs of the flux distribution equals to the value of p, which is one in this case. Thus, a steady torque is yielded by synchronizing the coil MMF to the flux rotation. It is also observable that the flux distribution changes 90 electrical degrees with the indicated difference of the rotor position.

A small movement of the rotor makes a large change of the flux, which results in a high torque. This phenomenon based on the rule, can be denoted as the 'magnetic gearing effect.' It can be also mentioned that the cogging torque and the torque ripple become substantially low so as to be negligible in this type of machine.

1.5.1 Dual-Excitation Permanent Magnet Vernier Machine

The Dual-Excitation Permanent Magnet Vernier Machine [14] has the structure ofwhich is shown in Fig. 1.6.

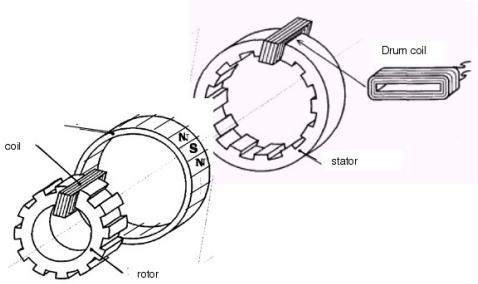

Figure 1.6: Dual excitation PM Vernier machine.

There exist two stators both inside and outside of the rotor, for a large rotor diameter and a good use of space. Another feature of the DEPMVM is the adoption of the 'drum windings,' in which the coils are wound around the yokes with small number of winding poles at the same time, while its major performance becomes the same to the conventional windings.

1.6 The transverse flux machine

The transverse flux machine (TF) Fig. 1.7 was first proposed and named by Weh in the '80s. Several variants of TF machines have been designed by now, but no mass production has been reported yet. The basic principle is the same for all variants. A stator phase winding having a circular form produces a homopolar MMF distribution in the air-gap.

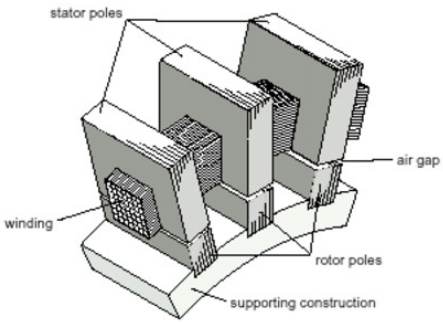

Figure 1.7: Transverse flux machine.

This MMF is modulated by a pattern of stator poles or teeth to interact with a heteropolar pattern of permanent magnets placed on the rotor. The number of stator poles is usually half of the number of rotor permanent magnets, but much greater than for the conventional machines with heteropolar topology.

The TF machine topology allows the pole number to be increased without reducing the MMF per pole, exactly as in the claw-pole type structures. The machine thus obtained is capable of producing power densities up to three times greater than conventional machines. It is expected that the TF machine will occupy an important segment of the low-speed, high-torque, variable-speed drive market.

TF machines have some important shortcomings, the most notable being the very complex construction, with a true 3D field pattern. As yet reported, the TF machine also has a quite low power factor , which increases the power rating required for the drive inverter substantially.

The TF machines can have permanent magnets placed on the rotor, this being the main topology, or they can have only salient poles on the rotor. In the last case, the machine is a true SR machine, but with a homopolar type stator winding [15]. Either way, with or without permanent magnets on the rotor, the TF machine must have two or more than two phases, to produce continuous rotation and to avoid the starting difficulties.

There are two possible topologies for the TF machine as far as the stator construction is concerned:

- the single-sided;
- the double-sided one;

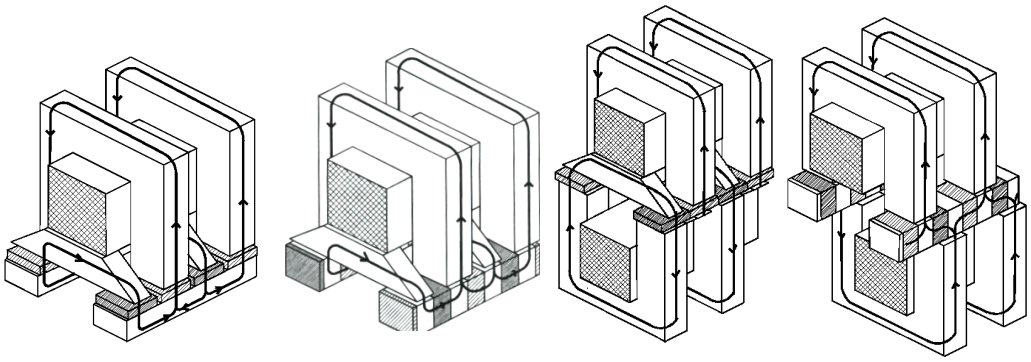

Figure 1.8: Transverse flux machine a) single sided surface mounted permanent magnets b) permanent magnets inserted in the rotor with flux concentrating poles c)double sided d)surface mounted permanent magnets e)double sided inserted permanent magnets.

The TF machine's rotor can be built up with surface or with buried permanent magnets. For the TF machine rotor with buried permanent magnets, there are two possibilities. One with radially magnetized magnets and rotor nonmagnetic pieces in between them, and the other one with magnetized permanent magnets parallel to the air-gap and flux concentrating poles of steel inserted between successive permanent magnets. This last rotor topology may work with a double-sided symmetrical excited stator.

Four winding variants, Gramme, Drum, Pole and Ring windings are shown in Fig 1.9.

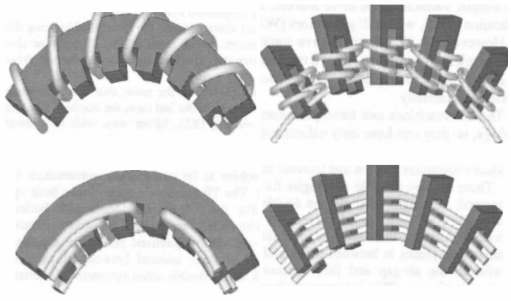

Figure 1.9: TFM Winding variants, Gramme, Drum, Pole and Ring.

The choice of one of these winding topologies may influence the air-gap MMF produced by the current flowing through the winding, and it may change the machine construction essentially.

If the choice is a ring-type winding, then the homopolar features of such a topology allow the MMF distribution with one pole pattern modulated by a toothed structure to produce an air-gap MMF with a different pole pattern offers the possibility of achieving more mechanical force with less armature

current. This means that, at a given machine diameter and armature winding current, the current loading is essentially increased by simply enlarging the number of pole pairs. This effect is used by the transverse flux (TF) machine to obtain high specific torque.

The TF machine stator windings must be supplied from an electronic power converter, which is controlled function of the rotor position. The control of the TF machine with permanent magnets on the rotor is done just as in the case of the synchronous machines; the control of the TF machines without permanent magnets on the rotor is done almost as for the SRM.

For a relatively new proposed machine, the TF machine shows an important number of variants as far as the topology is concerned.

The homopolar features of the TF machine alow that for a given machine diameter and armature winding current, the current loading is increased simply by enlarging the number of pole pairs. This effect is used by the TF machine to obtain high specific torque.

The transverse machine may have a single sided or double sided or a double sided stator structure. In both cases, the rotor can be build up with surface mounted permanent magnets (flat magnets rotor) or with permanent magnets inserted between the flux concentrating poles (concentrating flux rotor).

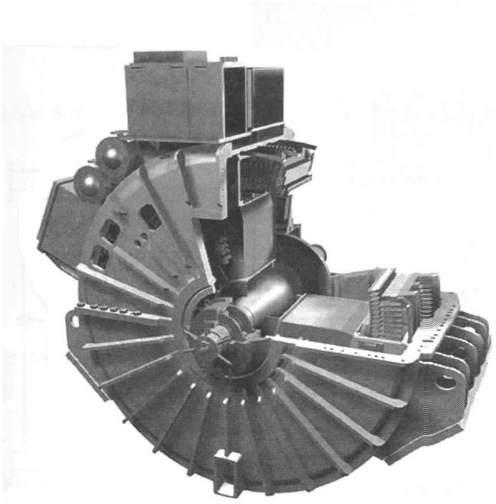

Figure 1.10: Transverse flux motor for ship propulsion.

The transverse flux PM-rotor machine though uses PMs is basically a variable reluctance machine. So some notable PM-flux is lost as leakage flux.

1.6.1 Advantages and disadvantages of the transverse flux machines

The TFM has several advantages over a standard PM brushless motors;

- better utilization of active materials than in standard (longitudinal flux) PM brushless motors for the same cooling system, i.e., higher torque density or higher power density;
- less winding and ferromagnetic core materials for the same torque;
- simple stator winding consisting of a single ring-shaped coil (cost effective stator winding, no end connection);
- unity winding factor ($k_{ti}, i = 1$);
- the more the poles the higher the torque density, higher power factor and less the torque ripple;
- a three phase motor can be made of three (or multiples of three) identical single-phase units[20];
- a three phase TFM can be fed from a standard three phase inverter for PM brushless motors using a standard encoder;
- the machine can operate as a low speed generator (Fig.1.10).
- although the stator winding is simple, the motor consists of a large number poles ($2p > 24$).
- There is a double saliency (the stator and rotor) and each salient pole has a separate ”transverse flux” magnetic circuit.

Careful attention must be given to the following problems:

- to avoid a large number of components, it is necessary to use radial laminations (perpendicular to the magnetic flux paths in some portions of the magnetic circuit), sintered powders or hybrid magnetic circuits (laminations and sintered powders);
- the motor external diameter is smaller in the so-called ”reversed design”, i.e., with external PM rotor and internal stator;
- the TFM uses more PM material than an equivalent standard PM brushless motor;
- the power factor decreases as the load increases and special measures must be taken to improve the power factor;
- as each stator pole faces the rotor pole and the number of stator and rotor pole pairs is the same, special measures must be taken to minimize the cogging torque.

The TF machine looks perfectly fitted for direct drive applications, windmill generators or ship propulsion systems Fig 1.10.

1.7 Axial flux Circumferential Current Machine

The power density can be increased by an increase in the pole number while the speed remains unchanged. In other words, the torque capability can be increased by simply increasing the pole number of the machine. However, limits exist (such as the leakage between poles with different polarity, rotating magnets, complexity of the structure) which still requires further research.

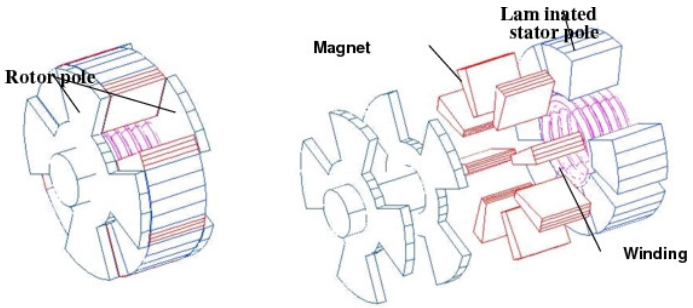

Figure 1.11: Axial Flux Circumferential Current prototype.

In essence, Axial flux circumferential current machine is a new realization of the doubly salient permanent magnet machine structure. An AFCC machine consists of three parts Fig. 1.11 :

- a stator with iron poles and permanent magnets (PMs);
- a circumferential armature winding;
- a rotor with salient poles and a center cylindrical portion.

The main flux provided by two nearby PMs are focused in the stator pole and become axially oriented when passing across the gap. The flux then passes the air-gap, the rotor pole, the rotor cylinder, the rotor pole on the other side and returns to the next stator pole. The rotor poles on the two end plates are shifted by one pole pitch.

For a generator application, a rotating rotor causes the flux linked by the winding to be reversed periodically to generate a back emf.

For a motor application, an injected current will then create a reluctance torque. It should be noted that the rotor and stator of the AFCC machine can be interchanged depend on the specific application. The armature winding should always be mounted to the stationary part in order not to rotate.

Because the main flux path in the AFCC machine has a complicated three dimensionally distribution, the material of the stator pole and rotor must be tailored to meet such a situation. For this purpose, novel materials such as powdered metal could be utilized for manufacturing. On the other hand, the AFCC machine can also be constructed with traditional laminated silicon-iron to reduce the cost. Fig. 1.12 illustrates one of the possible arrangements.

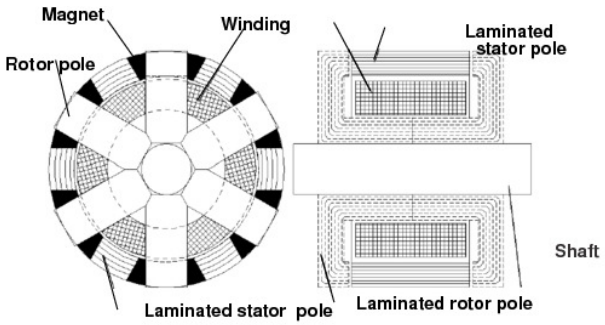

Figure 1.12: The AFCC machine using laminated silicon-iron.

Specifically the topology eliminates the end-winding portion to provide less copper losses and reduce leakage. It has stationary, not rotating, magnets to eliminate the excitation penalty. It has a strong flux focusing capability, which allows the use of low cost material such as ferrite magnets. The approach also has bipolar rather than unipolar (pulsating) phase flux even though the magnets are not rotating. Other features include simple armature winding construction, tape wound stator core and high pole number capability with low aspect ratio.

In order to achieve practical results, the design and analysis of the AFCC machines should based on the fact that the flux paths are three-dimensionally distributed.

The AFCC machine has higher power density than a traditional induction machine. As the pole number increasing, this advantage becomes increasingly apparent. For example, a 12-pole AFCC machine ideally has 2.8 times the power density of an induction machine. Later by comparing the prototype to a commercial induction machine, it is found that the power density (or torque density) of the prototype is about 3 times as the same as that of the induction machine.

The circumferential winding totally eliminates the end-winding portion of the machine. This will significantly reduce the amount of copper used in the machine, which not only reduces the cost, but also reduces the copper losses and stator leakage inductance. Considering that the copper losses may account as many as 80% of the total losses in many forced cooling induction machines, this advantage is clearly attractive. By placing the poles with different polarities on the opposite sides of the machine, the pole-to-pole leakage, a severe problem with the TFM type machines and claw-pole machines, is eliminated. Also, the flux-focusing structure in the stator provides the application of inexpensive materials such as ferrite permanent magnets. At the same time, the structure of the machine remains reasonably simple and the use of traditional laminated silicon-iron would make the manufacturing cost acceptable.

The torque ripple of the AFCC machine has been identified as the major drawback with this machine. The situation can be improved by introducing

several identical machines on the same shaft. Although additional machines could be introduced, two machines coupled on the same shaft would appear to provide an optimized structure. Use of the proper winding arrangement provides the possibility of using this twin machine structure with either a two or three phases. To further improve the torque ripple, current modulation can be employed as has been successfully demonstrated for SRMs.

1.8 The Flux Reversal Machine (FRM)

The formidable performance of high energy PMs allowed recently to look for direct drives for low speeds, in the hope that the low speed machine will have competitive (or better) overall torque machine will have competitive (or better) overall torque/losses at less total weight than the indirect drive which includes the high speed motor and the mechanical transmission.

Also the overall costs are to be reduced. The additional advantage is that the configuration is more rugged, and needs less maintenance.

finally the absence of backlash makes the precision position control much simpler with direct drives. As a travelling field winding stator is not feasible, unless a travelling field winding stator is not feasible, unless the torque is in the thousands of Nm, to allow pole pitches above $60mm$ or so, other machine configurations have to be considered.

Compared with a commercial 2-D flux machine (i.e. one with no useful axial flux component), a 3-D flux machine adds complexity to machine manufacturing and needs special magnetic materials, such as iron powder. These facts make it difficult to justify the cost-effectiveness for commercial applications except for certain special situations.

In an attempt to retain the advantages of both transverse flux machine, the flux reversal machine (FRM) has been proposed [21] Fig.1.13 .

A flux reversal machine FRM is doubly salient stator permanent magnet machine with a windingless rotor where the flux reverses polarities in the concentrated coils. The FRM machine may be build in single or multiple phase configurations.

In essence the FRM has a magnetic configuration typical to the switched reluctance machine but with multipole PMs of alternate polarity on each stator salient pole embraced by concentrated coils. The coils are connected into a three phase configuration. The double pole pitch of stator PMs corresponds to the pole plus interpole rotor span. Thus the PM flux linkage with stator coils reverses sign.

In essence the FRM has a magnetic configuration typical Fig. 1.14 to the switched reluctance machine but with multipole PMs of alternate polarity on each stator salient pole embraced by concentrated coils.

The general relationship between the number of stator and rotor poles N_s, N_r, and the number of phases m can be expressed as:

$$\frac{N_s}{N_r} = \frac{m}{m+1} \tag{1.19}$$

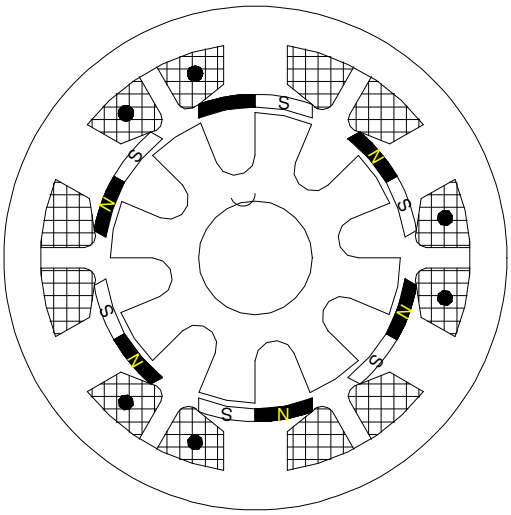

Figure 1.13: FRM topology.

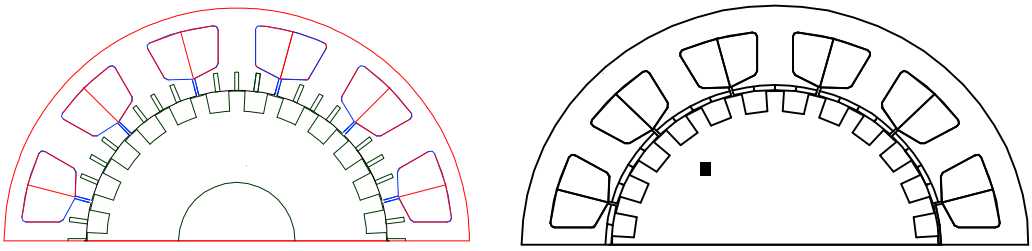

Figure 1.14: FRM machine a) inset magnets b) pole magnets.

The coils are connected into a three phase configuration. The double pole pitch of stator PMs corresponds to the pole plus interpole rotor span. Thus the PM flux linkage with stator coils reverses sign. There is, again, notable PM flux fringing (leakage), but an adequate geometry should manage to produce rather large force density up to $5N/cm^2$. Also, by rotor pole skewing, the EMF may be made almost sinusoidal and the cogging torque may be reduced below 3% of the rated torque.

The sinusoidal emf allows for typical vector control of the FRM. The phase self-inductance varies little with the rotor position [8, 36]. So the reluctance torque component is negligible. Hence the interaction torque pulsation with sinusoidal current may be reduced under 2-3%.

These low torque pulsations machines are typical requirements for high performance servo drives. As vector control is performed on account of sinusoidal EMF, we may be tempted to consider the FRM similar in behavior to travelling field machines.

Typical configurations for $Qs = 12$ are shown in Fig. 1.15 and 1.16 . The one in Fig. 1.15 has the PMs on the stator pole shoes, very close to the airgap.

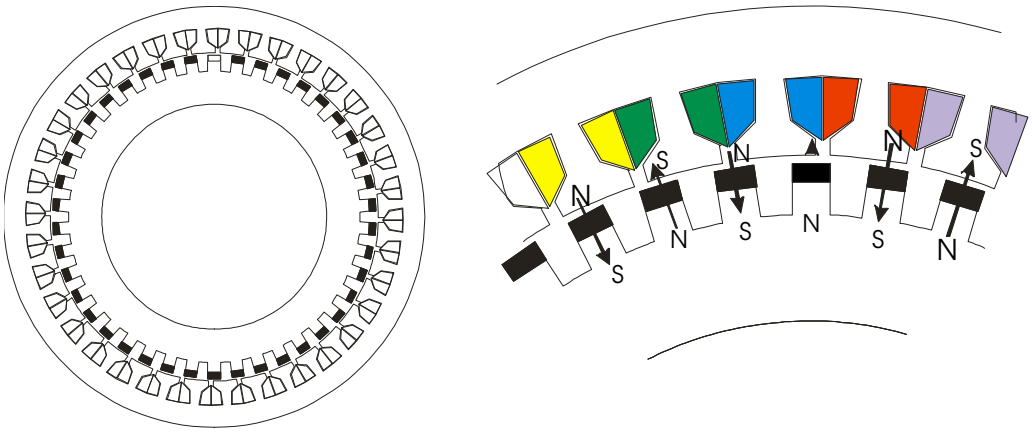

Figure 1.15: FRM withpole-PMs.

We may say it has pole-PMs. On the other hand the configuration in Fig. 1.16 has inset magnets.

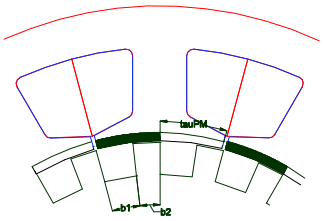

Figure 1.16: FRM with pole magnets.

The inset PM FRM has the PMs parallel to the stator magnet flux lines and thus are much more difficult to demagnetize. As a bonus the flux in the magnets varies less (especially under load). Thus the eddy currents induced with PMs are notably smaller than for the pole- PM configuration whose PMs experience directly the stator current additional field. The much lower total (magnetic) airgap of the inset-PM FRM leads to much larger inductance which is limited by heavy saturation of the core for high currents (over load). So the stator current limits are mainly governed by stator temperature and magnetic over-saturation in the inset PM configuration and stator temperature and PM demagnetization limit the currents for the pole-PM FRM.

In the FRM with N_r rotor salient poles the speed n and frequency f are related by:

$$f_1 = nN_r \tag{1.20}$$

The two pole pitch angle corresponds to two PM poles of alternate polarities on the stator, that is:

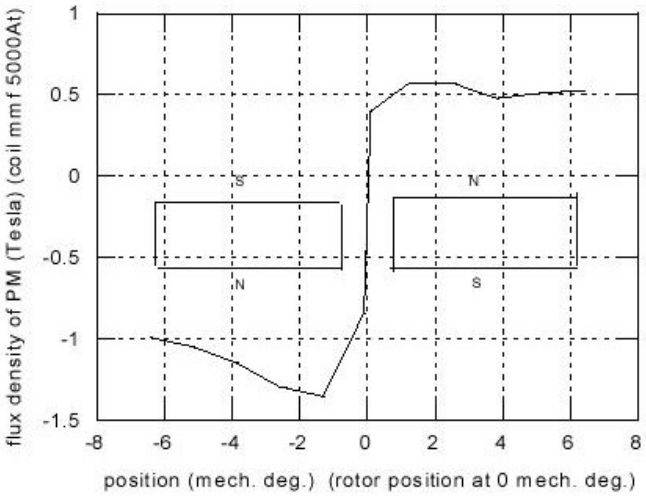

Figure 1.17: FRM flux per pole

$$2\tau_{PM} = 2\tau_{rot} = \frac{2D_r}{N_r} \tag{1.21}$$

A stator pole may accommodate $2np$ permanent magnets. The electrical angle of the space between two neighboring stator pole PMs should be 120 electrical degrees or $120/Nr$ geometrical degrees or $2\tau_{\mathrm{PM}}/3$. Thus:

$$Q_s\left(2n_p\tau_{PM} + \frac{2\tau_{PM}}{3}\right) = \pi\left(D_r + 2g\right) \tag{1.22}$$

where Qs is the number of stator poles and g is the mechanical airgap.

For the inset-PM FRM the airgap should be as small as mechanically feasible and the PM thickness $h_{PM} > 6g$. Also the stator and rotor teeth should be equal to each other while the rotor interpole will span the rest of the double-pole pitch.

$$\begin{aligned} \tau_{PM} &= h_{PM} + b_{t1} \\ 2\tau_{PM} &= b_{t2} + b_{s2} \\ b_{t2} &= b_{t1} \end{aligned} \tag{1.23}$$

Also the stator and rotor teeth should be equal to each other while the rotor interpole will span the rest of the double-pole pitch:

A configuration of a 12 pole FRM machine is presented in [11]. The machine has pole-PMs on stator; number of stator slots $Q_s = 12$, number of poles $n_p = 2$, number os rotor slots $Nr = 28$, base speed n$= 128rpm$ at $f_1 = nNr = 60Hz$

The PM flux per pole is presented in Fig 1.17 were it is obviously that the form of the flux versus position is perfect sinusoidal. Instead the cogging torque is too large for a servo quality drive (10% rated servo drive). Skewing

the rotor by various angles seems to be indicate as a solution to eliminate this drawback. For 1.8 degrees mechanical skewing we obtain a reduction below 1.5% which allows the use of the FRM machine for servo drives. A 7% loss in the maximum PM flux per phase is encountered with 1.80 (mechanical) degrees of skewing. reduced below 1.5%, which qualifies FRM for servodrives.

The skewing has the additional effect of shifting the phase PM flux (as expected). This effect is important when designing the control system.

The FEM analysis shows that the flux density in the permanent magnet do not change sign. The permanent magnets are not demagnetized mainly because the fringing effect of the magnets in large gap structure.

1.8.1 Flux Reversal Machine performances

The three phase FRM is a new class of machine with a robust structure and is well suited both for high (or very low speed applications and industrial drives systems). The great advantage that it has a simple easy manufacturable configuration with a true 2D flux pattern. Control strategies with may be applied as for the brushless DC motors .

In-depth FEM study shows a high torque density and less than 3% torque pulsation with sinusoidal three phase vector control. The self inductance is almost independent of rotor position and the mutual inductance is negligible. Depending on the potential low speed application, two configurations are feasible (with pole magnets or with inset magnets).

The FRM for low speed drives has the following distinct features:

– it uses conventional stamped laminations both on the stator and on the rotor

– it has no PMs or windings on the rotor.

– it has PMs on the stator where their temperature can be easily monitored and controlled.

– the stator has concentrated coils which are easy to manufacture.

– the lowest pole pitch τ_{PM} is to be larger than (PM +airgap) thickness [5-6] to limit flux fringing PM utilization as is with the transverse-flux PM machine which has the PMs placed on the rotor.

– the higher the rotor diameter (or torque), the larger the maximum number of pole pairs (2 PM) and thus the lower the speed at 50 Hz.

–the pole-PM FRM has lower inductances than the inset PM FRM as expected. Also the cogging torque of the latter is intrinsically smaller.

1.9 Comparison between PM non-overlapping winding machines

The great variety of electrical machines makes a comparison between different types of machines difficult [24-25]. In order to do this a general sizing equation would be a very useful and can easily be applied to every radial flux machines (RFM) , axial flux machines (AFM) and transverse flux machines

(TFM) and which takes different waveforms and machine characteristics into account. In [2] a general approach is presented based on a general set of equations.

1.9.1 Sizing Equation Analysis and Torque Density for (RFPM, AFPM, TFM)

The output power is given by 1.24:

$$P_R = \eta \frac{m}{T} \int_0^T e(t)i(t)dt = \eta m K_p E_P I_{PK} \tag{1.24}$$

where

$e(t)$ and Epk are phase air gap EMF and its peak value,
$i(t)$ and Ipk are phase current and the peak phase current,
η is machine efficiency
m is number of phases of the machine;
T is period of one cycle of the EMF.
The quantity K is termed the electrical power waveform is defined by :

$$K_p = \frac{1}{T} \int_0^T \frac{e(t) \times i(t)}{E_{PK} \times I_{PK}} dt = \frac{1}{T} \int_0^T f_e(t) f_i(t) dt \tag{1.25}$$

where $fe(t) = e(t)/Epk$ and $f_i(t) = i(t)/Ipk$ are the normalized EMF and current waveforms.

To indicate the effect of the current waveform, a current waveform factor K_i is defined:

$$K_i = \frac{I_{PK}}{I_{rms}} = \sqrt{\left(\frac{1}{T} \int_0^T \frac{i(t)}{I_{PK}} dt \right)} \tag{1.26}$$

The peak value of the phase airgap EMF in (1.24) is given by:

$$E_{PK} = \begin{cases} K_e N_t B_g \frac{f}{p} \lambda_o D_o L_e & \text{RFM} \\ K_e N_t B_g \frac{f}{p} (1 - \lambda^2) D_o^2 & \text{AFM} \\ K_e N_t B_g \frac{f}{p} \lambda_o D_o L_e & \text{TFM} \end{cases} \tag{1.27}$$

where

Ke is the EMF factor which incorporates the winding distribution factor K_w and the per unit portion of the total air gap area spanned by the salient poles of the machine (if any),
N_t is the number of turn per phase,
B_g is the flux density in the airgap,
f is the converter frequency,
p is the machine pole pairs,
λ_o is the diameter ratio for RFM defined as D_g/D_o , l

λ is the diameter ratio for AFM defined as D_i/D_o , D o is the diameter of the machine outer surface,

D_g is the diameter of the machine airgap surface,

D_i is the diameter of the machine inner surface and

L_e is the effective stack length of the machine.

The peak phase current in (1.24) is given by

$$I_{PK} = \begin{cases} \frac{1}{1+K_\phi} K_i A \pi \lambda_o \frac{D_o}{2m_1 N_t} & \text{RFM} \\ \frac{1}{1+K_\phi} K_i A \pi \frac{1+\lambda}{2} \frac{D_o}{2m_1 N_t} & \text{AFM} \\ \frac{1}{1+K_\phi} K_i A \frac{L_e}{2N_t} & \text{TFM} \end{cases} \tag{1.28}$$

where

A is the total electrical loading in. $K_\Phi = A_r/A_s$ is the ratio of electrical loading on rotor and stator. In a machine topology without a rotor winding, $K_f = 0$. In general case, the total electrical loading, A, should include both the stator electrical loading A_s and rotor electrical loading A_r.

Combining 1.24 through 1.28 , the general purpose sizing equations take the following form for RFM, AFM and TFM:

$$P_R = \begin{cases} \frac{1}{1+K_\phi} \frac{m}{m_1} \frac{\pi}{2} K_e K_i K_p K_L \eta B_g A \frac{f}{p} \lambda_o^2 D_o^2 L_e \\ \frac{1}{1+K_\phi} \frac{m}{m_1} \frac{\pi}{2} K_e K_i K_p K_L \eta B_g A \frac{f}{p} \lambda_o^2 D_o^3 \end{cases} \text{RFPM} \tag{1.29}$$

$$P_R = \begin{cases} \frac{1}{1+K_\phi} \frac{m}{m_1} \frac{\pi}{2} K_e K_i K_p K_L \eta B_g A \frac{f}{p} \left(1-\lambda^2\right) \frac{1+\lambda}{2} D_o^2 L_e \\ \frac{1}{1+K_\phi} \frac{m}{m_1} \frac{\pi}{2} K_e K_i K_p K_L \eta B_g A \frac{f}{p} \left(1-\lambda^2\right) \frac{1+\lambda}{2} D_o^3 \end{cases} AFPM \tag{1.30}$$

$$P_R = \begin{cases} \frac{1}{1+K_\phi} \frac{m}{m_1} \frac{\pi}{2} K_e K_i K_p K_L \eta B_g A \frac{f}{p} \lambda_o^2 D_o^2 L_e \\ \frac{1}{1+K_\phi} \frac{m}{m_1} \frac{\pi}{2} K_e K_i K_p K_L \eta B_g A \frac{f}{p} \lambda_o^2 D_o^3 \end{cases} TFM \tag{1.31}$$

where

$K_L = L_e/D_g$ is the aspect ratio coefficient for the RFM and the TFM and

$K_L = D_o/L_e$ is the aspect ratio coefficient for AFM.

Torque density is defined as:

$$T_{den} = \frac{T_R}{\frac{1}{4} D_{tot}^2 L_{tot}} = \frac{P_R}{\Omega_r \frac{1}{4} D_{tot}^2 L_{tot}} \tag{1.32}$$

Where T_R is the rated torque;

Power density is:

$$P_{den} = \frac{P_R}{\frac{1}{4} D_{tot}^2 L_{tot}} \tag{1.33}$$

Based on this approach a general comparation between Axial flux and Radial flux PM machine it has been made.

$$Densityratio = \frac{T_{den}}{T_{den} - RFSM} = \frac{P_{den}}{P_{den} - RFSm} \tag{1.34}$$

In Fig. 1.18 the ratio Power/Torque density is used to illustrate the difference between radial flux and axial flux topologies[2].

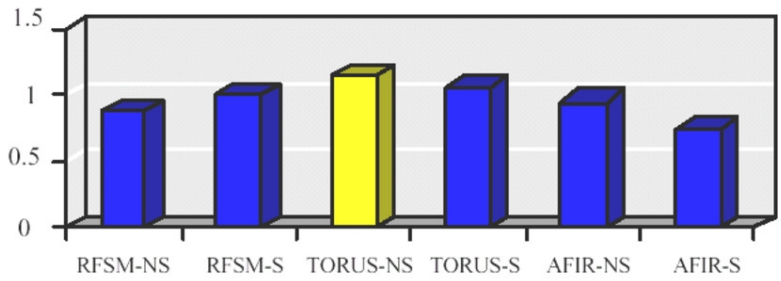

Figure 1.18: Power/torque comparison of different topologies

1.10 Conclusion

From this information and data gathered from literature, following conclusions are obviously:

Axial flux type machines can be better than the other machines in terms of power/torque density and efficiency. In addition, Axial Flux TORUS-NS topology has the highest power/ torque density and efficiency. Considering the drawback for TFM and AFCC machine (Low power factor, mechanichal complexitivity)

AFPM type machines are better than the others in terms of weight and utilization. Furthermore, the AFPM topology has the lowest weight and the highest utilization factor.

· Generally, the external rotor topologies are better than the internal rotor topologies in terms of power/torque density and efficiency[1].

· Non- slotted topologies of AFM are always better than slotted topologies of AFM in terms of power /torque density, efficiency and heat dissipation.

· The internal rotor topology of AFM can be easily used with cooling plate for conductor heat transfer.

· The slotless TORUS topology has the highest torque density ratio compared to other topologies.

However for simple applications the complexity of the axial flux PMSm can be a big drawback so other challengers can face better the challenge to obtain a low speed high torque and good power density like the FRM. Our work will be focused on both of this topologies axial flux PMSM and flux reversal machines.

Bibliography

[1] A.Cavagnino, M Lazzari, F. Profumo, A. Tenconi, "A comparison between the axial flux and the radial flux structures for PM synchronous motors", IEEE Trans. on Ind. Appl Vo138, issue 6 Nov Oct. 2002

[2] S. Huang, J. Liuo, F. Leonardi, T A. Lipo "A comparison of power density

for axial flux machines based on general purpose sizing equations" IEEE Trans. on Energy Conversion Vol.14 n.2 June 1999

[3] Neil Brown, L. Haydock and J. Bumby, "An Idealised Geometric Approach to Electromagnetically Comparing Axial and Radial flux Permanent Magnet Machines 1 ICEM200226-28 Aug. 2002 Bruges

[4] K.Sitapati, R.Krishnan, "Performance Comparisons of Radial and Axial field, Permanent-Magnet, Brushless Machines" IEEE Trans. on Ind. Appl. Vol.37 n.5 Sept.-Oct. 2001

[5] S. Huang, J. Liuo, T A. Lipo "Analysis and evaluation of the transverse flux circumferential current machinee" Proc. IEEE Industry Applications Society Annual Meetmg, Oct. 1997

[6] M.M. Radulescu, F. Laza and I. Husain, "Development of a Small Flux-Reversal Doubly-Salient Permanent-Magnet Motor ", Proceedings of the 15th International Conference on Electrical Machines (Brugge, Belgium, August 25 - 28, 2002)

[7] M. M. Radulescu, F. Laza, Mihaela Scortescu, S. Marinescu and Emilia Luchian, "Design and Analysis of a Small Flux-Reversal Doubly-Salient Permanent-Magnet Motor", Proceedings of the International XIII Symposium on Micromachines Servodrives - MiS '02 (Krasiczyn, Poland, 15-19 September 2002) Wydawnictwo Ksiazkowe Instytutu Elektotechniki, Warsaw, Poland, 2002, Vol. I, pp. 129-133.

[8] F.Laza, D. Cazacu, G. Champenois, M.M. Radulescu, "Finite element analysis of a small flux-reversal doubly-salient permanent-magnet motor", Proceedings of the 6th International Symposium on Electric and Magnetic fields - EMF 2003, Aachen, Germany, October 6-9, 2003, CD-ROM, Paper 5/1

2 Computation of Fractional Winding PMSM Machines Performances Using Analytical Models: a Review

2.1 Analytical model for flux density due to permanent magnet

Many research papers concentrate on the design of electrical machines. Especially, the influence on the design of the combination of pole and slot numbers is investigated in . Some examples and short studies based on FE simulations of PMSMs with concentrated windings illustrate some of the choices that have to be made during the design process In the following paragraphs, we perform a synthetic review of analytical models developed by several authors [1, 4, 3] for calculating magnetic fields of fractional winding permanent magnet motors.

The analytical model will be used to develop a symbolic solution using Wolfram Mathematica (c) software Using the literature models presented in [10] the magnetic fields due to radial permanent magnet and armature reaction in the case of internal iron-cored rotor are presented. The analytical modeling of slotless permanent magnet motors is studied by many authors. Using the analytical model of a slotless machine is possible to obtain the with enough accuracy the field of a slotted structure with the help of conformal transformations as presented in [11]

The presented model is analyzed considering no-load operating conditions. In order to obtain the air-gap field distribution, the following assumptions are necessary:

The analytical model shown in is divided into two annular regions, in which region II is magnet, region I is air-gap. In Fig. 2.1 and for internal rotor machines, Rs, Rm, Rr are the outer bore radius, the outer and inner radii of the magnet, respectively. In order to obtain an analytical solution for the field distribution produced in a multipole machine, the following assumptions are made [1].

- Two-dimensional study model,
- The permeability of magnets equals the permeability of vacuum $\mu = 4\pi \cdot 10^{-7}\ Vs/Am$,

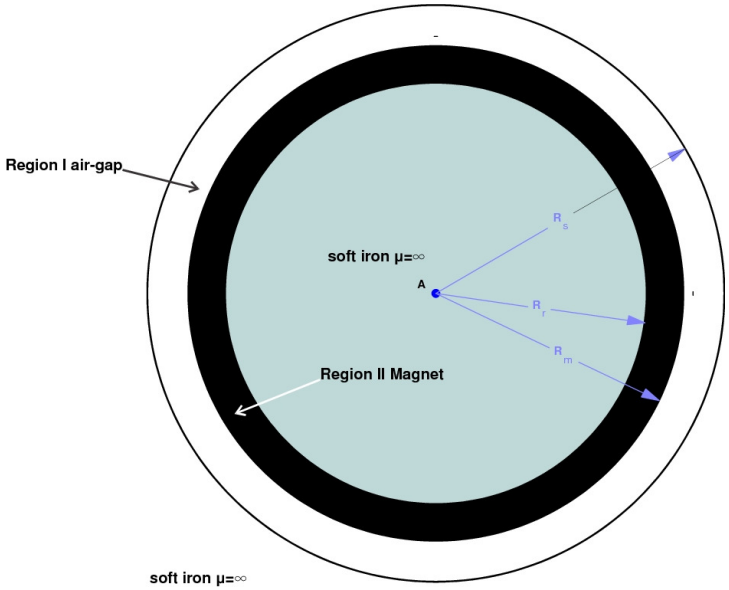

Figure 2.1: Model of slotless permanent magnet machine.

- Stator and rotor core steel has infinite permeability,
- The conductivity of all regions is assumed to be zero, i.e., eddy current effects are ignored. The model is based on the solution of Laplace and Poisson equation which are issued from Maxwell equations.

Permanent magnet machines can be build using different type of magnetization of permanent magnet exists, radial, parallel, Quasi-Halbach and Halbach array. All of these magnetization can be constituted by one bloc or segmented magnets. In order to simplify this model development , we consider only the radial magnetization case.

2.1.1 Radial permanent magnet magnetization

Different type of magnetization of permanent magnet exists, radial, parallel, Quasi-Halbach and Halbach array. All of these magnetizations can be constituted by one bloc or segmented magnets. In this study, we consider only the radial magnetization. In order to integrate the magnetic field of the permanent magnet the magnetization needs to expressed as a piecewise linear set of functions of rotor angle [1]

$$M_r(\theta) = \begin{cases} 0 & 0 \leq \theta \leq \frac{\pi}{2p} - \frac{\beta}{2} \\ \frac{B_r}{\mu_0} & \frac{\pi}{2p} - \frac{\beta}{2} \leq \theta \leq \frac{\pi}{2p} + \frac{\beta}{2} \\ 0 & \frac{\pi}{2p} + \frac{\beta}{2} \leq \theta \leq \frac{3\pi}{2p} - \frac{\beta}{2} \\ \frac{B_r}{\mu_0} & \frac{3\pi}{2p} - \frac{\beta}{2} \leq \theta \leq \frac{3\pi}{2p} + \frac{\beta}{2} \\ 0 & \frac{3\pi}{2p} + \frac{\beta}{2} \leq \theta \leq \frac{2\pi}{p} - \frac{\beta}{2} \end{cases} \tag{2.1}$$

After the expression of the magnetization as a piecewise linear set of functions it is necessary to decompose this set of functions in form of Fourier series:

$$M_r(\theta) = \sum_{n=1}^{nh} a_n \cos(np\theta) + b_n \sin(np\theta) \tag{2.2}$$

where

$$a_n = 2\,\frac{B_r\,\sin(1/2\,n\beta\,p)\,(\cos(1/2\,n\pi) - \cos(3/2\,n\pi))}{\mu_0\,n\pi} \tag{2.3}$$

$$b_n = 2\,\frac{B_r\,\sin(1/2\,n\beta\,p)\,(\sin(1/2\,n\pi) - \sin(3/2\,n\pi))}{\mu_0\,n\pi} \tag{2.4}$$

For p=2 the decomposition of permanent magnet magnetization if presented in Fig. 2.2

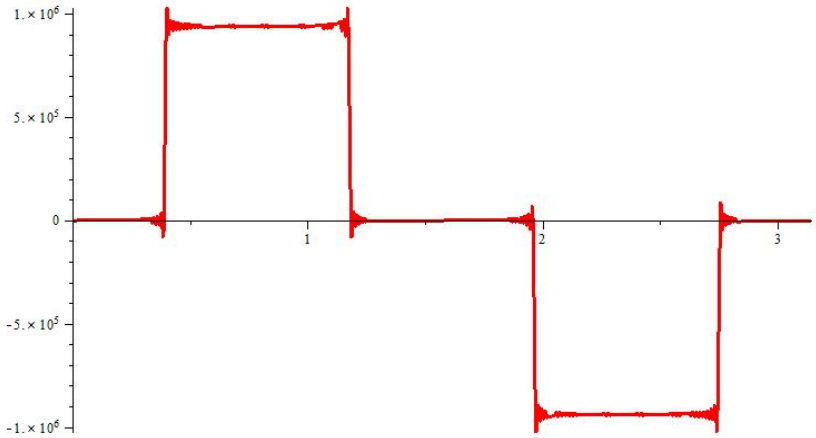

Figure 2.2: Radial magnetization decomposition using Fourier terms.

2.1.2 Vector potential and flux density due to permanent magnet

When we consider only the vector potential due to radial magnet (Fig. 2.1) where $Mt(\theta) = 0$ and $Jz(r,\theta) = 0$ the Poisson equation is reduced to:

$$-\frac{\frac{\partial}{\partial r}A_z(r,\theta)r + r^2\frac{\partial^2}{\partial r^2}A_z(r,\theta)r + \frac{\partial^2}{\partial \theta^2}A_z(r,\theta)}{r^2\mu} = \frac{\frac{d}{d\theta}Mr(\theta)}{\mu_r r} \tag{2.5}$$

This equation is valid on the permanent magnet region where permanent magnet exists. The second member of Poisson equation above is constituted by

two terms in $sin(np\theta)$ and $cos(np\theta)$. Two particular solutions are found. [2]

$$-\frac{\frac{\partial}{\partial r}A_z(r,\theta)r + r^2\frac{\partial^2}{\partial r^2}A_z(r,\theta)r + \frac{\partial^2}{\partial \theta^2}A_z(r,\theta)}{r^2\mu} = \frac{a_n \sin(np\theta)np)}{\mu_r r} \tag{2.6}$$

$$-\frac{\frac{\partial}{\partial r}A_z(r,\theta)r + r^2\frac{\partial^2}{\partial r^2}A_z(r,\theta)r + \frac{\partial^2}{\partial \theta^2}A_z(r,\theta)}{r^2\mu} = \frac{b_n \cos(np\theta)np)}{\mu_r r} \tag{2.7}$$

$$\tag{2.8}$$

$$A_z = R_s(r)\cos(np\theta) \tag{2.9}$$

$$A_z = R_c(r)\sin(np\theta) \tag{2.10}$$

$$-\frac{\frac{d}{dr}R_s(r)cos(np\theta)r + r^2\frac{d^2}{dr^2}R_s(r)cos(np\theta)r - R_s(r)cos(np\theta)n^2p^2}{r^2\mu} = \frac{b_n cos(np\theta)np)}{\mu_r r} \tag{2.11}$$

$$-\frac{\frac{\partial}{\partial r}R_c(r)sin(np\theta)r + r^2\frac{\partial^2}{\partial r^2}R_c(r)\sin(np\theta) - R_c(r)sin(np\theta)n^2p^2}{r^2\mu} = \frac{a_n sin(np\theta)np}{\mu_r r} \tag{2.12}$$

The equations can be simplified by:

$$-\frac{\frac{d}{dr}R_s(r)r + r^2\frac{d^2}{dr^2}R_s(r) - R_s(r)n^2p^2}{r^2\mu_r\mu_0} = \frac{b_n np}{\mu_r r} \tag{2.13}$$

$$-\frac{\frac{d}{dr}R_c(r)r + r^2\frac{d^2}{dr^2}R_c(r) - R_c(r)n^2p^2}{r^2\mu_r\mu_0} = \frac{a_n np}{\mu_r r} \tag{2.14}$$

The solutions of the equation and are:

$$R_s(r) = r^{-np}C_2 + r^{np}C_1 - \frac{b_n \cdot n \cdot p \cdot \mu_0 \cdot r}{n^2p^2 - 1} \tag{2.15}$$

$$R_c(r) = r^{-np}C_2 + r^{np}C_1 + \frac{a_n \cdot n \cdot p \cdot \mu_0 \cdot r}{n^2p^2 - 1} \tag{2.16}$$

In permanent magnet region, the general solution is given by

$$A_z = \left(r^{-np}C_2 + r^{np}C_1 - \frac{b_n \cdot n \cdot p \cdot \mu_0 \cdot r}{n^2p^2 - 1}\right)\cos(np\theta) + \tag{2.17}$$

$$+\left(r^{-np}C_2 + r^{np}C_1 - \frac{b_n \cdot n \cdot p \cdot \mu_0 \cdot r}{n^2p^2 - 1}\right)\sin(np\theta) \tag{2.18}$$

In the air-gap region which is constituted by air-space, the Poisson equation is reduced to Laplace equation:

$$-\frac{\frac{\partial}{\partial r}A_z(r,\theta)r + r^2\frac{\partial^2}{\partial r^2}A_z(r,\theta)r + \frac{\partial^2}{\partial \theta^2}A_z(r,\theta)}{r^2\mu} = 0 \tag{2.19}$$

$$A_z = R_s(r)\cos(np\theta) \tag{2.20}$$
$$A_z = R_c(r)\sin(np\theta) \tag{2.21}$$

$$-\frac{\frac{d}{dr}R_s(r)\cos(np\theta)r + r^2\frac{d^2}{dr^2}R_s(r)\cos(np\theta)r - R_s(r)\cos(np\theta)n^2p^2}{r^2\mu} = 0 \tag{2.22}$$

$$-\frac{\frac{\partial}{\partial r}R_c(r)\sin(np\theta)r + r^2\frac{\partial^2}{\partial r^2}R_c(r)\sin(np\theta) - R_c(r)\sin(np\theta)n^2p^2}{r^2\mu} = 0 \tag{2.23}$$

The equations can be simplified by :

$$-\frac{\frac{d}{dr}R_s(r)r + r^2\frac{d^2}{dr^2}R_s(r) - R_s(r)n^2p^2}{r^2\mu_r\mu_0} = 0 \tag{2.24}$$
$$-\frac{\frac{d}{dr}R_c(r)r + r^2\frac{d^2}{dr^2}R_c(r) - R_c(r)n^2p^2}{r^2\mu_r\mu_0} = 0 \tag{2.25}$$

The solutions of the equation and are:

$$R_s(r) = r^{-np}C_2 + r^{np}C_1 \tag{2.26}$$
$$R_c(r) = r^{-np}C_2 + r^{np}C_1 \tag{2.27}$$

$$A_a = (r^{-np}C_1 + r^{np}C_2)\cos(np\theta) + (r^{-np}C_1 + r^{np}C_2)\sin(np\theta) \tag{2.28}$$

The general solution of potential vector in the air-gap is given by:

$$A_a = (C_5r^{np} + C_6r^{-np}\cos(np\theta) + (C_7r^{np} + C_8r^{-np})\sin(np\theta) \tag{2.29}$$

The radial component of flux density in permanent magnet region is:

$$B_{mr}(r,\theta) = \frac{\frac{d}{d\theta}A_z(r,\theta)}{r} \tag{2.30}$$

$$B_{mr}(r,\theta) = \frac{-\left(r^{-np}C_1 + r^{np}C_2 - \frac{b_n n\cdot p\cdot \mu_0\cdot r}{n^2p^2-1}\right)\sin(np\theta)np}{r} \tag{2.31}$$

$$\frac{+\left(r^{n*p}C_4 + r^{-n*p}C_3 + \frac{a_n\cdot n\cdot p\mu_0 r}{n^2p^2-1}\right)\cos(np\theta)np}{r} \tag{2.32}$$

The tangential [2] component of flux density in permanent magnet region is:

$$B_{mt}(r,\theta) = -\left(\frac{r^{np}npC_2}{r} - \frac{r^{-np}npC_1}{r} - \frac{b_npp\mu_0 r}{(n^2p^2-1)}\right)cos(np\theta) - \tag{2.33}$$

$$-\left(\frac{r^{np}C_4}{r} + \frac{r^{-np}C_3}{r} + \frac{a_npp\mu_0 r}{n^2p^2-1}\right)\sin(np\theta) \tag{2.34}$$

The radial component of flux density in the air-gap region is:

$$B_{ar}(r,\theta) = \frac{1}{r}\frac{\partial A_a(r,\theta)}{\partial\theta} \tag{2.35}$$

$$B_{ar}(r,\theta) = \frac{(-(C_5 r^{np} + C_6 r^{-np})\sin(np\theta)np + (C_7 r^{np} + C_8 r^{-np})\cos(np\theta)np)}{r} \quad (2.36)$$

The tangential component of flux density in the air-gap region is:

$$B_{at}(r,\theta) = -\frac{\partial A_a(r,\theta)}{\partial r} \quad (2.37)$$

$$B_{at}(r,\theta) = -\left(\frac{C_5 r^{np} np}{r} - \frac{C_6 r^{-np} np}{r}\right)\cos(np\theta) - \left(\frac{C_7 r^{np} np}{r} - \frac{C_8 r^{-np} np}{r}\right)\sin(np\theta) \quad (2.38)$$

In the air-gap, the radial magnetic excitation H is given by:

$$H_{ar}(r,\theta) = \frac{B_{ar}(r,\theta)}{\mu_0} \quad (2.39)$$

$$H_{ar}(r,\theta) = \frac{-(C_5 r^{np} + C_6 r^{-np})\sin(np\theta)np + (C_7 r^{np} + C_8 r^{-np})\cos(np\theta)np}{r\mu_0} \quad (2.40)$$

In the air-gap, the tangential magnetic excitation H is given by:

$$H_{ar}(r,\theta) = \frac{B_{at}(r,\theta)}{\mu_0} \quad (2.41)$$

$$H_{ar}(r,\theta) = \frac{-\left(\frac{C_5 r^{np} np}{r} - \frac{C_6 r^{-np} np}{r}\right)\cos(np\theta) - \left(\frac{C_7 r^{np} np}{r} - \frac{C_8 r^{-np} np}{r}\right)\sin(np\theta)}{\mu_0} \quad (2.42)$$

In the permanent magnet region, the radial and tangential magnetic excitation H take into account the radial and tangential magnetization of permanent magnet as:

$$M_t(\theta) = 0 \quad (2.43)$$

$$M_r(\theta) = a_n\cos(np\theta) + b_n\sin(np\theta) \quad (2.44)$$

$$H_{mr}(r,\theta) = \frac{B_{mr}(r,\theta) - \mu_0 M_r(\theta))}{\mu_0\mu_r} \quad (2.45)$$

$$\begin{aligned} H_{mr}(r,\theta) = {} & \frac{1}{(\mu_0\mu_r)}\left(\frac{-(r^{np}C_2 + r^{-np}C_1 - \frac{b_n np\mu_0 r}{n^2p^2-1})\sin(np\theta)np}{r} - \right. \\ & \left. -\frac{(r^{np}C_4 + r^{-np}C_3 - \frac{a_n np\mu_0 r}{n^2p^2-1})\cos(np\theta)np}{r}\right) - \\ & -\frac{a_n\cos(np\theta) + b_n\sin(np\theta)}{\mu_0\mu_r} H_{mt}(r,\theta) = \frac{B_{mt}(r,\theta) - \mu_0 M_t(\theta)}{\mu_0\mu_r} \end{aligned} \quad (2.46)$$

$$\begin{aligned} H_{mt}(r,\theta) = {} & \frac{-\left(\frac{r^{np}npC_2}{r} - \frac{r^{-np}npC_1}{r} - \frac{b_n npmu0}{n^2p^2-1}\right)\cos(np\theta)}{\mu_0\mu_r} \\ & -\frac{\left(\frac{r^{np}npC_4}{r} - \frac{r^{-np}npC_3}{r} + \frac{a_n np\mu_0}{n^2p^2-1}\right)\sin(np\theta)}{\mu_0\mu_r} \end{aligned} \quad (2.47)$$

The first boundary condition is is due to the ferromagnetic material of stator where relative permeability is considered infinity [3-4]:

$$H_{at}(R_s, \theta) = 0 \tag{2.48}$$

$$\frac{-\left(\frac{(C_5 R_s^{np})np}{R_s} - \frac{C_6 R_s^{-np} np}{R_s}\right)\cos(np\theta) - \left(\frac{C_7 R_s^{np} np}{R_s} - \frac{C_8 R_s^{-np} np}{R_s}\right)\sin(np\theta)}{\mu_0} = 0 \tag{2.49}$$

The interface condition between magnet and air-gap regions in term of radial flux density is given by:

$$B_{ar}(R_m, \theta) = B_{mr}(R_m, \theta) \tag{2.50}$$

$$\frac{-(C_5 {R_m}^{np} + C_6 {R_m}^{-np})sin(np\theta)np + (C_7 {R_m}^{np} + C_8 {R_m}^{-np})\cos(np\theta)np)}{R_m} \tag{2.51}$$

$$= \frac{\begin{array}{c}-({R_m}^{np} C_2 + {R_m}^{-np} C_1 - \frac{b_n np\mu_0 R_m}{n^2p^2-1})\sin(np\theta)np + ({R_m}^{np} C_4 + {R_m}^{-np} C_3 \\ + \frac{a_n np\mu_0 R_m}{n^2p^2-1})\cos(np\theta)np)\end{array}}{R_m}$$

The interface condition between magnet and air-gap regions in term of tangential magnetic excitation is given by:

$$H_{at}(R_m, \theta) = H_{mt}(R_m, \theta) \tag{2.53}$$

$$\frac{-\left(\frac{C_5 R_m^{np} np}{R_m} - \frac{C_6 R_m^{-np} np}{R_m}\right)\cos(np\theta) - \left(\frac{C_7 R_m^{(np)} np}{R_m} - \frac{C_8 R_m^{-np} np}{R_m}\right)\sin(np\theta)}{\mu_0} = \tag{2.54}$$

$$\frac{-\left(\frac{R_m^{np} npC_2}{R_m} - \frac{R_m^{-np} npC_1}{R_m} - \frac{b_n np\mu_0}{n^2p^2-1}\right)\cos(np\theta)}{\mu_0\mu_r} -$$

$$\frac{\left(\frac{R_m^{np} npC_4}{R_m} - \frac{R_m^{-np} npC_3}{R_m} + \frac{a_n np\mu_0}{n^2p^2-1}\right)\sin(np\theta)}{\mu_0\mu_r}$$

Below boundary condition is due to the ferromagnetic material of rotor where relative permeability is considered infinite:

$$H_{mt}(R_r, \theta) = 0 \tag{2.55}$$

$$\frac{-\left(\frac{R_r^{np} npC_2}{R_r} - \frac{R_r^{-np} npC_1}{R_r} - \frac{b_n np\mu 0}{n^2p^2-1}\right)\cos(np\theta)}{\mu_0\mu_r} - \tag{2.56}$$

$$\frac{-\left(\frac{R_r^{np} npC_4}{R_r} - \frac{R_r^{-np} npC_3}{R_r} + \frac{a_n np\mu_0}{n^2p^2-1}\right)\sin(np\theta)}{\mu_0\mu_r} = 0$$

From 2.49, we can write the two equations below:

$$\begin{aligned}\frac{1}{\mu_0}\frac{-C_5{R_s}^{np}np}{R_s}+\frac{C_6R_s^{-np}np}{R_s}=0\\ \frac{1}{\mu_0}\frac{-C_7{R_s}^{np}np}{R_s}+\frac{C_8R_s^{-np}np}{R_s}=0\end{aligned} \tag{2.57}$$

From 2.50, we have:

$$\begin{aligned}\frac{(C_7{R_m}^{np}+C_8{R_m}^{-np})np}{R_m} &= \frac{\left({R_m}^{np}C_4+{R_m}^{-n*p}C_3+\frac{a_nnp\mu_0R_m}{(n^2p^2-1)}\right)np}{R_m}\\ -\frac{(C_5{R_m}^{np}+C_6{R_m}^{-np})np}{R_m} &= \frac{-({R_m}^{np}C_2+R_m^{-np}C_1-\frac{b_nnp\mu_0R_m}{n^2p^2-1})np}{R_m}\end{aligned} \tag{2.58}$$

From 2.53, we have:

$$\begin{aligned}\frac{1}{\mu_0}\frac{-C_5{R_m}^{np}np}{R_m}+\frac{C_6{R_m}^{-np}np}{R_m}=\frac{\left(\frac{-R_m{}^{np}npC_2}{R_m}+\frac{R_m{}^{-np}npC_1}{R_m}+\frac{b_nnp\mu_0}{n^2p^2-1}\right)}{\mu_0\mu_r}\\ \frac{1}{\mu_0}\left(-\frac{C_7{R_m}^{np}np}{R_m}+\frac{C_8{R_m}^{-np}np}{R_m}\right)=\frac{1}{\mu_0\mu_r}\left(-\frac{{R_m}^{np}npC_4}{R_m}+\frac{{R_m}^{-np}npC_3}{R_m}-\frac{a_nnp\mu_0R_m}{(n^2p^2-1)}\right)\end{aligned} \tag{2.59}$$

From 2.55, we have:

$$\left(-\frac{R_r^{np}npC_2}{R_r}+\frac{R_r{}^{-np}npC_1}{R_r}+\frac{b_nnp\mu_0}{n^2p^2-1}\right)\frac{1}{\mu_0\mu_r}=0 \tag{2.60}$$

$$\left(-\frac{R_r{}^{np}npC_4}{R_r}+\frac{R_r{}^{-np}npC_3}{R_r}-\frac{a_nnp\mu_0}{n^2p^2-1}\right)\frac{1}{\mu_0\mu_r}=0 \tag{2.61}$$

We have 8 equations with 8 variables. The solution is given by solving the system formed by equations 1 to 8 for variables $C_1, C_2, C_3, C_4, C_5, C_6, C_7, C_8$.

In this study, where we are interested to obtain the electromagnetic torque and back E.M.F. in the air-gap. For this reason the vector potential in the air-gap is given by:

$$A_a=\sum_{n}^{n_{max}}\left((C_5r^{np}+C_6r^{-np})\cos(np\theta)+(C_7r^{np}+C_8r^{-np})\sin(np\theta)\right) \tag{2.62}$$

Fig. 2.3 presents the resulting potential in the airgap

2.2 Analytical model for flux density due to stator current

In a similar manner to the prediction of the open-circuit magnetic field described above, the two-dimensional armature reaction field distribution is obtained for slotless non-overlapping PM machine with iron-cored internal rotor

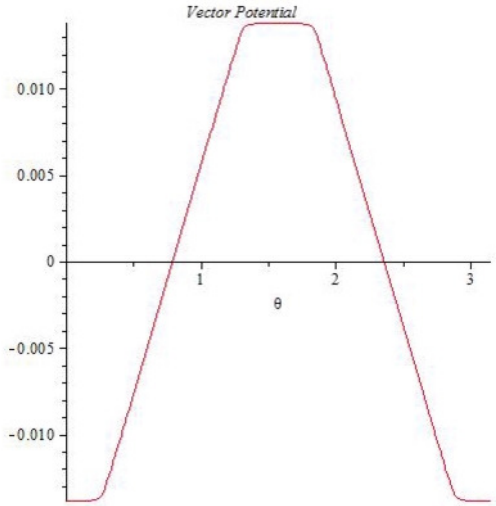

Figure 2.3: Vector potential due to permanent magnet.

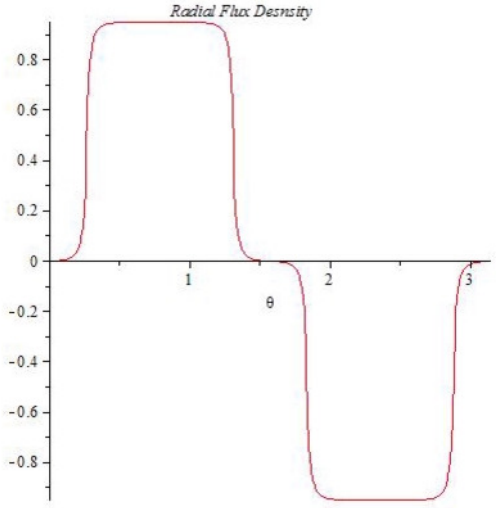

Figure 2.4: Radial flux density due to permanent magnet.

assuming a smooth air gap in polar coordinates and recoil permeability of the permanent magnets to be unity. A multiple pole case is analyzed in this section as above [1]; .

To determine flux density created by the three phases current, the entire winding must be stated as [2] The current sheet is distributed such that the current density is uniform along an arc at $r = R_s$ whose length is equal to the slot opening Fig. 2.6. the current sheet density for one phase is given by:

$$K_s = J_{cn} cos(n_i \theta + x_a) \tag{2.63}$$

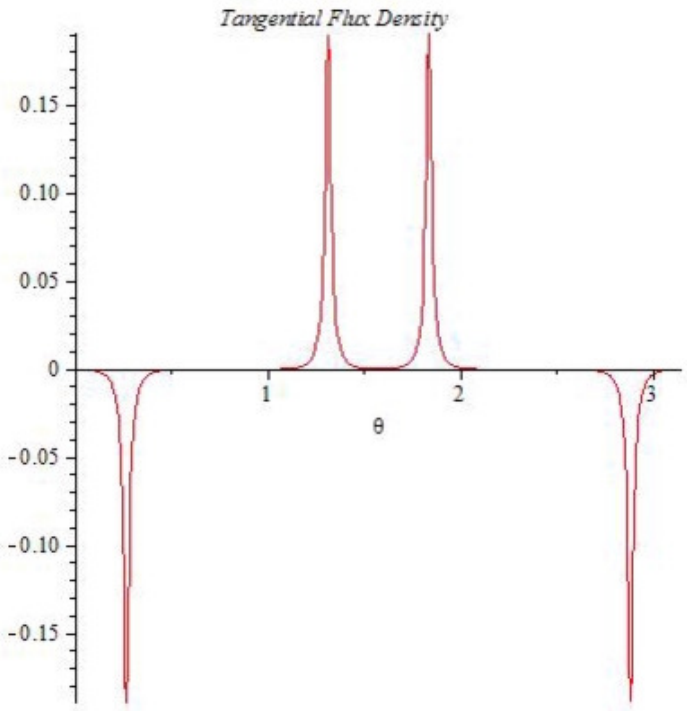

Figure 2.5: Tangential flux density due to permanent magnet..

In the magnetic air-gap (Fig. 2.6), the Laplace equation to be solved is:

$$\frac{\partial^2}{\partial r^2}u_i(r,\theta)+\frac{1}{r}\frac{\partial}{\partial r}u_i(r,\theta)+\frac{1}{r^2}\frac{\partial^2}{\partial \theta^2}u_i(r,\theta)=0 \tag{2.64}$$

By applying the method of separation of variables, the general solution is given by:

$$u_i(r,\theta)=R_i(r)\cos(n_i\theta+x_a) \tag{2.65}$$

$$R_i(r)=C_1r^{-ni}+C_2r^{ni} \tag{2.66}$$

$$B_{ri}(r,\theta)=\frac{1}{r}\frac{\partial}{\partial \theta}u_i(r,\theta) \tag{2.67}$$

$$B_{ri}(r,\theta)=\frac{-(C_1r^{ni}+C_2r^{-ni})sin(ni\theta+xa)ni}{r} \tag{2.68}$$

$$H_{ri}=\frac{B_{ri}}{\mu_0} \tag{2.69}$$

$$H_{ri}(r,\theta)=\frac{-(C_1r^{ni}+C_2r^{-ni})\sin(ni\theta+xa)ni}{r\mu_0} \tag{2.70}$$

$$B_{\theta i}(r,\theta)=-\frac{\partial}{\partial r}u_i(r,\theta) \tag{2.71}$$

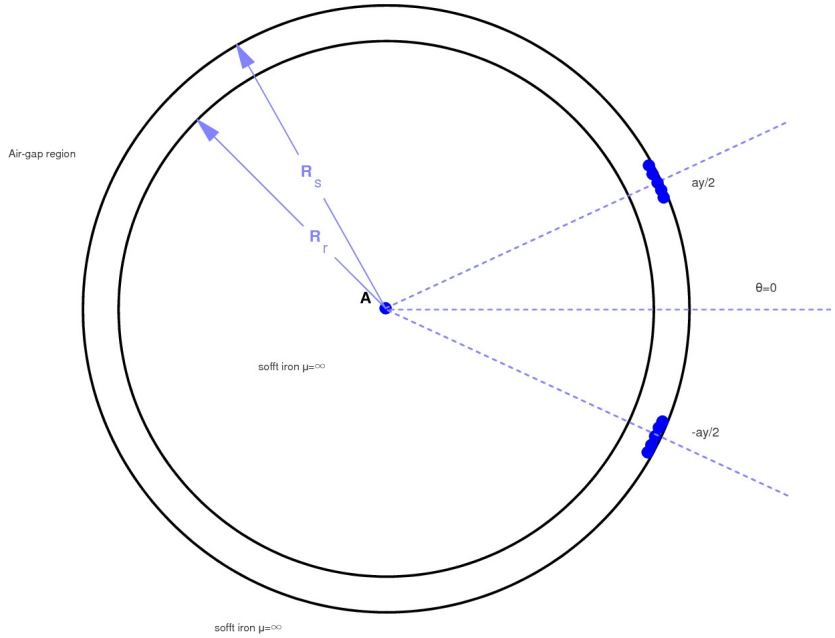

Figure 2.6: Slotless winding distribution in smooth air gap.

$$B_{\theta i}(r,\theta) = -\left(\frac{C_1 r^{ni} ni}{r} - \frac{C_2 r^{-ni} ni}{r}\right) cos(ni\theta + xa) \tag{2.72}$$

$$H_{\theta i}(r,\theta) = \frac{B_{\theta i}(r,\theta)}{\mu_0} \tag{2.73}$$

$$H_{\theta i}(r,\theta) = -\frac{\left(\frac{C_1 R_r^{ni} ni}{r} - \frac{C_2 R_r{}^{-ni} ni}{r}\right) \cos(ni\theta + xa)}{\mu_0} \tag{2.74}$$

Two boundary conditions are applied to determine constants C_1 and C_2 :

$$H_{\theta i}(r,\theta)_{r=R_r} = 0 \tag{2.75}$$

$$-\frac{\left(\frac{C_1 R_r^{ni} ni}{R_r} - \frac{C_2 R_r{}^{-ni} ni}{R_r}\right) \cos(ni\theta + xa)}{\mu_0} = 0 \tag{2.76}$$

$$H_{\theta i}(r,\theta)_{r=R_s} = 0 \tag{2.77}$$

$$H_t(r,\theta)_{r=R_s} = -K_s \tag{2.78}$$

$$-\left(\frac{C_2 R_r{}^{-2ni} R_s{}^{ni} ni}{R_s} - \frac{C_2 R_s{}^{-ni} ni}{R_s}\right) \frac{cos(ni\theta + xa)}{\mu_0} = -J_{cn} cos(n_i\theta + x_a) \tag{2.79}$$

$$C_1 = \frac{C_2 R_r{}^{-ni}}{R_r^{ni}} \tag{2.80}$$

$$C_2 = \frac{J_{cn} R_s \mu_0}{ni(R_r^{-2ni} R_s^{ni} - R_s^{-ni})} \tag{2.81}$$

$$X_{ti} = \frac{J_{cn} R_s \, \mu_0 \, \left(R_r^{-2\,ni} r^{ni} + r^{-ni}\right) \sin\left(ni\,\theta + x_a\right)}{r\left(R_r^{-2\,ni} R_s^{ni} - R_s^{-ni}\right)} \tag{2.82}$$

$$X_{ti} = -\frac{J_{cn}\, R_s \, \mu_0 \, \left(R_r^{-2ni} r^{ni} - r^{-ni}\right) \cos\left(ni\,\theta + x_a\right)}{r\left(R_r^{-2\,ni} R_s^{ni} - R_s^{-ni}\right)} \tag{2.83}$$

$$B_{xr} = -\frac{J_{cn}\, R_s \, \mu_0 \, \left(Rr^{-2\,ni} r + r^{-ni}\right)}{r\left(Rr^{-2\,ni} Rs^{ni} - Rs^{-ni}\right)} \tag{2.84}$$

$$B_{xt} = -\frac{J_{cn}\, R_s \, \mu_0 \, \left(R_r^{-2\,ni} r^{ni} - r^{-ni}\right)}{r\left(Rr^{-2\,ni} Rs^{ni} - R_s^{-ni}\right)} \tag{2.85}$$

$$Jc_n = \frac{2N_c I_{mx} \sin\left(\frac{ni \cdot pe}{2}\right) \sin\left(\frac{ni \cdot y \cdot \pi}{Q_s}\right)}{\pi R_s \left(\frac{ni \cdot pe}{2}\right)} \tag{2.86}$$

$$ang = n_i\theta + arg\left(sin\left(\frac{ni \cdot y \cdot \pi}{Q_s}\right) + I * \cos\left(\frac{ni \cdot y \cdot \pi}{Q_s}\right)\right) \tag{2.87}$$

The equivalent superficial current density is given 2.88 and represented by a Fourier series as follows:

$$Jc = \sum_{ni=1}^{nh} J_{cn} \cos(ang) \tag{2.88}$$

The three rectangular phase currents produce the current densities which can be expressed:

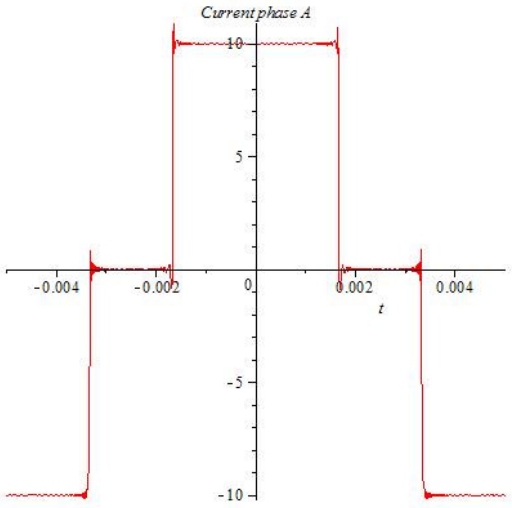

Figure 2.7: Phase A current.

$$Jc_A = \sum_{k=1}^{Q_{coil}} \left(\sum_{ni=1}^{nh} sgn_{A_k} Jcn \cos\left(ang_A\right) \right) \tag{2.89}$$

$$Jc_B = \sum_{k=1}^{Q_{coil}} \left(\sum_{ni=1}^{nh} sgn_{B_k} Jcn \cos\left(ang_B\right) \right) \tag{2.90}$$

$$Jc_C = \sum_{k=1}^{Q_{coil}} \left(\sum_{ni=1}^{nh} sgn_{C_k} Jcn \cos\left(ang_C\right) \right) \tag{2.91}$$

where ang_A is angular slot shift

$$ang_A = ang - n_i \, \alpha_{Ak}; \tag{2.92}$$

$$ang_B = ang - n_i \, \alpha_{Bk}; \tag{2.93}$$

$$ang_C = ang - n_i \, \alpha_{Ck}; \tag{2.94}$$

$$x_a = arg\left(\sin\left(\frac{n_i \, y\pi}{Qs}\right) + i\cos\left(\frac{n_i \, y\pi}{Qs}\right)\right) - ni\,\alpha_{A_k} \tag{2.95}$$

$$x_b = arg\left(\sin\left(\frac{n_i \, y\pi}{Qs}\right) + i\cos\left(\frac{n_i \, y\pi}{Qs}\right)\right) - ni\,\alpha_{B_k} \tag{2.96}$$

$$x_c = arg\left(\sin\left(\frac{n_i \, y\pi}{Qs}\right) + i\cos\left(\frac{n_i \, y\pi}{Qs}\right)\right) - ni\,\alpha_{C_k} \tag{2.97}$$

$$I_k = 4\,\frac{I_{mx}\,\sin\left(\frac{n_n\,\pi}{3}\right)}{n_n\,\pi} \tag{2.98}$$

$$i_1(t) = I_k \cos\left(n_n \, p\omega_{rm} \, (t + t_0)\right) \tag{2.99}$$

$$i_2(t) = I_k \cos\left(n_n \, p\omega_{rm} \left(t + t0 + \frac{\frac{2\pi}{3}}{\omega_{rm}\,p}\right)\right) \tag{2.100}$$

$$i_3(t) = I_k \cos\left(n_n \, p\omega_{rm} \left(t + t_0 + \frac{\frac{2\pi}{3}}{\omega_{rm}\,p}\right)\right) \tag{2.101}$$

$$n_n = 2\,k_x + 1 \tag{2.102}$$

The three phase currents have the following expressions:

$$\begin{aligned} I_A(t) &= \sum_{k_x=0}^{NHI} 4\,\frac{I_{mx}\,\sin\left(\frac{(2k_x+1)\pi}{3}\right)\cos(2(2k_x+1)\omega_{rm}(t+t_0))}{(2k_x+1)\pi} \\ I_B(t) &= \sum_{k_x=0}^{NHI} 4\,\frac{I_{mx}}{(2k_x+1)\pi}\,\sin\left(\frac{(2kx+1)\pi}{3}\right)\cos\left(2\,(2kx+1)\,\omega_{rm}\left(t + t_0 + \frac{\pi}{3\omega_{rm}}\right)\right) \\ I_C(t) &= \sum_{k_x=0}^{NHI} 4\,\frac{I_{mx}}{(2k_x+1)\pi}\,\sin\left(\frac{(2kx+1)\pi}{3}\right)\cos\left(2\,(2kx+1)\,\omega_{rm}\left(t + t_0 + \frac{3\pi}{3\omega_{rm}}\right)\right) \end{aligned} \tag{2.103}$$

The two components of the flux densitities are:

$$B_{ri}(\theta,t) = \sum_{k=1}^{Qcoil}\sum_{ni=1}^{nh}(B_{xr}\, i_{sa}\, sgn_{A_k}\sin(n_i\,\theta + x_a) + \\ +i_{sb}\, sgn_{B_k}\sin(n_i\,\theta + x_b) + i_{sc}\, sgn_{C_k}\sin(n_i\,\theta + x_c)) \tag{2.104}$$

$$B_{ti}(\theta,t) = \sum_{k=1}^{Qcoil}\sum_{ni=1}^{nh} B_{xt}\, i_{sa}\, sgn_{A_k}\cos(n_i\,\theta + x_a) + \\ i_{sb}\, sgn_{B_k}\cos(n_i\,\theta + x_b) + i_{sc}\, sgn_{C_k}\cos(n_i\,\theta + x_c)) \tag{2.105}$$

The waveform $B_{ri}(\theta,t)$ $B_{ti}(\theta,t)$ of produced by the currents are presented in Fig. 2.8 and Fig. 2.9.

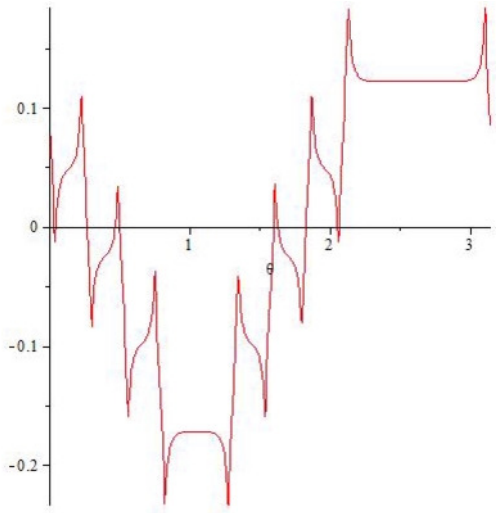

Figure 2.8: Radial component $B_{ri}(\theta,t)$.

The analytical model in polar coordinate and using vector potential to analyze open circuit magnetic field and armature reaction field in slotless PM machine with internal iron-cored rotor is presented by the Fig.2.8 and Fig.2.9. With given flux density distribution created by magnets alone, back-emf and electromagnetic torque are determined for 120 rectangular current. Results issued from analytical calculation can be compared for validation to those obtained from finite element method.

With the developed model, expressions of flux density due to radial magnet and armature reaction are given in a analytical form . The analytical model can be used in an analytical optimizer to determine the effect on magnetic field of different geometric parameters with any type of magnet magnetization for slotless PM motors.

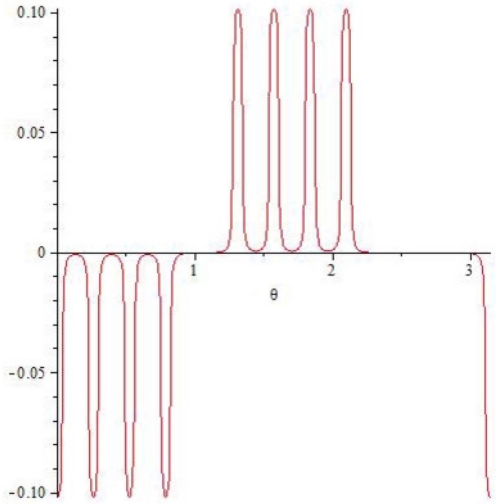

Figure 2.9: Tangential component of $B_{ti}(\theta, t)$.

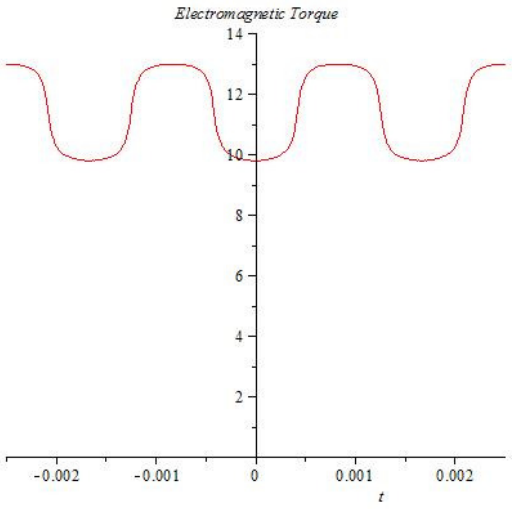

Figure 2.10: Electromagnetic torque of a slotsless PMSM.

2.3 Model of slotting effect in flux density

The effect of slotting was modeled in [1] by using relative air gap permeance obtained from a real conformal function which is able take into account only the effect of slotting in the radial flux density by multiplying the field distribution in the slotless air gap with this permeance. This field solution is reasonably accurate if the field is calculated at the radius far enough from the stator bore so that the influence of the tooth tips on the flux density waveform

is not significant.

This method allows one to calculate accurately both radial and tangential components of the air gap flux density. It uses the complex nature of the conformal transformation more extensively and defines the relative air gap permeance λ as a complex number. This method, presented in detail in [2], has been used in this [4] to calculate the flux density in motors with tangential surface mounted permanent magnets.

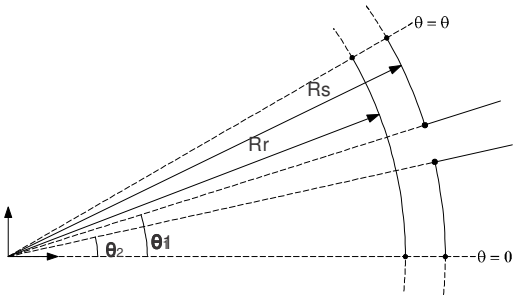

Figure 2.11: The geometric shape of slotted geometry. Single infinitely slot in S plane for conformal transformation

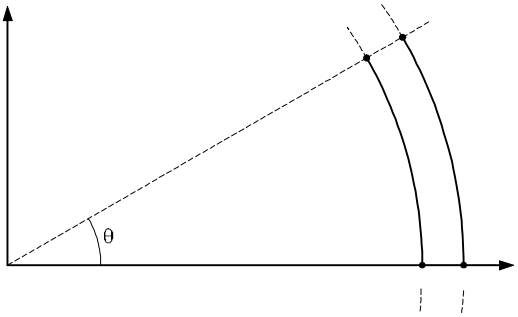

Figure 2.12: The geometric shape of slottless geometry in K plane

The basic principle of the method is to transform the geometric shape in Fig.2.11 into a slotless airgap in which the field solution can be easily found using previously presented analytical model (Fig. 2.12).

The flux density in the slotted air gap B_s in the S plane is:

$$B_s = B_k \left(\frac{\partial k}{\partial s} \right)^* \tag{2.106}$$

where B_k is the field solution in the slotless air gap K plane) given as

$B_k = B_r + jB_\theta$ with $B_r = B_{1r}$ or $B_r = B_{2r}$ and $B_\theta = B_{1\theta}$ or $B_\theta = B_{2\theta}$ The complex permeance is defined by the following equations:

$$\frac{\partial k}{\partial s} = \lambda = \frac{k}{s}\frac{w-1}{(w-a)^{\frac{1}{2}}(w-b)^{\frac{1}{2}}} \tag{2.107}$$

$$z = \ln(s) \tag{2.108}$$

$$s = re^{j\theta} \tag{2.109}$$

$$k = R_s^{(\frac{g\prime}{\pi}\ln w + \frac{\Theta_s}{2})} \tag{2.110}$$

$$p = \sqrt{\frac{w-b}{w-a}}; C = \ln R_s + j\theta_2; g\prime = \ln(\frac{R_s}{R_r}) \tag{2.111}$$

$$z = j\frac{g\prime}{\pi}[\ln|\frac{1+p}{1-p}| - \ln|\frac{b+p}{b-p}| - 2\frac{b-1}{\sqrt{b}}\tan^{-1}\frac{p}{\sqrt{b}}] + C \tag{2.112}$$

$$b = \left(\frac{b_0^{'}}{2g^{'}} + \sqrt{(\frac{b_0\prime}{2g^{'}})^2 + 1}\right)^2; a = \frac{1}{b}; b_0\prime = \theta_2 - \theta_1 \tag{2.113}$$

The value of s is known since it is a coordinate in the slotted air gap where the field is to be calculated. If it is required to calculate the flux density at a certain geometric point in the slotted air gap, then the value of w which corresponds to that point can be calculated from $z = f(w)$, where f is a non-linear complex function of w. An iterative techniques is required to solve this nonlinear equation and find the value of w for the given z.

Since λ is a complex number, it can be written in the form.

$$\lambda = \lambda_a + j\lambda_a \tag{2.114}$$

The real and imaginary part can be written in the form

$$\lambda_a = \lambda_0 + \sum_{n=1}^{N_\lambda} \lambda_{an}\cos(nQ_s\theta), \tag{2.115}$$

$$\lambda_b = \sum_{n=1}^{N_\lambda} \lambda_{bn}\sin(nQ_s\theta), \tag{2.116}$$

where Q_s is the number of slots and N_λ is the maximum order of the Fourier coefficients. The Fourier coefficients λ_{an} and λ_{bn} are calculated from the waveforms of λ_a and λ_b using discrete Fourier transform (FFT). With $B_s = B_{sr} + jB_{s\theta}$, the radial and tangential components of the flux density in the slotted air gap are then

$$B_{sr} = Re(B_k\lambda^*) = B_r\lambda_a + B_\Theta\lambda_b \tag{2.117}$$

$$B_{s\theta} = Im(B_k\lambda^*) = B_\Theta\lambda_a - B_r\lambda_b \tag{2.118}$$

The coefficients a and b represent the values of w at the comer points of the slot (points 3 and 4 in Fig. 2.11). The meaning of angles θ_1 and θ_2 is obvious

from Fig.2.11. The transformations of coordinates after solving (2.107-2.210) are given by

$$Tl : s = e^z \tag{2.119}$$

$$T2 : z = j\frac{g'}{\pi}[\ln|\frac{1+p}{1-p}| - \ln|\frac{b+p}{b-p}| - \frac{2(b-1)}{\sqrt{b}}\tan^{-1}\frac{p}{\sqrt{b}}] + C \tag{2.120}$$

$$C = \ln(R_s) + j\theta_2,\ (p = \sqrt{\frac{w-b}{w-a}}) \tag{2.121}$$

$$T3 : t = j\frac{g/}{\pi}\ln(w) + \ln(R_s) + j\frac{\theta_s}{2} \tag{2.122}$$

$$T4 : k = e^t. \tag{2.123}$$

The link between flux density in the S and K planes is given by:

$$B_s = B_k(\frac{\partial k}{\partial s})^* = B_k(\frac{\partial k}{\partial t}\frac{\partial t}{\partial w}\frac{\partial w}{\partial z}\frac{\partial z}{\partial s})^* \tag{2.124}$$

Substituting (2.117-2.120) into (2.121) yields

$$\begin{aligned} B_s &= B_k\left[\frac{k}{s}\frac{(w-1)}{(w-a)^{\frac{1}{2}}(w-b)^{\frac{1}{2}}}\right]^* \\ &= B_k\lambda^* = (B_r + jB_\theta)(\lambda_a + j\lambda_b)^* \end{aligned} \tag{2.125}$$

where λ^* represents the complex conjugate of the complex relative air-gap permeance with λ_a and λ_b as its real and imaginary parts.

The flux density B_k with its real and imaginary parts B_r and B_θ represents the field solution in the slotless air gap given by (2.113). Since k is a function of t, which in turn is a function of w, and s is the known coordinate in the actual geometry, which is also a function of w, the complex permeance λ is indirectly a nonlinear function of w as well. For each known coordinate s in the air gap of a motor given by radius r and angle $\theta(s = r\cos\theta + jr\sin\theta)$, a value of λ can be found using (2.117) and (2.120).

In order to calculate the complex permeance λ, the coordinate w must be calculated from $T2$ using some numerical method for solving nonlinear equations. The code for the numerical solution is presented in the following listing using numerical minimisation technique indicated by [11]

The Fourier coefficients λ_0, λ_{am}, and λ_{bm} in (2.113) are calculated from the real and imaginary parts of λ at geometric points along a circular arc at radius $R_m \leq r \leq R_s$ and an angular span of one slot-pitch using the discrete Fourier transform.

Listing 2.1: w coordinate identification using Matlab *lsqmin* optimization function

```
w0 = 1                          % Starting guess
[w,resnorm] = lsqnonlin(@myobj,w0)
```

Listing 2.2: *lsqmin* objective function

```
function norm=myobj(w,z)

Rs=300;  %definim parametrii
Rr=299;
g=log(Rs/Rr);
b=1.5;
a=1/b;
teta2=2;
j=sqrt(-1);  %Imaginary unit

%Current value of z coordinate
z=log(Rs)+j*teta2;
zw=log(Rs)+j*teta2+j*(g/pi)*(log(abs((1+sqrt((w-b)/(w-a)))/...
(1-sqrt((w-b)/(w-a)))))-log( abs((b+sqrt((w-b)/(w-a)) )/...
(b-sqrt((w-b)/(w-a))))) - ...
 2*(b-1)/ (sqrt(b) * tan( sqrt((w-b)/(w-a))/sqrt(b)))) ;
%% we compute the norm wich is used for minimization
% in the optimal solution

norm=real(z-zw)^2+imag(z-zw)^2
```

The radial and tangential components of the flux density in the slotted air gap can be written as:

$$\begin{aligned} B_{sr}(r,\ \theta,\ \alpha) &= B_r(r,\ \theta,\ \alpha)\lambda_a(r,\ \theta) + B_\theta(r,\ \theta,\ \alpha)\lambda_b(r,\ \theta) \\ &= \lambda_0(r)\sum_n B_{rn}(r)\cos[np(\theta-\alpha)] \\ &\quad + \sum_n\sum_m B_{rn}(r)\lambda_{am}(r)\cos[np(\theta-\alpha)]\cos(mQ_s\theta) \\ &\quad + \sum_n\sum_m B_{\theta n}(r)\lambda_{bm}(r)\sin[np(\theta-\alpha)]\sin(mQ_s\theta) \end{aligned} \tag{2.126}$$

$$\begin{aligned} B_{s\theta}(r,\ \theta,\ \alpha) &= B_\theta(r,\ \theta,\ \alpha)\lambda_a(r,\ \theta) - B_r(r,\ \theta,\ \alpha)\lambda_b(r,\ \theta) \\ &= \lambda_0(r)\sum_n B_{\theta n}(r)\sin[np(\theta-\alpha)] \\ &\quad + \sum_n\sum_m B_{\theta n}(r)\lambda_{am}(r)\sin[np(\theta-\alpha)]\cos(mQ_s\theta) \\ &\quad - \sum_n\sum_m B_{rn}(r)\lambda_{bm}(r)\cos[np(\theta-\alpha)]\sin(mQ_s\theta). \end{aligned} \tag{2.127}$$

2.4 Analytical computation of cogging torque

The cogging torque represents the tendency of the rotor to line up with the stator in a particular direction where the permeance of the magnetic circuit

seen by the permanent magnets is maximized. Together with the ripple torque caused by the mismatch between the back-electromotive force (back-EMF) and the current waveforms it represents torque pulsations which are highly undesirable in some applications, such as servo drives or electric steering.

There are three basic approaches to the analytical calculation of cogging torque. One approach is to calculate the torque as a derivative of co-energy inside the air gap [1]-[7]. The second approach is to integrate the lateral forces along the slot sides [8]-[12]. The third approach, which is used in this chapter, is to integrate the tangential component of Maxwell stress tensor along a circular contour inside the air gap. The analytical solution of this type is difficult to find in the literature since it requires a knowledge of both the radial and tangential components of flux density inside the slotted air gap.

The principle of complex relative air-gap permeance presented in [11] allows one to calculate both radial and tangential components of the air-gap flux density and, hence, leads to the analytical closed-form solution for cogging torque presented in this paper, which is based on the integral of Maxwell stress tensor. The solution is given in the form of Fourier series. One of the drawbacks of the proposed solution is the fact that the calculation of the complex relative air-gap permeance requires numerical solution of a nonlinear equation, which does not make the overall cogging torque solution entirely analytical.

The magnetic stress vector, i.e., the force per unit surface, is given by:

$$t_m = \left(\vec{n} \cdot \frac{\vec{B}}{\mu_0} \right) \vec{B} - \vec{n} \frac{1}{2} \frac{|\vec{B}|^2}{\mu_0} \tag{2.128}$$

where:

$\vec{n}$ is the surface normal vector and

$\vec{B}$ is the flux density vector on the surface of the body. From results that the stress vector consists of two components.

The surface which encloses the rotor of a surface PM motor is in the shape of a cylinder placed entirely inside the air gap.In that case the surface normal vector will be equal to the unit length vector in the radial direction, i.e.,

$$\vec{n} = \vec{a}_r \tag{2.129}$$

The field solution in the air gap of a surface PM motor at no-load operation is known from eq 2.128. The flux density vector $\vec{B}$ will have radial and tangential components, and can be written in the form

$$\vec{B} = B_r \vec{a}_r + B_\theta \vec{a}_\theta \tag{2.130}$$

Substituting (2.128) and (2.127) into (2.126) yields

$$
\begin{aligned}
t_m &= \frac{1}{\mu_0}[\vec{a}_r \cdot (B_r\vec{a}_r + B_\theta\vec{a}_\theta)](B_r\vec{a}_r + B_\theta\vec{a}_\theta) - \vec{a}_r\frac{1}{2}\frac{|\vec{B}|^2}{\mu_0} = \\
&= \frac{1}{\mu_0}B_r(B_r\vec{a}_r + B_\theta\vec{a}_\theta) - \vec{a}_r\frac{1}{2}\frac{|\vec{B}|^2}{\mu_0} \\
&= \frac{1}{\mu_0}(B_r^2 - \frac{1}{2}|\vec{B}|^2)\vec{a}_r + \frac{1}{\mu_0}B_rB_\theta\vec{a}_\theta.
\end{aligned}
\tag{2.131}
$$

The torque equation in the integral form can then be written as

$$
T = \frac{1}{\mu_0}l_a r^2 \int_0^{2\pi} B_{sr}(r,\ \theta,\ \alpha)B_{s\theta}(r,\ \theta,\ \alpha)d\theta \tag{2.132}
$$

where

μ_0 is the permeability of vacuum,
l_a is the stack length of the machine,
r is the radius of the integration surface,
B_{sr} is the radial and
$B_{s\theta}$ is the tangential component of the flux density at radius r.

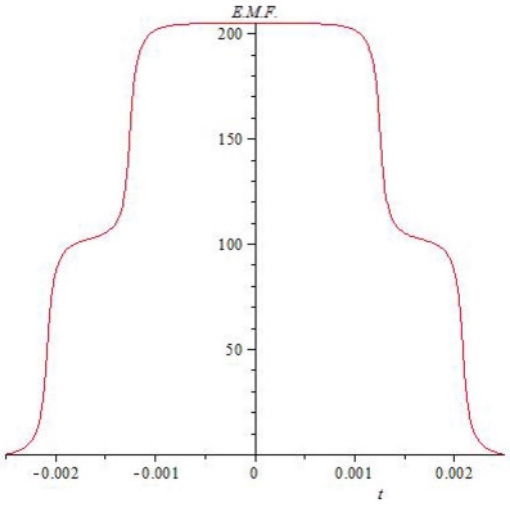

Figure 2.13: BEMF

2.4.1 Code implementation and results

Mathematica code implementation of the analytical models is presented in Apendix A.2 The ability of symbolic calculations make Wolfram mathematica capable to solve large scale equations The developed script and some results using were integrated in the Chapter 3 when a three phase PMSG generator with 72/68 slots was designed.

The folowing code was used to compute the effect of slots on BEM using a the model presented in [30].

Listing 2.3: *Zhu model for permeance determination*

```
qs=36 ; % no of slots
Rs=0.102; % radius of stator in meters
bo=0.002; % Slot opening in meters
g=0.001; % Physical air gap in meter
hm=0.013; % magnet height in meters
mur=1.3; % relative permeability
Kc= 1.003 % Carter's coeffient
gp= g+hm/mur; % effective air gap in meters
f1=gp*pi/bo;
a2=1+(2*gp/bo)^2;
z=16.6
c=a2+z^2;
cp=sqrt(c)+z;
cm=sqrt(c)-z
f2=0.5*log(cp./cm);
f3=(2*gp/bo)*atan(((2*gp/bo)*(z/sqrt(c))));
f4=f2+f3;
f=(gp*pi/bo) -f4; % a zero indicates your value of z is
correct
h2=(bo/(2*gp))^2;
d=(h2*(1+z^2)+1);
D= sqrt(d);
beta= 0.5*(1- 1/D);
alpho = 0.00624*pi; % stator slot opening in radians
alpht = 2*pi/qs; % stator slot pitch in radians
tau=2*pi*Rs/qs ; % slot pitch in meters
alph = 0:0.001:0.5;
% relative  Permeance Function
x=57.3*alph;
nmax=5000;
vold=0;
for n=1:1:nmax; % Determine the Fourier Series of
lambar
An= - beta*4/(pi*n)
Nn = (n*bo/tau).^2;
Dn =0.78125 - 2*(n*bo/tau).^2;
Mn =sin(1.6*pi*n*bo/tau);
v= vold +An*(0.5+ Nn/Dn)*Mn*(cos(n*qs*alph));
```

```
vold = v;
end
lambarf = v +(1-1.6*beta*bo/tau)/Kc
y =47.5*sin(qs*(alph+pi/15))+10*sin(qs*3*(alph+ pi/15))
permeance=lambarf.*y;
plotyy(x,y,x,lambarf)
grid
%%Summation to Obtain Eph
lambar = 1-beta-beta*cos((pi/(0.8*alpho))*alph);

for n=1:2:nmax
Mn=C1*(sin(C2*n)/(C2*n));
An=a*Mn*((n*p)/((n*p)^2-1))Rms^(p*n+1);
Nn=(n*p-1)+2*Rrm^(n*p+1)-(n*p+1)*Rrm^(2*p*n);
Dn=Mup*(1-Rrs^(2*p*n))-Mum*(Rms^(2*p*n)-Rms^(2*p*n));
v=vold+An*(Nn/Dn).*(cos(n*p*(theta)));
vold=v;
end
Eph=SCph*Kw*v*Lstk*(Rs/1000)*omeg;
%Harmonic Content of Eph
bar(0:max(size(f))-1,f)
axis([0 30 0 70])
grid
```

2.4.2 Conclusion

- The analytical model in polar coordinate and using vector potential to analyze open circuit magnetic field and armature reaction field in slotless PM machine with internal iron-cored rotor is presented. The use of the symbolic solution can both provide speed and precision in the case of magnetic field solution of major magnetic quantities of radial flux PMSMs. However some drawback needs to be noted. one is the limitation of the solution to take in consideration real lot geometry (without use of rather cumbersome conformal mapping techniques) Despite the versatility of the method the complexity of implementation limits the use of the model to rather simple case. For this reason we will use the method only for the evaluation of the winding influence on radial flux nonoverlapping PMSM on the emf.

- With given flux density distribution created by magnets alone, back-emf and electromagnetic torque are determined for 120° rectangular current. Results issued from analytical calculation can be compared for validation to those obtained from finite element method.

- With the developed model, expressions of flux density due to radial magnet and armature reaction are given in analytical form . The can be used in an analytical optimizer to determine the effect on magnetic field of

different geometric parameters with any type of magnet magnetization for any slotless PM motors.

- Mathematica code implementation of the analytical models is presented. The ability of symbolic calculations make Wolfram mathematica capable to solve large scale equations thus re-explores first-principles machine design by implementing analytical models using symbolic software exprimation. It is shown that the algebraic complexities previously impeding the application of the theory to many-layered structures are removed using this software. A slotless permanent magnet field investigation is used to verify the model's accuracy in predicting flux density in an electric machine.

Bibliography

[1] J. F. Gieras, "Analytical approach to cogging torque calculation in PM brushless motors," in *Int. Electr. Machines* & *Drives Conf*., Madison, WI, Jun. 2003, vol. 2, pp. 815-819.

[2] Z. Q. Zhu and D. Howe, "Analytical prediction of the cogging torque in radial-Field permanent magnet brushless motors," *IEEE Trans. Magn*., vol. 28, no. 2, pp. 1371-1374, Mar. 1992.

[3] A. B. Proca, A. Keyhani, A. El-Antably, W. Lu, and M. Dai, "Analytical model for permanent magnet motors with surface mounted magnets," *IEEE Trans. Energy Convers*., vol. 18, no. 3, pp. 386-391, Sep. 2003. [10] M. Markovič,

[4] M. Jufer, and Y. Perriard, "Reducing the cogging torque in brushless DC motors by using conformal mappings," *IEEE Trans*.*Magn*., vol. 40, no. 2, pp. 451-455, Mar. 2004.

[5] D. Zarko, D. Ban, and T. A. Lipo, "Analytical calculation of magnetic Field distribution in the slotted air gap of a surface permanent-magnet motor using complex relative air-gap permeance," *IEEE Trans. Magn*.,vol. 42, no. 7, pp. 1828-1837, Jul. 2006.

[6] M. Markovič, M. Jufer, and Y. Perriard, "Determination of tooth cogging force in a hard-disk brushless DC motor," *IEEE Trans. Magn*., vol. 41, no. 12, pp. 4421-4426, Dec. 2005.

[7] Z. Q. Zhu and D. Howe, "Instantaneous magnetic field distribution in brushless permanent magnet DC motors, part III: Effect of stator slotting," *IEEE Trans. Magn*., vol. 29, no. 1, pp. 143-151, Jan. 1993.

[8] X. Wang, Q. Li, S. Wang, and Q. Li, "Analytical calculation of air-gap magnetic Field distribution and instantaneous characteristics of brushless DC motors," *IEEE Trans. Energy Convers*., vol. 18, no. 3, pp. 424-432, Sep. 2003.

[9] U. Kim and D. K. Lieu, "Magnetic Field calculation in permanent magnet motors with rotor eccentricity: With slotting effect considered," *IEEE Trans. Magn*., vol. 34, no. 4, pp. 2253-2266, Jul. 1998.

[10] Z. Q. Zhu, D. Howe, E. Bolte, and B. Ackermann, 'Instantaneous magnetic Field distribution in brushless permanent magnet DC motors, part I: Open-circuit Field," *IEEE Trans. Magn*., vol. 29, no. 1, pp. 124-135,Jan. 1993.

[11] D. Zarko, "A systematic approach to optimized design of permanent magnet motors with reduced torque pulsations" Ph. D. dissertation, Univ. Wisconsin, Madison, Sep. 2004 [Online].

[12] Z. Q. Zhu, D. Howe, and C. C. Chan, "Improved analytical model for predicting the magnetic Field distribution in brushless permanent magnet machines," *IEEE Trans. Magn*., vol. 38, no. 1, pp. 229-238,Jan. 2002.

[13] S. Hwang and D. K. Lieu, "Design techniques for reduction of reluctance torque in brushless permanent magnet motors," *IEEE Trans*. *Magn*., vol. 30, no. 6, pp. 4287-4289, Nov. 1994.

[14] C. S. Koh and J.-S. Seol, "New cogging-torque reduction method for brushless permanent-magnet motors," *IEEE Trans. Magn*., vol. 39, no. 6, pp. 3503-3506, Nov. 2003.

[15] R. P. Deodhar, D. A. Staton, and T. J. E. Miller, "Modelling of skew using the flux-mmf diagram," in *Proc. 1996 Int. Conf. Power Electronics, Drives Energy Syst. For Ind. Growth*, 1996, vol. 1, pp. 546-551.

[16] T. A. Driscoll, *Schwarz Christoffel Toolbox Users Guide–Version 2.3* Dept. Mathematical Sciences, Univ. Delaware. Newark, DE, 2002 [Online]. Available: http://www.math.udel.edu/driscoll/SC

[17] Z. Zhu and D. Howe, "Analytical prediction of the cogging torque in radial-field permanent magnet brussless motors," in IEEE Trans. on Magnetics, vol. 28, no. 2, pp. 1371-1374, 1992.

[18] Z. Zhu, D. Howe, and C. Chan, "Improved analytical model for predicting the magnetic field distribution in brushless permanent-magnet machines," in IEEE Trans. on Magnetics, vol. 38, no. 1, pp. 229-238, 2002.

[19] Z. Zhu and D. Howe, "Instantaneous magnetic field distribution in brushless permanent magnet dc motors, Part III: Effect of stator slotting," in IEEE Trans. on Magnetics, vol. 29, no. 1, pp. 143-151, 1993.

[20] P. Salminen, J. Mantere, J. Pyrhonen, and M. Niemela, "Performance analysis of fractional slot wound PM-motors," in Proc. of Int. Conf. on Electrical Machines, (ICEM), paper no. 509, 2004.

[21] A. Mitcham, G. Antonopoulos, and J. Cullen, "Favourable slot and pole number combinations for fault-tolerant PM machines," in IEE Proc. on Electric Power Applications, vol. 151, no. 5, pp. 520-525, 2004.

[22] Z. Zhu and D. Howe, "Instantaneous magnetic field distribution in brushless permanent magnet dc motors, part I: open-circuit field," in IEEE Trans. on Magnetics, vol. 38, no. 1, pp. 124-135, 1993.

[23] Z. Zhu and D. Howe, "Instantaneous magnetic field distribution in brushless permanent magnet dc motors, part II: armature-reaction field," in IEEE Trans. on Magnetics, vol. 38, no. 1, pp. 136-142, 1993.

[24] A. Proca, A. Keyhani, A. EL-Antably, W. Lu, and M. Dai, "Analytical model for permanent magnet motors with surface mounted magnets," in IEEE Trans. on Energy Conversion, vol. 18, no. 3, pp. 386-391, 1993.

[25] Z. Zhu, D. Howe, and J. Mitchell, "Magnetic field analysis and inductances of brushless DC machines with surface-mounted magnets and non-overlapping stator windings," in IEEE Trans. on Magnetics, vol. 31, no. 3, 1995.

[26] Z. Zhu and D. Howe, "Winding inductance of brushless machines with surfacemounted magnets," in Proc. of IEEE Int. Electric Machines and Drives Conf., pp. WB2/2.1-WB2/2.3, 1997.

[27] F. Tourkhani and P. Viarouge, "Accurate analytical model of winding losses in round Litz wire windings," in IEEE Trans. on Magnetics, vol. 37, no. 1, pp. 538-543, 2001.

[28] J. Wang, Z. Xia, and D. Howe, "Three-phase modular permanent magnet brushless machine for torque boosting on a downsized ICE vehicle," in IEEE Trans. on Vehicular Technology, vol. 54, no. 3, pp. 809-816, 2005.

[29] A. Muetze, A. Jack, and B. Mecrow, "Alternate designs of low cost brushless-DC motors using soft magnetic composites," in Proc. of Int. Conf. on Electrical Machines, (ICEM), paper no. 237, 2002.

[30] J. Chen, C. Nayar, and L. Xu, "Design and finite-element analysis of an outer-rotor permanent-magnet generator for directly coupled wind turbines," in IEEE Trans. on Magnetics, vol. 36, no. 5, pp. 3802-3809, 2000.

[31] K. Kim and J. Lee, "The dynamic analysis of a spoke-type permanent magnet generator with large overhang," in IEEE Trans. on Magnetics, vol. 41, no. 10, pp. 3805-3807, 2005.

[32] B. Mecrow, A. Jack, J. Haylock, U. Hoefer, and P. Dickinson, "Simplifying the manufacturing process for electrical machines," in Proc. of Int. Conf. on Power Electronics, Machines and Drives (PEMD), vol. 1, pp. 169-174, 2004.

[33] T. Miller, M. Popescu and, C. Cossar, and M. McGilp, "Computation of the voltage driven flux-MMF diagram for saturated PM brushless motors," in Proc. of IEEE Industry Applications Society Conf., vol. 2, pp. 1023-1028, 2005.

[34] K. Sitapati and R. Krishnan, "Performance Comparisons of Radial and Axial Field, Permanent-Magnet, Brushless Machines," in IEEE Trans. on Industry Applications, vol. 37, no. 5, 2001.

[35] M.M. Radulescu: "Analytical modelling of a small slotless electronically-commutated neodymium-magnet motor", ELECTROMOTION, Vol. 1 (1994), No. 1, pp. 45-51.

[36] M.M. Radulescu: "Field and torque calculation in slotless permanent-magnet electronically-commutated servomotors", Proceedings of the 4th International Conference on Optimization of Electric and Electronic Equipments (Brasov, 12-14 mai 1994) University 'Transilvania' Brasov, Romania, 1994, Vol. III, 289- 294..

[37] http://www.ornl.gov/webworks/cppr/y2001/rpt/123938.pdf

3 Characterization of a NonOvelapping Winding Radial Flux Permanent Magnet Synchronous Generator

Radial-flux PM machines (RFPM) synchronous machines are the most conventional PM machines. The flux flows radially through the airgap of the machine while the current circulates in the radial direction. RFPM machines are the easiest and cheapest to manufacture among the PM machines. However, they are much larger than the axial-flux and transverse-flux machines in terms of active weight and axial length [1,3,4].

PMSMs with non-overlapping concentrated windings have become a competitive alternative to PMSMs with distributed windings for certain applications. PMSM with nonoverlapping concentrated windings are suitable selection for several reasons. Besides the short end-windings, a low cogging torque, good fault-tolerant capability, and a high constant power speed range can be achieved. Therefore, PMSMs with nonoverlapping concentrated windings have recently been widely investigated [1]. The design of such PMSMs differs from the design of PMSMs with distributed windings as it is presented in [22] and [1].

The goal of this chapter is to underline the particular design features of 3-phase PMSMs with concentrated windings. Especially, the influence on the design of the combination of pole and slot numbers is investigated. A nonoverlapping PMSG is studied based on FE simulations Also winding design of PMSMs with concentrated windings is presented in order to illustrate some of the choices that have to be made during the design process.[15]

3.1 Winding type for high number of slots PMSM

The higher the number of poles of the machine, the higher the number of slots. However,since the space for the slots is limited, resulting the pole pitch is small. Therefore, with high pole numbers it is usually not possible to have a number of slots per pole per phase q higher than 1. The higher q, the more sinusoidal the magneto-motive force (MMF) and thus the lower the torque ripple and losses. Non-overlapping concentrated windings are particularly suitable for low-speed direct drives since in these machines, the number of slots Q_s is

close to the number of poles ($Q_s \approx p$) and, thus, $q = \frac{Q_s}{3p} \approx \frac{1}{3} < 1$ for 3-phase machines. Therefore, the space available for the slots is not an issue.

3.1.1 Non-overlapping concentrated windings

Different terms can be found in the literature to refer to windings having with $q < 1$ non-overlapping coils. These terms include: "concentrated windings" ,"non-overlapping concentrated winding" [35], "tooth concentrated windings" [34], "tooth concentrated fractional windings" [40], "concentrated coil" [41], "fractional slot wound" [42], "fractional-slot with non-overlapped coils" [43], "fractional-slot pitch concentrated windings" [44].

PM machines with non-overlapping concentrated windings are can be classified into two categories: traditional brushless PM machines and modular PM machines [45, 46].

In traditional brushless PM machines with concentrated windings, the ratio between the slot and pole numbers is equal to $3/2$. This corresponds to a number of slots per pole per phase equal to $q = 0.5$ in the case of a 3-phase PMSM. The phases of the windings are alternated for each consecutive tooth and the coil span is 120° elec. This results in a relatively low "fundamental" winding factor equal to 0.867. Modular PM machines have a number of slot per pole per phase which is strictly lower than 0.5 and strictly higher than 0.25 Fig. 3.2.

For $q<1$ two consecutive teeth or more are wound with the same phase. This results in a high "fundamental" winding factor, low torque ripple but also possible vibration and noise issues and high rotor losses. Modular PM machines have an MMF distribution with fewer poles than rotor poles as illustrated in Fig 3.2 for a 48-pole, 40-slot modular PMSM. Thus, the MMF harmonic component that interacts in the mean torque production is not the fundamental but a higher harmonic component of the same order as the number of pole pairs p/2 [47]. It is then called main harmonic component in [47] or synchronous frequency component in [39].

The order of the synchronous frequency component for the 40-pole, 48 -slot machine is then 48/2=20 (see also first line under the spectra in Fig. 3.5). The corresponding winding factor is then called winding factor of main harmonic [47] or synchronous-component winding factor [39]. The relation between the two sets of harmonic orders is shown under the spectra of Fig. 3.5 for the 40-pole, 48-slot machine.

This implies that all the subharmonics of "mechanical" order lower than $p/2$ have, when considering "electrical", orders with fractional values lower than 1.

3.1.2 Selection of number of layers

The harmonic components in the MMF with fractional orders (or with orders other than $k_p/2$, k being an integer if considering mechanical angles) do not play any role in the analytical calculations of the back-EMF and the mean

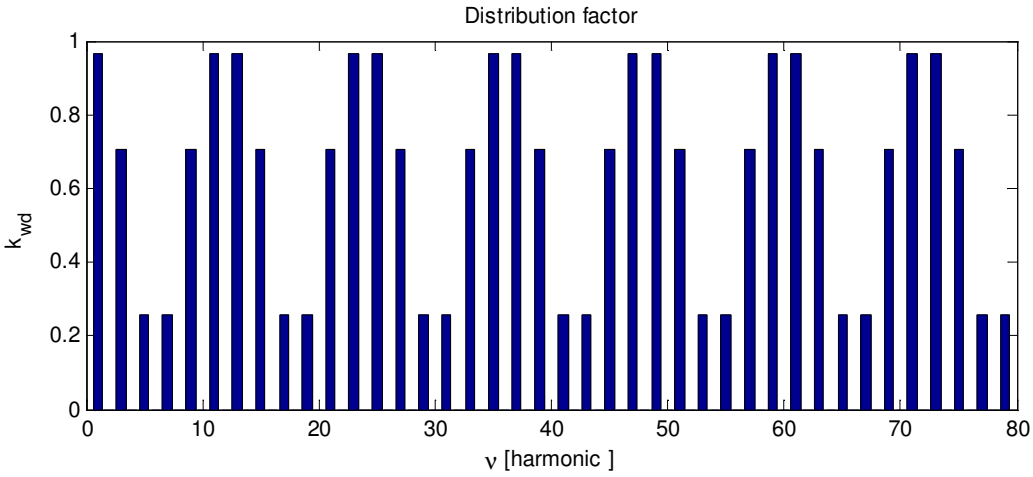

Figure 3.1: Distribution factor for 48 slots 40 poles winding

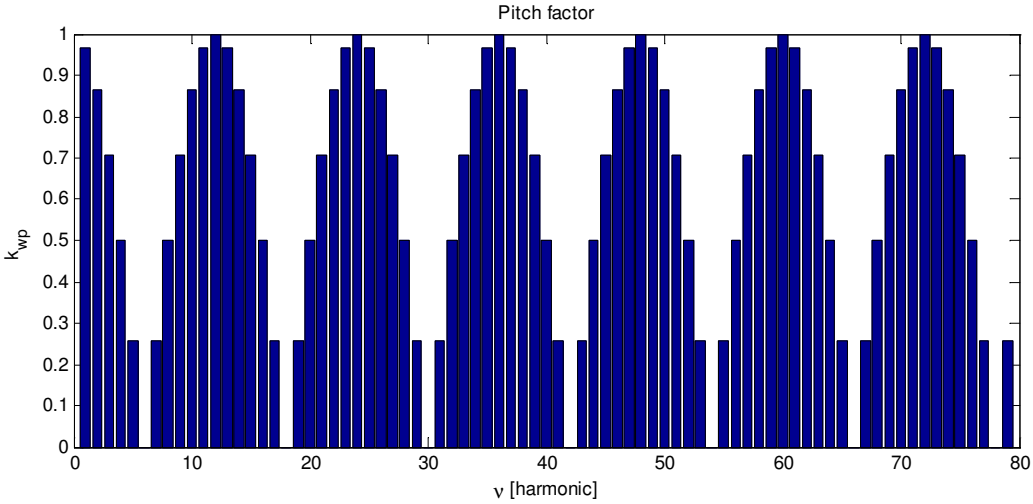

Figure 3.2: Pitch factor for 48 slots 40 poles winding

value of the torque, if the slot effects are not taken into account [3]. It is then convenient to have the "synchronous-component" winding factor equal to the component of order 1, disregarding the harmonics of fractional orders. Interestingly, if all the harmonics of fractional values are removed from the true MMF, the reduced MMF is corresponding to the distribution of a PMSM with distributed windings. This is illustrated for the 40-pole, 48-slot PMSM in Fig. 3.5. If rotor loss or vibrations are to be investigated, the complete spectrum of the MMF has to be considered. The term fundamental winding factor is used to refer to the winding factor used in the mean torque calculation.

The number of layers of the nonoverlapping windings can be single layer and double layer windings. Single-layer windings have coils wound only on

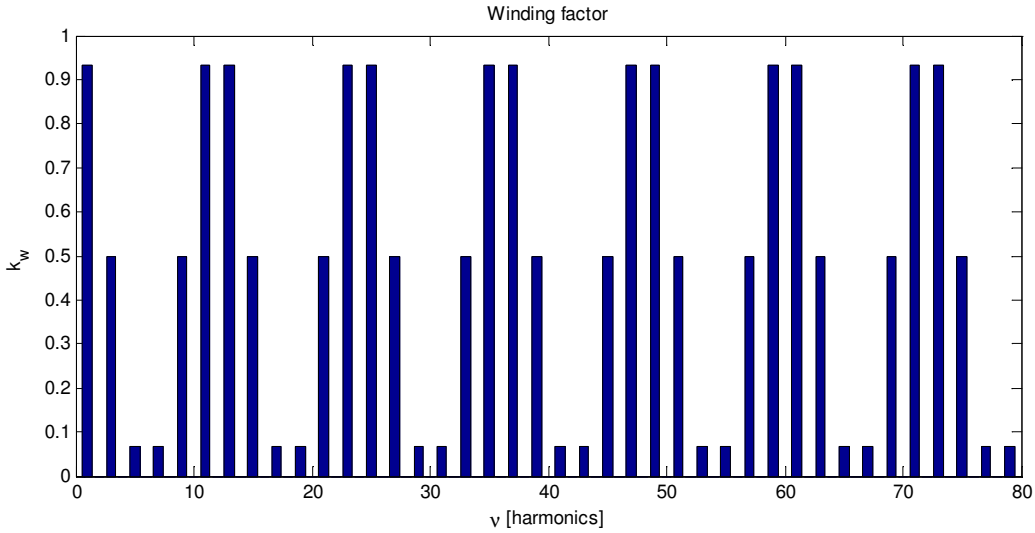

Figure 3.3: Winding factor for 48 slots 40 poles winding

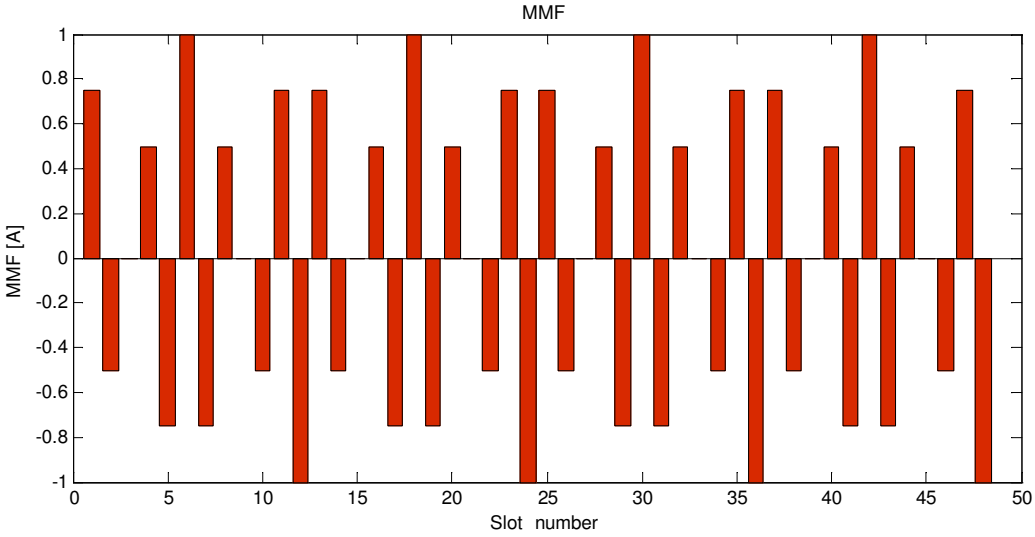

Figure 3.4: MMF for 48 slots 40 poles winding

alternate teeth, whereas each tooth of the double-layer windings carries a coil Table 3.1.

Single-layer windings are preferred to double-layers windings when a high fault tolerance [1] is required since the phases of the windings are thermally and electrically isolated, the self-inductance is high (which limits the short circuit currents), and the mutual inductance is very low (which isolate the phases magnetically). Due to their higher inductance, single-layer windings

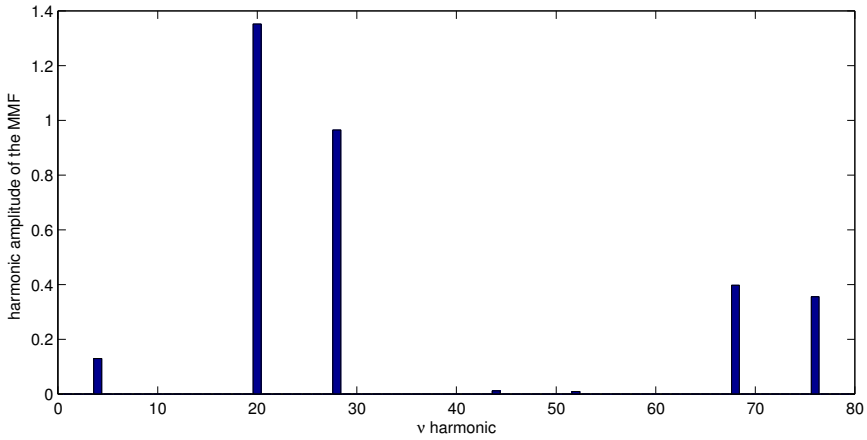

Figure 3.5: MMF harmonics for 48 slots 40 poles winding

Table 3.1: Characteristics of single and double layer fractional non-overlapping windings

	Single-layer	Double layer
Fundamental winding factor	higher	lower
End-windings	longer	shorter
Slot fill factor	higher	lower
Self-inductances	higher	lower
Mutual-inductance	lower	higher
EMF	more trapezoidal	more sinusoidal
Harmonic content of MMF	higher	lower
Eddy current losses in the PM	higher	lower
Overload torque capability	higher	lower

are also preferred in applications requiring a wide speed range of constant power operation. Otherwise, double-layer windings are preferable to limit the losses and torque ripple. Furthermore, there are more possible combinations of pole and slot numbers to choose between with double-layer windings than with single-layer windings. Single-layer windings with unequal tooth widths are interesting for brushless DC operation [2]. The teeth that are not carrying any coils are thinner than the other teeth. The winding flux-linkage and the fundamental winding factor are then increased, which gives a more trapezoidal phase back-EMF [15].

3.2 Selection of number of poles and number of slots

After selecting the number of layers next step is to determine the number of poles and the number of slots. A range of possible pole numbers is possible function of the nominal speed or frequency. Then, the pole number should be selected in combination with the number of slots. This selection is done by looking at the winding factor, the cogging and torque ripple, the vibration, rotor losses and inductance of the machine associated with the specific combination.

3.2.1 Winding layout and winding factor identification

For a given combination of pole and slot numbers, there are many possibilities to arrange the coils of each phase in the slots to form the winding layout [18]. The most interesting winding layout is the one that gives the highest fundamental winding factor. The winding layout and winding factor of a PMSM with concentrated winding depends on its combination of pole and slot numbers. Therefore, this combination should be carefully chosen in order to maximize the fundamental1 winding factor and thus the torque.

There are different methods to find the winding layout. One method is similar to the one used for the synchronous machine with fractional slot windings [36], while another method is based on the star of slots [19]. The first method is easy to apply for finding the layouts of double-layer concentrated-windings, but it is, in some cases, difficult to find the layouts for the single-layer windings. However, the method provided in [19] allows to find the layout of the single-layer windings from the double-layer windings layout in all possible cases.

The winding factor can be calculated by following different methods:

1. using the EMF phasors [37, 47],
2. using the winding function [39] or
3. using closed-form expressions [19, 20].

The relation between the combination of pole and slot numbers and the winding factor has been investigated by the author using the method based on the EMF phasors.

3.3 Design of a non overlapping winding layout - Methods to find the winding layout of concentrated windings

The winding layout can be found using one of the method described in following paragraph. Two different methods to find the winding layout that gives

the highest winding factor are presented.

3.3.1 Winding layout using Viarouge method

This method proposed in [36] is based on the decomposition of the number of slots per pole per phase q. It is similar to the method used for the large synchronous machines with a fractional value of q [35]. The method is illustrated using $Qs = 12$ and $p = 10$ and a double-layer winding as an example.

a) The number of slots per pole per phase q is written as a fraction which is cancelled down to its lowest terms: $q = nu/d = 2/7$ where nu and d are integers.

b) A sequence of $d - nu = 5$ zeros ("0") and $nu = 2$ ones ("1") is found, the ones being distributed in the sequence as regularly as possible.

c) The found sequence is repeated $3p/d = Qs/nu = 12$ times. It is compared to the layout of the distributed winding with $3p$slots and $q = 1$.

d) Those conductors from the distributed winding that correspond to the "1" are kept and form one layer of the double-layer concentrated winding. The second winding layer is obtained by writing the corresponding return conductor on the other side of the tooth for every obtained conductor, i.e. A' for A.

e) A vector S is written to describe the layout of phase A. It will be used to calculate the winding factor. Thereby, the slots are numbered from 1 to Qs.

The vector S consists of the numbers corresponding to these slots that contain conductors of the phase A. If both layers of one slot contain conductors of phase A, the number of the slot is written twice in the vector. S has thus $2Q_s/3$ elements. For conductors A', a minus is added to the corresponding slot number.

The layout for the single layer winding can be found from step d). The single layer winding layout for the 24-slot 28-pole is simply

$$A|A|C|C|B|B|A|A|C|C|B|B \tag{3.1}$$

For other cases, such as when $Q_s = 18$ and $p = 14$, the layout cannot be found applying the described method. The layout that gives the highest winding factor for this combination of slot and pole numbers is indeed

$$A|A|C|C|A|A|C|C|B|B|C|C|B|B|A|A|B|B. \tag{3.2}$$

The following script can be used to compute the winding layout using this method.

Listing 3.1: Wolfram Mathematica code for slot coil identification using Viarouge Method

```
seq1=Table[0,{d-nu}];
seq2=Table[1,{nu}];
sequence=Riffle[seq1,1,{1,d-nu,d-nu-2}];
wind1=Flatten[Table[sequence,{3*p/d}]];
wind2={"A","-B","C","-A","B","-C"};
winding=Table[wind2,{3*p}];
wind3=Flatten[winding[[1;;3*p/d]]]

n=0;
LayerOne={};
For[i=0,i\[LessSlantEqual]Length[wind3],i++,
If[wind1[[i]]==1,{LayerOne={LayerOne,wind3[[i]]}}]]
LayerOne1=Flatten[LayerOne];
Grid[{LayerOne1},Frame->All]


LayerTwo1=LayerOne1;
For[i=1,i\[LessSlantEqual]Length[LayerOne1],i++,
{Switch[LayerOne1[[i]],
"-A",LayerTwo1[[i]]="A",
"A",LayerTwo1[[i]]="-A",
"-B",LayerTwo1[[i]]="B",
"B",LayerTwo1[[i]]="-B",
"-C",LayerTwo1[[i]]="C",
"C",LayerTwo1[[i]]="-C"
]}
];
Grid[{LayerTwo1},Frame->All]
```

3.3.2 Winding layout from the star of slot

The winding layout can also be found by using the star of slots [51]. The method is fully described by Bianchi in [51] for different cases. "The star of slot is the phasor representation of the main EMF harmonic induced in the coil side of each slot", [51]. The method described in Section 3.2.3 is thus related to the star of slot. The winding layout for single-layer windings can be found in any of the possible cases with the star of slot.

The star of slot is constituted of $Q_s/GCD(Qs, p/2)$ spokes. The angle between the phasors of two consecutive slots is $\frac{\pi p}{Q_s}$ in electrical radians. Two opposite sectors covering π/m radians (m is the number of phases) are plotted on the star of slots.

The phasors inside the sectors are those belonging to a same phase. The phasors in the opposite sector give the slots containing the coil sides with negative polarity.

From this star of slot, the winding layout of double-layer windings can be

found. Different rules to find the winding layout of single-layer windings are defined in [51], starting from the defined star of slot.

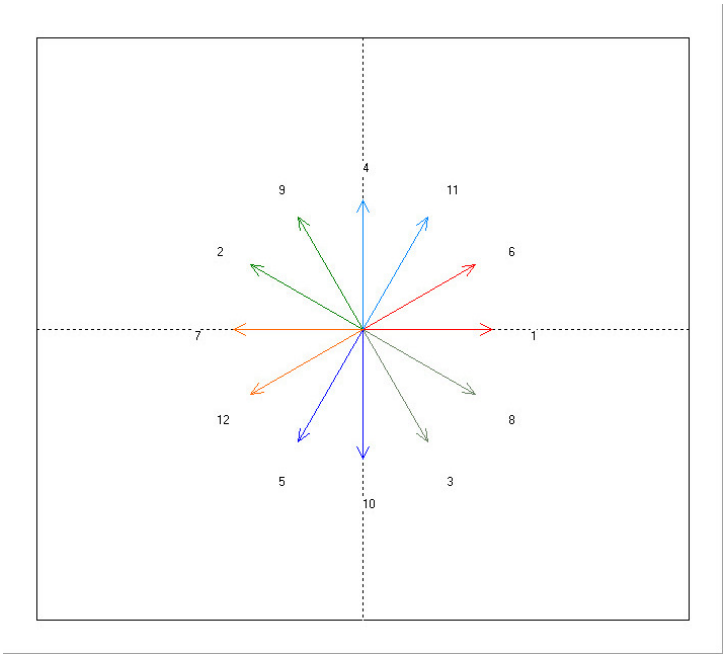

Figure 3.6: Star of slots for 48 slots 40 poles winding

Figure 3.6 illustrates this method with the example of a double-layer 40-pole, 48-slot PMSM. As can be seen, the phasors numbered 2,3,8,9 belongs to phase A. The winding layout is then completed as in step d) of Cros' method, and the same winding layout is found. The vector S describes the layout of phase A of the machine. The slots are numbered from 1 to Q_s. The vector S consists of the numbers corresponding to the slots that contain conductors of phase A. If both layers of one slot contain conductors of phase A, the number of the slot is written twice in the vector. S has thus $\frac{2Q_s}{3}$ elements. For conductors of the returning A', a minus is added to the corresponding slot number.

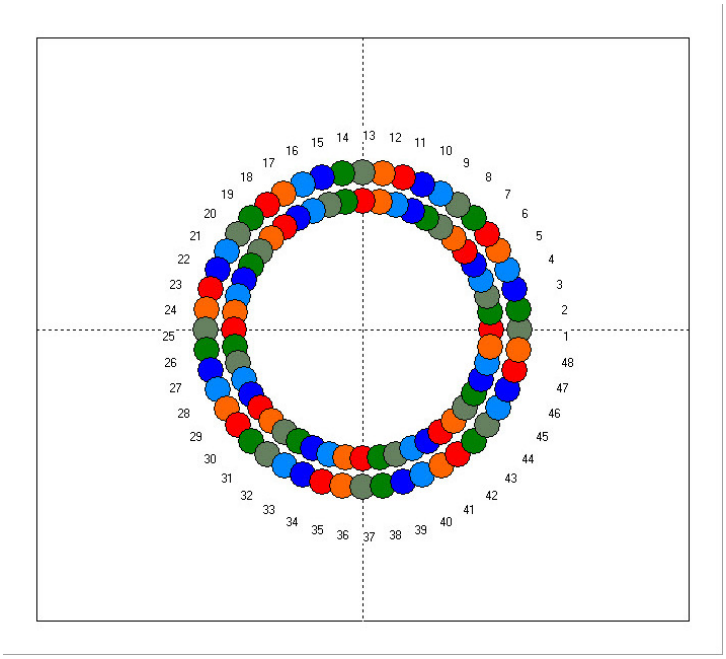

Figure 3.7: Winding configuration green phase A, red phase B blue phase C.

3.4 Design and experimental characterization of a low speed Permanent Magnet Synchronous Generator with fractionary nonoverlaping windings

The performance of a specially designed low speed radial flux permanent magnet fractionary winding generator is evaluated using FEM and laboratory tests. A fractional winding tooth concentrated winding prototype machine with number $q = 0.35$ for the slots per pole and per phase, 1.8 kW output power and 88 rpm speed is build constructed to verify the calculations. The specifications of the design of the machine are given in table 3.2.

3.4.1 Design of a low speed PSMG with nonoverlapping windings

The initial design of the low speed fractionary PMSM was performed using the program in apendix A.2 and verified with the EMETOR software which offers good performances and is oriented toward the design of fractionary winding SPMSM

The figure below shows the geometry of a SMPM motor and the definition of the geometrical parameters. The dimensions are expressed in equations

Table 3.2: PMSG Characteristics

Pn	$1.8kW$
n_n	$88rpm$
V_n	$138V$
$Slots$	72
$poles$	68
m	3
D_i	$208mm$
D_o	$305.2mm$
l_c	$70mm$

(3.4) to (3.9), where Q_s is the number of stator slots. The parameter k_{open} is the ratio of the stator slot opening to the slot width (3.9). The teeth are straight, which means that the tooth width b_{ts} is constant all along the tooth.

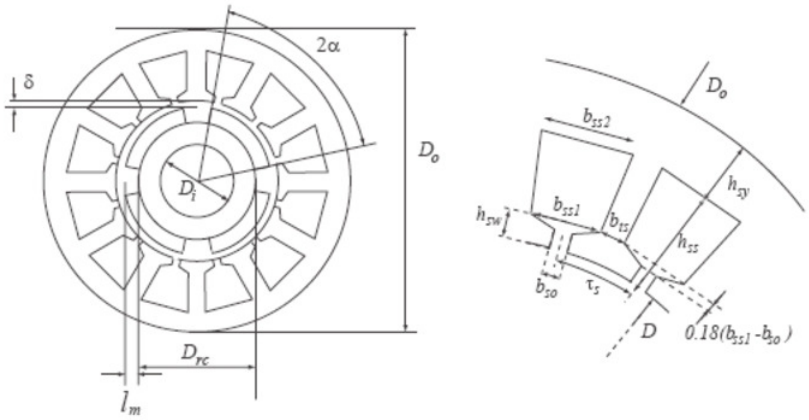

Figure 3.8: Definition of the geometrical parameters for the surface-mounted PMSMs.

$$D = D_{rc} + 2l_m + 2\delta; \quad (3.3)$$

$$\tau_s = \pi\frac{D + 2h_{sw}}{Q_s} \quad (3.4)$$

$$h_{sy} = \frac{1}{2}(D_o - D - 2h_{ss}) \quad (3.5)$$

$$b_{ss} = \pi\frac{D + 2h_{ss}}{Q_s} \quad (3.6)$$

$$k_{open} = \frac{b_{so}}{b_{ss1}} \quad (3.7)$$

The inner stator diameter D is very large compared to the slot pitch τ_s. Therefore, b_{ss1}, b_{ss2} and b_{ts}, which actually are arcs of circle, are approximated as straight lines in equations (3.6) and (3.8).

The slot area A_{sl} is given by equation (3.8).

$$A_{sl} = \frac{1}{2}(b_{ss1} + b_{ss2})(h_{ss} - h_{sw}) \tag{3.8}$$

Instead of defining an extra parameter to describe completely the tooth tip, the height of the tooth tip top (see figure above) is arbitrary defined as $hsw - 0.18\ (b_{ss1} - b_{so})$. This influences only the calculation of the leakage inductance. When setting $h_{sw} = 0$ and $k_{open} = 1$, the slots are completely opened.

3.4.2 Open-circuit airgap flux density

The open-circuit airgap flux density is calculated using the analytical models described in [1] and [2], in the case of radially magnetized PMs.

The stator is assumed to be slotless. The PM axis is chosen as a reference for the angular position θ as shown in Fig. 3.9 in the case of a PMSM with $q = 2$. For all the different geometries, the first slot containing conductors of phase A is facing the middle of the interpole. The angle between the PM axis and the axis of phase A is θA at $t = 0$.

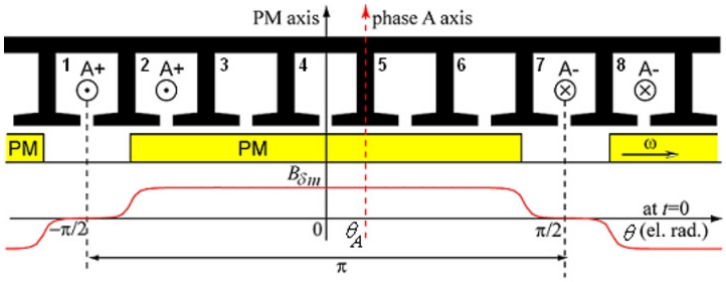

Figure 3.9: Open-circuit airgap flux density for a PMSM with $q = 2$.

The open-circuit airgap flux density B_{3b4m} is given by:

$$B_{\delta m}(\theta) = \sum_{h=1.3.5}^{\infty} B_{mh} \cos(h\theta - h\omega t) \tag{3.9}$$

The winding factor can be used in the calculation of the magneto-motive force (MMF), the flux linkage and back-emf . It allows to take the distribution of the coils in the slots and the slot pitch into account. There are several methods to calculate the winding factor. The method used in this tool is based on the calculation of the EMF phasors [3]. The winding layout, i.e. the arrangement of the coils in the slots, should be known when using this method.

The vector S is used to describe the layout of phase A. If the slots are numbered from 1 to Q_s, the vector S consists of the numbers corresponding

to these slots that contain conductors of the phase A. If the winding has two layers and both layers of one slot contain conductors of phase A, the number of the slot is written twice in the vector. For return conductors, a minus is added to the corresponding slot number.

Vector S can be calculated automatically for distributed windings. For concentrated windings, the winding layout (and thus vector S) can be found by using the method in [4] or the star of slot [5].

The corresponding EMF phasor $\overrightarrow{E}_i h$ of harmonic h for a coil side numbered i from phase A is:

$$\overrightarrow{E}_{ih} = sign(S(i))e^{f\frac{h\pi p}{Qs}|S(i)-1|} \tag{3.10}$$

The amplitude of the h^{th} harmonic component of the winding factor is then:

$$k_{wh} = \frac{1}{nlQ_s}\left|\sum_{i=1}^{\frac{nlQs}{3}} \overrightarrow{E}_{ih}\right| \tag{3.11}$$

$$\alpha_{kwh} = \arg(\sum_{i=1}^{\frac{nlQs}{3}} \overrightarrow{E}_{ih}) \tag{3.12}$$

The angle θ_A between the PM axis and phase A axis at t=0 (see Fig. 3.9) is equal to α_{kw1}. As the winding factor kwh is an absolute value (which is not the case when using the closed-form expression of the winding factor), the phase α_{kwh} is required in order to obtain the right sign of the winding factor.

3.4.3 Inductances - Armature reaction flux density

The self inductance L_a of the machine is the sum of the slot leakage inductance L_{leak}, magnetizing inductance L_{magn} and end-winding inductance L_{ew}.

At this stage in the procedure, the number of conductors in the slots is still unknown. Therefore, the inductances over the squared number of conductor are first calculated.

- Slot leakage inductance:
- The slot leakage inductance over the squared number of conductors is calculated as in [6].
- Magnetizing inductance:

In order to calculate the magnetizing inductance, the airgap flux density from the armature reaction due to a current ia in phase a is first computed. Since the current and number of conductors are not known yet in the procedure, it is the flux density over the current over the number of conductors per slot, $B_{wind,nsia}$ that is calculated:

$$B_{wind,ia} = \sum_{h=1}^{\infty} \frac{2q\mu_0(-1)^h}{h} k_{wh}k_{soh}F_h \cos(hp_p\theta + \alpha_{kwh}) \tag{3.13}$$

A coil of phase A carrying a current creates in the airgap a flux density that is a step function (as for the MMF). This step function is corrected with k_{soh} that is

the slot opening factor defined in [7], and F_h that is a function which accounts for the effect of curvature also defined in [7]. The function F_h depends on the radius and is calculated here for the radius corresponding to the middle of the airgap. The term $2(-1)^h/(nh)$ comes from the Fourier series of the step functions. The armature airgap flux density from all the coils of phase A are added which introduce the winding factor.

The flux linkage due to the armature reaction is then calculated from $B_{wind,nsia}$ and gives the magnetizing inductance over the squared number of conductors per slot.

$$L_{mag,ns} = \frac{4}{\pi}\frac{2q\mu_0(-1)^h}{\pi\delta}\frac{(-1)^2}{h}k_{wh}k_{soh}F_h\cos(hp_p\theta + \alpha_{kwh}) \tag{3.14}$$

The flux linkage due to the armature reaction is then calculated from $B_{wind,nsia}$ and gives the magnetizing inductance over the squared number of conductors per slot.

3.4.4 End-winding inductance:

The end-winding inductance over the squared number of conductors is calculated as in ref.

$$L_w = \frac{4m}{Qs}\mu_0 L_i N_{ph}^2 q\lambda_s \tag{3.15}$$

where $\lambda_s = 2h_b\lambda_e + b_b\lambda_w$
and $N_{ph} = \frac{2pqN_{n1}}{a}$

3.4.5 Resistance

The resistance over the squared conductor number is calculated using the following equation:

$$R_0 = \rho_{cu}\frac{Q_s L + (D + h_{ss})\pi k_{coil}}{3f_s A_{st}} \tag{3.16}$$

L is the active length of the machine. ρ_{cu} is the copper resistivity that is temperature dependent (resistivity $\rho_{cu} = 1.72e^{-8}$ at 20°C, temperature coefficient $\alpha = 0.0039K^{-1}$). The temperature used to calculate the copper resistivity is the one set as an input. f_s is the slot fill factor that is also an input. The end-windings are taken into account by introducing the term $(D + h_{ss})\pi k_{coil}$, where k_{coil} is given in the table below [9].

Table 3.3: Coil factor

	Distributed	Concentrated	Concentrated
	winding	1 layer	2 layers
k_{coil}	$1.6Q_s/p$	1.46	0.93

3.4.6 Current loading

The fundamental current loading S_1 is calculated from the following equation:

$$S_1 = \frac{4T}{\pi(D-\delta)^2 L \widehat{B}_{\delta m1} k_{w1} \sin\beta} \tag{3.17}$$

T is the torque (input value).

$B_{\delta m1}$ is the fundamental of the PM airgap flux density.

β is the angle between the magnet flux linkage and the current.

It depends on the saliency of the machine. For a non-salient machine, as the PMSM machine, β is $\pi/2$.

The current loading is used to calculate the total stator current per slot ns, I and the current density J:

$$n_s = S_1 \tau_s \tag{3.18}$$

$$J = \frac{n_s I}{A_{sl} f ls} \tag{3.19}$$

3.4.7 Back-emf

The phase back-emf $E_{a,ns}$ over the number of conductor per slots is obtained by integrated the PM flux linkage over the time. R is the airgap radius and α_c is the angular position of the coil axis in mech. rad.

$$E_{a,ns} = \sum_{h=1,2,3..}^{\infty} 2 k_{wh} \omega B_{mh} R L n_s q \sin(h\omega t + \alpha_{kwh}) \tag{3.20}$$

3.4.8 Number of conductors

The number of conductors is obtained by deriving the equation from the phasor diagram. The method is fully described in [10]. V is the maximum value of the phase supplied voltage (its RMS value is an input).

$$n_s = \frac{V}{\sqrt{(E_{a,n_s} + R_{n_s} n_s I)^2 + (L_a, n_s \omega n_s I)^2}} \tag{3.21}$$

Knowing the number of conductors per slots, the resistance, inductances and back-emf can now be calculated:

$$\begin{aligned} L_a &= n_s^2 L_{a,n_s} \\ R &= n_s^2 R_n \\ E_a &= n_s E_{a,n} \end{aligned} \tag{3.22}$$

3.4.9 Torque

The torque T_{calc} is calculated using the phase back-emfs E_a, E_b, E_c and sinusoidal currents i_a, i_b, i_c. These currents have an amplitude of E_a, E_b and E_c obtained from equation (3.22) by shifting the phase with $2\pi/3$ and $4\pi/3$. The torque ripple can then be calculated.

$$T_{calc} = p_p(E_a i_a + E_b i_b + E_c i_c) \tag{3.23}$$

3.4.10 Flux-densities

The maximum flux densities in the teeth B_{st}, stator and rotor back (B_{sy} and B_{ry}) at open circuit (no-load conditions) are calculated.

$$Bst = \frac{B_{m1}\alpha(\frac{D}{2} - \delta)}{p_p q b_{ts} k_j}; Bst = \frac{B_{m1}\alpha(\frac{D}{2} - \delta)}{p_p q h_{sy} k_j}; Bst = \frac{B_{m1}\alpha(\frac{D}{2} - \delta)}{p_p q h_{ry} k_j} \tag{3.24}$$

3.4.11 Losses - performance

The stator iron losses at open-circuit (no-load conditions) P_{iron} are calculated using a simple model described in [6].

$$p_{iron} = p_{hyst} + p_{eddy} = k_{hyst} B^{\beta_{st}} + k_{eddy} B^2 \omega_{el}^2 \tag{3.25}$$

where p_{hyst} and p_{eddy} are the hysteresis and the eddy current loss-density respectively. k_{hyst} and k_{eddy} are hysteresis and eddy current constants and β_{St} is the Steinmetz constant.
In the teeth, the hysteresis loss density is:

$$p_{hyst}(teeth) = k_{hyst} B^{\beta_{St}} \omega_{el} \text{ů} \tag{3.26}$$

In the stator yoke, the hysteresis loss density is:

$$p_{hyst}(teeth) = k_{hyst} B^{\beta_{Sy}} \omega_{el} \text{ů} \tag{3.27}$$

For the eddy current it is convenient to represent the average loss density as a function of the time rate of change of the vector flux density [10].

$$p_{eddy} = 2k_{eddy}\left(\frac{dB}{dt}\right)^2 \tag{3.28}$$

The instantaneous eddy current loss density can be expressed as:

$$p_{eddy}(teeth) = \frac{12}{\pi^2} q \cdot k_{eddy} \cdot k_q \cdot k_c(\omega_{el} \cdot B_{st}^2) \tag{3.29}$$

where k_q and k_c are correction factors depending on the geometry.

The average eddy current loss density in the teeth can then be expressed as

$$P_{eddy}(yoke) = \frac{1}{cov}\frac{8}{\pi^2}k_{eddy}(\omega_{el} \cdot B_{sy})(1 + \frac{8k_q h_{sy}^2}{27cov \cdot q \cdot \tau_{s2}^2}) \tag{3.30}$$

where τ_{s2} is the projected slot pitch at the middle of the yoke. The eddy current loss in the yoke is composed of a contribution of the longitudinal flux component and a contribution of the normal flux component.

$$P_{iron} = (p_{eddy}(teeth) + p_{hyst}(teeth))V_t + (p_{eddy}(yoke) + p_{hyst}(yoke))V_y \tag{3.31}$$

The iron losses are decomposed in the hysteresis losses and eddy current losses calculated in the teeth and stator yoke respectively. The values of the maximum flux-densities at no-load are used.

$$P_{cu} = 3/2RI_a^2 \tag{3.32}$$

$$\eta = \frac{\frac{Tn2\pi}{60}}{\frac{Tn2\pi}{60} + P_{cu} + P_{iron}} \tag{3.33}$$

Copper losses and efficiency are also calculated. In the efficiency, only the copper losses and no-load iron losses are taken into account. The input specifications are give in the following paragraphs:

Design Inputs

MATERIALS

Stator iron:
Material density $[kg/m3]$ $\rho_{statiron} = 7750$;
Stator iron stacking factor $k_j = 1$;
Lamination thickness $[m]$: $lam_{thick,stat} = 0.00065$;
Conductivity $[(\Omega.m)^{-1}]$ $\sigma_{stat} = 3333333$;

Rotor iron:
Material density $[kg/m^3]$ $\rho_{rotiron} = 7750$;
Rotor iron stacking factor $k_{jrot} = 1$;
Lamination thickness $[m]$ $lam_{thick,rot} = 0.00065$;
Conductivity $[(\Omega.m)^{-1}]$ $\sigma_{rot} = 3333333$;

The laminations BH curve is presented in the following figure

Permanent magnets:

Material density $[kg/m^3]$ ρ_{magn}=7500; Remanence flux density $[T]$ b_r=1.03;
Relative permeability μ_r=1.08;
The permanent magnet curve is presented in Fig. 3.11 below

Conductors:

Material density $[kg/m^3]$ $cond = 8920$;

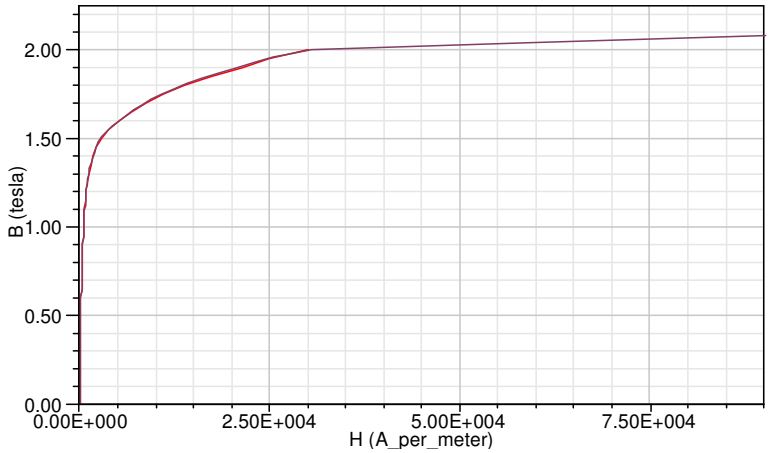

Figure 3.10: BH curve for steel laminations

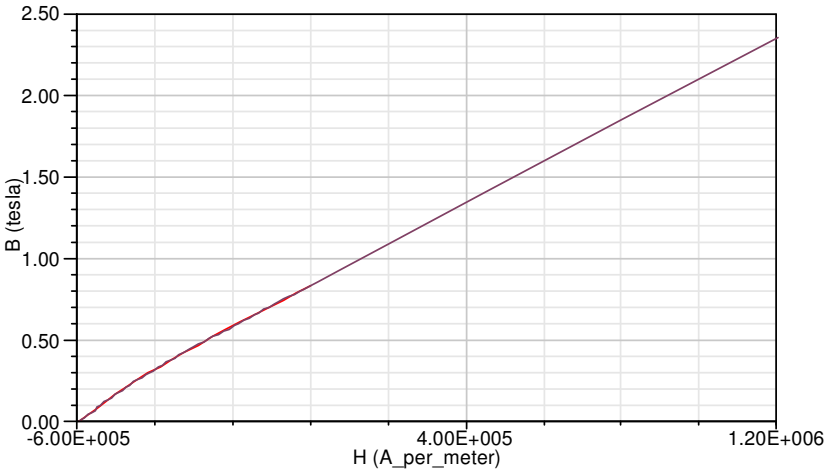

Figure 3.11: BH curve for permanent magnet properties

Windings

Winding type=Concentrated;
Number of poles: $p = 68$;
Number of slot per pole per phase $q = 0.35294117647059$; %
Fractional slot pitch number $pitch = 1$;
Number of stator slots: $Q_s = 72$;
Number of winding layers: $layer = 2$;
Temperature of the copper $[deg\ C]$ $temp_{cu} = 180$;
Stator slot fill factor $[p.u.]$ $f_s = 0.45$;
Supplied phase voltage $[V_{rms}]$ $V = 320$;

Motor Specifications

Rated speed [rpm] $n_n = 88$;
Rated torque [Nm] $T_n = 200$;

Geometrical input parameters:

Shaft diameter [mm] $D_i = 100$;
Rotor core diameter [mm] $D_{rc} = 208$;
Airgap length [mm] $\delta = 1$;
Magnet thickness [mm] l_{pm}=4;
Magnet angle [$el.\ deg.$] $\alpha = 120$;
Outer motor diameter [mm] $D_o = 305$;
Machine length [mm] $l = 70$;
Stator tooth width [mm] $b_{ts} = 6.8$;
Stator slot height [mm] $h_{ss} = 39$;
Stator slot opening / slot width [$p.u.$] $k_{open} = 1$;
Slot wedge height [mm] $h_{sw} = 1.3$;

The outputs of the design software are presented in the following. section

Design Outputs

Geometry

Inner stator diameter D_i [mm] $D_i = 218$;
Stator slot pitch [mm] $\tau_s = 9.5120444233691$;
Stator yoke height [mm] $h_{sy} = 4.5$;
Inner stator slot width [mm] $b_{ss1} = 2.8254908247487$;
Outer stator slot width [mm] $b_{ss2} = 6.115436464758$;
Slot area [mm^2] $a_{sl} = 168.5364794072$;
Slot opening width [mm] $b_{so} = 2.8254908247487$;
Rotor yoke height [mm] $h_{ry} = 54$;
Magnet coverage [%] $cov = 66.666666666667$;
Circumferential magnet width [mm] $w_{pm} = 6.652784442896$;

Flux densities

Fundamental open-circuit airgap flux density [T] $b_{delta} = 0.76291973741695$;
Max. no-load flux density in stator teeth [T] Ψ_{ts}=1.0162469666392;
Max. no-load flux density in stator yoke [T] Ψ_{rs}=0.54199838220757;
Max. no-load flux density in rotor yoke [T] $\Psi_{rr} = 0.045166531850631$;

Back EMF

Fundamental phase EMF (peak) [V] $E_{emf} = 105.70837634588$;

Torque

Torque ripple [%] $T_{ripple} = 2.7748254942468$;

Windings

Number of conductors per slot: $n_s = 87$;
Fundamental winding factor: $k_{w1} = 0.95250435856345$;
Conductors diameter $[mm]$: $cond_{diam} = 1.0535342252064$;
Phase resistance $[Ohms]$: $R = 5.381077673624$;

Currents

Phase current $[A]$ $i_a = 11.623352306449$;
Current density $[A/mm^2]$ $j_{current} = 9.4282095161297$;
Stator current loading $[A/mm]$ $s_1 = 106.31065264757$;
Total stator current per slot $[A]$ $n_{si} = 1011.231650661$;
Electrical frequency $[Hz]$ $f = 49.866666666667$;

Inductance

Self inductance $[H]$ $L_{tot} = 0.11663059492199$;
Mutual inductance $[H]$ $M_{iabtot} = 0.00061917201292599$;
Magnetizing inductance $[H]$ $L_{magn} = 0.0012381783461713$;
Slot leakage inductance $[H]$ $L_{leak} = 0.11395642076631$;
End-windings inductance $[H]$ $L_{ew} = 0.0014359958095069$;
d-axis inductance $[H]$ $L_d = 0.11601142290907$;
q-axis inductance $[H]$ $L_q = 0.11601142290907$;

Weights

Total active weight $[kg]$ $M_{tot} = 31.827019536897$;
Conductor mass $[kg]$ $M_{cu} = 3.9175563835064$;
PM mass $[kg]$ $M_{magnet} = 0.93242469958545$;
Iron mass $[kg]$ $M_{iron} = 26.977038453805$;
Stator's active mass $[kg]$ $M_{stator} = 16.721519492126$;
Rotor's active mass [kg] $M_{rotor} = 15.10550004477$;

Losses

Efficiency [%] $\eta = 62.476263102603$;
Rated power P[W] $P_{rated} = 1843.067690106$;
Power factor cos(phi) $cos\phi = 0.3699803364846$;
Copper losses $P_{copper} = 109.4941073458$; [W]
Stator iron losses : $P_{iron} = 16.466899173703$; [W]

Based on this specifications a prototype was build. The constructive parameters are given below

The lamination geometry is given in Fig 3.12.

Winding configuration of the 78/68 machine is presented in Fig. 3.13

3.5 Finite element analysis of 72 /68 PMSM generator

The finite element method was used in order to determine the effciency of the generator In Fig. 3.19 the no load flux lines are plotted.

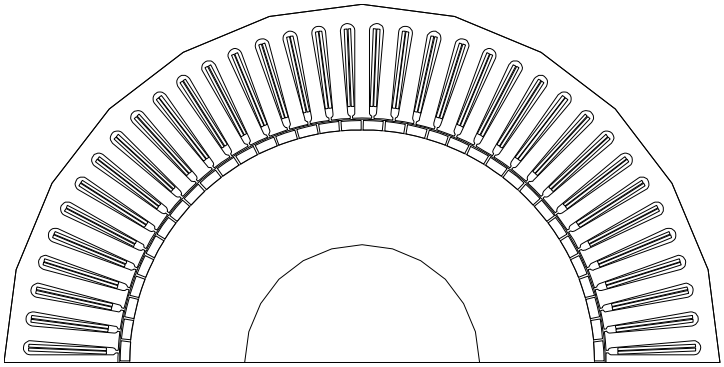

Figure 3.12: PMSG structure .

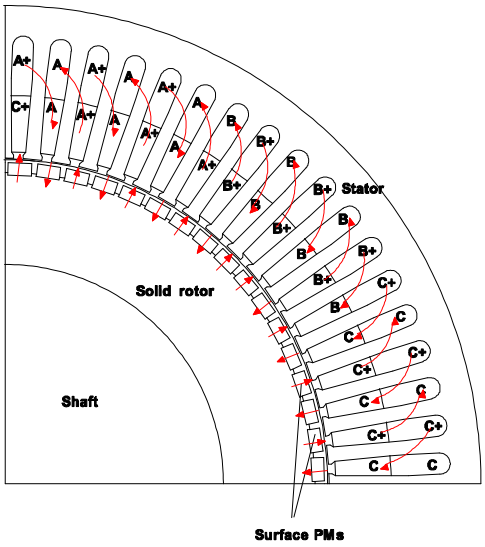

Figure 3.13: Cross section of the PMSG and winding configuration.

The PM airgap flux density distribution Fig. 3.18 shows that we may have a potentially harmonic induced content. The tooth concentric winding shows a low harmonic winding factor to filter the harmonics induced of induced voltage.

3.6 Parameter identification from finite elements

3.6.1 Inductances

The computation of inductances can be obtained from finite element solution by simulating the magnetic field produced by various currents applied to coils [3]. The inductances can be obtained from the energy stored in magnetic

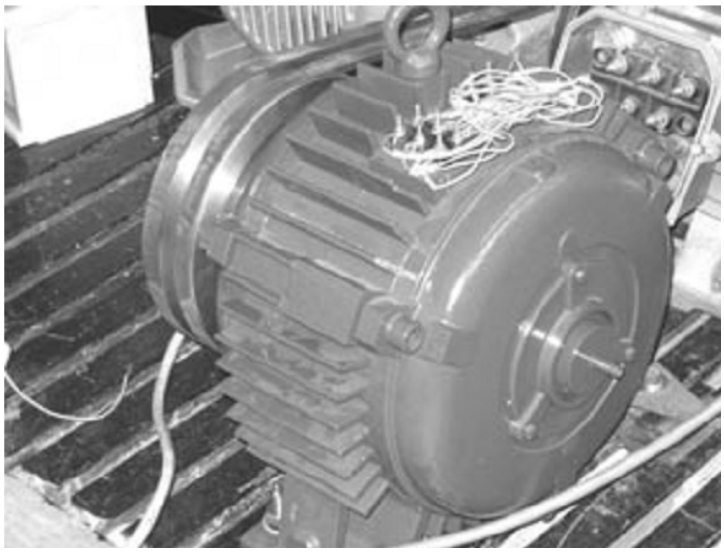

Figure 3.14: Low speed PMSM generator embodiment.

Table 3.4: Main Dimensions and characteristics of the PMSG

Rated Output Power (W)	250
No load Voltage (V)	38
Number of Poles	68
Frequency (Hz)	50
Number of Stator Slots	72
Number of turns in a coil	53
Outer Diameter of Stator (mm)	302.5
Inner Diameter of Stator (mm)	208
Length of Stator Core (mm)	70
Stacking factor of stator core	0.955
Stator Winding Factor	0.95
d-axis magnetizing reactance ( )	2.03
q-axis magnetizing reactance ( )	2.03
d-axis reactance Ω	31.61
q-axis reactance Ω	31.61
armature Leakage Reactance Ω	29.57
Airgap (mm)	1.5
PM radial thickness (mm)	4
PM pole pitch (mm)	9.2
Permanent magnet	*NeFeB*40
Br (T)	1.23
Hc (A/m)	97000
Armature Phase Resistance Ω	2.54

fields:

$$L = \frac{2W_m}{i^2} \tag{3.34}$$

where W_m is the total energy and i is the current producing Since the PMSG is a surface permanent magnet machine we can expect that the variation of the inductances with position to be neglected. Figure 3.15 presents the self inductance variation with position

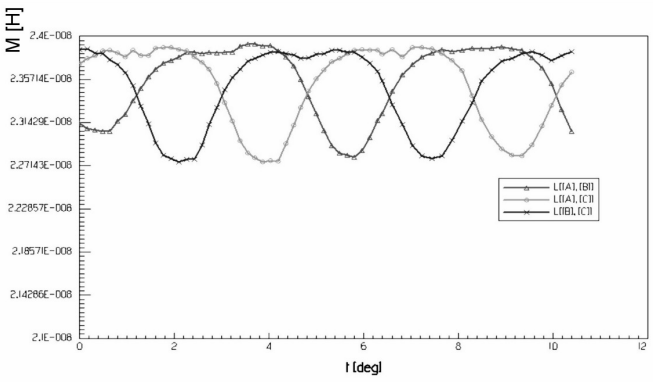

Figure 3.15: Self inductance variation with position

3.6.2 The flux linkage

The magnetic flux linkage is obtained solving the following relationship:

$$\Phi = \int BdA \tag{3.35}$$

From finite element time stepping analysis the flux linkage has been obtained, Fig 3.16. As it can be observed it has a sinusoidal variation with position which is a good performance, considering the fact that non overlapping winding [10] configurations may be a subject to high harmonics influence.

For a generator it is important that the PM flux linkage has a sinusoidal shape. The PM flux linkage has this sinusoidal shape which qualifies the fractionary winding generator with 72/68 poles for vector control .

3.6.3 The no load voltage

In order to provide a full comparison with the tests performed on the real prototype the no load voltage is needed to be identified. From finite element time stepping analysis it is possible to obtain this quantity. The induced voltage is given by:

$$E_{PM} = 2\pi \frac{f_s N_{ph} \xi_1 \phi_{\delta,PM}}{\sqrt{2}} \tag{3.36}$$

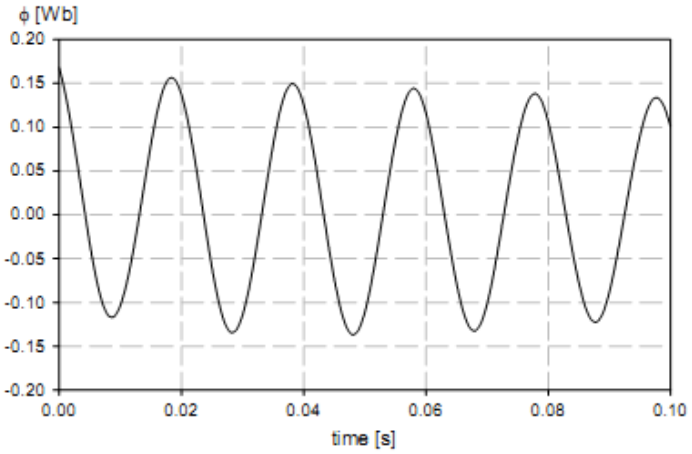

Figure 3.16: The flux linkage

where

N_{ph} is the amount of winding turns in series of stator phase,

f_s is the frequency of stator field and;

$\phi_{\delta,PM}$ is the fundamental air-gap ux due to magnet. The $\phi_{\delta,PM}$ can be analytically solved from FEA. The emf from FEA and from tests Fig. 3.17 fare well while the amplitudes differs by less in general, 8%. The influence of iron losses is not visible as it can be seen in Fig. 3.17.

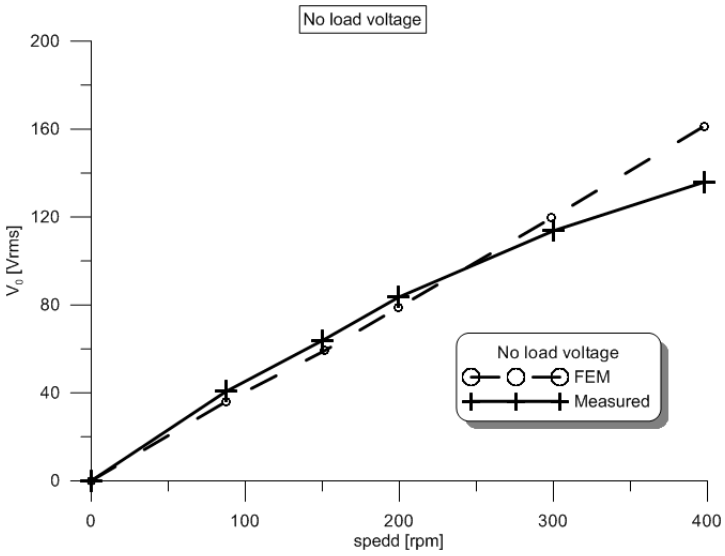

Figure 3.17: No load phase voltage.

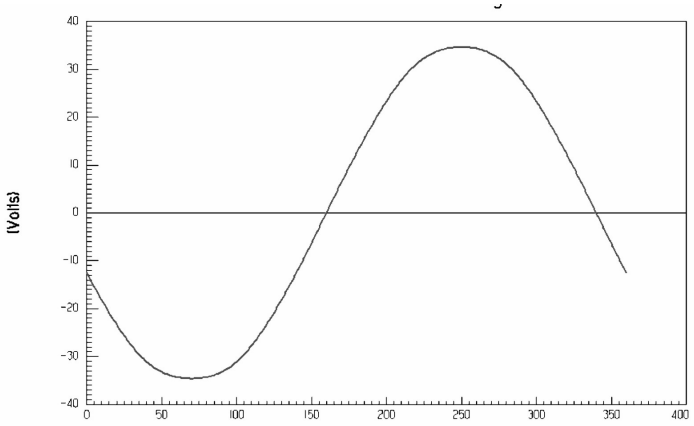

Figure 3.18: No load voltage waveform.

3.6.4 Time stepping finite element analysis

Time-stepped FEM was used as an effective tool to verify loss calculation based on simpler loss models [17], as it is economically and technically impractical to verify all loss predictions from experiments. The time depend field magnetic equation is expressed as:

$$\nabla \times v\nabla \times A = J_s - \sigma\frac{\partial A}{\partial t} - \sigma\nabla v + \nabla \times H_c + \sigma v \times \nabla \times A \tag{3.37}$$

where:
H_c is the coercivity of the permanent magnet;
v is velocity of the moving parts;
A is the magnetic vector potential;
J_s is the source current density.
Figure show the flux lines computed in transient mode at $n = 88rpm$

The magnetic circuit can be coupled with an external circuit which will allow to investigate no load voltage, short circuit current but also the full load characteristics. Fig. 3.21 presents the FEA coupled circuit configuration of the generator model.

The iron losses of the generator should carefully be taken in consideration both in the design stage and in performance analysis [4]. Many models for modeling iron losses are available in literature and may offer a good estimate of the iron loss if accurate data is provided [4]. In analytical designs the iron losses can only be approximated since the flux density does not have always a sinusoidal wave form. flux density varies in different parts of the lamination and this variation and is obtained from finite-element analysis. This can produce a good estimate of iron losses. Time stepping finite element analysis allows to investigate magnetic fields, energy force power loss, speed, and ux of a model at various stjpg over a specified period of time. The general expression of eddy current loss can be represented as a function of the rate change of the flux density vector [4]. The total eddy-current loss is then:

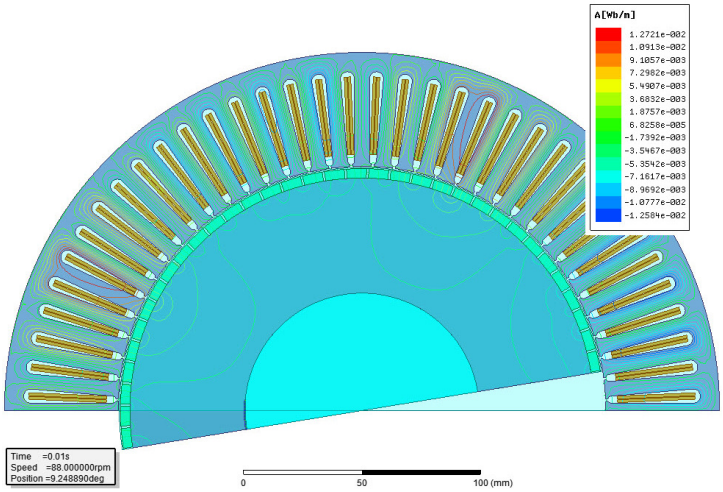

Figure 3.19: PMSG flux lines transient mode .

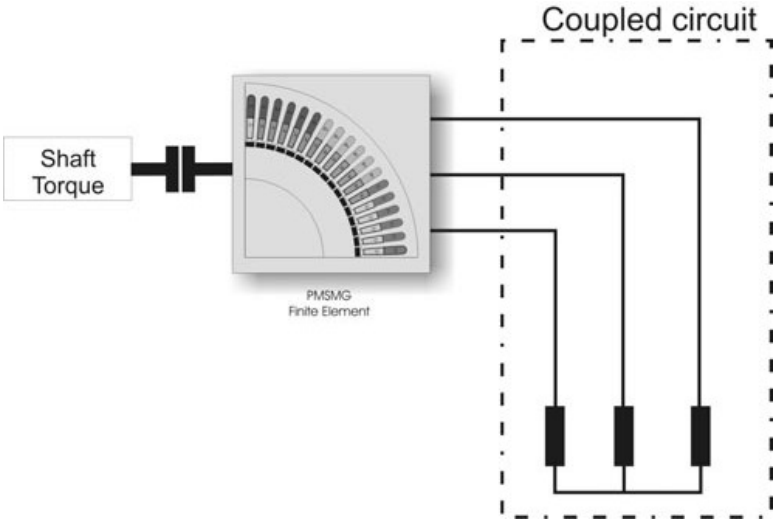

Figure 3.20: Time stepping circuit model

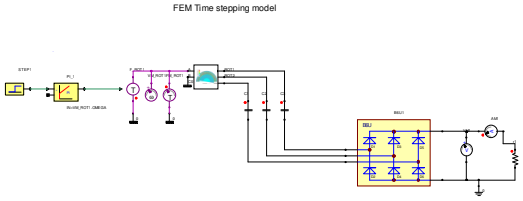

Figure 3.21: Time stepping coupled FEA (Maxwell solver for FEM model - Simplorer solver for circuit model)

$$P_e = \frac{2k_e}{T}\int_0^T \left(\frac{dB}{dt}\right)^2 dt \tag{3.38}$$

where T is the period.
The period T is

$$T = \frac{1}{f} = \frac{4\pi}{p\omega_{mec}} \tag{3.39}$$

where p is the number of poles and ω_{mec} is the mechanical speed. From the nite element method the eddy loss can written as:

$$P_e = p\sum_{m=1}^{M} A_m l_{fe} \frac{2k_e}{T}\int_0^{T/2} \left(\frac{dB}{dt}\right)^2 dt \tag{3.40}$$

$$P_e = 4pNkl_e f^2 \sum_{n=1}^{N}\left\{A_m\left(N\sum_{n=1}^{N}(B_{mx,n}-B_{mx,n-1})^2 + \sum_{n=1}^{N}(B_{my,n}-B_{my,n-1})^2\right)\right\}$$

where M is the total number of stjpg in the half time T=2 period,
l_{fe} is the stator core length,
A_m is the area of element , and N is the total number of elements in the teeth and the yoke of the stator. The hysteresis loss can be expressed as:

$$P_h = 2\pi f_h l_{fe}[A_m B_m^{\beta}] \tag{3.41}$$

Different loads have been used in order to identify the iron loss in the generator. Resistive load was used in order to observe losses in the generator. Of course no mechanical losses were taken in account since we have only an electromagnetic model. The losses during start up were evaluated.

Considering the moment of inertia of the generator $J = 0.18Kgm^2$ and applying a constant torque of $12Nm$ we have obtained the speed transient (Fig. 3.22), torque (Fig. 3.23) and electrical losses (Fig.3.24).

The losses obtained from finite element for various speeds are presented in Fig when capacitors are connected to the generator $C = 1000mF$ (Fig. 3.25). As it can be observed the increased value of the loses is due to capacitor connection.

3.6.5 Efficiency of the generator

With the iron losses determined from finite element the efficiency of the generator can be obtained. The efficiency as a function of power angle is presented in (Fig. 3.28). In order to obtain the efficiency as a function of load angle the variation of load angle was produced by modifying the id and iq in the generator (Fig. 3.28). As can be seen the efficiency of the generator without capacitors is limited to 70%.The reason for this is the fact the stator slot area is too small and thus the current capacity is limited.

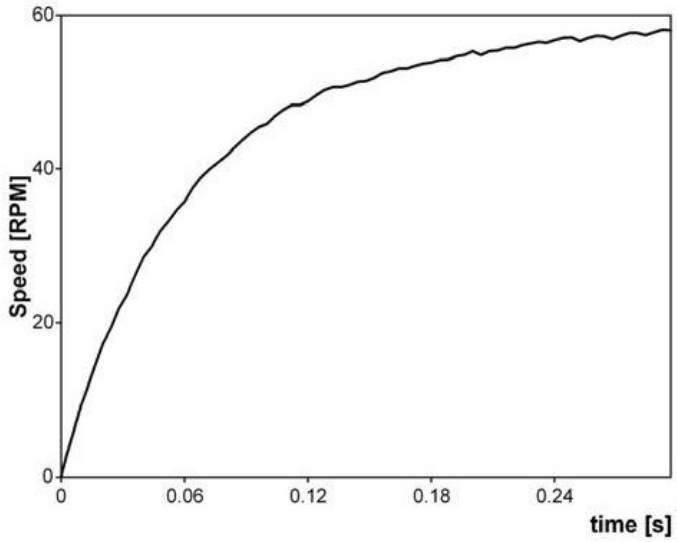

Figure 3.22: Speed of the generator

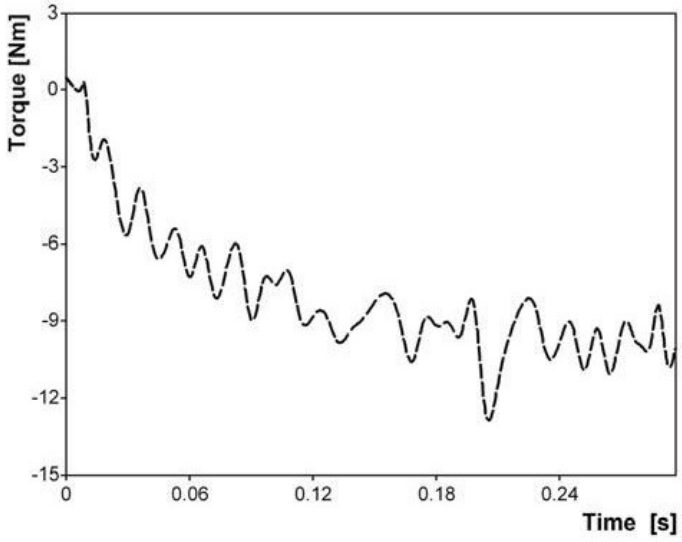

Figure 3.23: Torque of the generator

3.6.6 Torque pulsations

For a direct drive low speed generator the starting torque is another important issue because high starting torque prevents operation in cut-in wind speed. For this reason it is necessary to reduce the starting torque to acceptable values. Pulsations in torque are required to be Torque pulsations are mainly

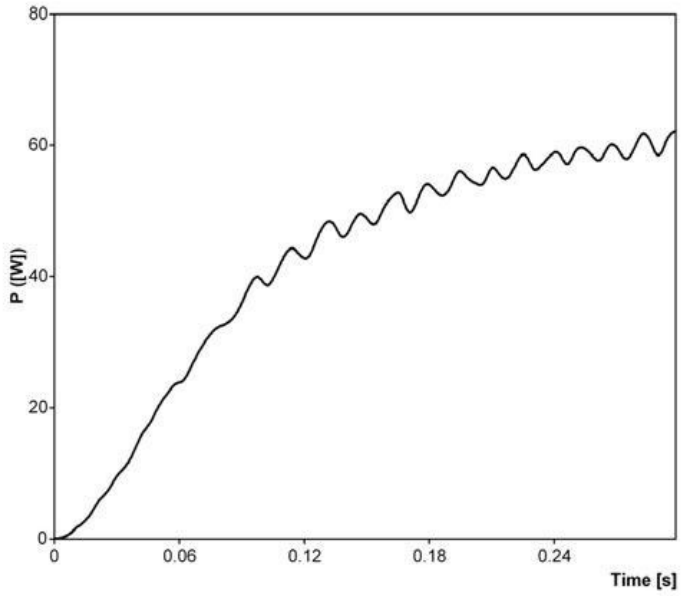

Figure 3.24: Iron powerlosses of the generator.

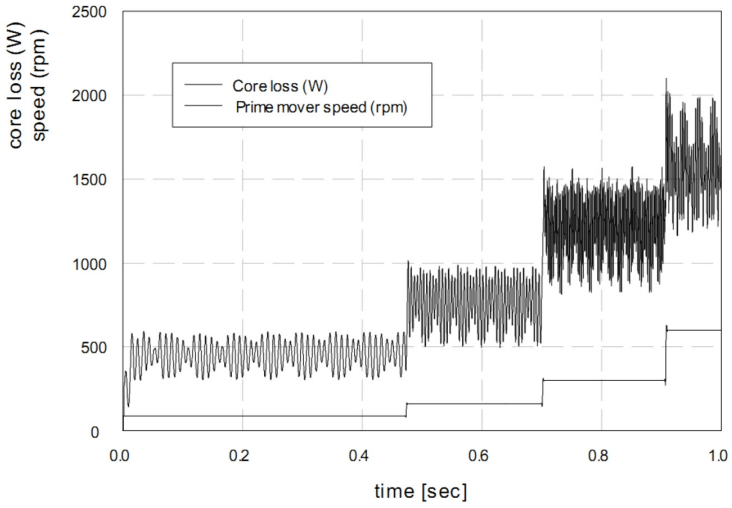

Figure 3.25: Capacitor power losses.

coming from three sources [10]:

a) cogging torque effect (detent effect), i.e interaction between the rotor magnetic flux and the variable permeance of the air gap due to the stator slot geometry;

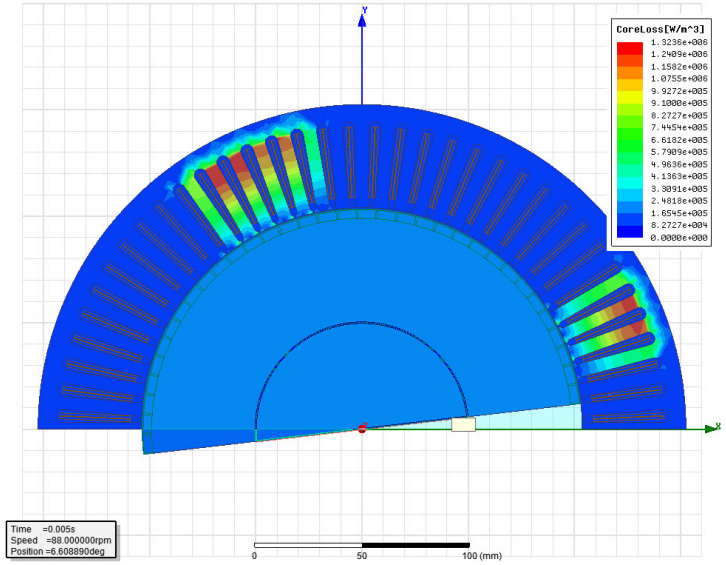

Figure 3.26: Electromagnetic iron core loss map from Finite Element time transient analysis

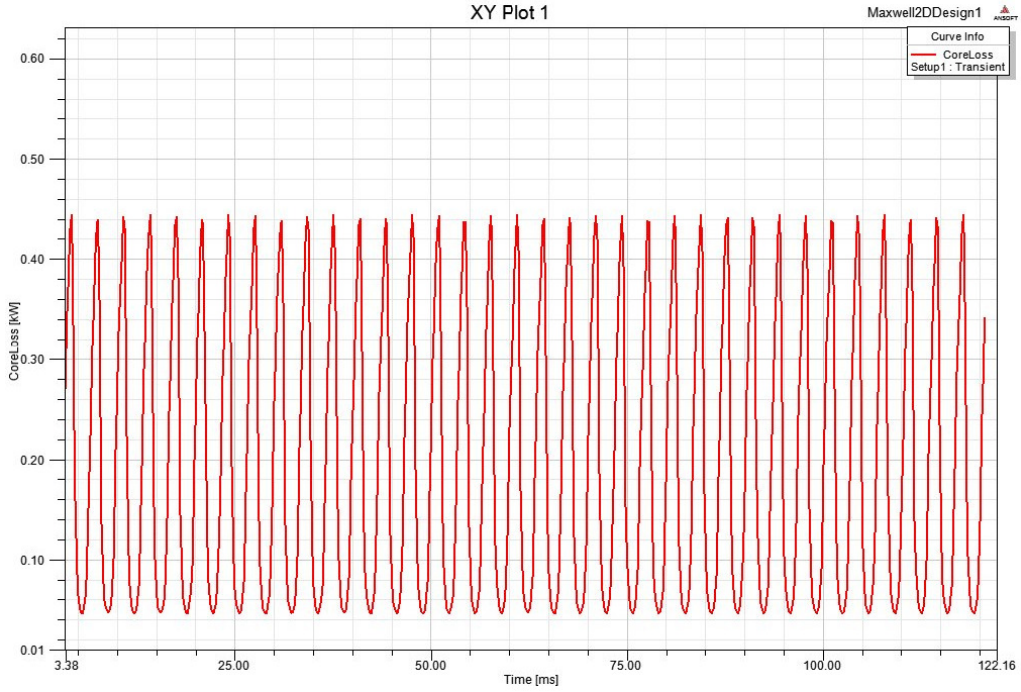

Figure 3.27: Iron losses obtained from transient analysis FEA $n = 88rpm$.

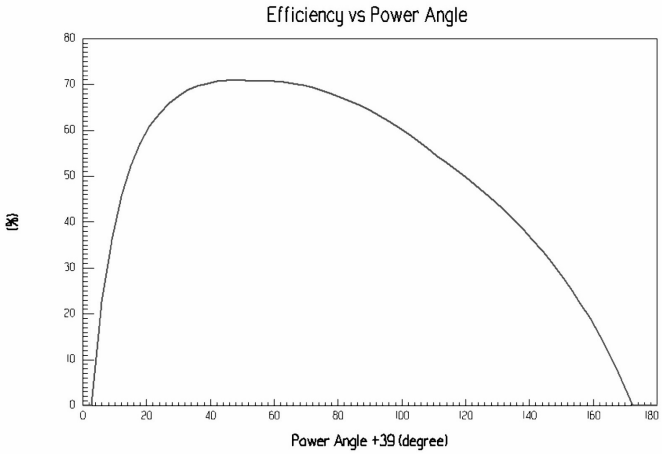

Figure 3.28: Efficiency of the generator obtained from finite elements .

b) distortion of sinusoidal or trapezoidal distribution of the flux density in the airgap;

c) the difference between permeances of the air gap in the d and q axis (rotor excentricity);

The torque pulsations were investigated with the PMSM working as a generator. The torque pulsations analysis obtained from finite element time stepping are presented in Fig.3.29. As can be seen in Fig.3.29 the amplitude of torque pulsations is small. The startup procedure for this generator was very simple since in our case only offgrid operation was considered. The prime mover is controlled in order to provide the necessary torque for the starting of the generator with load resistors connected.

3.6.7 Cogging torque

The starting torque of a permanent magnet generator is the total torque including the peak cogging torque, hysteresis torque and the torque necessary to overcome the bearing and seal friction of the generator [11]. The cogging torque is the dominant component, which is inherently generated from the interaction of the magnets with the stator teeth. The cogging torque it is the torque which is produced only by the interaction between the permanent magnet flux and the slot openings and thus it is independent on the stator current (load). An analytical formula is presented in [9] but evaluation of cogging torque requires the knowledge of several parameters which are not always available:

$$Tcog(\theta) = \approx \frac{\pi l_{stack} R_s}{2\mu_0 N_s} \sum_{m=1}^{N_s} \left(B_{PM}^2 \left(\frac{2\pi m}{N_s} + \theta \right) \right) (R_m + g_\alpha)\, ssg \tag{3.42}$$

$$R_m = R_s - g \tag{3.43}$$

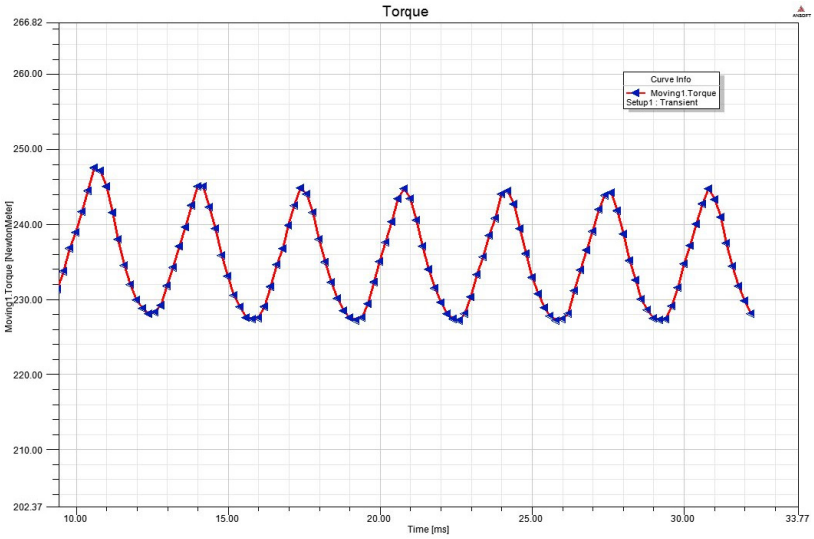

Figure 3.29: Torque pulsations.

where

l_{stack} is the stack length, m is the number of phases,

Rs is the interior stator radius,

B_{PM} permanent magnet flux density, g is the airgap interior stator radius,

g is the slot opening;

N_s number of slots;

$ssg = 1$:

From finite element the cogging torque is easy to be obtained displacing the rotor and computing the torque from the Maxwell stress tensor. The cogging torque is:

periodical function depending on the number of slots and on the number of poles. The frequency of the cogging torque is given by 3.44:

$$f_1 = LCM(Qs; p) \tag{3.44}$$

where Q_s is the number of stator slots; where z1 is the number of stator slots and the number of rotor poles; Fig. 3.30 and. 3.31 present the cogging torque, respectively, the cogging torque spectrum for a displacement equal to τ_{PM} :

As it can be observed, the frequency of fundamental is high and the amplitude of fundamental is small. The maximum value is $Tcog = 0,6Nm$. This value is half of the measured value $T_{cog} = 1.17Nm$ but this the measured value also includes the viscous friction in influence which can not be eliminated from measurements.

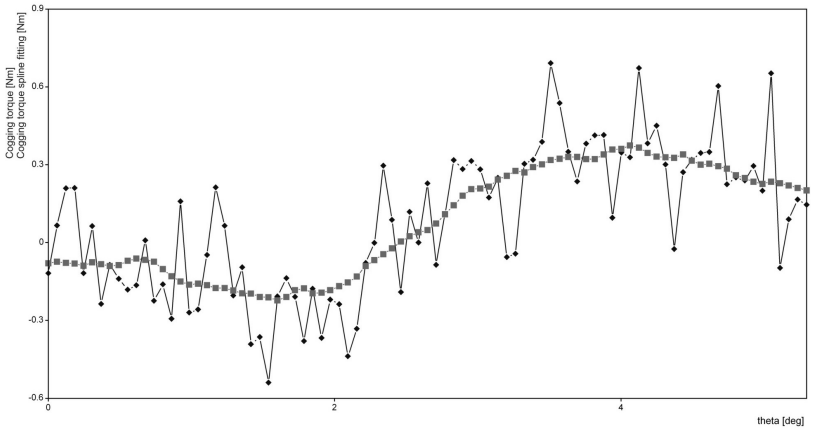

Figure 3.30: Cogging torque.

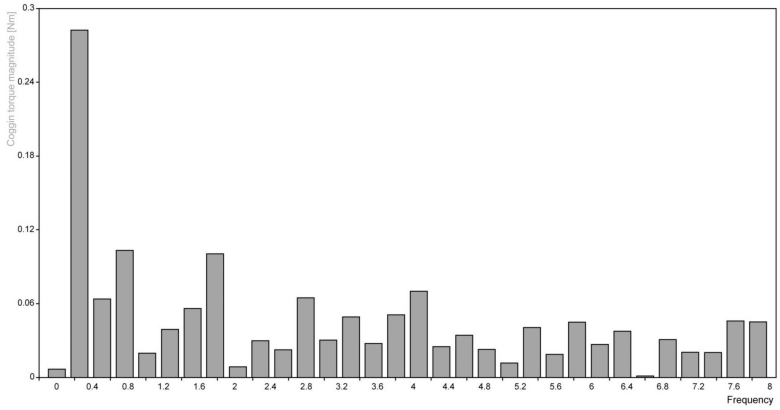

Figure 3.31: Cogging torque spectrum for a displacement equal to τ_{PM}.

3.7 PMSM Generator performance evaluation: test results

3.7.1 No load test results

The measured no load voltage waveform is shown in Fig 3.33 at 88 rpm. Also the input power was estimated from the output of an ABB ACS 600 drive (Fig. 3.32). Since we have used a belt transmission we had to include also the efficiency of the belt. From design specifications this was about: 0.8. As it can be observed the emf is pretty sinusoidal (Fig.3.33) which is also proven by the spectrum content of voltage (Fig. 3.34).

From the no load test the permanent magnet flux can be calculated as:

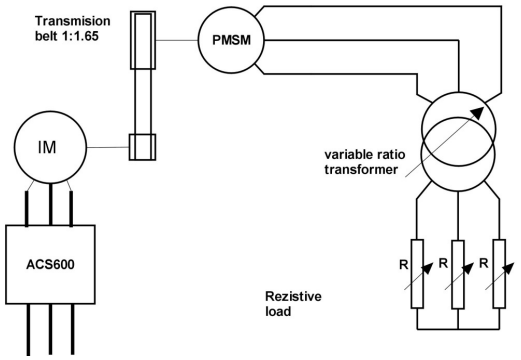

Figure 3.32: Test rig configuration.

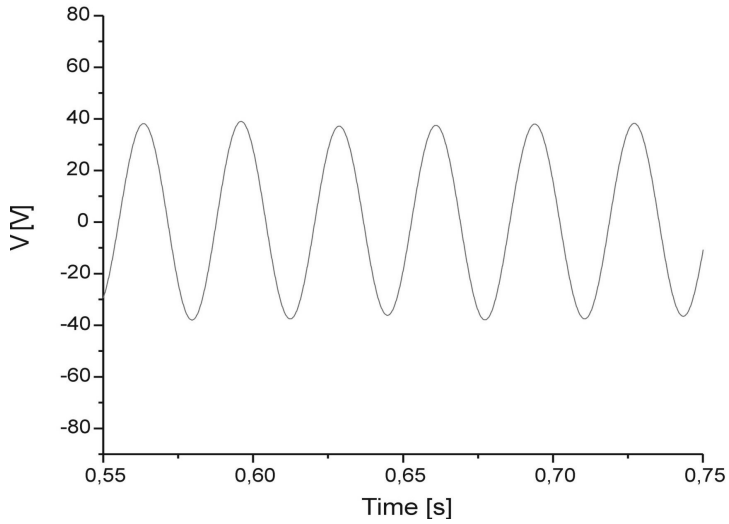

Figure 3.33: No load EMF waveform at 88rpm.

$$\Psi_{PM} = \frac{V_0\sqrt{2}}{\pi pf} \tag{3.45}$$

The permanent magnet measured flux value is

$$\Psi_{PM} = 0,093Wb \tag{3.46}$$

while the FEM value is $\Psi_{PM} = 0,103W$b.

The difference is explainable since the actual PM magnet material is not quite identical through close to the material which was used by the manufacturer. The no load mechanical power input Fig. 3.35 refer to the mechanical and core loss in the generator.

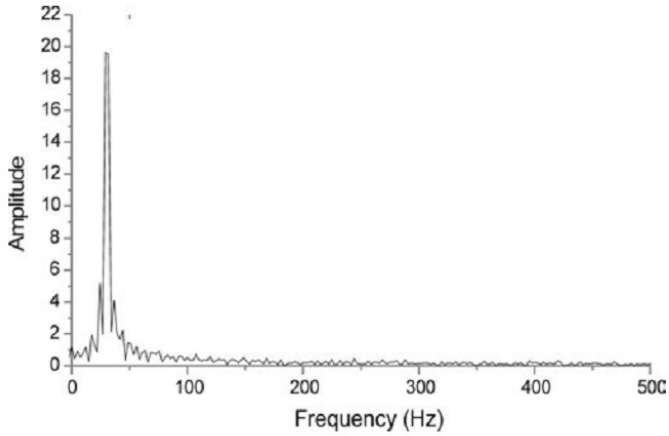

Figure 3.34: Harmonic components

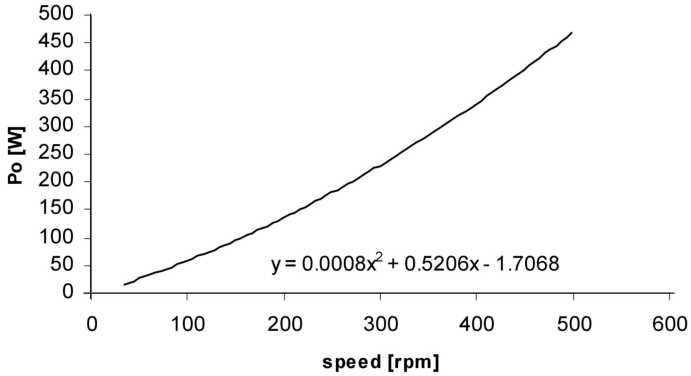

Figure 3.35: No load Power.

3.7.2 Short circuit test

Short circuit test shows a limited value of current (Fig. 3.18) which is caused by the relatively large inductance of generator.

From the short circuit tests the unsaturated inductance can be evaluated using the following relation:

$$L_d = \frac{E}{\omega_r I_{sc}} \tag{3.47}$$

3.7.3 Capacitor excitation tests

Capacitor excitation test (Fig. 3.38) was used in order to explore the voltage regulation capability of the generator [7-8]. Tests with capacitors added in

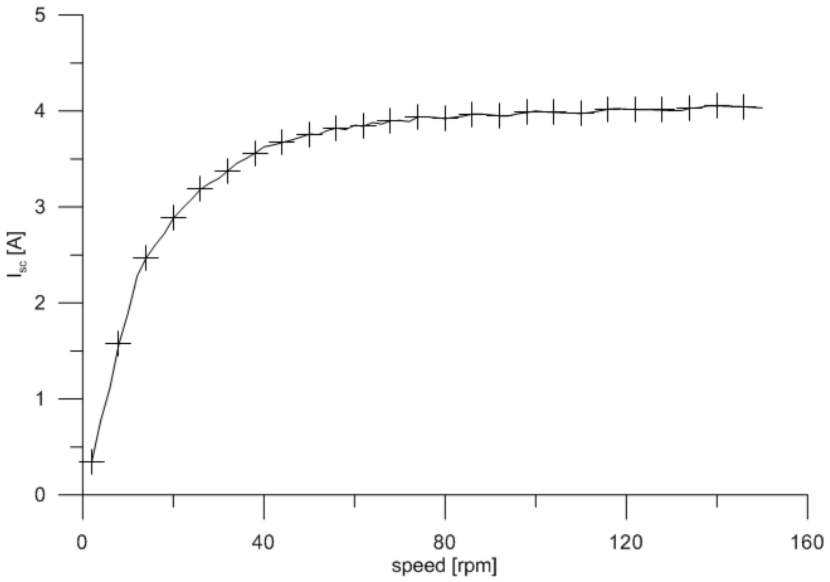

Figure 3.36: Shortcircuit current versus speed.

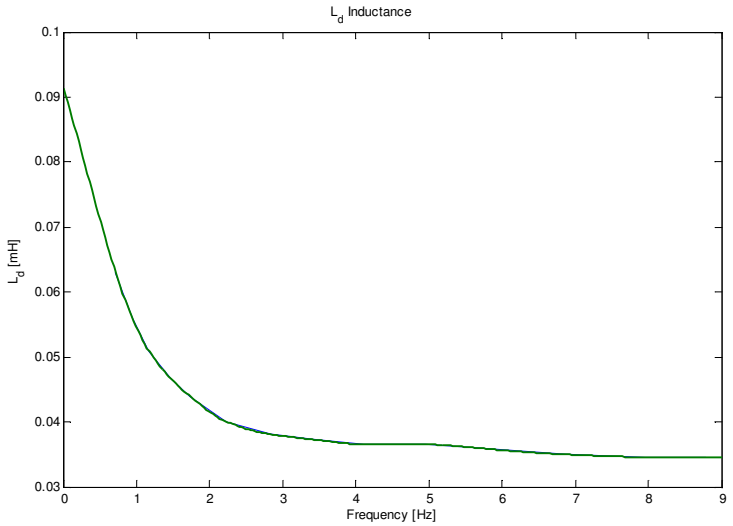

Figure 3.37: L_d inductance versus frequency.

parallel and in series showed that series connected capacitors can boost the value of the voltage. This is effect appears only at an limited value of the frequency.

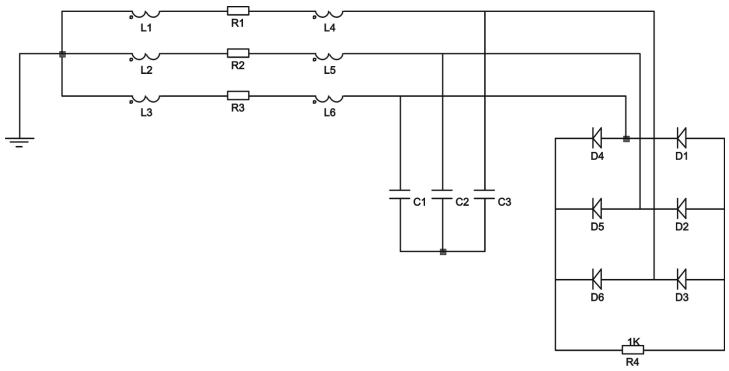

Figure 3.38: Parallel capacitor load test.

3.7.4 Losses segregation from capacitor excitation:

Capacitor only excitation test can provide useful information in order to obtain the efficiency of the generator [10]. The total losses when capacitor excitation is used can be written as:

$$\sum p = p_{mec}(\omega_r) + p_{Fe}(V_s^2) + \frac{3}{2}R_s I^2 \tag{3.48}$$

constant but P_{Fe} varies with square value of voltage $P_{Fe} = f(V_s^2)$(if eddy current core losses are notably larger than hysteresis losses). When representing this variation on a graph (Fig.3.39) the interception point with the vertical axis represents the mechanical losses for the given speed .From this method the mechanical losses were calculated and they have been found to be equal 65 W.

This losses are not only the mechanical losses of the generator but they include also the belt friction losses but and losses in the driving motor which could not be separated.

3.7.5 Series connected capacitor excitation a.c. load tests

The equations for the PMSG with series capacitors and a.c. load are:

$$s\Psi_d = V_d + R_s i_d + \omega_r \Psi_q + V_{cd} \tag{3.49}$$

$$s\Psi_d = V_q - R_s i_d - \omega_r \Psi_d + V_{cd} \tag{3.50}$$

$$\Psi_q = L_d i_q \tag{3.51}$$

$$\Psi_d = L_d i_q + \Psi_{PM} \tag{3.52}$$

$$\frac{dV_{cd}}{dt} = \frac{1}{C_Y} i_d \tag{3.53}$$

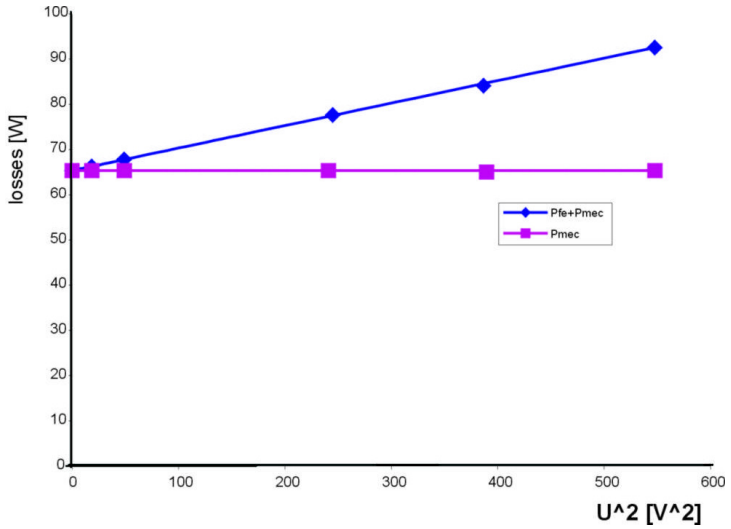

Figure 3.39: Losses segregation test.

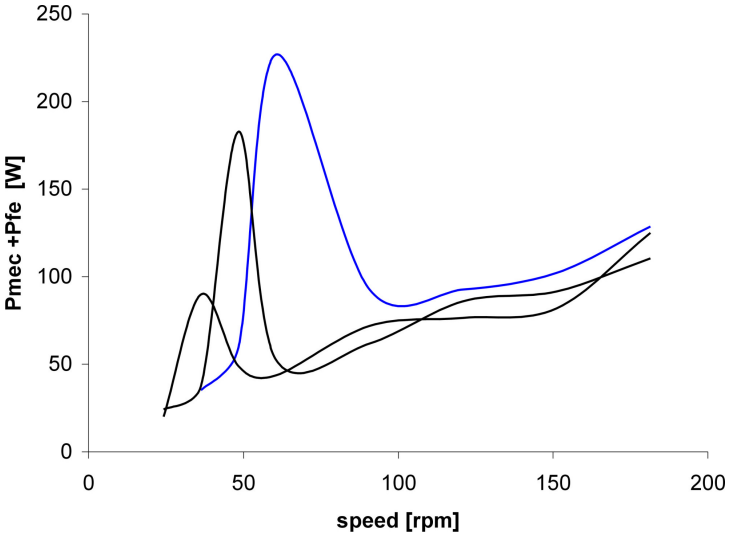

Figure 3.40: Capacitor losses for various capacitors.

Series connected capacitors improve the power capability of the generator as it was suggested in [18]. This is true only for a given frequency when the capacitor is compensating the phase inductance.

If the generator is working in variable speed range a careful choice of the capacitor should be made. A maximum power point on the speed/power curve is obtained (Fig. 3.43). The series capacitors at constant speed, move this maximum to higher values even for a small voltage regulation machine. This can be seen also on the load curve, where there is an maximum power/effi-

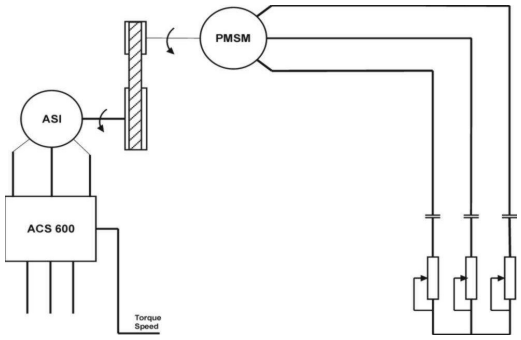

Figure 3.41: Series connected capacitor excitation.

ciency for a speficic value of speed Fig. 3.43 and Fig. 3.44. Fig.3.44 presents the electromagnetic torque of the generator for different values of load ranging from $R = 1$ up to 30Ω:

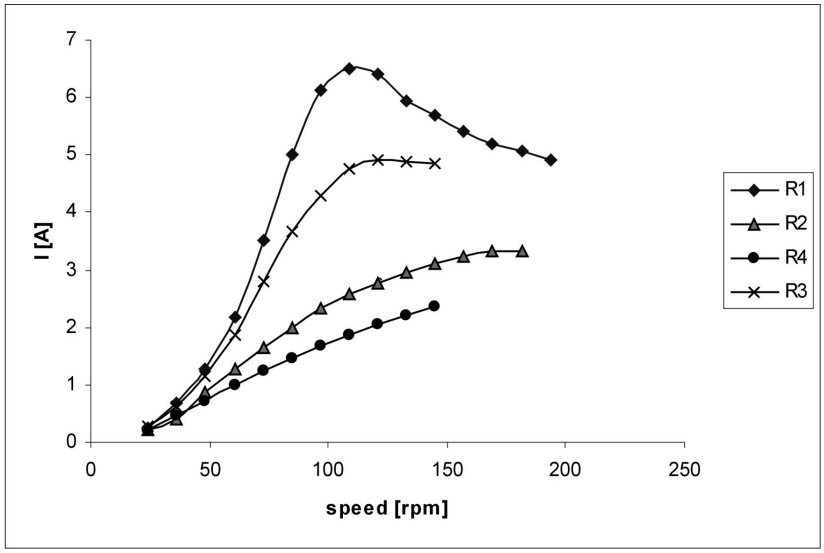

Figure 3.42: Load tests.

When series capacitors are used the machine has an improvement in efficiency as it can be observed in Fig. 3.45 this is more than the efficiency obtained from the generator with no capacitors connected as more power is delivered.

3.8 Conclusions

This chapter has presented a characterization of allow speed permanent magnet generator that is capable of generating mains frequency from a low speed

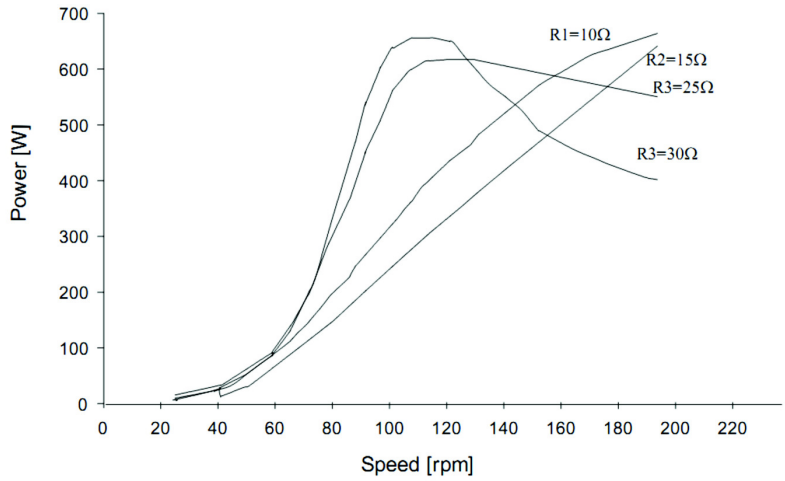

Figure 3.43: Power delivered by the prime mover to the PMSG.

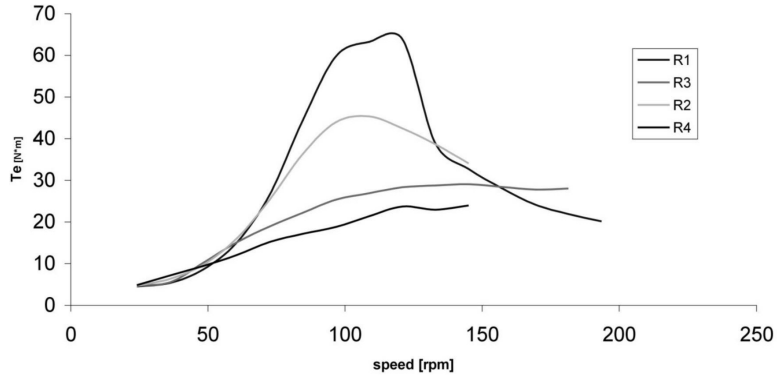

Figure 3.44: Torque of the generator for different values of load.

shaft input.

Iron losses for the selected configuration was also investigated in order to determine the efficiency of the generator. Capacitor excitation tests were used as an useful source of information for generator testing.

An increasing in the voltage regulation capability was observed which can lead to a better use of the generator. One of the limitations of permanent magnet generators is that it has high voltage regulation, as the magnet field cannot be controlled. Capacitive compensation is provided to improve the voltage regulation [10].

The voltage across the load can be maintained equal to no load voltage of machine under loaded condition. the voltage across the machine terminals increases depending upon the PU synchronous reactance of the machine. For 1 PU reactance, the voltage across the machine terminal at full load will increase

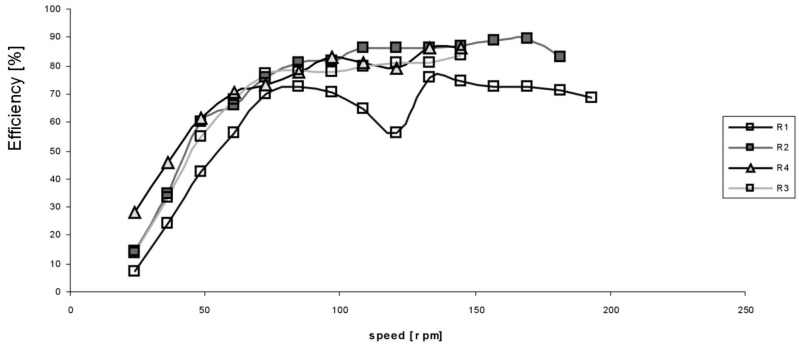

Figure 3.45: Efficiency

by 1.42 times the no load voltage. This increases the flux density in machine and therefore the iron losses.

Bibliography

[1] N. Bianchi, S. Bolognani, M. D. Pre, and G. Grezzani, "Design considerations for fractional-slot winding configurations of synchronous machines," in IEEE Trans. on Industry Applications, vol. 42, no. 4, pp. 997-1006, 2006.

[2] N. Bianchi and M. D. Pre, "Use of the star of slots in designing fractional-slot singlelayer synchronous motors," in IEE Proc. on Electric Power Applications, vol. 153, no. 3, pp. 459-466, 2006

[3] D. Ishak, Z. Zhu, and D. Howe, "Comparison of PM brushless motors, having either all teeth or alternate teeth wound," in IEEE Trans. on Energy Conversion, vol. 21, no. 1, pp. 95-103, 2006.

[4] D. Ishak, Z. Zhu, and D. Howe, "Eddy-curent loss in the rotor magnets of permanentmagnet brushless machines having a fractional number of slots per pole," in IEEE Trans. on Magnetics, vol. 41, no. 9, pp. 2462-2469, 2005.

[5] D. Ishak, Z. Zhu, and D. Howe, "Permanent magnet brushless machines with unequal tooth widths and similar slot and pole numbers," in IEEE Trans. on Industry Applications, vol. 41, no. 2, pp. 584-590, 2005.

[6] L. Wang, J. Shen, Y. Wang, and K. Wang, "A novel magnetic-geared outer-rotor permanent-magnet brushless motor," in Proc. of IET Int. Conf. on Power Electronics, Machines and Drives (PEMD), pp. 33-36, 2008.

[7] K. Maliti and C. Sadarangani, "Modelling magnetic noise in induction machines," in Proc. of IEE 8th International Conference on Electrical Machines and Drives, (EMD), 1997.

[8] D. Ishak, Z. Zhu, and D. Howe, "Unbalanced magnetic forces in permanent magnet brushless machines with diametrically asymmetric phase windings," in Proc. of IEEE Industry Applications Society Conf., vol. 2, pp. 1037-1043, 2005.

[9] U. Hoefer, A. Jack, and B. Mecrow, "Unbalanced magnetic pull in high-speed brushless permanent magnet motors - experimental observations and results," in Proc. of Int. Conf. on Electrical Machines, (ICEM), paper no. 426, 2006.

[10] J. Wang, Z. Xia, and D. Howe, "Comparison of vibration characteristics of 3-phase permanent magnet machines with concentrated, distributed and modular windings," in Proc. of Int. Conf. on Electrical Machines, (ICEM), paper no. 131, 2006.

[11] Henk Polinder, Member, Sjoerd W.H. de Haan, "Basic operation principles and electrical conversion systems of wind turbines" NORPIE 2004, conference proceedings CD ROM version 14 16 June, 2004;

[12] P. Thelin, H-P Nee "Suggestions regarding the number of pole number of inverter fed synchronous motors with buried magnets" International Conference Recordings on Power Electronics and Variable Speed Drives, London, September 1998 CD ROM Version;

[13] Salminen, P.; Niemela, M.; Pyhonen, J.; Mantere, J.; ÑPerformance analysis of fractional slot wound PM-motors for low speed applications Conference Record of the 2004 IEEE Industry Applications Conference, 2004. 39th IAS Annual Meeting. Volume 2, 3-7 Oct.2004 Page(s):1032 - 1037 vol.2;

[14] Mi, Chunting; Gordon R. Slemon, "Modeling of iron losses of permanent-magnet synchronous motors" IEEE Transactrions on in Industry applications vol 39 No 3 May/June 1998;

[15] Freddy Magnussen, Dmitry Svechkarenko "Analysis of a PM Machine with Concentrated Fractional Pitch Windings" Conference Recordings.Nordic Workshop on Power and Industrial Electro Trondheim, Norway, 2004-06-14 CD ROM version ;

[16] Mihai Comanescu, Ali Keyhani,"Design and Analysis of 42-V Permanent-Magnet Generator for Automotive Applications" IEEE Tansactions on Energy Conversion Vol. 18 No.1 pp.301-309 March 2003;

[17] Ion Boldea " Automotive electric generator systems. A review" 3rd International Symposium on advanced Electromechanichal Motion Systems, Patras, 1999 paper KN-02;

[18] Nobuyuki Naoe "Voltage compensation of permanent magnet with capacitors" Conference recordings IAS 2001 CD ROM version;

[19] Cheng Shukang; Pei Yulong; ”The torque pulsation analysis of a starter generator with concentrated winding based hybrid electric vehicles” IEMDC 2003;

[20] Gieras, J.F.; Gieras, I.A. ”Performance analysis of a coreless permanent magnet brushless motor . IAS .2002 Volume 4, 13- 18 Oct. 2002 p:2477 - 2482 vol.4;

[21] F. Magnussen and H. Lendenmann, “Parasitic effects in PM machines with concentrated windings,” in IEEE Trans. on Industry Applications, vol. 43, no. 5, pp. 1223-1232, 2007.
“Determination of saturated parameters“Determination of saturated parameters

[22] M. Rahman and P. Zhou, “Determination of saturated parameters of PM motors using loading magnetic fields,” in IEEE Trans. on Magnetics, vol. 27, no. 5, pp. 3947-3950, 1991.

[23] H. Jianhui, Z. Jibin, and L. Weiyan, “Finite element calculation of the saturation DQ-axes inductance for a direct-drive PM synchronous motor considering crossmagnetization,” in Proc. of Int. Conf. on Power Electronics and Drive Systems, (PEDS), vol. 1, pp. 677-681, 2003.

[24] B. Stumberger, B. Kreca, and B. Hribernik, “Determination of parameters of synchronous motor with permanent magnets from measurement of load conditions,” in IEEE Trans. on En
ergy Conversion, vol. 14, no. 4, pp. 1413-1416, 1999.

[25] R. Dutta and M. Rahman, “A comparative analysis of two test methods of measuring d- and q-axes inductances of interior permanent-magnet machine,” in IEEE Trans. on Magnetics, vol. 42, no. 11, pp. 3712-3718, 200.

[26] P. Mellor, F. Chaaban, and K. Binns, “Estimation of parameters and performance of rare-earth permanent-magnet motors avoiding measurements of load angle,” in IEE Proc. on Electric Power Applications, vol. 138, no. 6, pp. 322-330, 1991.

[27] K. Rahman and S. Hiti, “Identification of machine parameters of a synchronous motor,” in IEEE Trans. on Industry Applications, vol. 41, no. 2, pp. 557-565, 2005.

[28] H.-P. Nee, L. Lefevre, P. Thelin, and J. Soulard, “Determination of d and q reactances of permanent-magnet synchronous motors without measurements of the rotor position,” in IEEE Trans. on Industry Applications, vol. 36, no. 5, pp. 1330-1335, 2000.

[29] J. Wang, Z. Xia, and D. Howe, “Analysis of three-phase surface-mounted magnet modular permanent magnet machines,” in Proc. of IEE Int. Conf. on Power Electronics and Electrical Machines, (PEMD), 2004.

[30] V. Petrovic and A. Stankovic, "Modeling of PM synchronous motors for control and estimation tasks," in Proc. of IEEE Conf. on Decision and Control, vol. 3, pp. 2229- 2234, 2001.

[31] D. Pavlik, V. Garg, J. Repp, and J. Weiss, "A finite element technique for calculating the magnet sizes and inductances of permanent magnet machines," in IEEE Trans. on Energy Conversion ,vol. 3, no. 1, pp. 116-122, 1988.

[32] N. Demerdash, F. Fouad, and T. Nehl, "Determination of winding inductances in ferrite type permanent magnet electric machinery by finite element," in IEEE Trans. on Magnetics, vol. 18, no. 6, pp. 1052-1054, 1982.

[33] N. Demerdash and T. Nehl, "Electric machinery parameters and torques by current and energy perturbations from field computations - Part I: Theory and formulation," in IEEE Trans. on Energy Conversion, vol. 14, no. 4, pp. 1507-1513, 1999.

[34] J. Hsu, B. Scoggins, M. Scudiere, L. Marlino, D. Adams, and P.Pillay, "Nature and assessments of torque ripples ofpermanent-magnet adjustable-speed motors," in Proc. of IEEE Industry Applications Society Conf., pp. 2696-2702, 1995.

[35] Z. Zhu and D. Howe, "Influence of design parameters on cogging torque in permanent magnet machines," in IEEE Trans. on Energy Conversion, vol. 15, no. 4, pp. 407- 412, 2000.

[36] J. Ede, K. Atallah, G. Jewell, J. Wang, and D. Howe, "Effect of axial segmentation of permanent magnets on rotor loss of modular brushless machines," in Proc. of IEEE Industry Applications Society Conf., vol. 3, pp. 1703-1708, 2004.

[37] K. Atallah, D. Howe, P. Mellor, and D. Stone, "Rotor loss in permanent-magnet brushless AC machines," in IEEE Trans. on Industry Applications, vol. 36, no. 6, pp. 1612-1618, 2000.

[38] A. EL-Refaie and T. Jahns, "Impact of winding layer number and magnet type on synchronous surface PM machines designed for wide constant-power speed range operation," in IEEE Trans. on Energy Conversion, vol., no. 1, pp. 53-60, 2008.

[39] A. EL-Refaie, T. Jahns, and D. Novotny, "Analysis of surface permanent magnet machines with fractional-slot concentrated windings," in IEEE Trans. on Energy Conversion, vol. 21, no. 1, 2006.

[40] M. Nakano, H.Kometani, and M. Kawamura, "A study on eddy-current losses in rotors of surface permanent magnet synchronous machines," in Proc. of IEEE Industry Applications Society Conf., vol. 3, pp. 1696-1702, 2004.

[41] N. Bianchi, S. Bolognani, and E. Fornasiero, "A general approach to determine the rotor losses in three-phase fractional-slot PMmachines," in Proc. of Electric Machines and Drives Conf., (IEMDC), vol. 1, pp. 634-641, 2007.

[42] C. Deak, A. Binder, and K. Magyari, "Magnet loss analysis of permanent-magnet synchronous motors with concentrated windings," in Proc. of Int. Conf. on Electrical Machines, (ICEM), paper no. 457, 2006.

[43] Z. Zhu, K. Ng, N. Schofield, and D. Howe, "Improved analytical modelling of rotor eddy current loss in brushless machines equipped with surface-mounted permanent magnets," in IEE Proc. on Electric Power Applications, vol. 151, no. 6, pp. 641-650, 2004.

[44] W. Soong and T. Miller, "Field weakening performance of brushless synchronous AC motor drives," in IEE Proc. on Electric Power Applications, vol. 141, no. 6, pp. 331-340, 1994.

[45] F. Magnussen, P. Thelin, and C. Sadarangani, "Performance evaluation of permanent magnet synchronous machines with concentrated and distributed windings including the effect of field-weakening," in Proc. of IEE Int. Conf. on Power Electronics and Electrical Machines, (PEMD), vol.2, pp. 679-685, 2004.

[46] A. EL-Refaie and T. Jahns, "Scalability of surface PM machines with concentrated windings designed to achieve wide speed ranges of constant-power operation," in IEEE Trans. on Energy Conversion, vol. 21, no. 2, pp. 362-369, 2005.

[47] S. O. Kwon, S. I. Kim, and J. P. Hong, "Comparison of IPMSM with distributed and concentrated windings," in Proc. of Int. Conf. on Electrical Machines, (ICEM), paper no. 635, 2006.

[48] E. Lovelace, T. Jahns, T. K. Jackson Wai, J. Lang, D. D. Wentzloff, F. Leonardi, and J. Miller, "Design and experimental verification of a direct-drive interior PM synchronous machine using a saturable lumped-parameter model," in Proc. of IEEE Industry Applications Society Conf., vol. 4, pp. 2486-2492, 2002.

4 Nonoverlaping Winding Flux Reversal Permanent Magnet Synchronous Machines

4.1 Overview of existing low-speed with high torque density Flux Reversal PM Machines

Although a rather new machine type (first prototype in the 50s) , the flux reversal machine represents a superior choice from many points of view.

FRM with rotor-PM flux concentration is preferred for manufacturability benefits. The absence of three-dimensional flux paths means that powder metallurgy solutions are not required and the widespread solution of laminations suits perfectly our needs.

A FRM is also much easier to model because it does not have three-dimensional flux paths. This allows us to simulate all in 2D, easing much the task of preliminary investigations.

An alternative to the FRM is the TFM (Transverse flux Machine), first proposed and named in the 80s by Weh [2]. However, it has the drawback of difficult manufacturability. Generally, TFMs have 3D configurations, which do not allow for the use of traditional laminations. To prevent the high eddy current losses in such cases, powder metallurgy is the solution. This is a quite new and therefore expensive technology, mainly because of the lack of experience in the field. Special three-dimensional flux paths are also necessary to minimize the stray flux that can reduce considerably the performances of such a machine. Although TFMs are mainly PM machines [3], configurations of TF reluctant machines have also been reported [4]. Although the TFM promises better performance than the FRM, the difficulties in building it (entailing higher production costs) and the fact that it not a "ripe" technology yet, make the FRM an important competitor[35, 7].

4.2 Topology description of a new linear flux reversal PM oscillo-machine with effective flux concentration

Linear motion oscillo-machines – as motors or generators are suitable for compressors and, respectively, as electric generators for small residential (or space) or vehicular electric energy production.

The present work introduces a novel configuration with PM mover flux concentration capable of high thrust density while retaining high efficiency and good power factor ($6\text{N/cm}^2, \eta = 0.9, \cos(\varphi) = 0.78$). Linear permanent magnet PM oscillo-machines have been proposed as linear single phase alternator and oscillo-motors. Potential prime movers for linear alternators are free piston Stirling engines and linear internal combustion engines for automotive applications. Linear piston compressors for refrigeration are potential loads for linear oscillo-motors. Most linear oscillo-motors work connected to the commercial energy system (at 50 -60Hz).

Among the existing versions of linear PM oscillo-machines those with PM-mover [1-3], coil mover [4-5] and iron movers [6-9] are predominant Fig. 4.1.

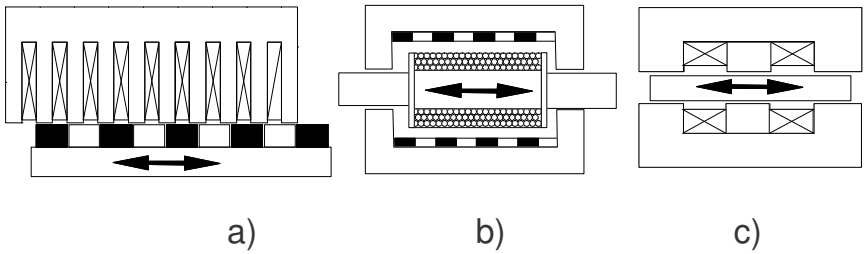

Figure 4.1: Oscilo machines a) PM mover b) coil mover c) iron mover.

Having a cylindrical shape, existing PM mover and coil mover configurations are not easy to manufacture from laminations and do not allow in general PM flux concentration

The iron mover flux reversal machine with stator PMs [40], in contrast, is easy to manufacture, provides good efficiency but at moderate thrust density ($1 - 2N/cm^2$), Fig. 4.2. Again, the difficulty in PM – flux concentration due to high fringing is the main obstacle to produce higher thrust density but maintain high efficiency and good power factor.

In an effort to circumvent this difficulty, the present chapter introduces a novel configuration of linear flux reversal (LFRM) oscillo-machine with efficient PM flux concentration.

The novel configuration is first introduced and a conceptual design methodology is presented related to a case study. FEA is then used to calculate more exactly the thrust for various current and mover positions. The efficiency

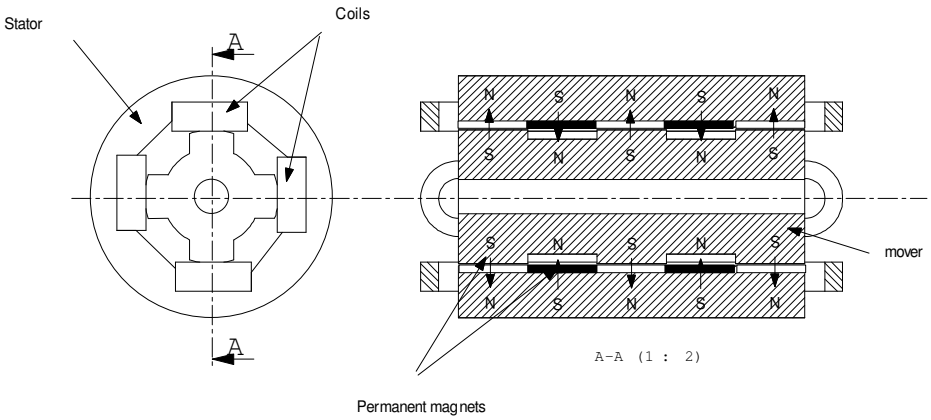

Figure 4.2: Original LFRM.

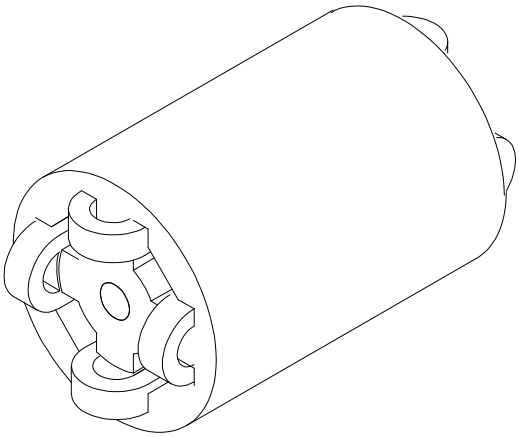

Figure 4.3: 3D view of LFRM.

and power factor are treated through thrust/watt of losses and IX_s/E rates as speed independent indexes.

4.3 Proposed configuration and operation principles

The configuration proposed here, Fig. 4.4, is made of two longitudinal-lamination stator cores which accommodate 4 identical coils which may be connected in series or series – parallel to (from) a single phase AC power grid.

The PM mover is also made of longitudinal laminations with flux barriers filled with permanent magnets of alternating polarity.

The stator poles have smaller poles and inter-poles, where $\tau_{PM}$is equal to the PM placement pitch on the mover, Fig. 4.4. The big slots in the stator

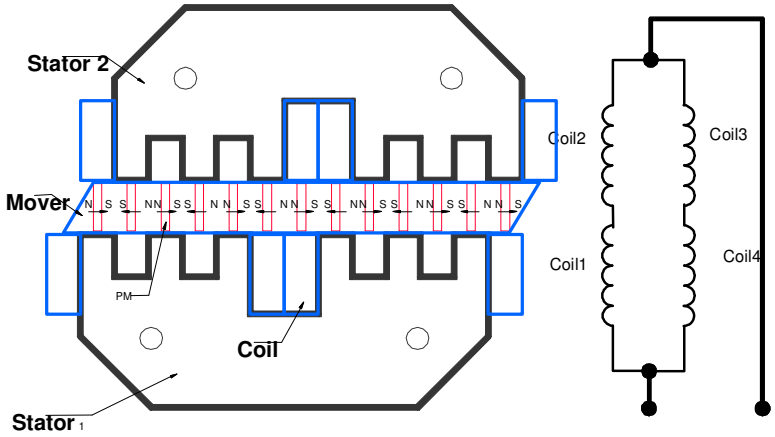

Figure 4.4: Cross section of the LFRM and winding connections.

which host the coils have an opening equal to $2 \cdot \tau_{PM}$

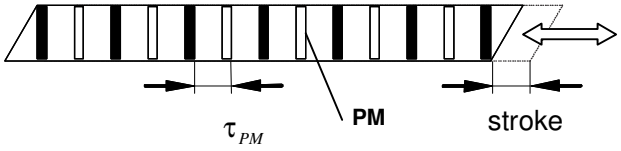

Figure 4.5: Mover PM placement.

The two stator slots are shifted by τ_{PM} along the direction of motion. The ideal excursion length from extreme left to extreme right is equal to τ_{PM}. As long as mover height h_r is larger than τ_{PM} flux concentration takes place. The higher h_r/τ_{PM}, the larger the PM flux concentration effect.

All PMs are participating all the time to reverse the PM flux in the coils when the mover moves from extreme left to extreme right position.

This complete use of all PMS all the time offsets the rather large imminent fringing flux present in any variable reluctance PM topology, and makes the configuration unique.

4.3.1 Conceptual design of the linear flux reversal oscillo machine

Specifications for the prototype are:

Power: 1 kW (motoring);

Excursion length: $\tau_{PM} = 12mm$;

Frequency f_1: $f_1 = 60Hz$;

Supply voltage V_1: V_1 =120V;

Average speed: $u_s = 2\tau_{PM} f_1 = 1.44$ m/s

The conceptual design is based on the following main relationships:

The developed thrust is:

$$F_x = 4\frac{2}{\tau_{PM}}(\phi_{PM})_{coil\,\max}\frac{1}{\sqrt{2}}(n_c I_n)K_{end} \tag{4.1}$$

where:

$(\phi_{PM})_{coil\,\max}$ is the maximum flux in a coil;

n_c number of coils;

I_n the rated current;

The maximum flux in a coil is:

$$(\phi_{PM})_{coil\,\max} = 2.5B_{gPM}l_{stack} \tag{4.2}$$

Considering harmonic motion:

$$x(t) = X_m \sin(\omega t) \tag{4.3}$$

The linear speed is:

$$\mathrm{u} = \frac{\mathrm{dx}}{\mathrm{dt}} = \mathrm{X_m}\omega_1 \cos(\omega_1 \mathrm{t}) \tag{4.4}$$

And quasi-linear flux variation in the coils with position:

$$\Psi_{PM} = \Psi_{coil\,\max}(1 - \frac{2x}{\tau_p}) \tag{4.5}$$

will produce a sinusoidal emf E per coil:

$$E(t) = -n_c\frac{d\Psi_{PM}}{dx}\frac{dx}{dt} = \Psi_{PMm}\frac{2}{\tau_p}\omega_1 X_m \cos(\omega_1 t) \tag{4.6}$$

Now if the phase current is in phase with emf maximum thrust is obtained.

The thrust is:

$$F_x = \frac{d(\phi_{PM})}{dx} i\sqrt{2}\cos(\omega_1 t) \tag{4.7}$$

The average linear speed is

$$\mathrm{u_{av}} = 2\mathrm{X_m f_1 f_1} = \frac{\omega_1}{2\pi} \tag{4.8}$$

In this particular (ideal) case the current is in phase with the linear speed and if: $\omega_1 = \sqrt{\frac{\mathrm{K}}{\mathrm{m}}}$, with:

K- mechanical springs (flexures) rigidity (N/m)

m- mover total mass;

In this situation the machine works at resonance and yields good performance. In order to precisely calibrate the springs the latter can be built from flexure bearings, Fig 4.6 which can be easily selected to obtain the desired rigidity.

The various phase relations are shown in Fig 4.7

The final results are presented in table 4.1 where:

$(\phi_{PM})_{coil\,\max}$is the maximum flux in a coil;

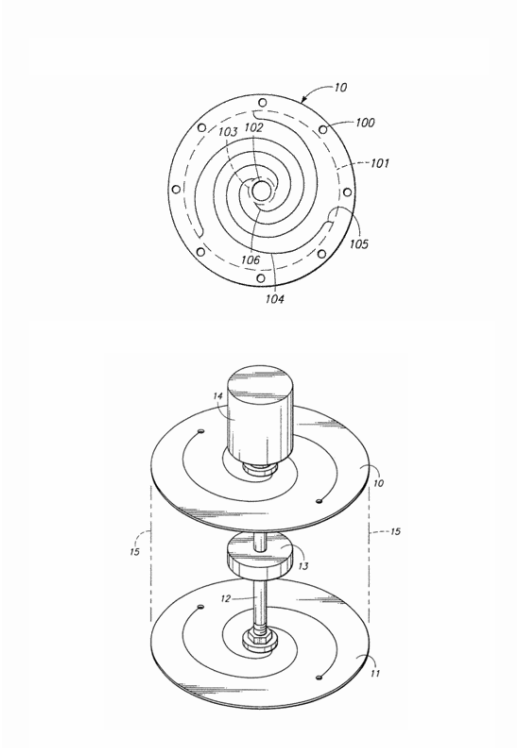

Figure 4.6: Flexures springs which can be used for energy recovery at the and of displacement.

Table 4.1: Nominal data LFRM

Stack length	l_{stack}	$100mm$
Number of turn coils	nc	76
Rated coil current	I_n	$6.298A$
Terminal current	$2I_n$	$12.6A$
Coil resistance	R_s	0.4107Ω
Coil inductance	L_s	$0.01792H$
Apparent power	S_n	$1KVA$
Efficiency	η	0.938
Power factor	$cos(\varphi)$	0.706
Stator core weight	G_{stator}	$9.7036kg$

n_c number of turns per coil;
I_n the rated current.

Based on this preliminary geometry rather detailed 2D–FEM calculations have been performed to validate the conceptual design.

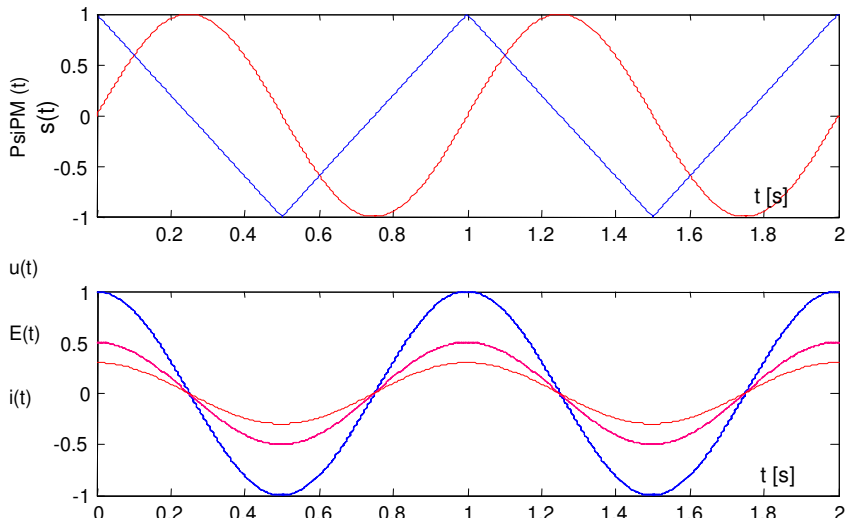

Figure 4.7: Phase relationship for max (ideal) thrust/current operation a) displacement and PM flux (ideal case).

4.3.2 LFRM FEM Analysis

For the geometry of the $1kW$ machine, designed in paragraph 3, using PMs made of NeFeB and usual machinery silicon steel laminations, the PM flux distribution for the extreme left position was investigated and it is shown in Fig. 4.8 . flux reversal is visible.

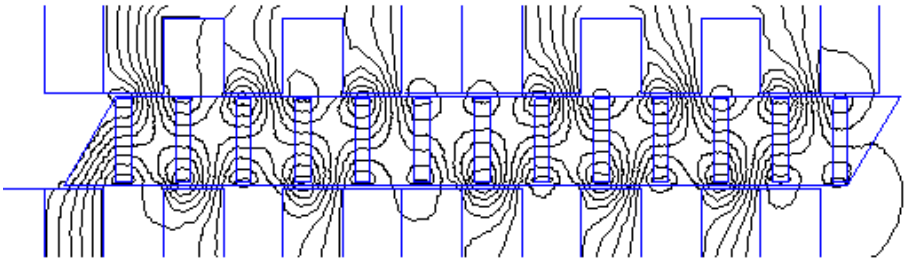

Figure 4.8: Flux lines path path for middle position (no load).

The PM flux in the coils for various mover positions shows some departure from the linear (ideal) distribution. This is more evident in the $d\Psi_{PM}/dx$ curve, Fig. 4.9.

We may calculate the armature reaction flux and machine inductance L_s from the flux variation in the coils:

$$L_s(x,i) \approx \frac{\Psi(i+\Delta i,x) - \Psi(i,x)}{\Delta i} \tag{4.9}$$

The variation of the L_s with position indicates a low reluctance thrust compo-

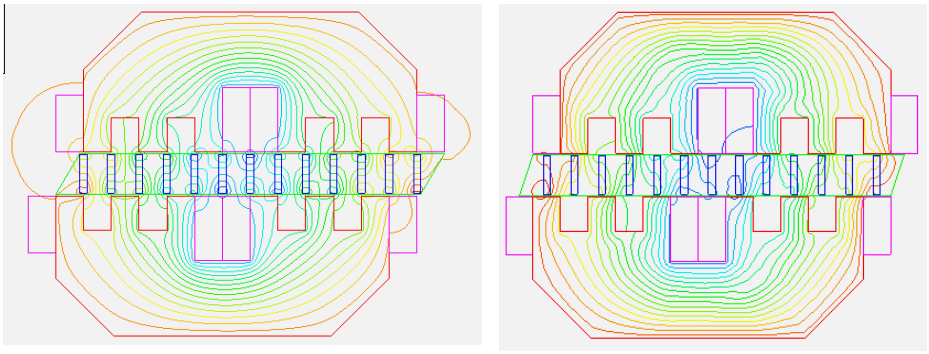

Figure 4.9: Flux path for extreme extreme right position and extreme left (no load).

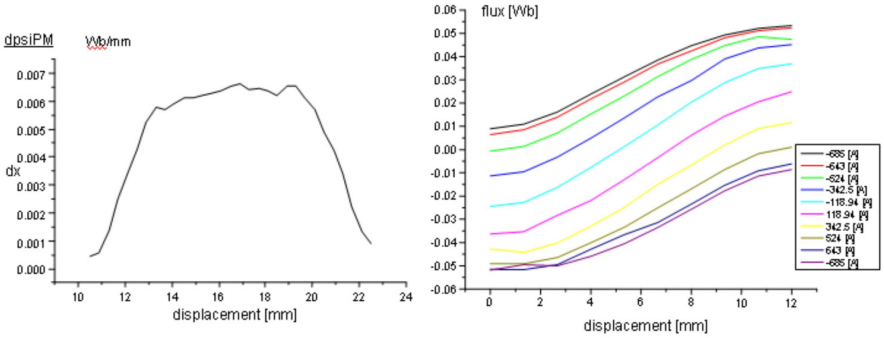

Figure 4.10: $d\Psi_{PM}/dx$ curve and flux variation for different values of current.

nent while saturation influence seems to be notable, Fig 4.11.

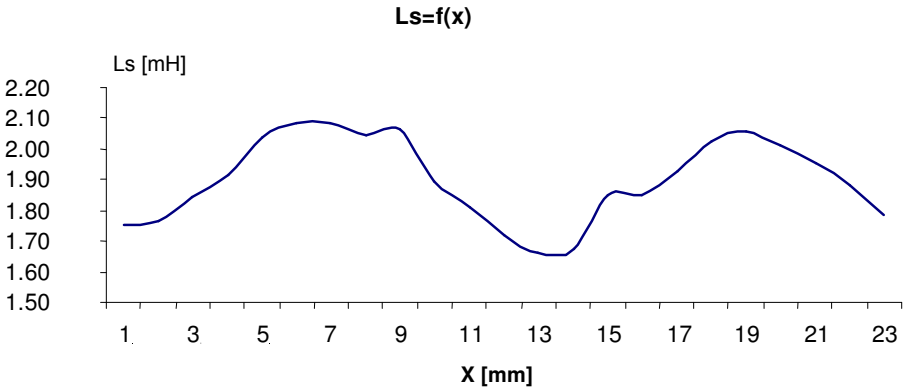

Figure 4.11: Inductance versus position for maximum current.

Analytical approximations for the thrust coefficient K_F and inductance can be obtained, to be used in eventual transient or steady state analysis.

The flux density at the airgap under one stator versus position for extreme left position Fig. 4.12 evidentiate the flux concentration high level (the maximum PM flux density is $1.2T$).

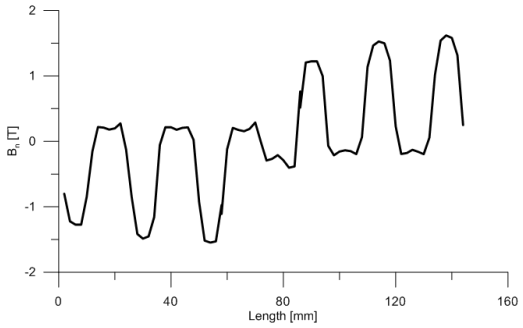

Figure 4.12: Initial prototype PM airgap flux density at extreme left position.

The armature reaction influence is given by:

$$K_{\cos(\varphi)} = \frac{X_s}{\underline{E}} \tag{4.10}$$

$$\cos(\varphi_1) = \frac{E + R_s I}{\sqrt{(E + R_s I)^2 + X_s I^2}} \tag{4.11}$$

$$\cos(\varphi_1) \approx \frac{E}{\sqrt{E^2 + (X_s I)^2}} = \frac{1}{\sqrt{1 - K_{\cos(\varphi_1)}{}^2}} \tag{4.12}$$

(I in phase with E)

It is evident that with smaller the larger power factor as the armature reaction in smaller .

The coefficient $K_{\cos(\varphi)}$ is very useful to calculate the resultant maximum flux density in the airgap and thus becomes a key factor for the magnetic circuit of the machine:

$$B_{\max} = B_{PM}\sqrt{1 + K_{\cos(\varphi)}} \tag{4.13}$$

4.3.3 FEM analysis for LFRM

After initial design and investigation two prototype have been developed and extensively investigated in collaboration with Hanyang University of Seoul South Korea . One prototype was build with inset magnets and another with surface place magnets. First tests were performed by FEM magnetostatic analysis. The prototypes are investigated also dynamically in order to obtain the dynamic characteristics .

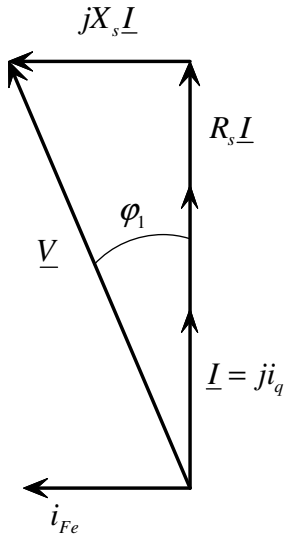

Figure 4.13: Phasor diagram For *E* and *I* in phase.

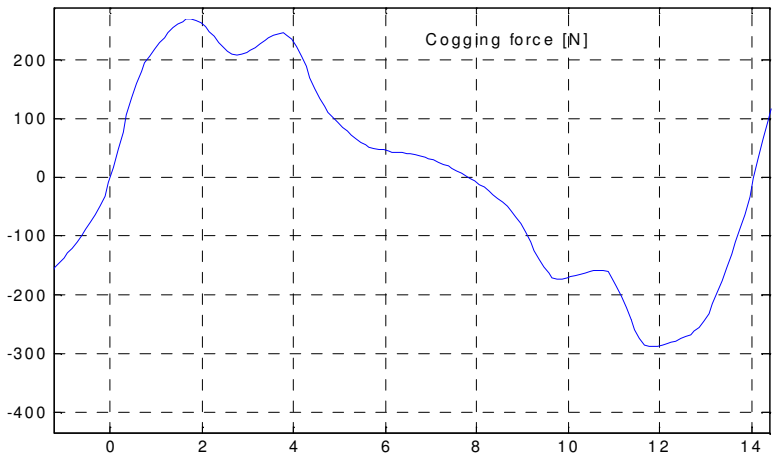

Figure 4.14: Cogging force obtained from FEM (initial prototype).

At zero current there is a cogging force acting on the mover due to the interaction between the PMs and the stator cores, Fig 4.19. This force is zero in the middle position and it is characteristic to a mechanical spring. If it were a linear characteristic spring it would have helped the mechanical flexures placed to store the energy at travel ends. Unfortunately, towards the ends of travel the cogging force drops and thus it may bring some instabilities in the oscillatory motion, unless the mechanical flexures are designed to overcome

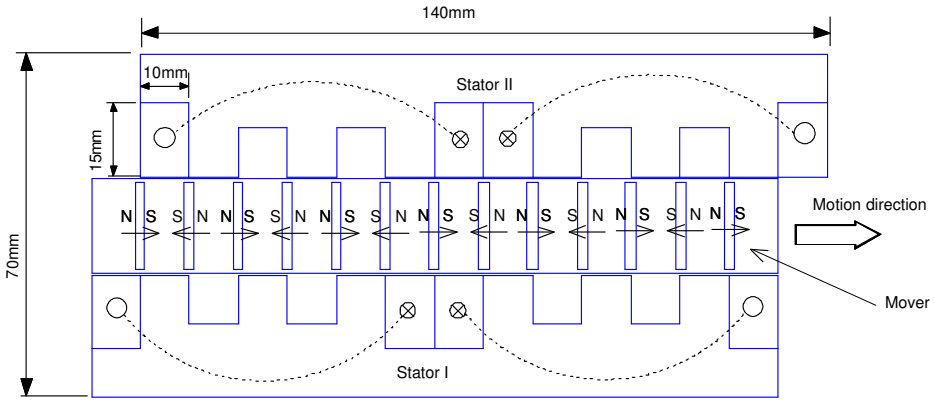

Figure 4.15: Inset permanent magnet prototype build.

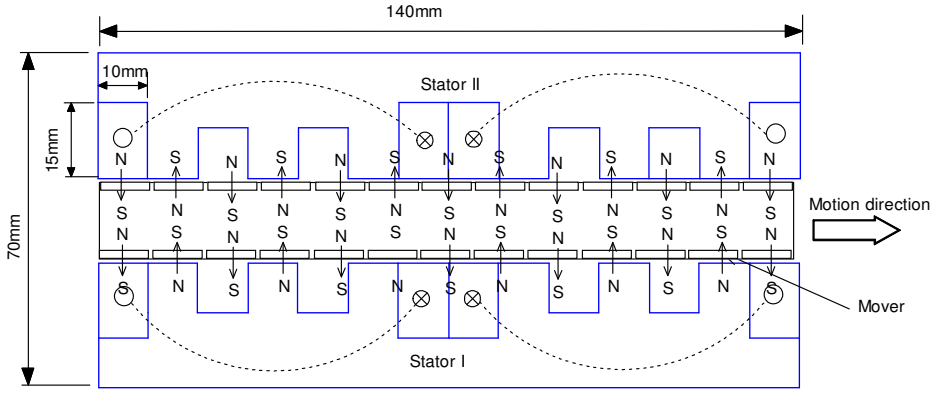

Figure 4.16: Second prototype build with surface PM.

this.

The FEM analysis could be used for this scope. The FEM setup and magnetic field lines are shown in Fig. 4.20 for interior PM flux concentration linear oscillatory machine. Moreover, the FEM analysis could provide a piece of information otherwise difficult to measure: the air-gap flux density shown in Fig. 4.20. The FEM analysis is validated by the measured thrust Fig. 4.21 and inductance Fig. 4.22.

The inset permanent prototype respectively the surface permanent are presented in Fig [4.14-4.15] The investigation are made in order to validate the both the analytical model and the built prototypes:

The FEM inductance does not contain the overhang leakage inductance so it is below the measured inductance with about $20mH$. Also for small current the FEM inductance is constant compared with measured inductance. The core magnetic saturation curve is linearised around zero current in order to improve the algorithm convergence. The agreement between FEM and test results is satisfactory, considering the measurement errors.

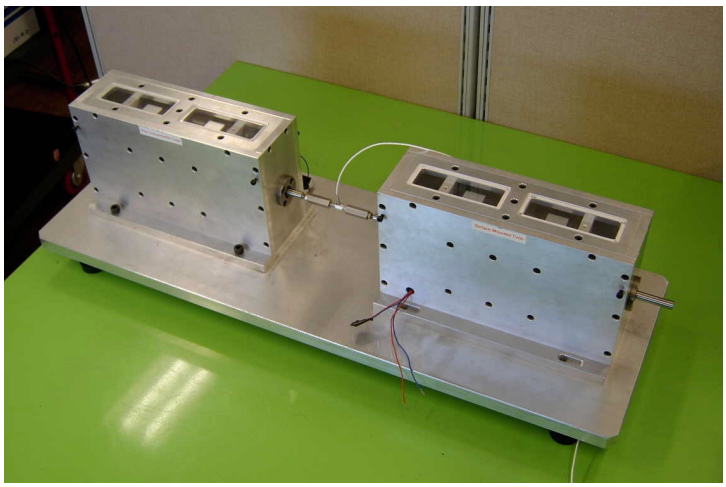

Figure 4.17: Connection of the two prototypes Back to back.

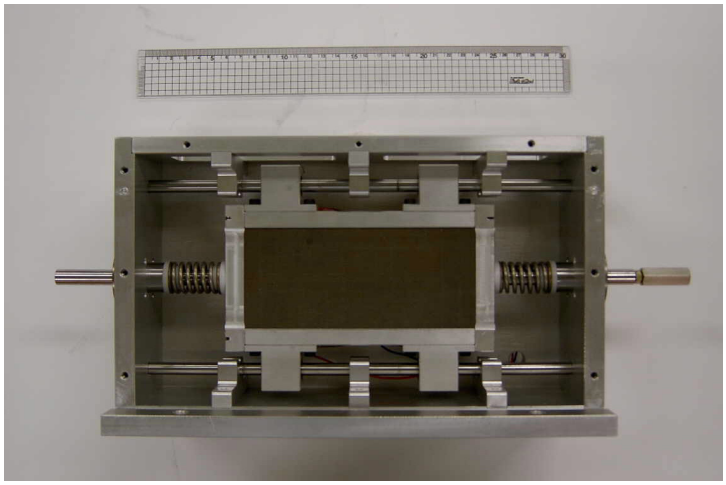

Figure 4.18: Mover construction for the inset PM prototype.

4.3.4 Fringing efect

Since the LFRM both with inset PM and surface PM is a double saliency machine the inductance versus position is required to be investigate. It has been observed that the fringing effect is not possible to correctly investigated by means of simple 2D FEM models 4.24.

The actual model is two dimensional one and this is not taking in account the additional inductance produced by the end windings.

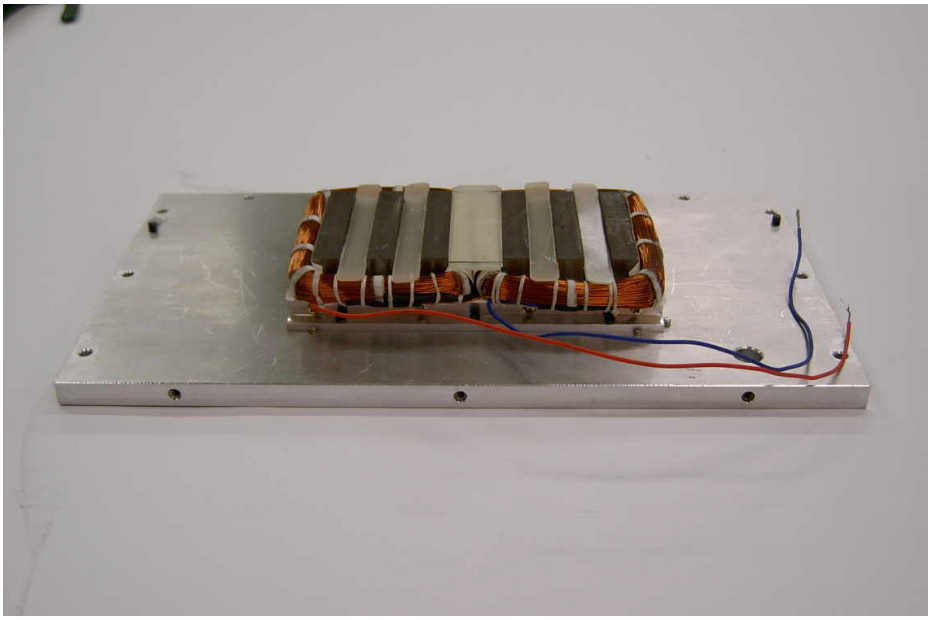

Figure 4.19: Stator with coils.

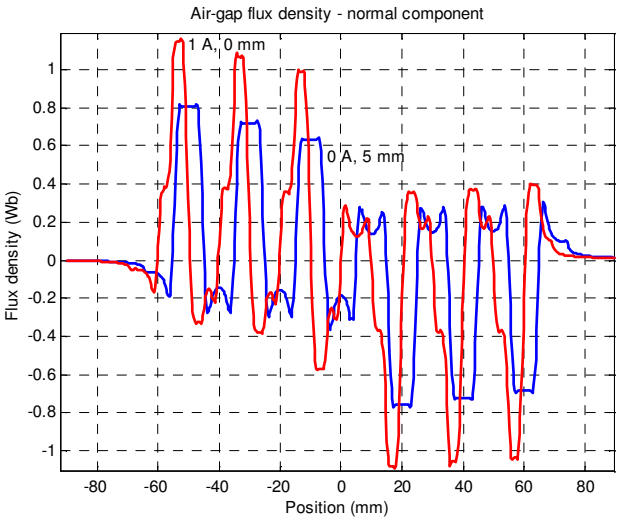

Figure 4.20: Air gap flux density by FEM for the two prototypes (red for inset blue for surface PM).

4.3.5 The state space model of non overlapping LFRM

The model of the linear machine is based on voltage and mechanical differential equations:

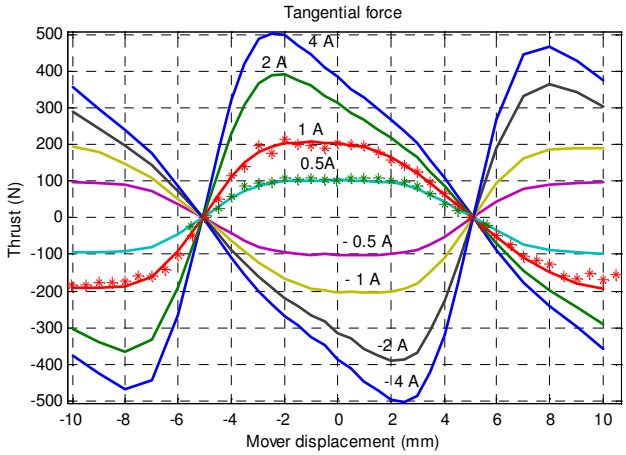

Figure 4.21: Thrust versus mover position and coil current; -solid line – FEM simulation.

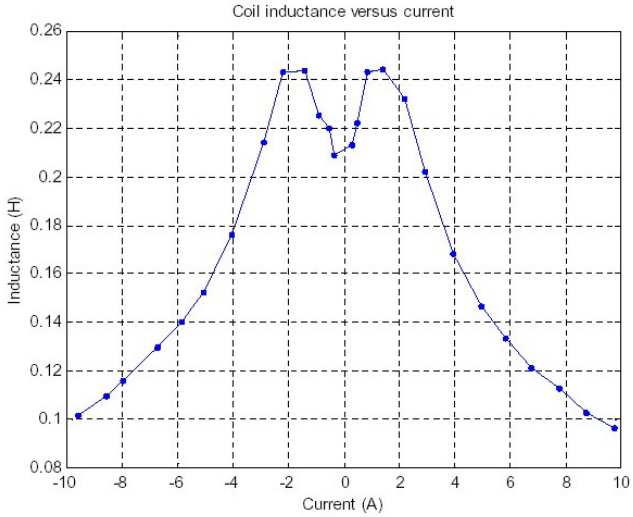

Figure 4.22: Machine inductance versus current – 2 parallel path.

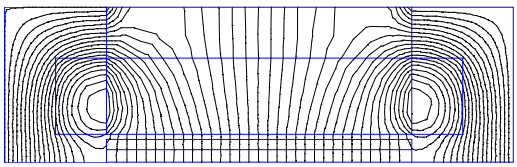

Figure 4.23: Flux lines in the axial section of the surface LFRM.

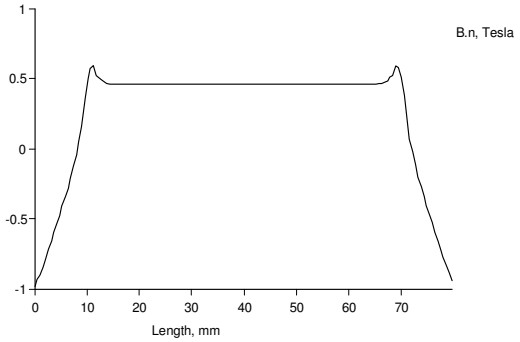

Figure 4.24: B_n axial.

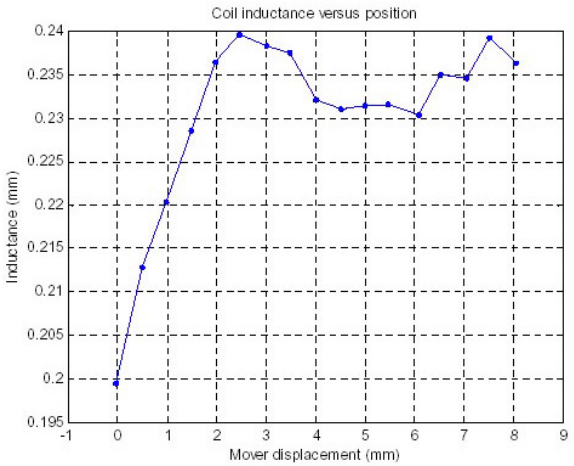

Figure 4.25: Coil inductance with position.

$$V = RI + \frac{d\Psi}{dt} \tag{4.14}$$

$$m\frac{du}{dt} = F_{em} - F_{cg} - F_{load} - F_f - F_s \tag{4.15}$$

Where: V – armature voltage,
R – resistance,
I - current,
Ψ – total linkage flux,
m – the mover mass,
u – mover speed,
F_{em}- electromagnetic force,
F_{cg}-cogging force,

Ff – friction force,
F_s – spring force,
F_{load} – load force.

If the core saturation is small the superposition principle is operational and the total linkage flux is the sum of permanent magnet flux and the flux produced by current. Moreover, if the inductance variation with mover position is negligible then the voltage equation becomes:

$$V = RI + L\frac{dI}{dt} + \frac{d\Psi_{pm}}{dx} \cdot \frac{dx}{dt} \tag{4.16}$$

The electromagnetic force depends on the total flux derivative versus mover position and armature current.

The electromagnetic force is given in (4.17) for a constant inductance:

$$F_{em} = \frac{d\Psi_{pm}}{dx} I \tag{4.17}$$

The linear oscillo-motor has a strongly nonlinear behavior that will be illustrated in the next chapter.

Now we are interested to find an analytical solution which is feasible for a linearization model around the mover equilibrium position. The linearization model presented in equations (4.18) considers the load force proportional to the speed, while viscous friction force is proportional to c_f (friction coefficient) and the flux derivative versus position is equal with k_f :

$$V_1 = (R_s + sL_s)i + k_f sx \tag{4.18}$$

$$m_t s^2 x + c_f sx + kx = k_f i \tag{4.19}$$

The model is reliable for small oscillations around equilibrium position and is totally wrong when the oscillation magnitude is larger than half tooth pitch.

The analytical solution of the linear model is:

$$x = \frac{k_f V_1}{(R_s + sL_s)(s^2 m_t + sc_f + k) + sk_f^2} \tag{4.20}$$

$$i = V_1 \frac{(s^2 m_t + sc_f + k)}{(R_s + sL_s)(s^2 m_t + sc_f + k) + sk_f^2} \tag{4.21}$$

The poles locus of transfer function is shown in Fig. 4.26 for $Rs = 93a9$, $Ls = 0.22H$, $mt = 2kg$, $k = 146N/mm$, $kf = 100Wb/m$, and the loading coefficient cf varies between 0 and $500[Kg/s]$.

All poles have negative real part, even for zero friction coefficient, so the system is stable and its response is finite for finite inputs. The sinusoidal steady state current and mover displacement is obtained by a formal substitution of Laplace operator, s, by $j\omega$ operator in (4.20) and (4.21).

The current magnitude versus frequency is shown in Fig. 4.31 and the displacement magnitude of the mover in Fig. 4.33, for $180V$ voltage magnitude. The maximum magnitude of the mover displacement is given by the

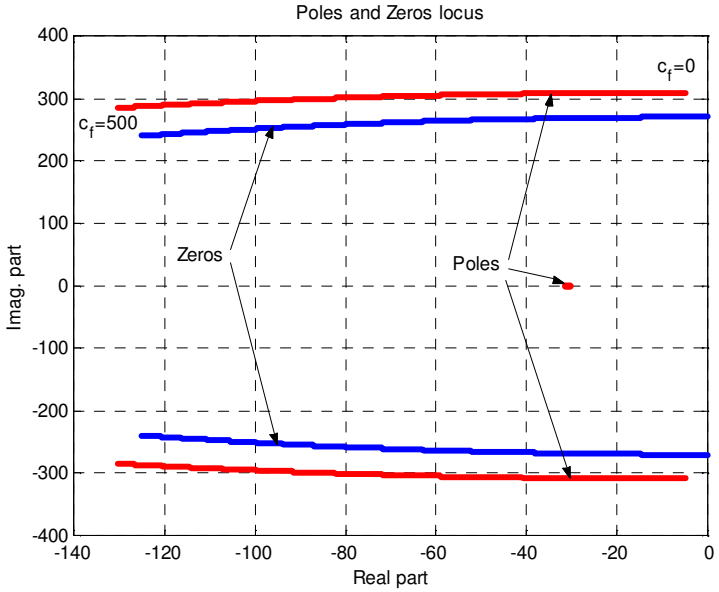

Figure 4.26: Poles and zeros locus of transfer functions.

imaginary part of the poles of transfer function (electromagnetic resonance frequency). The electromagnetic resonance frequency is $49.16Hz$ for no-load and $48.82Hz$ for a load with an equivalent friction coefficient of $c_f = 166Kg/s$.

The current minimum magnitude depends on the imaginary part of zeros and only mildly on the poles of the current transfer function (4.20). The minimum current magnitude is zero for ideally no-load frequency response. In this case the minimum current frequency is equal to mechanical resonance frequency, $f_0 = 43Hz$. In general the minimum current is reached for a little smaller frequency than the mechanical resonance frequency, which depends on load. The maximum current magnitude is reached for a little larger frequency than electromechanical resonance frequency as it is shown in Fig. 4.27.

The loading friction coefficient, $cf = 166$ was chosen to produce the maximum mechanical power at mechanical resonance frequency. The voltage magnitude $V_1 = 180V$ was chosen to keep the displacement magnitude closer and under its maximum value of $5mm$ for loading conditions. For this voltage the no-load displacement is very large. In fact for the real machine the maximum mechanical available displacement is 8 mm and the force is changing the sign at 5mm. The linear model is approximately correct only for mover displacement smaller than 5mm. However, the model shows that is necessary to reduce the voltage magnitude about nine times for the no-load regime.

The mechanical power (for harmonic oscillation) is:

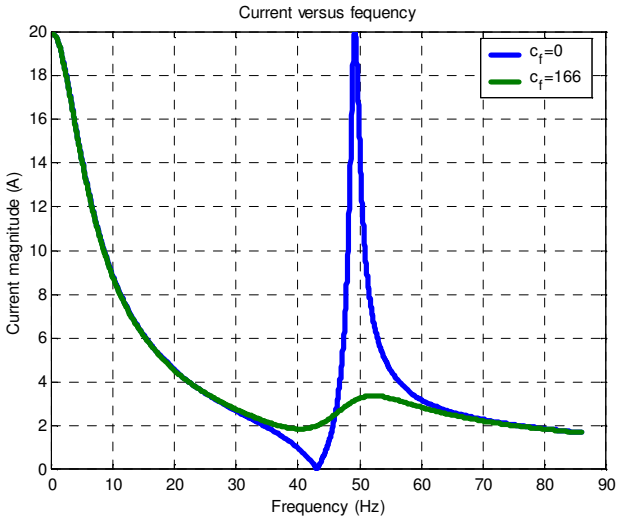

Figure 4.27: Current magnitude frequency response.

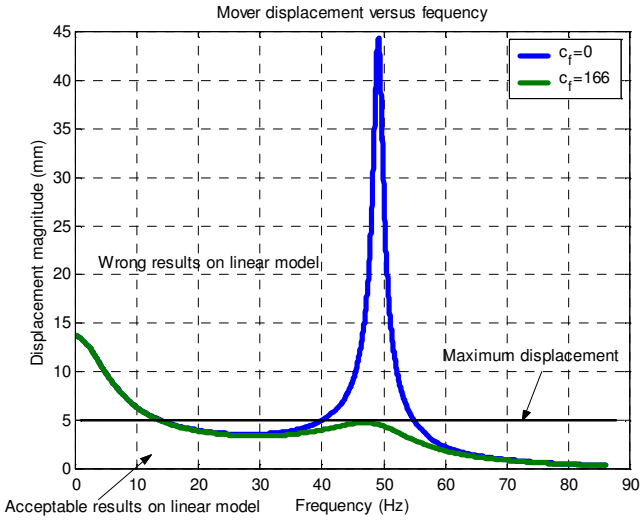

Figure 4.28: Magnitude displacement frequency response.

$$P_{mec} = \frac{1}{2} c_f (\omega X_m)^2 \tag{4.22}$$

The mechanical power reaches its maximum at electromechanical resonance frequency, Fig. 4.29, while the maximum efficiency reaches its maximum value around the mechanical resonant frequency, Fig. 4.28

The current and mover speed are in phase at mechanical resonance fre-

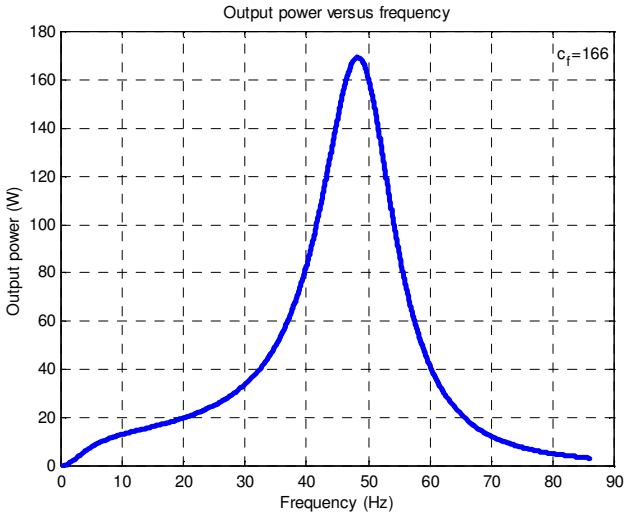

Figure 4.29: Output power at constant load coefficient.

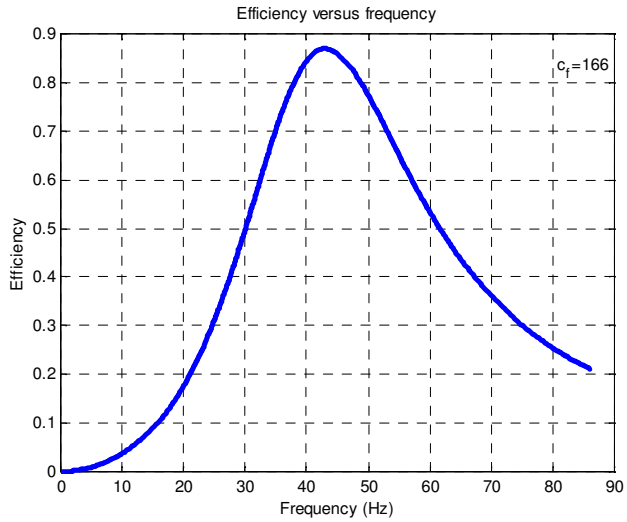

Figure 4.30: Efficiency at constant load coefficient.

quency as it is shown in Fig. 4.28. The current phase, considering the voltage phase as reference, changes from a large negative value to a large positive value when the electrical frequency passes trough the mechanical resonant frequency, for no-load regime. The mechanical and electro-mechanical resonance frequencies are points of extreme for machine behavior. The machine features are totally different at these frequencies as it shown in Fig. 4.32, for current versus load coefficient, and respectively, in Fig. 4.28, for the mover

displacement versus load coefficient.

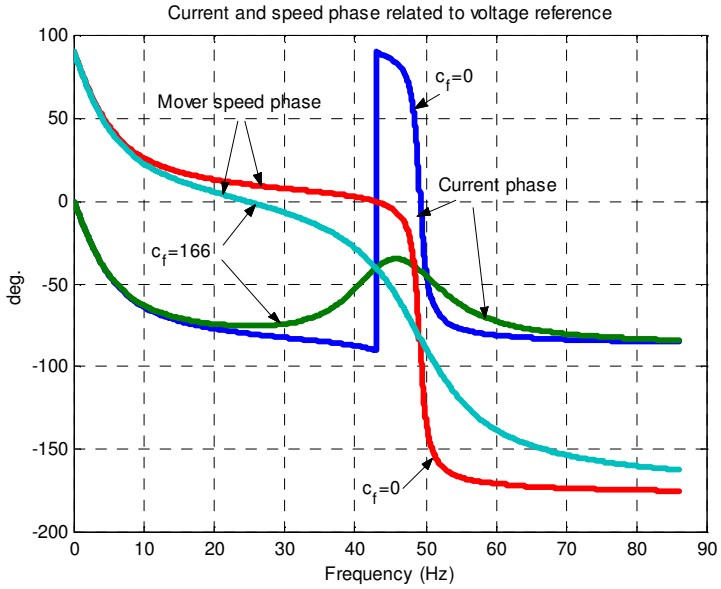

Figure 4.31: Current and speed phase versus frequency.

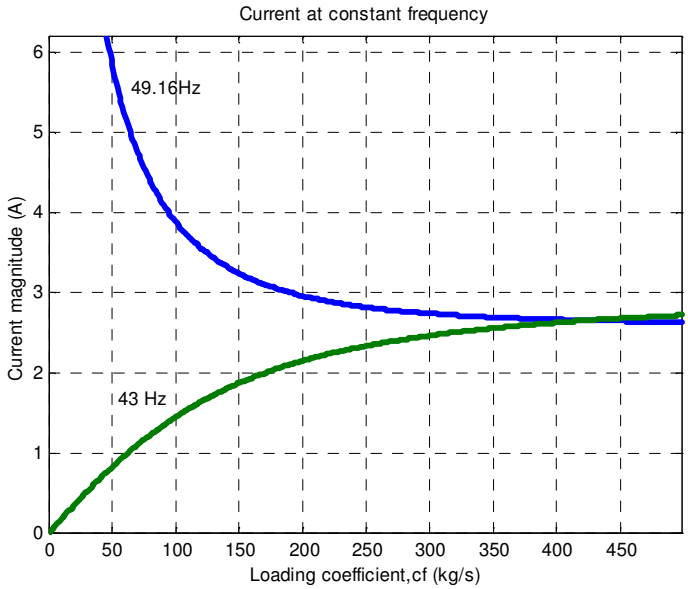

Figure 4.32: Current versus loading coefficient.

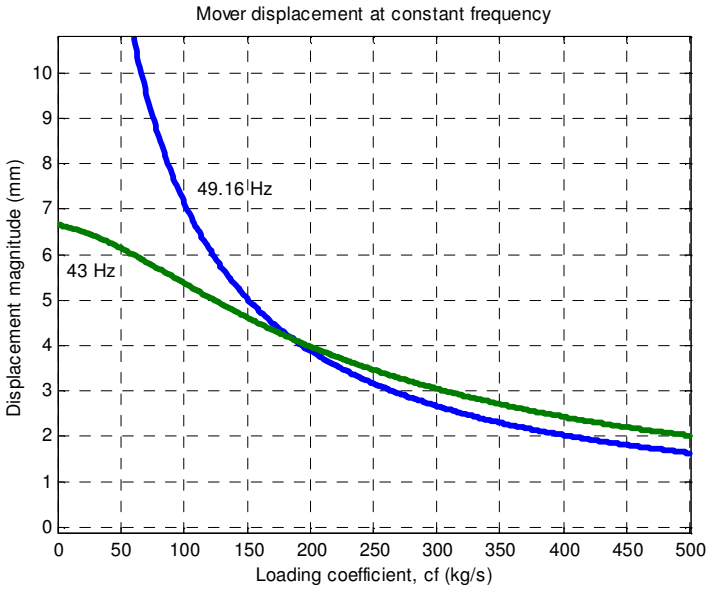

Figure 4.33: Displacement magnitude versus loading coefficient.

The efficiency versus output power at constant frequency (mechanical, respectively, electromechanical resonance frequency) is shown in Fig. 4.34. The curves in solid line are for displacement smaller than 5mm and only these points could be obtained with the real machine.

The efficiency is computed considering only the copper losses.

4.3.6 Non linear state space model development for LFRM

The nonlinearities are produced by the dependence of flux derivative on position and by magnetic saturation and cogging force. The permanent magnet flux derivative depends on the mover position and could be available in the model via a table. A trapezoidal shape may be considered, as shown in Fig 4.35 .

The cogging force dependence on the mover position is introduced in the MATLAB Simulink model also as a look-up table from test results, after noise filtering, Fig. 4.36.

The friction force could be divided into viscous friction force F_{vf} and Coulomb friction force F_{Cf} which is the other non linearity source, especially in small oscillations around equilibrium position.

$$F_f = F_{cf} + F_{vf} \tag{4.23}$$

$$F_f = \begin{cases} F_c sign(u) + k_{vf} u \quad , \ for \ u \neq 0 \\ min(|F_{rez}|, Fc) sign(F_{rez}) \quad , \ for \ u = 0 \end{cases} \tag{4.24}$$

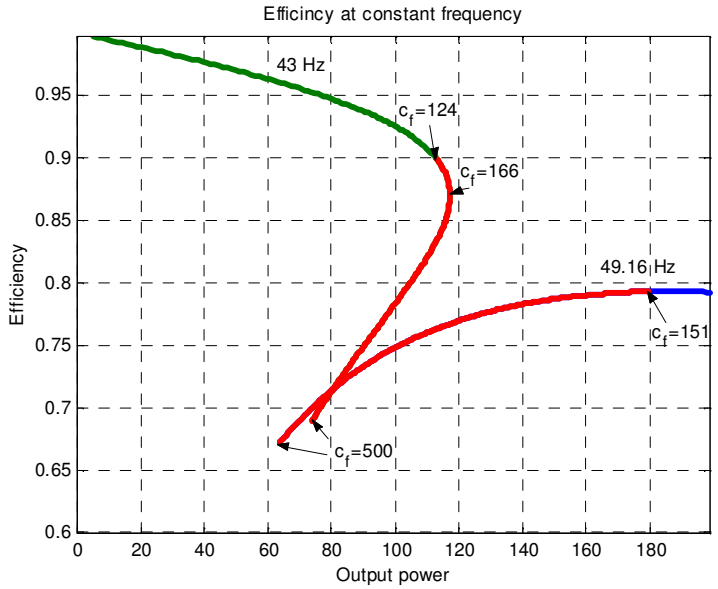

Figure 4.34: Efficiency versus output power.

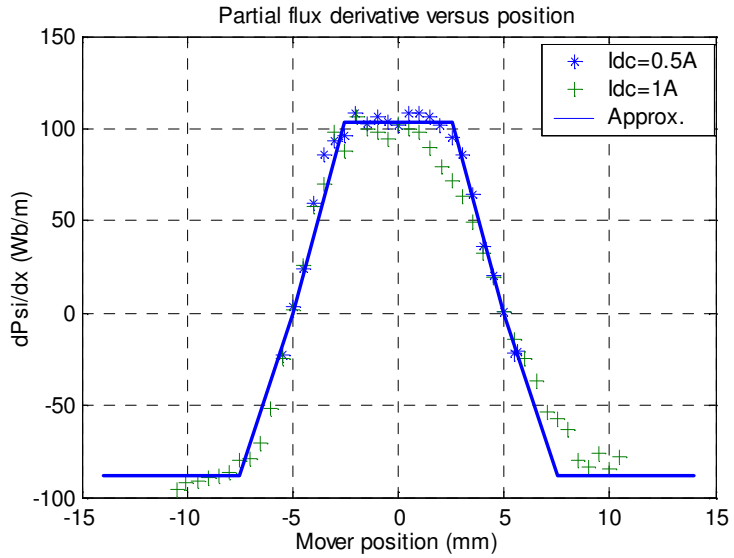

Figure 4.35: Flux derivative distribution.

Where F_{rez} is the sum of electromagnetic force and mechanical spring force.

The mechanical spring force is assumed to vary linearly with mover displacement, except for the accidental situation when the mover hits the frame, or the spring is fully compressed, when the elastic force suddenly increases.

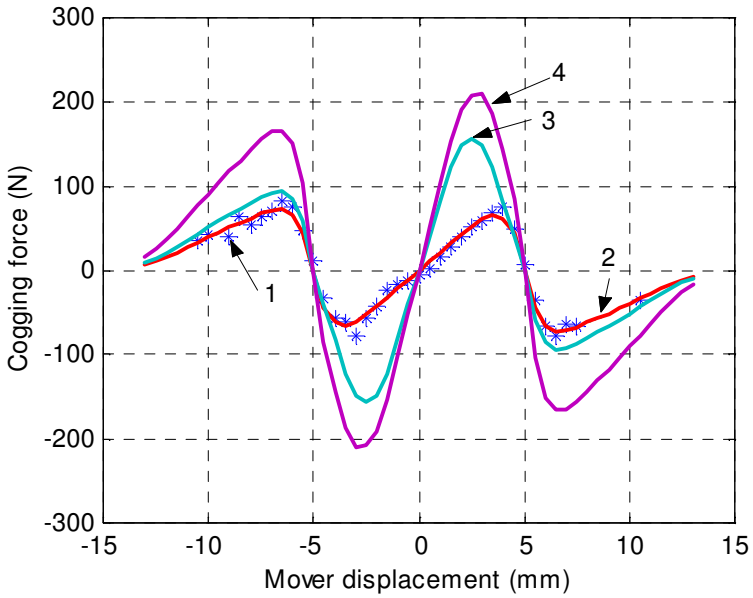

Figure 4.36: Cogging force: -1 measured points for FCPM, -2 approx. curves for FCPM, - 3 approx. curves for SPM, -4 sum of 2 and 3.

The constant term equal to the $0.02H$ term is the end coil leakage inductance.

The block diagram of non linear model, considering the force coefficient and inductance dependence on current, is shown in Fig. 4.37.

A larger current was observed in the test results than in the simulation results. This is produced by a construction particularity, as a screw bolt was used to tighten the lamination core. The effect of this equivalent short circuited cage was observed also in the dc decay stand still tests, when the current did not fall along a single exponential wave. Also, the force versus current hodograph had a loop when it was acquired in stand still tests at low frequency (1Hz) ac current.

Finally, the nonlinear model of the linear machine is shown in Fig. 4.37 considering constant parameters as:

R – coil resistance,
L – coil inductance,
k_f – force coefficient (maximum value of flux derivative versus position),
m- mover mass,
k_s – spring constant,
F_c – Columbian friction force,
c_f,- viscous friction coefficient,
x_{max}-maximum mechanical stroke.

Moreover, the model contains two distributions:
flux derivative versus position and cogging force versus position already presented in Fig.4.35, and, respectively Fig. 4.36.

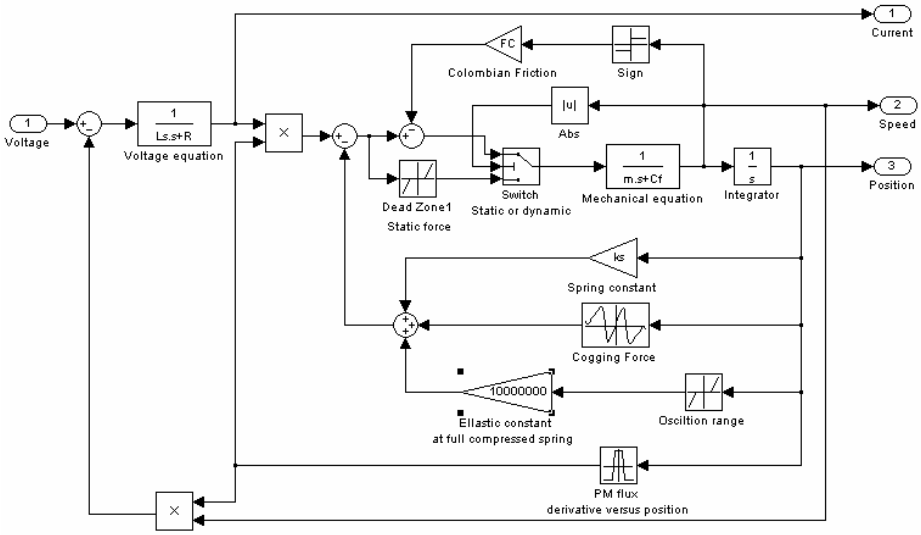

Figure 4.37: The block diagram of the linear machine model.

The force coefficient and, respectively, the inductance dependence on current can not be neglected when the linear oscillatory machine is working in heavy magnetic saturation conditions, as for our prototype for a large output power. The look-up table method could be used also in this case. In order to preserve the model simplicity, a singly dimensional look-up table was used. The inductance dependence on the mover position was neglected and the force coefficient dependence on the mover position and current is considered as a multiplication of two functions; and the other one depending only on mover position, on current.

The cage introduced in this particular construction is increasing the current and is producing the additional voltage drop on the coil resistance and inductance leakage. Only the additional voltage drop on the resistance was considered in the model.

The parameter of equivalent cage: $L_2 = 0.35H$, and $R_2 = 40\Omega$ were chosen, in order to minimize the simulation current and efficiency error related to test values for several load points (45W to 230W output power). A constant parameter of the equivalent cage when the main inductance has large variations was a compromise and thus the simulation results do not fit closely the test results but, however, they are better than in rough, the case of other models. A comparison of results produced with different models and tests are shown in Fig.4.41 - voltage magnitude versus mechanical output power, Fig.4.31 - current magnitude, Fig 4.30 efficiency; where the curves 1 represents the test results, curves 2 simulations on non-linear model considering the prototype construction particularity, curves 3 simulations on nonlinear model and curves 4 simulations on linear model.

$$K_f(i,x) = k_{if}(x)k_{xf}(i) \tag{4.25}$$

The force coefficient dependence on the current, k_{if}, is shown in Fig. 4.38 , while the force dependence coefficient versus mover displacement k_xf has the same variation as it was shown in Fig. 4.33, except for the magnitude that is unity.

The ac inductance, computed from FEM results 4.26, is used in the look-up table and it is shown in Fig. 4.39.

$$L_{ack} = \frac{\Psi(I_{k+1}) - \Psi(I_k)}{I_{k+1} - I_k} + 0.02 \tag{4.26}$$

$$I_{ak} = \frac{I_{k+1} + I_k}{2} \tag{4.27}$$

Where: the 0.02H term is the end coil leakage inductance.

The block diagram of non linear model, considering the force coefficient and inductance dependence on current, is shown in Fig.4.40.

A larger current was observed in the test results than in the simulation results. This is produced by a construction particularity, as a screw bolt was used to tighten the lamination core. The effect of this equivalent short circuited cage was observed also in the dc decay stand still tests, when the current did not fall along a single exponential wave. Also, the force versus current hodograph had a loop when it was acquired in stand still tests at low frequency (1Hz) ac current.

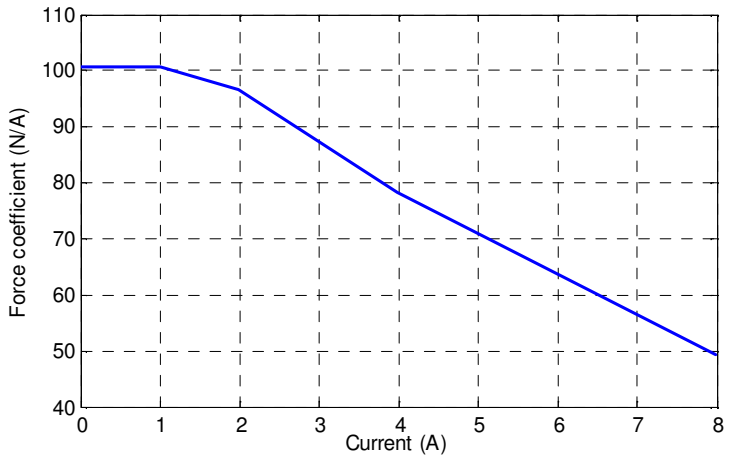

Figure 4.38: Force coefficient versus current.

The cage introduced in this particular construction is increasing the current and is producing the additional voltage drop on the coil resistance and inductance leakage. Only the additional voltage drop on the resistance was considered in the model.

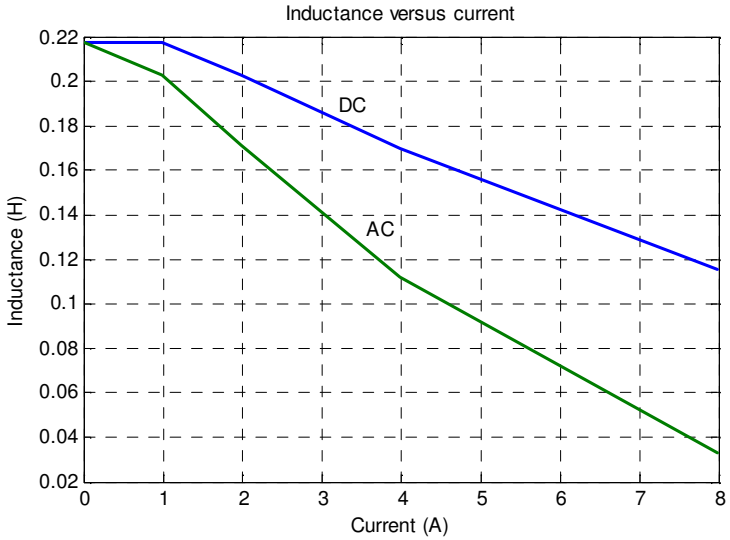

Figure 4.39: DC and AC inductance versus current.

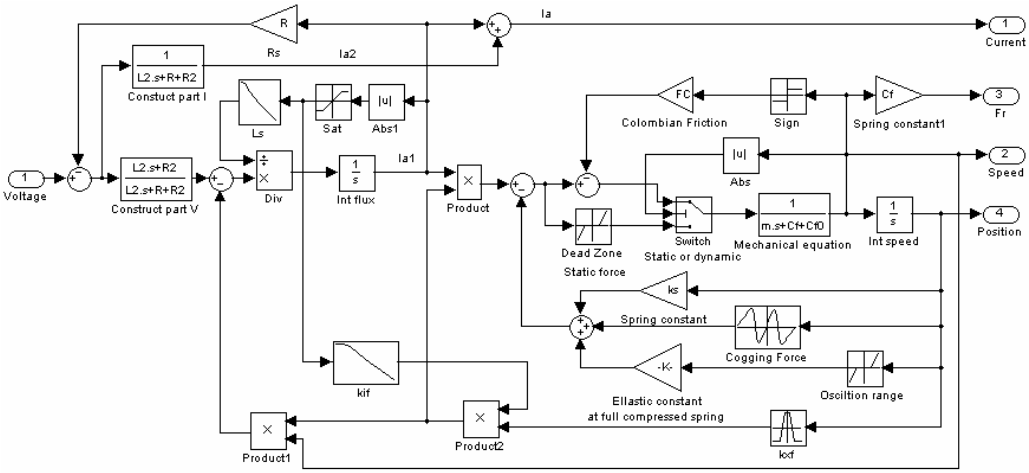

Figure 4.40: Nonlinear model block diagram considering inductance and force coefficient dependence by current.

The parameter of equivalent cage: $L_2 = 0.35H$, and $R_2 = 40\Omega$ were chosen, in order to minimize the simulation current and efficiency error related to test values for several load points (45W to 230W output power). A constant parameter of the equivalent cage when the main inductance has large variations was a compromise and thus the simulation results do not fit closely the test results but, however, they are better than in rough, the case of other models. A comparison of results produced with different models and tests are shown in Fig. 4.41 - voltage magnitude versus mechanical output power, Fig. 4.42

- current magnitude, Fig 4.43 efficiency; where the curves 1 represents the test results, curves 2 simulations on non-linear model considering the prototype construction particularity, curves 3 simulations on nonlinear model and curves 4 simulations on linear model.

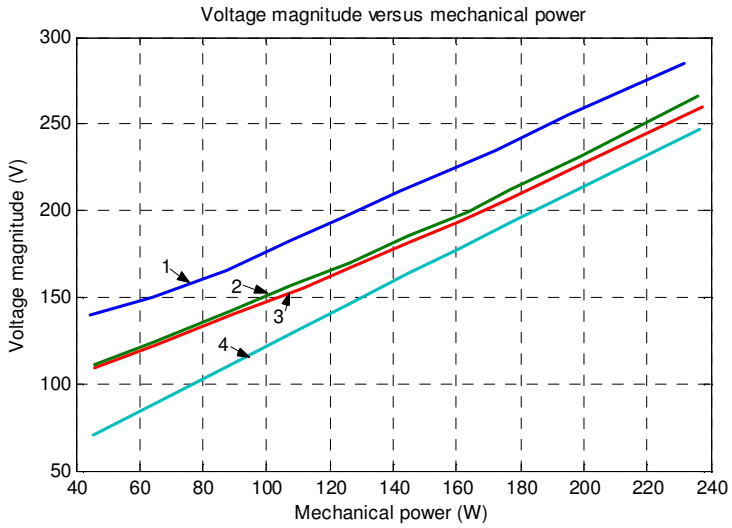

Figure 4.41: Supplied voltage: 1) test results, 2) simulation on nonlinear model considering construction particularity, 3) simulation on nonlinear model, 4) simulation on linear model.

Simulations show that efficiency could increase by around 15%-20% by eliminating the construction particularity (short circuit cage).

The dynamic simulation and test results are shown in Fig. 4.43 where the current and position waves are presented.

The distortion of the measured current is larger than the distortion of the simulation current. The simulation base times were shifted in order to overlap the simulation position and measured position. The currents are in different phase. The current–speed (position) phase is very sensitive to frequency around to the resonance frequency, Fig. 4.44, so a small error in the model parameters (resonance frequency) could produce a large error in current-speed phase. And, much more, it is the short circuit cage, which was not fully modeled, will be eliminated in the next prototype.

Simulations show that efficiency could increase by around 15%-20% by eliminating the construction particularity (short circuit cage).

The distortion of the measured current is larger than the distortion of the simulation current. The simulation base times were shifted in order to overlap the simulation position and measured position. The currents are in different phase. The current–speed (position) phase is very sensitive to frequency around to the resonance frequency, Fig. 4.47, so a small error in the model parameters (resonance frequency) could produce a large error in current-

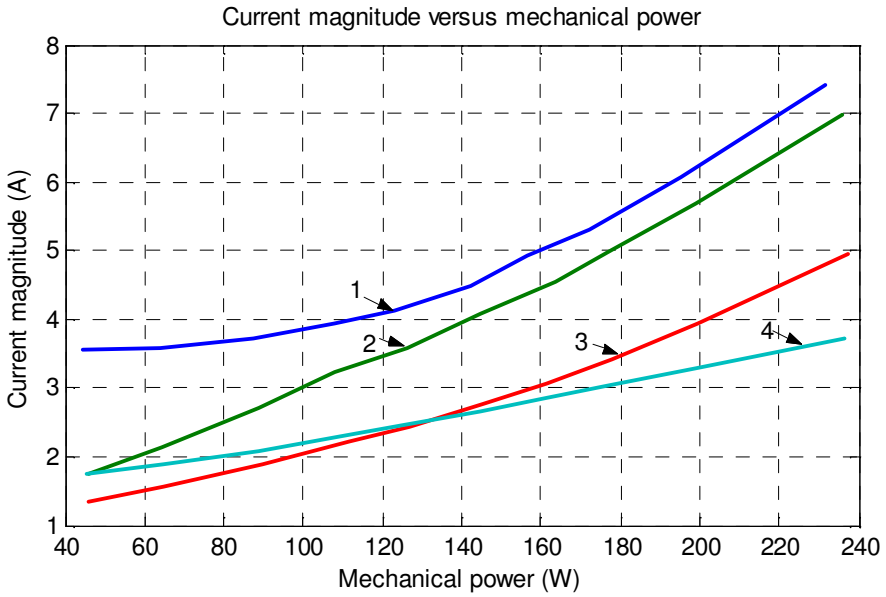

Figure 4.42: Current magnitude : 1) test results, 2) simulation on nonlinear model considering construction particularity, 3) simulation on nonlinear model, 4) simulation on linear model.

speed phase. And, much more, it is the short circuit cage, which was not fully modeled, will be eliminated in the next prototype.

Free deceleration of back to back coupled machines simulation is in good agreement with test results, Fig 4.45.

4.3.7 Parameters determination

Some of the model parameters, such as the resistance, could be measured directly while others are computed from standstill tests. The resistance is measured in dc current tests while the inductance is measured using dc decay methods. Moreover, the distribution of the flux derivative with mover position, Fig. 4.35, and also cogging force (after mechanical spring force segregation) versus mover position Fig, 4.36 are computed from standstill tests. The static thrust was also measured versus mover position and current. The spring constant is known from the catalog data or it is computed assuming zero cogging force (and zero current force) at half of maximum stroke length. The cogging force (Fig. 4.36 curve 1) is the difference between thrust measured at zero current and mechanical spring thrust.

Free oscillation of mover during free deceleration test was recorded in order to find the mechanical resonance frequency for each machine and also for the two machines, when mechanically coupled back to back as in dynamic tests. The Coulombs friction force, F_c, and viscous coefficient, c_f, are adjusted in order to produce the same mover displacement in the simulation as in

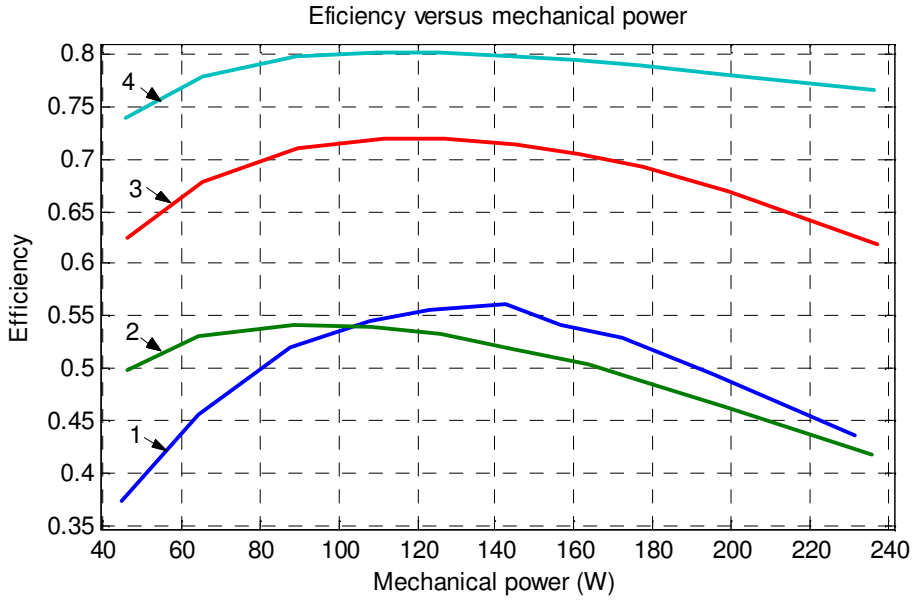

Figure 4.43: Efficiency: 1) test results, 2) simulation on nonlinear model considering construction particularity, 3) simulation on nonlinear model, 4) simulation on linear model.

recorded data that were measured by a Laser-based transducer. The machines parameters are shown in table 4.2.

Table 4.2: The two LFRM Machines parameters compared

Parameters	FCPM	SPM	UNIT
Resistance	9	9	Ω
Inductance	0.22	0.125	H
k_f	104	90	N/m
k_s	146000	146000	N
F_c	2.35	3	N
c_f	17	16	N s/m

4.3.8 Conclusion concerning Linear FRM with FC

The novel linear reversal PM machine characterized by mover PM flux concentration has been proposed and proven by FEM capable of 1 kW, 50 Hz, power delivery (generator) at $6N/cm^2$ of thrust for a calculated electrical efficiency of 0.938. and a power factor about 0.7.

The calculated copper losses it is $65W$ which translated into more than 10N/W of losses. The total active weight of the machine is 13.64 Kg (44N/Kg).

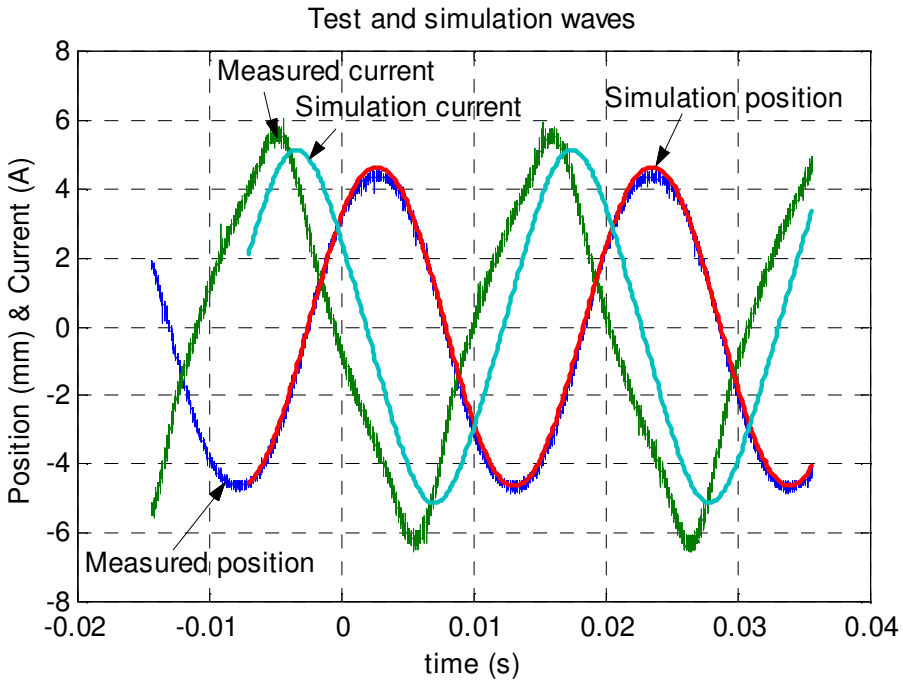

Figure 4.44: Current and position waves.

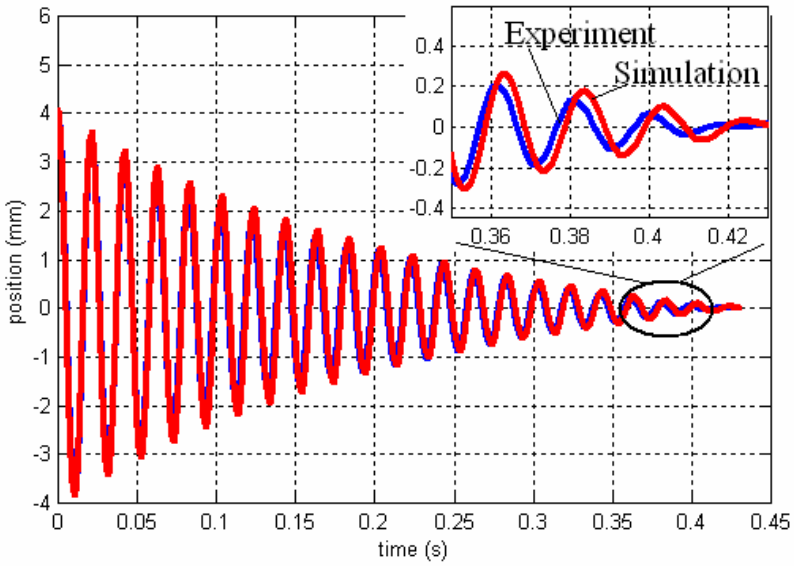

Figure 4.45: Free oscillation test and simulation for coupled machines.

And the mover weight is about 2.3 Kg. The efficiency is high for an average speed of 1.44 m/s, and this explains why the weight is not so small.

The weight may be further reduced, for lower efficiency. Design optimization may also bring some improvements.The theoretical results are notably better than for most existing linear PM machines.

4.4 The flux Reversal Machine with Rotor-PM Flux Concentration

This section presents the analysis of a flux reversal machine (FRM) configuration, designed for low speed (below $150rpm$). The machine consists of two stators, of which the outer one is fitted with a three-phase fractionary winding and the rotor carries alternate polarity permanent magnets placed for heavy flux concentration. The inner stator is slotted, but passive. The results of the finite element analysis show high torque density. Through skewing the cogging torque can be considerably reduced, making the machine suitable for servo applications.

4.4.1 Theoretical Characterization of flux Reversal Machine with Rotor-PM flux Concentration

This section contains the analysis of a flux reversal machine (FRM) configuration, designed for low speed (below 150 rpm). The machine consists of two stators, of which the outer one is fitted with a three-phase fractionary winding and the rotor carries alternate polarity permanent magnets placed for heavy flux concentration. The inner stator is slotted, but passive. The results of the finite element analysis show high torque density. Through skewing the cogging torque can be

Nowadays a large number of applications require low speed motors and yet high torques. This means that machines with speeds under 128 rpm and a torque of hundreds of Newton meters are necessary. Therefore, new designs are centered on motors with large numbers of poles (and accordingly small pole pitches). This of course brings about new challenges for the designers. The most popular solution is still a traditional induction machine with a gearbox. Synchronous machines begin to gain more and more acclaim, due to superior overall performances and the unique ability of working with variable power factor, both inductive and capacitive.

Building machines with low rated speeds is still a new trend [8] . However, the benefits of such designs are increased by the development of new PM materials that ensure superior performance and open the door to direct drives at low speeds. Ruling out the mechanical transmission both increases reliability and reduces costs, total weight and overall maintenance costs. Also, by eliminating the backlash in mechanical systems, the precision in positioning can be increased, an important feature when choosing a servo drive.

For this purpose, a flux reversal machine is a good choice, because it allows for a large number of poles. Furthermore, as experience shows, interpolar PMs yield better performances than polar PMs. This is what we tried to take advantage of in this design.

4.4.2 Radial FRM FC Configuration

The potentially high torque density of the FRM owes to its unique feature of producing a reversible flux. This way PM material is more effectively used and the energy conversion loop covers all four quadrants. This applies to traditional BLDC machines, but FRMs of the same rated power have generally a smaller frame size. As for the control strategy, it is rather similar to BLDC control: sinusoidal or rectangular current control. This means that usual control designs and strategies do not need major changes to comply with this type of machine. In addition, a major advantage over other machine types consists in the fact that power can be increased by adding stack length rather than choosing a larger diameter.

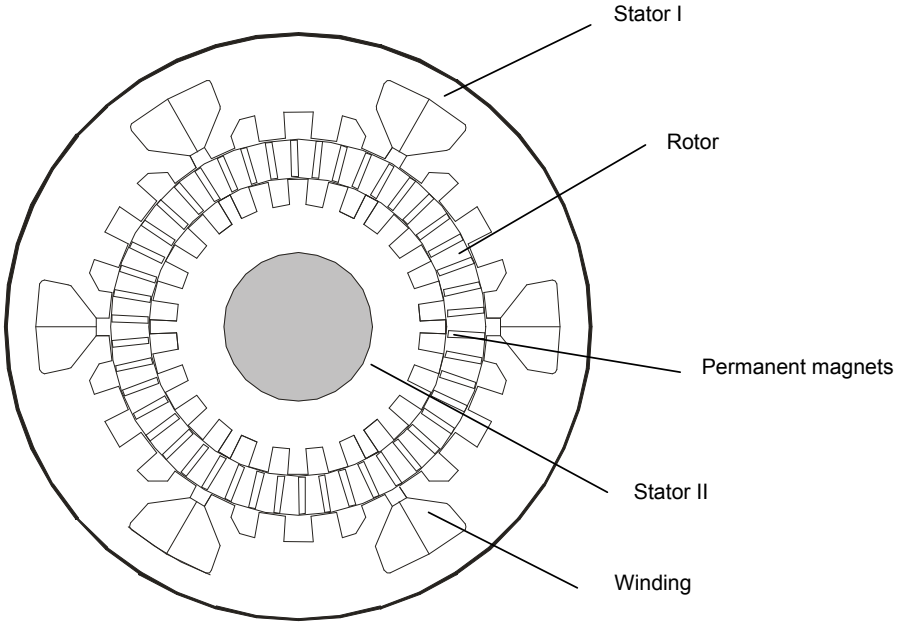

Figure 4.46: Radial cross-section of the FRM-FC.

The chosen topology comprises 2 stators and a hollow rotor. The outer stator is fitted with six poles that carry 4 smaller poles, each, in order to achieve the flux concentration. The 6 coils (2 for each phase) are hosted by the large slots of the outer stator, that separate the main poles. The inner rotor has a large hole in the middle through which passes the shaft. The inner stator is also slotted, our machine being doubly salient. A careful look at the inner rotor unveils the fact that the tooth facing the large slot on the outer rotor (that contains the coils) is somewhat smaller than the other teeth. This is to achieve symmetry along the stator circumference. The rotor is formed of ring-shaped radial laminations that have rectangular slots to hold the PMs. At one end, the rotor is fixated on a non-magnetic plate that is mounted on the shaft. The rotor holds 46 rare earth PMs, oriented in such way as to face each other with the same pole, to avoid a magnetic short in the rotor.

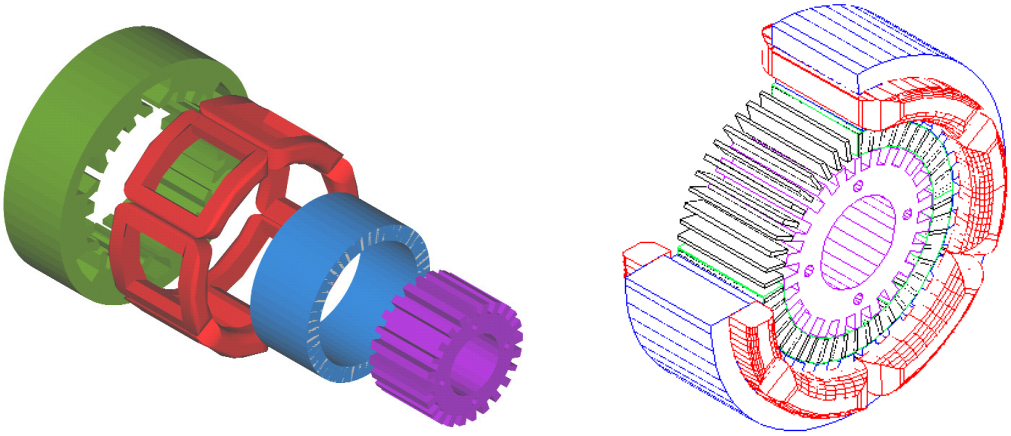

Figure 4.47: 3D view of FRM-FC.

In order to achieve low speeds at industrial operating frequency (50/60 Hz), it is necessary to increase the number of poles and subsequently to decrease the pole pitch. This is entirely justified by the formula that links frequency and speed:

$$f_1 = n \cdot N_r \tag{4.28}$$

with Nr being the number of the poles on the rotor.

According to this relationship, to achieve a rated speed of 130 rpm, at line frequency (50 Hz), it is necessary to have:

$$n_n = f_1 p = 50 * 23 rps = 130.43 rpm \tag{4.29}$$

where nn is the synchronous (rated) speed and p is the number of pole pairs on the rotor. As such, with 23 pairs of poles on the rotor (46 poles) 46 PMs, as mentioned above, are needed to be embedded into the rotor.

The aim is to design a machine with a specific tangential force (f_t) higher than 4 N/cm2, with a peak torque of 150 Nm. The total stack length (lstack) should be around 70 mm, the external diameter less than 300 mm and the current density 12 A/mm2, at a rated line-to-line voltage of 380 V. The efficiency is expected to be above 90% and the power factor bigger than 0.7.

4.4.3 Preliminary Design

With the given design data, first the machine diameter was determined, which is:

$$IDS = \sqrt{\frac{2 \cdot T_{eb}}{\pi \cdot f_t \cdot l_{stack}}} = 176 mm \tag{4.30}$$

There will be 6 large outer stator poles, surrounded by concentrated coils. The two coils corresponding to the same stator pole of each phase will be connected in parallel. Each pole will have in addition 3 slots and will face 4

PMs. The slots on the main poles have a width of $2/3\ \tau_{PM}$, to provide 120° phase shift between phases. In our case, the PM pole pitch:

$$\tau_{PM} = \frac{\pi \cdot IDS}{2 \cdot p} = 12.02mm \tag{4.31}$$

We can consider $\tau_{PM} = 12mm$.

The airgap will be chosen $g = 0.7mm$.

It is advisable to curve the slot corners in order to avoid local saturation. One tooth on one stator is supposed to face a gap of the other stator, obtaining this way a flux concentration. The rotor is supposed to exceed a little the length of the stators. By adding to the stator stack length 4 times the length of the airgap, we have 73 mm for rotor stack length, which will be considered the final design value. At this stage both the inner and the outer rotor diameter can be calculated. This step involves the calculation of the dimensions of the PMs. The PMs on the rotor will naturally face each other with the same pole. The maximum airgap flux produced by the PMs is chosen now: $B_{PMg} = 1.1T$, to leave room for $B_{ag} = 0.766T$ of armature reaction field. This is to assure, that the power factor will be above 0.7. The ideal power factor is calculated as:

$$\cos\varphi_i \cong \frac{B_{PM_g}}{\sqrt{B_{PM_g}^2 + B_{a_g}^2}} = 0.8206 \tag{4.32}$$

The leakage reactance will reduce this value probably to around 0.7. In contrast, the losses will slightly improve it. In addition, lower B_{ag} may be required to produce the rated torque. We choose NeFeB PMs with a remanent field of 1.2 T at 75◦ and with $\mu_{rec} = 1.3\mu_0$. Consequently, the ideal height of the rotor is obtained from:

$$\frac{h_r}{\tau_{PM}} = \frac{B_{PM}/B_r}{2 \cdot k_{fringe} \cdot \left(1 - \frac{B_{PM_g}}{B_r} \cdot \frac{2 \cdot g \cdot \mu_{rec}/\mu_0}{h_{PM}}\right)} = 1.8773 \tag{4.33}$$

We will choose $hr = 1.876\ \tau_{PM} = 22.56mm$. The two bridges, that enclose the PM have a height of $h_b = 0.5mm$. The PM thickness will be considered $h_{PM} = 3mm$. The fringe coefficient was taken $k_{fringe} = 0.55$.

The amount of turns per coil is calculated via:

$$n_c I_c = \frac{\sqrt{2} \cdot T_{eb} \cdot \tau_{PM}}{3 \cdot \pi \cdot \phi_{PM_{pole}}} = 638.84 Aturns/coil(RMS) \tag{4.34}$$

Let us suppose parallel connection of the two coils. Considering the leakage inductance at this point by introducing a correction coefficient $k_{cor} = 0.1$, we may calculate the number of turns from:

$$n_c \cdot \left(\frac{d\psi_{PM}}{d\theta_{er}}\right)_{\max} \cdot \frac{d\theta_{er}}{dt} \cdot \sqrt{1 + \left(\frac{B_{ag}}{B_{PM_g}}\right)^2} \cdot (1 + k_{cor}) \approx V_1\sqrt{2} \tag{4.35}$$

$$V_1 = 220V \tag{4.36}$$

The calculations yield $n_c = 228 turns/coil$. Now the RMS current / coil, $I_{nc} = 2.802A$. Accordingly, the total current / phase $I_n = 5.604A$.

Now we can calculate the rated apparent power as follows:

$$S_n = 3 \cdot V_1 \cdot I_n = 3698 VA \tag{4.37}$$

Then, the rated electromagnetic power is:

$$P_{en} = 2\pi \cdot n_1 \cdot T_{eb} = 2731 W \tag{4.38}$$

So the electric efficiency multiplied by the power factor has following value:

$$\frac{P_{en}}{S_n} = \eta_e \cdot \cos\varphi_1 = 0.7386 \tag{4.39}$$

As a conclusion we may point out that $cos(\varphi) = 1$ is to be greater than 0.73.

Now we come to determine the dimensions of the outer stator. The core flux density is determined by the back iron height h_c. The maximum coil flux may be considered the PM maximum flux because the flux produced by the current in the d-axis is always demagnetizing whereas the current in the q-axis acts in presence of zero PM flux in the coil. As a consequence:

$$h_c \approx \frac{\phi_{PM_{pole}}}{2 \cdot B_{cs} \cdot l_{stack}} = 15.4 mm \tag{4.40}$$

For safety we adopt $hc = 16mm$.

Each one of the large slots hosts one side of 2 coils. Considering the slot's active (copper filled) area, at a fill factor $k_{fill} = 0.5$, we obtain:

$$A_{sa} = \frac{2 \cdot n_c \cdot I_{nc}}{k_{fill} \cdot j_{co}} = 730 mm^2 \tag{4.41}$$

Here we consider $j_{con} = 5A/mm^2$. So there are 228 turns of conductor for each coil with the diameter:

$$d_{co} = \sqrt{\frac{4 \cdot I_{nc}}{\pi \cdot j_{co}}} = 0.845 mm \tag{4.42}$$

To find the losses and subsequently the efficiency, we calculate the phase resistance based on coil-turn length coil:

$$l_{coil} \approx 2l_s + 8\tau_{PM} + \pi \cdot \frac{b_{s1} + b_{s2}}{2} = 342.97 mm \tag{4.43}$$

$$R_c = \frac{R_{coil}}{2} = \rho_{co} \cdot \frac{l_{coil} \cdot n_c}{\frac{\pi \cdot d_o^2}{4}} = 2.93\Omega \tag{4.44}$$

The copper losses are:

$$p_{co} = 3 \cdot 2 \cdot R_c \cdot I_{nc}^2 = 138 W \tag{4.45}$$

At 50 Hz mains frequency the core losses are not significant and should not be above 50 W. Assuming mechanical losses of 1% of the rated power we then have $27W$ losses and a total efficiency of:

$$\eta_t = \frac{P_{en} - p_{mec}}{P_{en} + p_{co} + p_{iron}} = 0.9263 \tag{4.46}$$

The power factor is:

$$\cos\varphi_1 \approx \frac{\eta_e \cdot \cos\varphi_1}{\eta_t} = 0.7973 \tag{4.47}$$

The forecasted performance is good. The total motor weight could be as low as $40kg$, yielding a rated torque/mass ratio of $5Nm/kg$.

4.4.4 FEM Analysis at No Load

The initial geometry has been modified by reducing the initial airgap from $0.7mm$ to $0.5mm$ (it should be as small as mechanically feasible), to increase the torque Fig. 4.48. This is an imposed change because of the fact that the machine has two instead of (traditionally) one airgaps.

First we determined the PM flux variation with rotor position. With the straight machine the 3rd order harmonic was quite large: about 12% of the fundamental. With an appropriate skewing, this was reduced, the flux waveform being closer to a sinusoid (with the 3rd order harmonics being 7.3% of the fundamental), but the amplitude decreasing to 92.8% of the initial amplitude (Fig. 4.49). This means that the back EMF will not be considerably reduced by 7.2 %.

The skewing angle is 0.44° mechanical, one of the two angles for which maximum cogging torque reduction was obtained. This is the primary aim of the skewing. For the other value, 2.2° mechanical the amplitude of the flux was dramatically reduced and the waveform was far from sinusoidal. With a skewing 0.44° mechanical, the cogging torque was reduced to 1.12% (Fig. 4.52) of the rated torque $(150Nm)$, below 1.5%, which is the limit requirement for servo drives. It must be noted in addition, that neither of the two angles for which minimum cogging torque was obtained, is 1/3 of the pole pitch, as theoretically assumed.

Additionally the skewing shifts the PM flux. This has to be taken into consideration when designing the control system of the machine. Although the flux versus position looks quite sinusoidal, the derivative (shown in Fig. 4.51., for the skewed machine) suggests rather trapezoidal control than sinusoidal one.

4.4.5 FEM Analysis On Load at Steady State

By letting sinusoidal currents flow in the three phases, load conditions at steady state can be modeled.

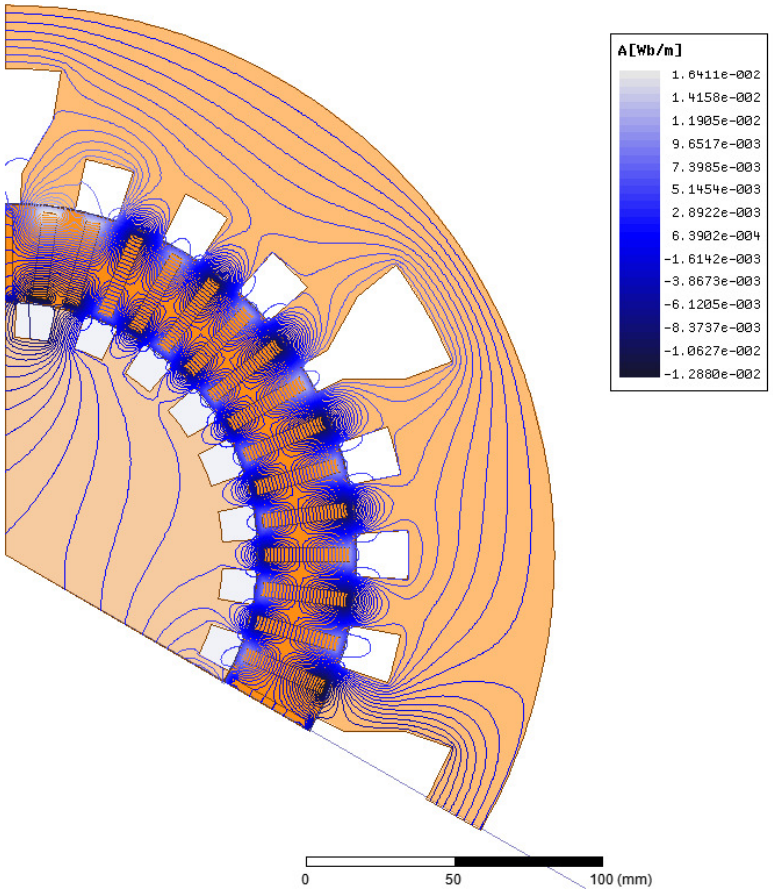

Figure 4.48: Flux lines for FRM-FC.

We maintained the maximum current against rotor position, finding this way the value for the peak torque, as well as its position, confirming that this position is precisely the "zero flux" position. The explanation is very simple: for this value of the flux the derivative of the PM flux is maximum.

We may also simulate the operation of the machine, in motoring mode, by letting sinusoidal currents flow through the three phases and adjusting the rotor position accordingly, in such a way, that they are "in phase".

With this configuration in mind, we can study the influence of saturation on performance. First, we will determine the maximum torque for different current densities. This way the torque pulsations can also be visualized.

In evaluating the performance of a machine one decisive parameter is the loss in the coils due to the Joule-Lenz effect:

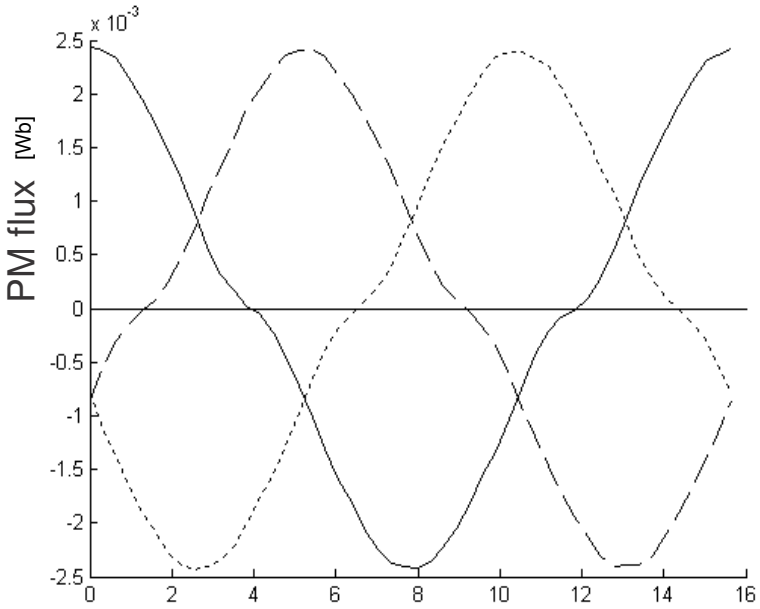

Figure 4.49: PM flux in all 3 phases vs. mechanical angle (straight machine) for a coil with 1 turn.

$$p_{co} = 3 \cdot R_s \cdot I_n = 3 \cdot \rho_{co} \frac{l_{coil} \cdot j_{co}}{n_c \cdot I_n} \cdot \frac{N_s}{3} \cdot n_c^2 \cdot I_n^2 = 144.15W \tag{4.48}$$

We obtain these losses at rated current, which is $1640Aturns$ or a current density of 12 A/mm2. Under the same conditions, with a coil length of:

$$l_{coil} \approx 2l_{stack} + 8\tau_{PM} + \pi \frac{b_{s1} + b_{s2}}{2} = 348.8mm \tag{4.49}$$

we have a torque density of:

$$f_{tn} = \frac{2 \cdot T_{en}}{\pi \cdot D_r^2 \cdot l_{stack}} = 5N/cm^2 \tag{4.50}$$

This is a good result because most machines achieve torque densities of up to 4 N/cm2 at rated current. The overall efficiency also is good, under rated conditions, if iron and mechanical losses are neglected:

$$\eta_n \approx \frac{T_{en} \cdot \Omega_n}{T_{en} \cdot \Omega_n + p_{coil}} = 0.94325 \tag{4.51}$$

We can assume that even with the mechanical and iron losses included into the formula, the result will exceed 0.9 for rated current and frequency. A notable

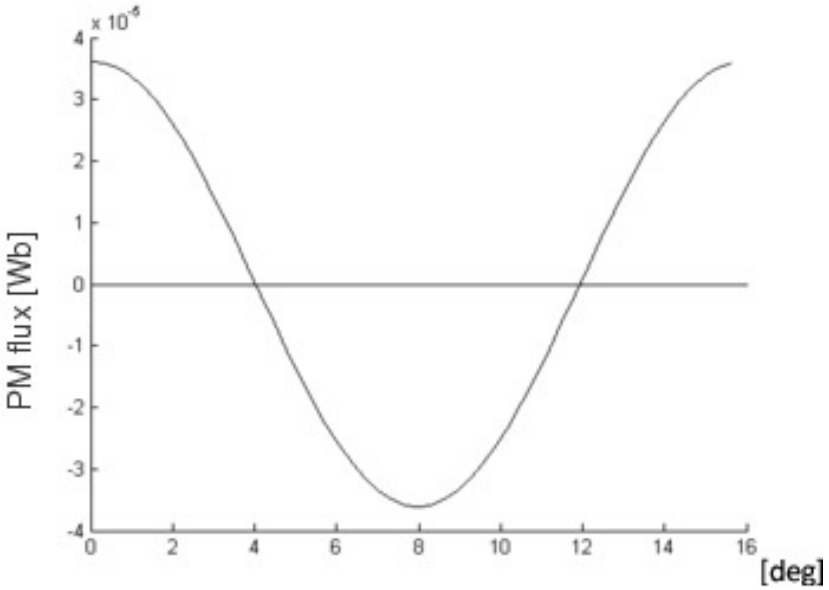

Figure 4.50: PM flux in phase vs. mechanical angle (straight machine) for a coil with 1 turn.

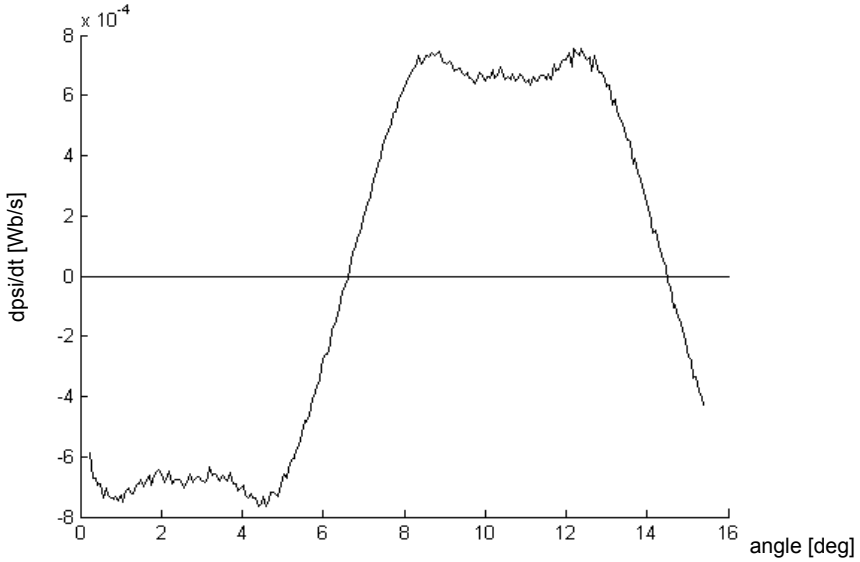

Figure 4.51: Derivative of the PM flux in one phase (filtered) vs. mechanical angle for a coil with 1 turn.

result is the fact, that at a current density of 18 A/mm2, where saturation effects are quite considerable, the machine still works at 88.86% efficiency,

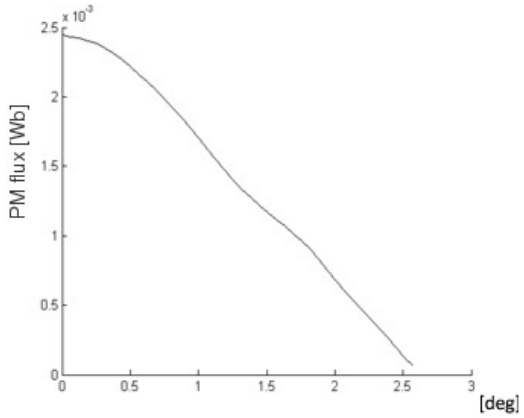

Figure 4.52: PM flux in one phase variation with the skew angle for a coil with 1 turn.

although the torque does not increase too much (from 176 Nm to 190 Nm). After this point, efficiency plummets.

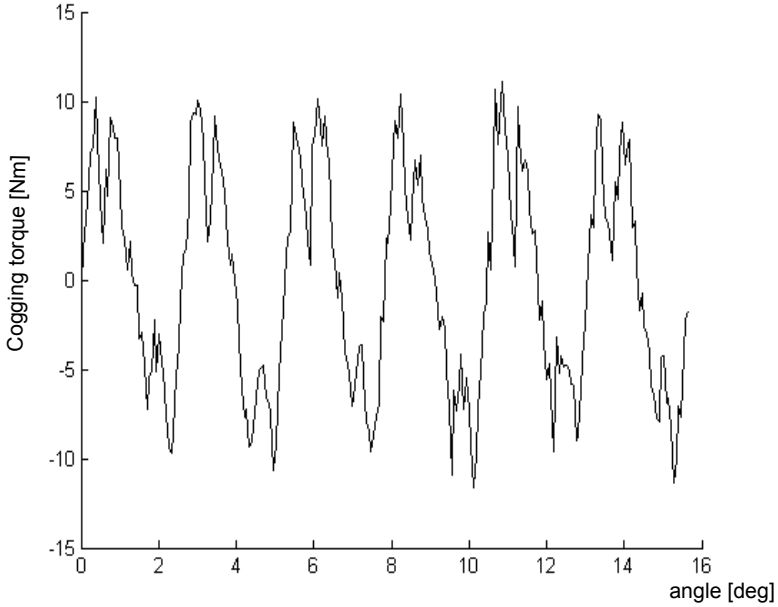

Figure 4.53: Cogging Torque vs. mechanical angle.

Now it is of great interest to see how the skewed version of the machine behaves under load. To study this we have simulated the torque versus position at various current densities. As we can see (Fig. 9), at low current densities the pulsation is large, being the smallest at $12A/mm^2$ and then rising

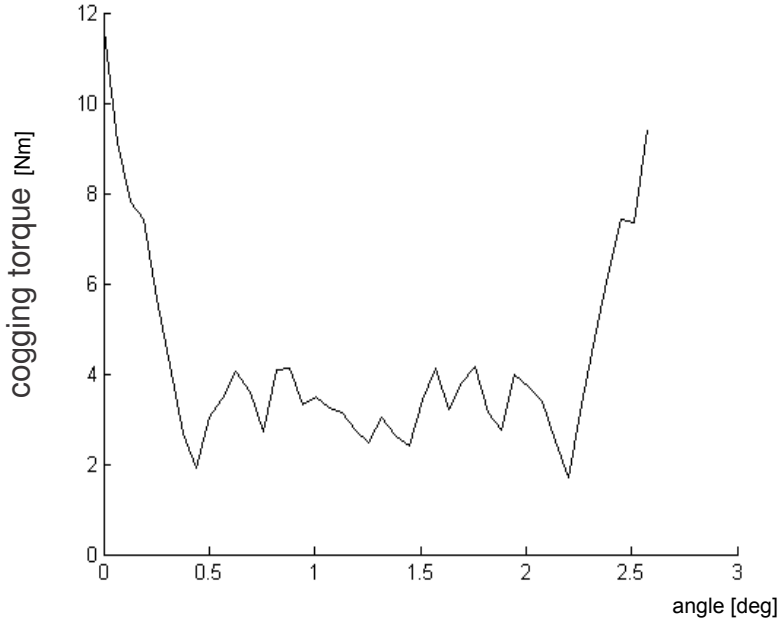

Figure 4.54: Amplitude of cogging torque vs. skewing angle.

again, as the machine gets more and more saturated. The torque pulsation at optimum operation mode are 2,94% of the average torque, that is some 4.42 Nm out of 150 Nm, qualifying the machine at this point as servo drive.

4.4.6 Inductances Calculated with FEM

Inductances are of major interest for control design. We will calculate for this purpose the self and mutual inductances of the coils. The question arises whether it is appropriate to calculate the inductances with all phases energized or only with the phases for which the calculation is performed. Based on former experience, we can affirm, that all phases should be energized. We have set up our model accordingly. The ripple of the self-inductance occurs due to some rotor saliency, saturation and computation error (Fig. 4.56).

Still, the sinusoidal variation of the inductance is clearly visible. The self-inductance is under 3 μH for a coil with 1 turn. The mutual inductance is smaller, as expected and oscillates around 0.75 μH, for a coil with 1 turn. Ideally, the inductances of the three phases are shifted 120° electrical with respect to each other:

$$\begin{aligned} L_{aa} &= L_s + L_0 \cdot \cos(\theta_{er}) \\ L_{bb} &= L_s + L_0 \cdot \cos\left(\theta_{er} + \tfrac{2\pi}{3}\right) \\ L_{cc} &= L_s + L_0 \cdot \cos\left(\theta_{er} - \tfrac{2\pi}{3}\right) \end{aligned} \tag{4.52}$$

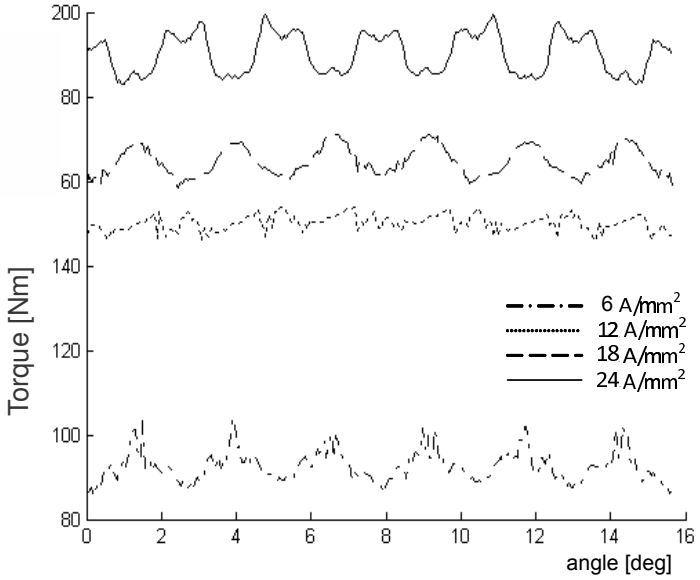

Figure 4.55: Torque vs. mechanical angle.

where, from Fig. 4.56:

$$L_s = 2.88\mu H/turn$$
$$L_0 = 0.155\mu H/turn \tag{4.53}$$

4.4.7 Conclusions concerning Radial Flux Reversal with Flux Concentration

The topology of the machine accounts for difficulties in building it (fixation of the rotor on the shaft) and therefore the costs are higher.

The torque pulsation problems have to be sorted out, too, in order to fully qualify the machine for servo applications. So far, the machine fulfills the requirements.

On the other hand, the machine performs well even under heavy saturation, which makes us think that it is a viable model. The torque density is superior to most of the machines built these days at very low speed and the rated efficiency is also high.

Bibliography

[1] S. E. Rauch, L. J. Johnson – "Design Principles of flux Switch Alternator", AIEE Trans. vol. 74 III, pp 1261-1268, 1955

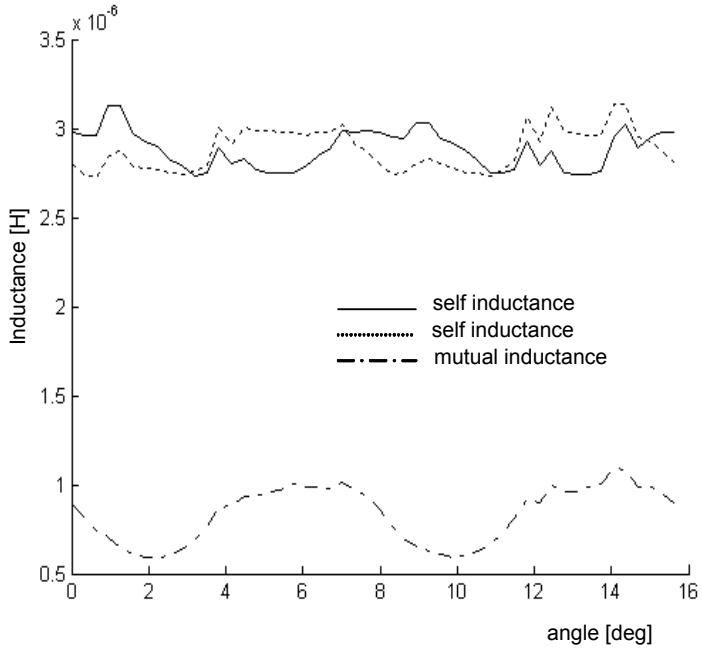

Figure 4.56: Self- and mutual inductances vs. mechanical angle for a coil with 1 turn.

[2] H. Weh – "Transverse flux (TF) Machines in Drive and Generator Applications", Stockholm Power Tech, June 1995

[3] G. Henneberger, M. Bork – "Development of a New Transverse flux Motor", Electromotion, vol. 5, no. 1, 1998, pp. 1-8;

[4] R. Kruse – "Calculation Methods for a Transverse flux Reluctance Motor", Proc. Of OPTIM Int. Conf., 2000, Brasov, Romania, pp. 387-392;

[5] I. Boldea, J. Zhang, S. A. Nasar – "Theoretical Characterization of flux Reversal Machine in Low-Speed Servo Drives – The Pole-PM Configuration", in IEEE Trans. Ind. Applicat. vol. 38, no. 6, Nov/Dec 2002 pp. 1549 – 1557;

[6] C. Wang – "Three Phase flux Reversal Machine (Dissertation)", Lexington, Kentucky, 1999

[7] B. Chalmers, W. Wu, and E. Spooner, "An axial-flux permanent-magnet generator for a gearless wind energy system," in IEEE Trans. on Energy Conversion, vol. 14, no. 2, pp. 251-257, 1999.

[8] E. Muljadi, C. Butterfield, and Y. Wan, "Axial flux, modular, permanent-magnet generator with a toroidal winding for wind turbine applications," in IEEE Trans. on Industry Applications, vol. 35, no. 4, pp. 831-836, 1999.

[9] L. Soderlund, J. Eriksson, J. Salonen, H.Vihria and R. Perala, "A permanentmagnet generator for wind power applications," in IEEE Trans. on Magnetics, vol. 32, no. 4, pp. 2389-2392, 1996.

[10] H. Weh and H. May, "Achievable force densities for permanent magnet excited machines in new configurations," in Proc. of Int. Conf. on Electrical Machines, (ICEM), vol. 3, pp. 1107-1111, 1990.

[11] M. Dubois, N. Dehlinger, H. Polinder, and D. Massicotte, "Clawpole transverse-flux machine with hybrid stator," in Proc. of Int. Conf. on Electrical Machines, (ICEM), paper no. 412, 2006.

[12] D. Svechkarenko, "On analytical modeling and design of a novel transverse flux generator for offshore wind turbines." Licentiate thesis, Department of Electrical Machines and Power Electronics, Royal Institute of Technology, Stockholm, Sweden, 2007.

[13] F. Caricchi, F. Crescimbini, and O. Honorati, "Modular axial-flux permanent-magnet motor for ship propulsion drives," in IEEE Trans. on Energy Conversion, vol. 14, no. 3, pp. 673-679, 199.

[14] B. Bean, "Invasion of the Azipods: The first change to screws in 200 years causes quite a stir," in The TRITON-Megayacht News, www.thetriton.com/megayachtnews/, 2005.

[15] A. Mitcham, "Transverse flux motors for electric propulsion of ships," in IEE Colloquium on New Topologies for Permanent Magnet Machines, Digest NORPIE 1997/090, pp. 3/1-3/6, 1997.

[16] R. Lain and A. Bedford, "Recent developments in the design of gearless machines for elevators," in Proc. of Int. Conf. on Electrical Machines and Drives, pp. 334-338, 1993.

[17] R. Ficheux, F. Caricchi, F. Crescimbini, and H. Onorato, "Axial-flux permanentmagnet motor for direct-drive elevator systems without machine room," in IEEE Trans. on Industry Applications, vol. 37, no. 6, pp 1693-1701, 2001.

[18] H. Lim and R. Krishnan, "Ropeless elevator with linear switched reluctance motor drive actuation systems," in IEEE Trans. on Industrial Electronics, vol. 54, no. 4, pp. 2209-2218, 2007.

[19] Kone, "www.kone.com."

[20] A. Bianchi and L. Buti, "Three-Phase A.C. Motor Drive and Controller for Clothes Washers," in Int. Appliance Technical Conference, available on www.appliancemagazine.com, 2003.

[21] S. Evon and R. Schiferl, "Direct-drive induction motors: using an induction motor as an alternative to a motor with reducer," in IEEE Industry Application Magazine, vol. 11, no. 4, pp. 45-51, 2005.

[22] P. Salminen, "Fractional slot permanent magnet synchronous motors for low speed applications." Doctoral thesis, Lappeenranta University of Technology, Finland, 2004.

[23] J. Hallberg, "Conceptual evaluation and design of a direct-driven mixer." Master thesis, Department of Mechanical Engineering, Linkopings University, Linkoping,Sweden, 2005.

[24] M. Mueller, A. McDonald, and D. Macpherson, "Structural analysis of low-speed axial-flux permanent-magnet machines," in IEE Proc. on Electric Power Application, vol. 152, no. 6, pp. 1417-1426, 2005.

[25] M. Cistelecan, M. Popescu, and M. Popescu, "Study of the number of slots/pole combinations for low speed permanent magnet synchronous generators," in Proc. of IEEE Int. Electric Machines and Drives Conf., (IEMDC), vol. 2, pp. 1616-1620, 2007.

[26] J. Germishuizen, "Design and performance characteristics of IPM machines with single layer non-overlapping concentrated windings," in Proc. of IEEE Industry Applications Society Conf., pp. 141-147, 2007.

[27] J. Cros and P. Viarouge, "Synthesis of high performance PM motors with concentrated windings," in IEEE Trans. on Energy Conversion, vol. 17, no. 2, pp. 248-253, 2002.

[28] F. Magnussen and C. Sadarangani, "Winding factors and joule losses of permanent magnet machines with concentrated windings," in Proc. of Electric Machines and Drives Conf., (IEMDC), vol. 1, pp. 333-339, 2003.

[29] R. Wrobel and P. Mellor, "Design considerations of a direct drive brushless machine with concentrated windings," in IEEE Trans. on Energy Conversion, vol. 23, no. 1, pp. 1-8, 2008.

[30] A. EL-Refaie, "High speed operation of permanent magnet machines." Doctoral thesis, University of Wisconsin-Madison, USA, 2005.

[31] M. Cistelecan, B. Cosan, and M. Popescu, "Tooth Concentrated Fractional Windings for low speed three phase a.c. machines," in Proc. of Int. Conf. on Electrical Machines, (ICEM), paper no. 362, 2006.

[32] A. Rix, M. Kamper, and R. Wang, "Design and performance evaluation of concentrated coil permanent magnet machines for in-wheel drives," in Proc. of IEEE Int. Electric Machines and Drives Conf., (IEMDC), vol. 1 pp. 770-775, 2007.

[33] P. Salminen, M. Niemela, and J. Pyrhonen, "Performance analysis of fractional slot wound PM-motors for low speed applications," in Proc. of IEEE Industry Applications Society Conf., vol. 2, pp. 1032-1037, 2005.

[34] N. Bianchi, S. Bolognani, and M. D. Pre, "Magnetic loading of fractional-slot threephase PM motors with non-overlapped coils," in Proc. of IEEE Industry Applications Society Conf., vol. 1, pp. 37-43, 2006.

[35] A. EL-Refaie, M. Shah, and J. K. R. Qu, "Effect of number of phases on losses in conducting sleeves of high speed surface PM machines rotors," in Proc. of IEEE Industry Applications Society Conf., pp. 1522-1529, 2007.

[36] Rubicek Z. Peicek, O. Podzincek Progress in the development of electric linear drives intendended for technological applications" EMAS, vol. 14, no. 2, pp 73-81.

[37] B. Lequesque Permanent magnet linear motors for short strokes" Record of IEEE – IAS 1991, Annual meeting part I p162-169.

[38] J. Oyama, T Miguchi et all Application of linear motors on artificial sattelite fuel pump system" Ibid pp.156-161.

[39] Ion.Boldea, S. A. Nasar, B Pensweick, B Ross, R Olan New linear reciprocating machine with stationary permanent magnets" Record of IEEE IAS 1996 Annual meeting vol 2 pp 825- 829.

[40] Boldea S. A. Nasar US patent No. 5, 564, 596.

[41] Boldea, C. Wang, B Yang, S. A Nasar Linear actuators and generators book, Cambridge University press, 1997

[42] Boldea, S A Nasar Linear electrodevices" book Taylor and Francis publ. 2001

[43] W. Cawthorne, P. Famouri, N. Clark Integrated design of linear alternator engine system for HEV auxiliary power unit" Record of IEEE – IEMDC- 2001, MIT,pp 267-274.

[44] S. E. Rauch, L. J. Johnson – "Design Principles of flux Switch Alternator", AIEE Trans. vol. 74 III, pp 1261-1268, 1955

[45] H. Weh – "Transverse flux (TF) Machines in Drive and Generator Applications", Stockholm Power Tech, June 1995

[46] G. Henneberger, M. Bork – "Development of a New Transverse flux Motor", Electromotion, vol. 5, no. 1, 1998, pp. 1-8

[47] R. Kruse – "Calculation Methods for a Transverse flux Reluctance Motor", Proc. Of OPTIM Int. Conf., 2000, Brasov, Romania, pp. 387-392

[48] I. Boldea, J. Zhang, S. A. Nasar – "Theoretical Characterization of flux Reversal Machine in Low-Speed Servo Drives – The Pole-PM Configuration", in IEEE Trans. Ind. Applicat. vol. 38, no. 6, Nov/Dec 2002 pp. 1549 – 1557.

[49] C. Wang – "Three Phase flux Reversal Machine (Dissertation)", Lexington, Kentucky, 1999

5 Axial flux Permanent Magnet Machines with Nonoverlaping Windings

Axial flux Permanent Magnet Machines (AFPMM) first appeared in the technical literature in mid 70's [1-3]. Soon their fields of application spread widely [3] . Today, among the most prominent appliances are fans, elevators, ship, vehicle and airplane propulsion [2], [4-10]. Compact permanent magnet generators can be connected directly to an intemal combustion (IC) engine for use in hybrid electric vehicles [11]. Axial flux generators can be connected directly on to the engine in place of the engine flywheel and can be used as brushless motors for engine starting [12], [18]. The interest towards such machine topology is partially due to its small aspect ratio, and also to its torque-density. Quite a few studies have been focused on the comparison between radial- and axial-flux machines [14-17]. As for all electrical machines,This chapter presents two applications of Axial-flux PM Synchronous Motor (AFPMSM) for a direct wheel drive.The special feature of this protoytpe were presented in [] Its main feature AFPMSM is that the stator is build upon the configuration of one stator and two rotors and the winding is characterized by $q < 1$ of the fractional tooth wound type.

The choice of a concentrated non-overlapping winding allows a large number of pole pairs to be designed. This chapter is aimed at emphasizing the special features of the whole axial flux motor and drives integrations of nonoverlapping AFPMSM . Therefore, both machine and control design aspects are targeted. In first part of the chapter some imrouvements concerning cogging torque of a 18/16 pole AFPM are presented .
For large poles machines encoder-less operation of the drive is particularly critical. Firsts a vector control scheme is illustrated for a specialy designed machine with 48/40 slots/pole. Also sensorless control using a sliding-mode rotor flux estimation scheme is investigated. Its performances are experimentally compared to the encoder operation.

In order to increase the power to weight ratio, an increase both of the back e.m.f and of the rated current is requested. Authors generally agree on the fact that major advantages are achieved only in the case the number of poles is high enough. In plain words, by operating the motor at higher frequencies, the number of turns of the winding can be decreased at the same back e.m.f., and therefore the current can be increased accordingly [18]. Furthermore, the torque of axial flux machines presents a maximum whenever the ratio K

between inner and outer radius is:

$$K = 1/\sqrt{3} \approx 0.58 \tag{5.1}$$

However, in axial flux machines with traditional windings, increasing the number of poles represents a complex question. In fact, one coil of the winding normally links the flux of one pole. If the pole number of the machine is increased, then the flux linked by each coil decreases rapidly due both to the reduction of the pole pitch and to the relative increase of the fringing flux. Also, the wave shape of the back e.m.f. becomes more distorted due to the reduction of the number of slots per pole and phase. Moreover, in the region closer to the inner circumference the reduction of the tooth pitch may lead to high levels of saturation as it is reported in [19].

Therefore the number of poles cannot be whatsoever selected . Instead, fractional slot windings with a number of slots per pole lower than unity allow a larger number of poles to be designed by placing less than one slot per phase under each pole. In this way, a larger room for the stator winding conductors is yielded. Some combinations of slots/poles allow also the construction of compact, tooth-wound non overlapping windings with high winding factors [20], thus reducing the length of the end windings. Furthermore, an optimised choice of the number of slots and poles improves the shape of the back e.m. f. However, reducing the pole pitch of PM machines poses obvious threats to position sensorless control systems, where rotor position must be either measured or identified precisely. This issue is targeted experimentally in this chapter. Results obtained from a vector control scheme are presented. A sliding-mode scheme was implemented. Its performances are compared to standard encoder-with operation.

5.1 Analysis of a 18 slots /16 poles fractional winding Axial flux Permanent Magnet Synchronous machine (AFPM)

5.1.1 Presentation of 18/16 slots/poles Axial flux PM Motor Structure

Fig. 5.1 shows the basic structure of the slotted AFPM motor with double stator and single rotor which was investigated in south Korea at KERI (Korea Electrotechnics Reserch Institute). The rectangular-shaped teeth and fan-shaped PM in AFPM are shown in Fig. 5.1. Fig. 5.2 shows the picture of prototype AFPM motor. The motor has two stators with two sets of 3 phase stator winding. In the structure of the AFPM motor, the rotor with PM is located in the middle of the motor and the stator with exciting coils is attached on the both sides. To increase the power density of motor, Neodymium-Iron-Boron

is selected due to its high energy product. Table I shows the specifications of the AFPM motor.

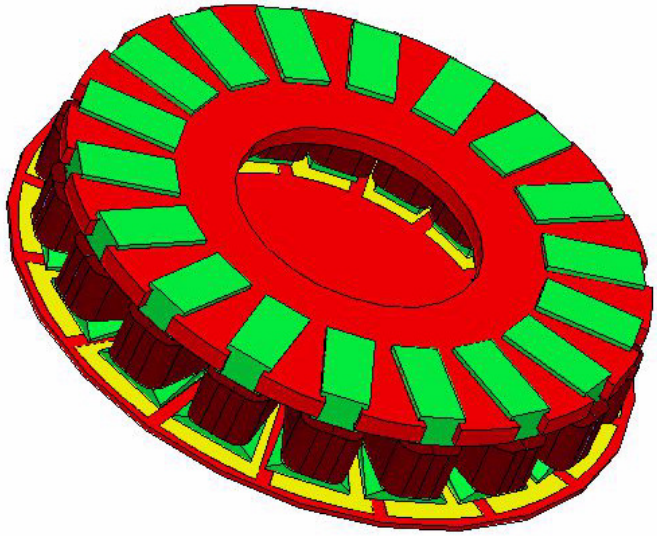

Figure 5.1: 3D view of the structure of 18/16 axial flux prototype

5.2 Design of the axial flux machine using power density equations

5.2.1 Sizing Equations of AFPM Motors

In general, if stator leakage inductance and resistance are neglected, the output power for any electrical machine can be expressed as

$$P_{out} = \eta \frac{m}{T} \int_0^T e(t) i(t) dt = m K_p \eta E_{pk} I_{pk} \tag{5.2}$$

where $e(t)$ and E_{pk} are phase air gap EMF and its peak value, $i(t)$ and I_{pk} are phase current and the peak phase current, η is machine efficiency, m is number of phases of the machine and T is period of one cycle of the EMF.

The quantity K_p is termed the electrical power waveform factor and defined as:

$$K_p = \frac{1}{T} \int_0^T \frac{e(t) \times i(t)}{E_{pk} \times I_{pk}} dt = \frac{1}{T} \int_0^T f_e(t).f_i(t) dt \tag{5.3}$$

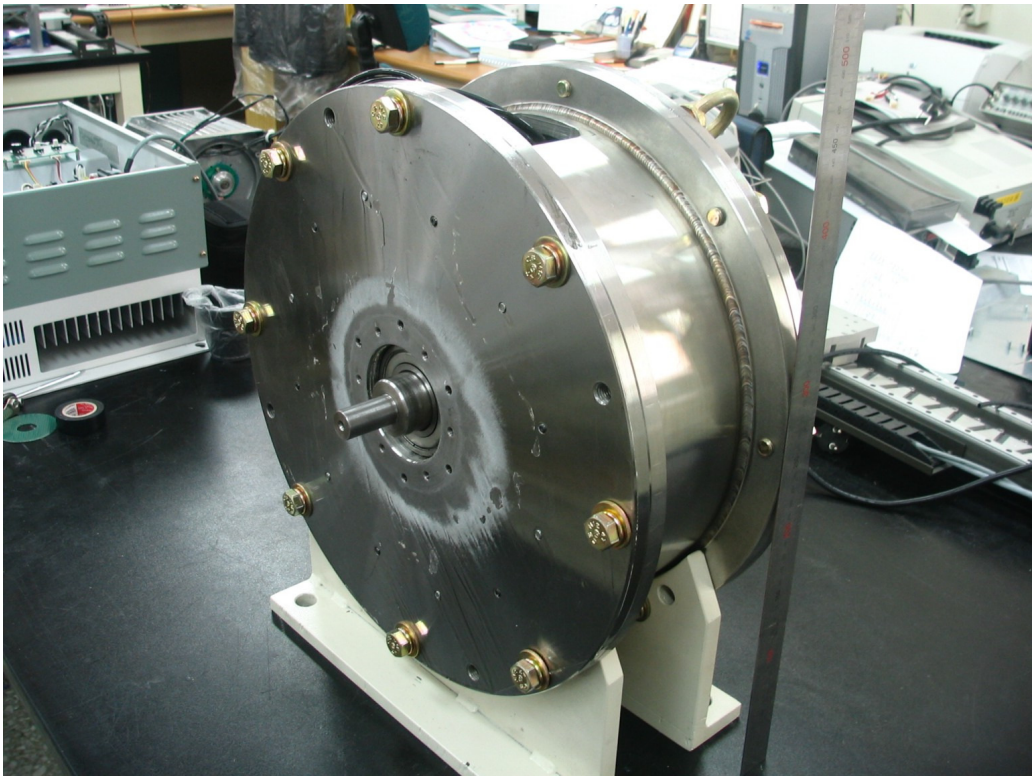

Figure 5.2: 18/16 Axial flux internal rotor build prototype.

where $f_e(t) = \frac{e(t)}{E_{pk}}$ and $f_i(t) = \frac{i(t)}{I_{pk}}$ are the expressions for the normalized EMF and current waveforms. In order to indicate the effect of the current waveform, a definition for current waveform factor, K_i, is also useful,

$$K_i = \frac{I_{pk}}{I_{rms}} = [\frac{1}{T}\int_0^T (\frac{i(t)}{I_{pk}})^2 dt]^{-0.5} \tag{5.4}$$

where I_{rms} is the rms value of the phase current. The peak value of the phase air gap EMF for AFPM in (1) is given by:

$$E_{pk} = K_e N_{ph} B_g . \frac{f}{p} . (1 - \lambda^2) D_o^2 \tag{5.5}$$

where K_e is the EMF factor which incorporates the winding distribution factor

K_w and the per unit portion of the total air gap area spanned by the salient poles of the machine (if any),

N_{ph} is the number of turn per phase,

Bg is the flux density in the air gap,

f is the converter frequency,

p is the machine pole pairs,
λ is the diameter ratio for AFPM defmed as D_i/D_o,
D_o is the diameter of the machine outer surface,
D_i is the diameter of the machine inner surface. The peak phase current in (5.5) is given by:

$$I_{pk} = A\pi K_i \frac{1+\lambda}{2} \frac{D_o}{2m_1 N_{ph}} \tag{5.6}$$

m_1 is number of phases of each stator and A is the electrical loading. Combining (5.2) through (5.5), the general purpose sizing equations take the following form for AFPM:

$$P_{out} = \frac{m}{m_1}\frac{\pi}{2} K_e K_p K_i A B_g \eta \frac{f}{p}(1-\lambda^2)(\frac{1+\lambda}{2})D_o^3 \tag{5.7}$$

$$P_{den} = \frac{P_{out}}{\frac{\pi}{4} D_{out}^2 L_{tot}} \tag{5.8}$$

where D_{out} is the total machine outer diameter including the stack outer diameter and the protrusion of the end winding from the iron stack in the radial direction,
L_{out} is the total length of the machine including the stack length and the protrusion of the end winding from the iron stack in the axial direction
The outer surface diameter D_o is obtained from 5.7
The machine total outer diameter $D_{out/}$ for the AfiR (Axial flux two-stator-one-rotor) type machines is given as

$$D_{out} = D_o + 2W_{cu} \tag{5.9}$$

where W_{cu} is the protrusion of the end winding from the iron stack in the radial direction and can be calculated as

$$W_{cu} = \frac{D_i - \sqrt{D_i^2 - (D_g/K_{cu}J_s)}}{2} \tag{5.10}$$

The axial length of the machine L_e is :

$$L_e = L_r + 2L_s + 2g \tag{5.11}$$

where L_s is axial length of the stator,
L_r is axial length of the rotor and g is the air gap length.
The axial length of a stator L_s is:

$$L_s = L_{cs} + 2W_{cu} \tag{5.12}$$

where L_{cs} is the axial length of the stator core.
The axial length of the stator core L_{cs} can be written as:

$$L_{cs} = \frac{B_g \pi \alpha_p D_o (1+\lambda)}{8pB_{cr}} \tag{5.13}$$

Since there is no rotor core in rotor PM topologies, the axial length of rotor Lr is

$$L_r = L_{PM} \tag{5.14}$$

The PM length L_{PM} can be calculated as:

$$L_{PM} = \frac{2\mu_r B_g}{B_r - (\frac{K_f}{K_d} B_g)}(g + W_{cu}) \tag{5.15}$$

$$P_R = \frac{1}{1+K_\phi}\frac{m}{m_1}\frac{\pi}{2}K_e K_i K_p \eta B_g A \frac{f}{p}\left(1-\lambda^2\right)\frac{1+\lambda}{2}D_o^3, \tag{5.16}$$

In this equation K_φ is the ratio of electrical loading on rotor and stator.

m number of phases of the machine.

m_1 number of phases of each stator (if there is more than one stator, each stator has the same m_1).

K_e emf factor incorporating the winding distribution factor Kd, and the ratio between the area spanned by the salient poles and the total airgap area

K_i, current waveform factor.

K_p electrical power waveform factor.

η machine efficiency.

B_g flux density in the air gap.

A total electrical loading including both the stator electrical loading A, and rotor electrical loading A,.

f converter frequency.

p machine pole pairs.

D_o diameter of the outer surface of the machine.

L_e effective stack length of the machine.

K_L, aspect ratio coefficient L_e/D_o of the effective stack length over the gap diameter in radial air-gap machines.

λ. ratio of the diameter of the air-gap surface vs. the diameter of the outer surface of the machine.

From this model the efficiency of the machine can be expressed as:

$$\eta = \frac{P_{in}}{P_{out}} \tag{5.17}$$

The ratio is an important factor which depends on the lengths L_s, and L_r, also depends upon the stator equivalent electrical loading A_s, the current density J_s, the slot fill factor K_{cu}, and flux densities in the different parts of the machine. The permanent magnet length L_{PM} depends on the air gap flux density required and air gap length.

An optimal value of K_L determines maximum efficiency and power density of the machine. This parameter can be estimated from experience [2] or it can be identified by integrating FEM analysis result. For the double stator axial flux K_L can be expressed as:

$$K_L = \frac{Do}{L_e} = f(L_s, Lr, L_{PM}, \lambda, D_o, g, p) \tag{5.18}$$

5.2.2 Sensitivity analysis of key design parameters in the design of AFPMSM

Finite element method represent today a common approach to investigate electric machine. The reliability of the results make this an mandatory step in the design of the electric machinery. One may find a large spectrum of software capable to handle all the tasks required in investigation. How in design stage which is an very important step the need of accurate models is vital. In most of the cases models used for design include more or less a set of parameters which are not deterministic or which are experience based. Finite element represents an analysis tool and is not supposed to replace the design of the prototype. By means of finite element is possible to evaluate the accuracy of the design equations and to provide useful information about the parameters and coefficients which may used in order to improve the performance of the prototype. Therefore we consider that is necessary that in design stage to include an evaluation method which can be used to appreciate the model and to tune the model in order to define the most critical parameters which can be used for optimisation.

A solution for this is represented by sensitivity analysis [1-2]. Sensitivity analysis is a statistical method suitable to be used for determination of the interactions between factors that contribute to the greatest variability of the model response;

In this chapter we use a combined method which integrates the design of the machine with the powerful features of finite element method and sensitivity analysis. The method is applied for an axial flux permanent magnet machine. For the design of the axial flux machine a very simple model was used based on the power density equations developed in [3]. For evaluation of the results a corresponding two dimensional parametric FEM model is used . This model allows that optimization to be performed directly on the FEM model without the necessity of using expensive 3D software.

The equations 5.2 and 5.8 are used in order to identify the parameters that are most likely to influence the efficiency of the prototype. Some parameters are kept constant and others considered to have a known distribution. In table 5.1 the parameters with corresponding distributions are presented.

Table 5.1: Sensitivity test parameters and distribution

Parameters	*Distributions:*	*Description*
Bg	Uniform	airgap flux density
K_L	Uniform	form factor
A	Normal	electric loading
f	Uniform	frequency
B_{cs}	Uniform	flux density
D_o	Uniform	external diameter
g	Normal	airgap

In order to verify the influence of this factors in improving the efficiency of the machine FEM method is applied for the 2D equivalent model. In order to evaluate the sensitivity of the design model a sample for each parameters is generated by eq.5.19 since the number of parameter is reduced to only four.

$$M = \begin{Bmatrix} z_1^1 & z_2^1 & \dots z_r^1 \\ z_1^2 & z_2^2 & \dots z_r^2 \\ \dots & \dots & \dots \\ z_1^{(N)} & z_2^{(N)} & \dots z_r^{(N)} \end{Bmatrix} \tag{5.19}$$

$$y = \begin{Bmatrix} y^1 \\ y^2 \\ \dots \\ y^{(N)} \end{Bmatrix} \tag{5.20}$$

The output parameters are used to build the corresponding model output eq 5.20. Fig. 5.3 presents the responses obtained after the variation of the selected parameters. After the evaluation of responses for each factor is obtained a regression model is developed by regressing the responses over the M samples. The regression model coefficients actually represent the sensitivity coefficients. In order to rank input factors in terms to their contribution to the variability of the output the sensitivity matrix is used by ordering of the parameters function of PCC coefficient. The sensitivity analysis was implemented with software SIMLAB which integrates all the necessary stjpg in evaluating sensitivity analysis models. The sampling of the model was considered to be random with a number of 1000 samples for each factor.

Table 5.2: Test parameters for SA

Factor	D_o	g	L_e	J_s	B_{cs}	B_g	A
PCC	-0.194	0.3698	0.0013	-0.121	-0.492	0.0333	0.0017

The Partial Correlation Coefficient PCC table gives the strength of correlation between the response and the given input factor. In Fig 3 the scattered plot of the resulted coefficients is presented . Based on the PCC analysis the factors with a good influence on the efficiency are selected. The flowing factors are considered for the improvement of the performance of the prototype L_e (h_{pm} and the width of back iron), g, D_o (λ factor);

5.2.3 2D FEM analysis of sensitive model parameters

The axial flux topology presents 3D flux path lines and because of this a 3D FEM analysis is appropriate. The use of 2D finite element is more convenient especially when a large number of changes in the design have to be considered. It is possible to develop a simplified 2D model for the FEM analysis of the axial flux prototype. The 2D model represents a tangential cut of the machine for various radii Fig. [2]. The model is also simplified furthermore by the use of the symmetric boundary conditions. Using different radius for

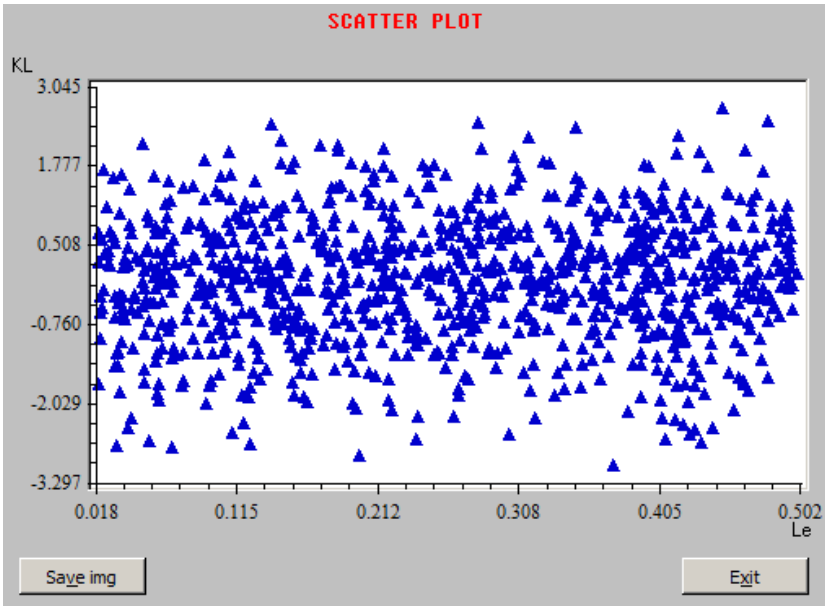

Figure 5.3: K_L response function of axial length of the machine.

cutting the 3D model a number of equivalent geometries can be obtained. These geometries can be easily analyzed by 2D FEM.

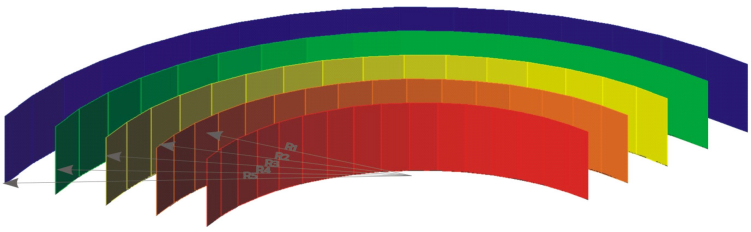

Figure 5.4: Decomposition of axial geometry in several slices.

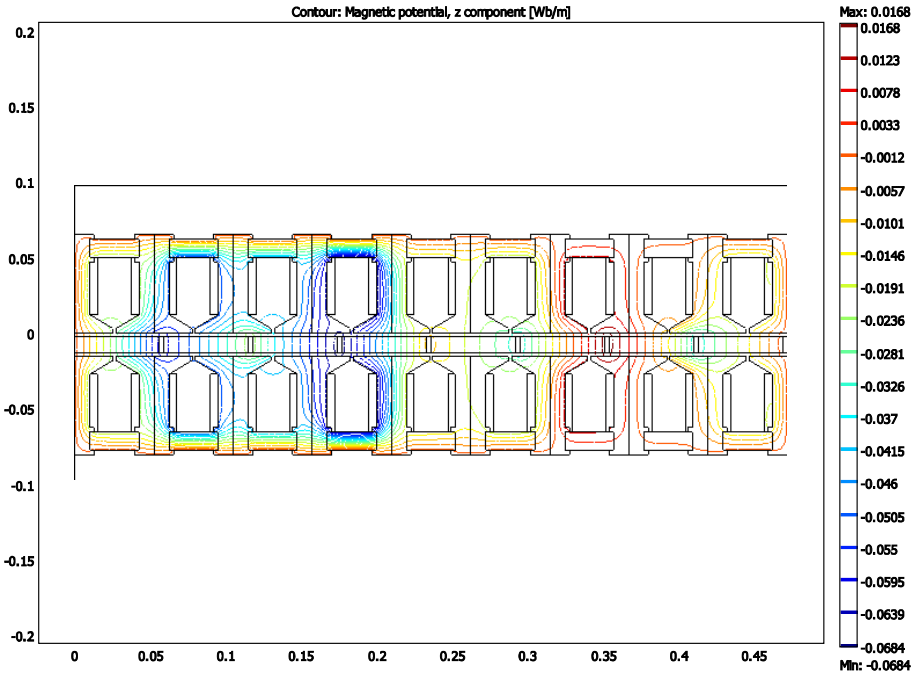

Figure 5.5: Circumferential slicing planes and the 2D FEA Equivalent parametric model at radius $R = Do/2$.

The B_{emf} and the torque the machine can be obtained as sum of the 2D values corresponding to each equivalent slice:

$$B_g = \frac{\sum_i^N B_{gi}}{N} \tag{5.21}$$

The no-load phase voltage produced by the magnets only is first evaluated from the air-gap flux density distribution for each computation plane as:

$$E_i(t) = -N_{ph1}\frac{\Delta\phi}{\Delta t} \tag{5.22}$$

The no-load phase voltage for the whole machine is then computed as:

$$E_i(t) = \sum_i^N E_i(t) \tag{5.23}$$

The torque of the machine results as:

$$T = \sum_i^N T_i(\theta) \tag{5.24}$$

The following parameters were considered for performance improvement of prototype all of them being mechanical parameters : L_s back iron length, h_{pm}, permanent magnet height , g airgap, external diameter D_o. These parameters are present in the power density model will be varied in order to evaluate the sensitivity of the model parameters. The influence of each parameters is evaluated by means of an equivalent parametric 2D model which can be solved by 2D FEM. In this case the FEM model is used as a reference (instead of experimental data) .

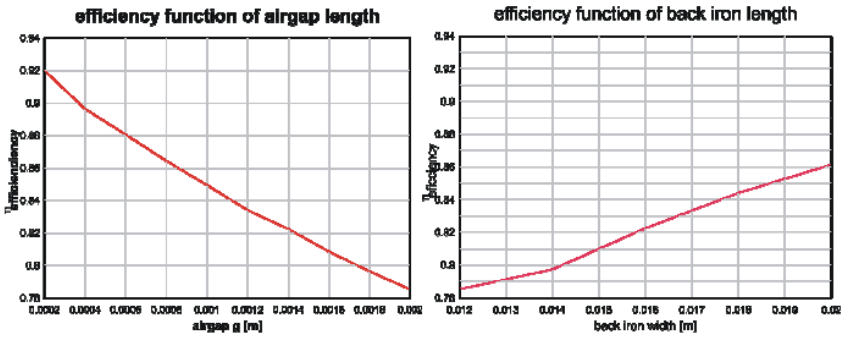

Figure 5.6: Response of the 2D equivalent FEM parameters model to a change in the airgap length and backiron width.

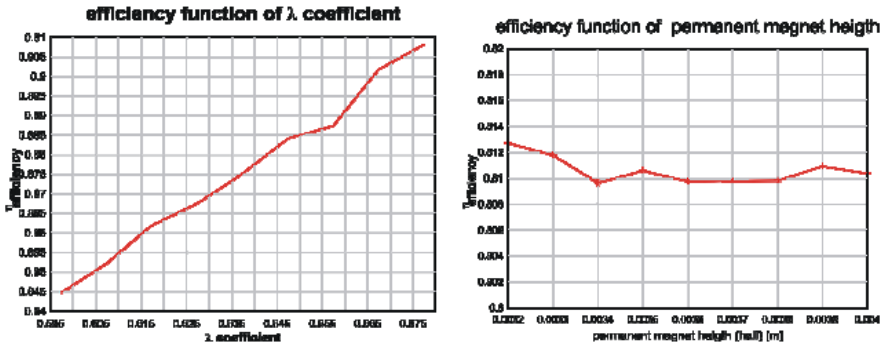

Figure 5.7: Response of the 2D equivalent FEM parameters model to a change in λ and permanent magnet heigth.

Evaluation of efficiency to airgap length presents the largest variation as it can be noticed. But evolution is evident from the fact that the torque is proportional with the airgap dimension. The variation of the efficiency in case of lambda coefficient λ and back iron length is due to the fact that the machine is sensibly saturated.

5.2.4 Reduction of Cogging Torque for a 18/16 fractional winding axial flux PMSM

In general, cogging torque is a source of vibration and noise in permanent magnet (PM) machines. It is proportional to the PM flux and the reluctance variation, and it is independent of the load current. The reduction of the torque ripple has been important concern in the design of AFPM motor. The torque ripple contains both cogging torque and commutation torque components. Cogging torque occurs from the slotting on the stator or rotor of the motor, and causes the primary ripple component in the torque. There are various techniques for reducing the cogging torque in permanent magnet (PM) machines such as shoe of stator teeth, fractional pitch, change of PM magnetization shape and skewing [5-6]. However, there is a trade off relationship between the cogging torque and average torque [6]. Accordingly, it is difficult to satisfy the objectives simultaneously.

The slot shape and the slot skewing factors are important parameters matters which have an effect on the cogging torque and the average torque characteristics. Therefore, it must be considered in design step of AFPM motor. In order to investigate the various design schemas of AFPM, 3-D finite element analysis of magnetic fields with the aid of commercial package. The effects of slot shapes and the slot skewing on the cogging torque have been investigated in detail.

The $7.5kW$ two stator one rotor axial flux permanent magnet machine was designed for use in multistage application for industrial fan in KERI South Korea . Fig. 5.2 The axial building of the machine can facilitate the direct drive construction of the assembly reducing the manufacturing costs and higher drive efficiency [3]. The performance of the existing prototype and the prototype parameters are presented in table 5.3. It can be noticed that the prototype presents a limited efficiency. For this particular reason it was mandatory to reinvestigate the possibilities to improve the performance of the machine.

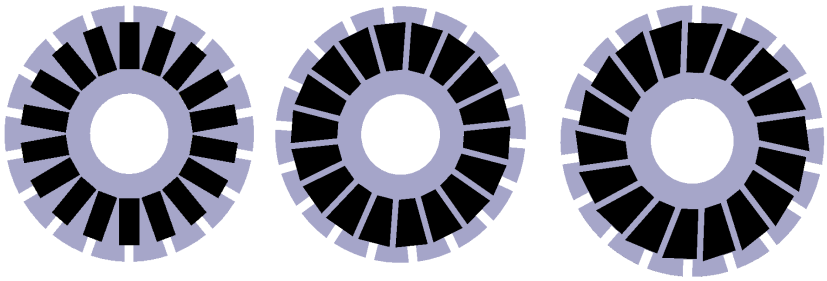

Figure 5.8: (a) rectangular (case 1) (b) trapezoidal (case 2) (c) asymmetric (case 3,4,5) Stator teeth arrangement for cogging torque reduction.

Fig. 5.8 shows the stator teeth arrangement for the cogging torque reduction in AFPM motor. The teeth shapes are classified as rectangular (case 1), trapezoidal (case 2) and asymmetric skwed with 5 (case 3), 10 (case 4), 15 (case 5) [deg], respectively.

Table 5.3: 18/16 AFPM Parameters data

Parameter	Value	Unit
Power	7.5	kW
Nominal speed	1800	rpm
Voltage	380	V
Nominal current	20	A
Phase resistance	3.4	Ω
Ld inductance	12	mH
Lq inductance	13.5	mH
Nr of slots	18	
Nr of poles	16	
External diameter	305	m
Internal diameter	208	mm
PM material	NeFeBr 40	-
PM height	12	mm
PM width	–	–
Max Efficiency	0.75	
Power factor	0.78	-

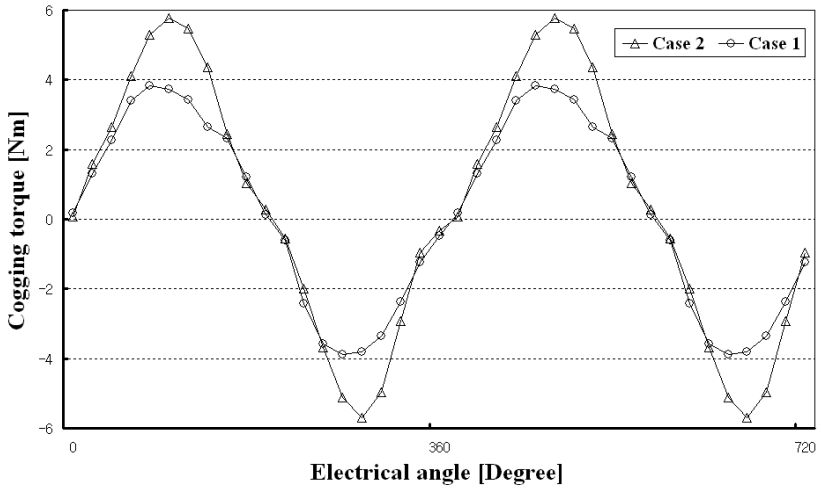

Figure 5.9: Comparisons of cogging torque between rectangular and trapezoidal teeth.

Fig. 5.9 shows the comparions of cogging toruqe between rectangular and trapezoidal teeth. Comparing to the rectangular shape, the peak value of cogging torque in trapezoidal shape is decreased to 35.3%.

Fig. 5.10 shows the comparison of cogging torque according to the stator skewing angle. From the result, we can know that the increment of the skew

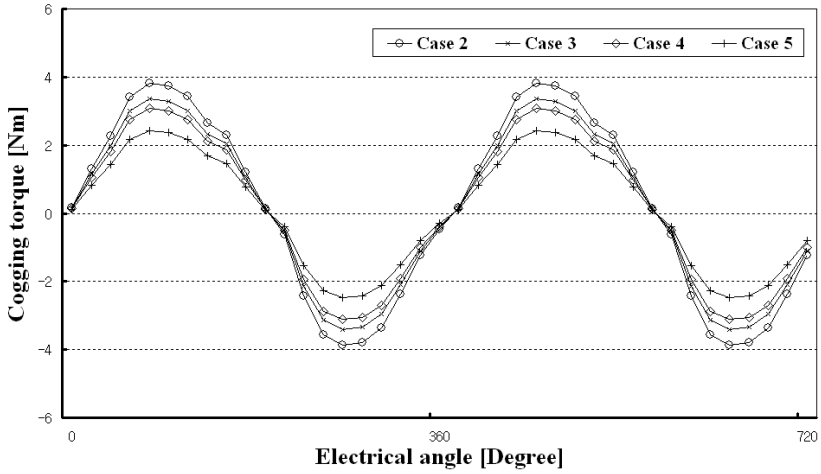

Figure 5.10: Comparisons of cogging torque according to the variation of the skew angle.

angle decreases the cogging torque. Compare to the no skewing (case 2), the cogging torque from the case 3 to case 5 are decreased to 12%, 19.5% and 35% respectively.

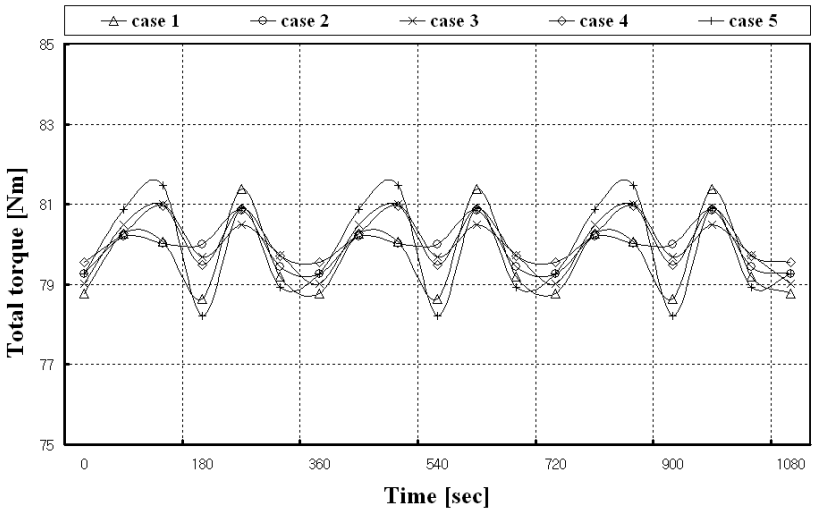

Figure 5.11: Comparison of average torque characteristics according to the change of the teeth shape.

Fig. 5.10 shows the comparison of torque characteristics according to the change of the teeth shape. Table II shows the average torque and torque ripple characteristics according to the teeth shape variation. From the cogging torque reduction point of view, we can select case 5 for the best solution.

However, in order to consider the average torque and the torque ripple totally, case 4 is better than case 5. (table 5.4)

Table 5.4: Average torque and torque ripple according to the teeth shape variation

	Average Torque (Nm)	**Torque ripple (%)**
Case 1	79.66	3.45
Case 2	79.9	1.95
Case 3	80.01	2.49
Case 4	80.11	1.86
Case 5	79.91	4.05

The influence of several parameters was investigated and the correlation between the predicted results from FEA and analytical model evaluated. From the SA results it was noticed that the most important parameters that mostly contribute to the output variability of the efficiency is the back iron length, respectively the airgap g and permanent magnet height h_pm.

5.3 The 48 slots /40 poles fractional nonoverlapping winding Axial flux Permanent Magnet Synchronous machine (AFPM)

In this section we present an application of fractional tooth wound machine wich has been designed to be integrated in the wheels of a light Electric Vehicle. Its nominal power is $2kW$. In order to achieve a base speed of 90 rad/s with a frequency no higher than $300Hz$, the number of poles has been chosen equal to 40, while the number of slots is 48. This makes a number of slots per pole and per phase equal to $q = 2/5$ and there are eight repetitions of a six-slots five-poles elementary structure. This ensures a large zone factor ($K_q = 0.966$), a back emf sinusoidally shaped and short windings overhang.

The basic idea here was to obtain an axial flux PM machine designed for low-speed generator applications. In order to perform this, the number of poles and slots was selected to be 40 poles respectively 48 slots. In [2-4] it was proven that the higher is the number of poles the better are the performance of the axial flux topology with respect to the traditional counterpart. Many authors agree that the higher the number of poles, the larger the power-density is in axial-flux machines. In order to keep dimensions below a reasonable limit, the winding topology was selected to be fractionary with the number of slots/pole/phase less than 0.50. This conducted to a particular topology of a non-overlapping winding Fig. 5.12.

The structure is of the single stator-double rotor type. The basic building block of such windings is represented by an elementary machine structure

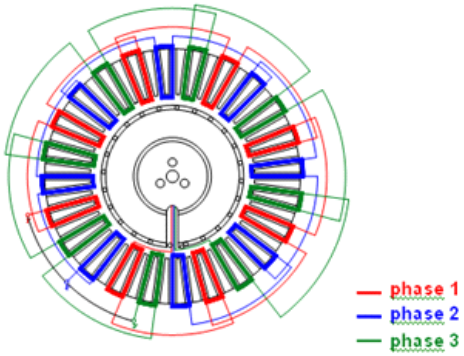

Figure 5.12: Winding configuration.

having a number of slots and poles equal to their respective numbers divided by their GCD [20].

Furthermore, the cogging torque makes 256 periods per revolution and is quite ineffective, even with open slots. Other design specifications are summarized in Table 5.5.

Table 5.5: Design Specifications

Parameter	Value	Unit
Rated Power	2000	W
Rated Torque	31.5	Nm
Base Speed	88.8	rad/s
External diameter	0.274	m
Internal Diameter	0.172	m

Fig. 5.14 shows the rotor structure.

The value of the flux-density has been evaluated by finite elements, both in $2D$ by cutting the machine with cylindrical surfaces with different radiuses (this technique is often referenced as quasi-3D mode [21][22]) and has been validated in $3D$ mode.

The waveform of the flux-density is a distinctive feature, as the semi period of the first harmonic is five times the pole pitch. It is illustrated in Fig. 5.16 at mean radius.

Table 5.6 gives the amplitudes of the flux-density harmonics. The mean amplitude of the first harmonic of the no-load flux- density distribution was found to be $B_M = 0.55T$. The voltage per each conductor was found:

$$E_1 = 2.22 \times K_{q1} \times K_r \times f \times \Phi_1 = 0.2V \tag{5.25}$$

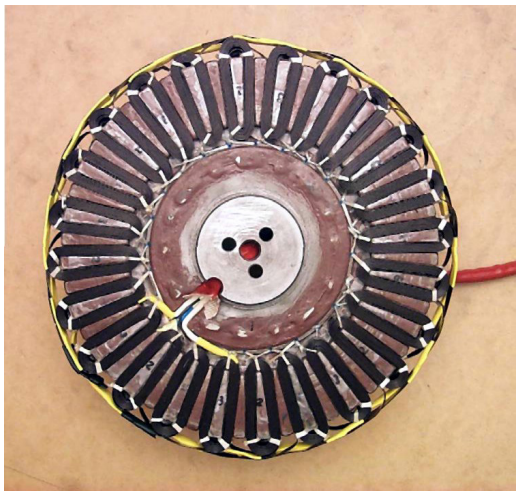

Figure 5.13: The stator realised before assembly.

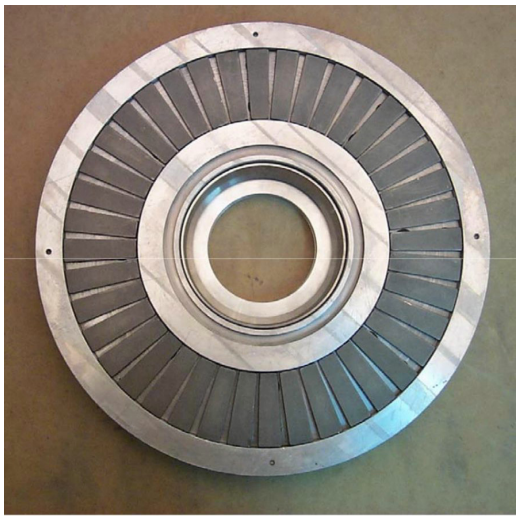

Figure 5.14: The 40 poles rotor structure before assembly.

5.3.1 Characterization of 48/40 Nonoverlaping Axial flux Prototype

First we will present the experimental investigations concerning the axial flux permanent magnet machine prototype build in collaboration with Cassino University Italy

In order to determine the generator parameters two kind of tests were performed:

1. standstill tests for parameter identification

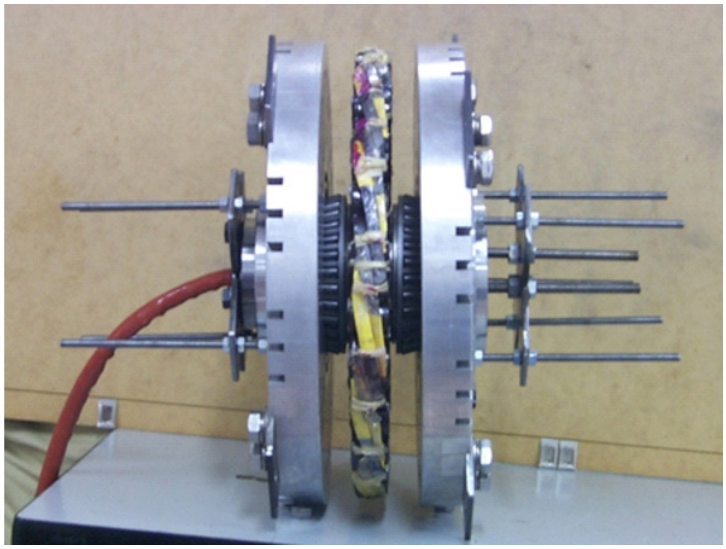

Figure 5.15: Stator view and prototype before assembly.

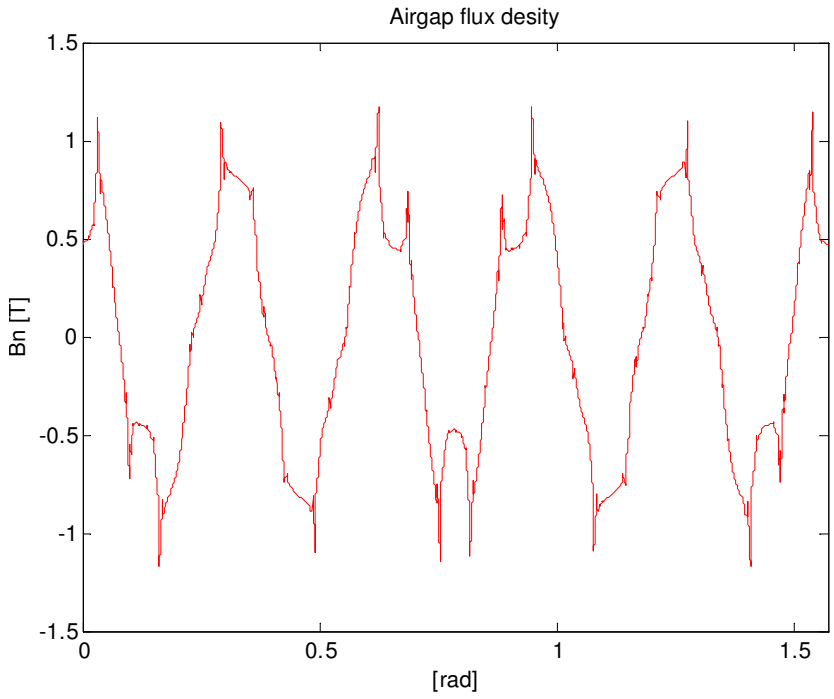

Figure 5.16: Waveform of the flux density at mean radius.

2. load tests.

It is known that axial flux PM machines have a low inductance value. Accu-

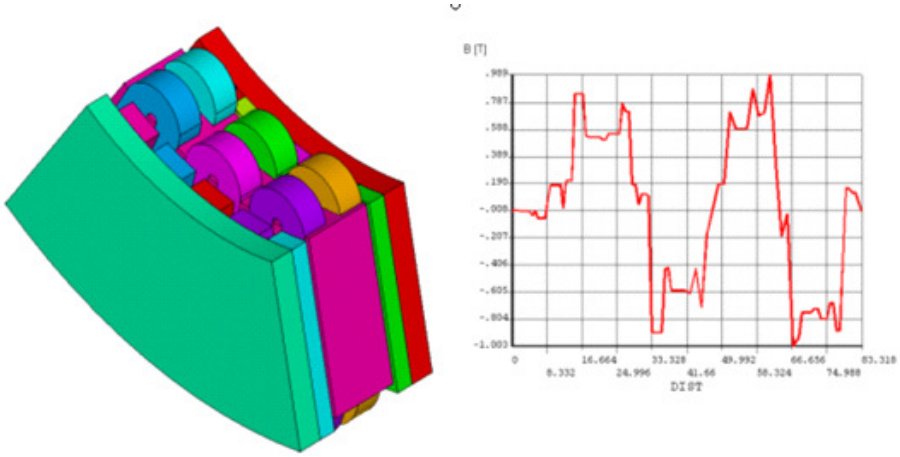

Figure 5.17: The 3D model used and the airgap flux from 3D model.

rate measurements of the inducatnce are not practically possible using standart multimeter tests. Another difficulty is the fact that in this case the generator has a large number of poles which makes the positioning procedure extremely sensitive to errors. Using an encoder is not safe enough to provide the exact position (the encoder precision for this number of poles is less 255 lines/degree). It was observed that, because of the very low inductance value, the positioning with standard alignment of the rotor in the d axis was very imprecise. Since the axial flux PM machine has surface mounted permanent magnets first we have performed an alignment of the machine according to phase A axis. The alignment was possible with a step pulse of phase A.

5.3.2 Phase resistance measurements

The resistance was measured after operation in order to take into account the steady-state value of the temperature. The value was found to be $R = 0.096\Omega$

$$\begin{aligned} V_d &= Ri_d + \frac{d\psi_d}{dt} \\ L_d &= \frac{\psi_d - \psi_{PM}}{i_d} \end{aligned} \tag{5.26}$$

5.3.3 Stand still tests

A standard procedure to evaluate the parameters of permanent magnet machines at stand still is shown in Fig.5.20. Firstly, one has to correctly align the translator onto d axis. Small errors can result in significant variations of the impedance of the machine. The three phases must be connected in Y and only

Table 5.6: Amplitudes of the space harmonics of the harmonics at mean radius

Harmonic no.	Amplitude
1	0.0017
2	0
3	0.0026
4	0
5	05506
6	0
7	00728
8	0
9	0.0023
10	0
11	00005
2	0
13	00003
14	0

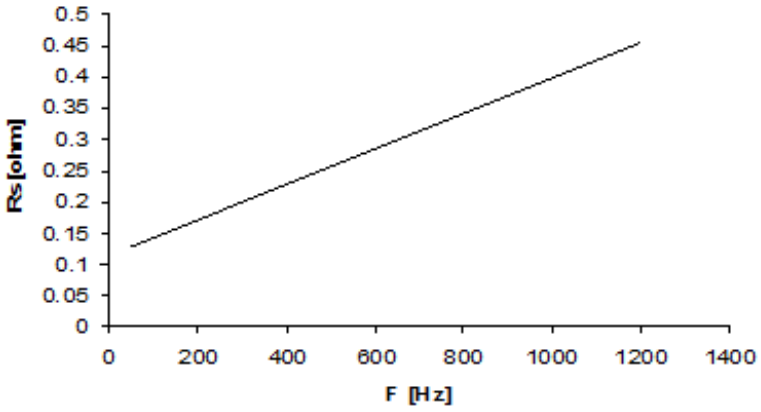

Figure 5.18: Phase resistance variation with frequency

phase a has to be fed with a sinusoidal current. The rotor has to be moved until the voltage between phases b and c is null.

$$L_d = \frac{E_0 - V_s \cos(\delta) - R_s I_s \cos(\delta + \varphi)}{2\pi f I_s \sin(\delta + \phi)} \tag{5.27}$$

$$L_q = \frac{V_s \sin(\delta) + R_s I_s \sin(\delta + \varphi)}{2\pi f \cdot I_s \sin(\delta + \phi)} \tag{5.28}$$

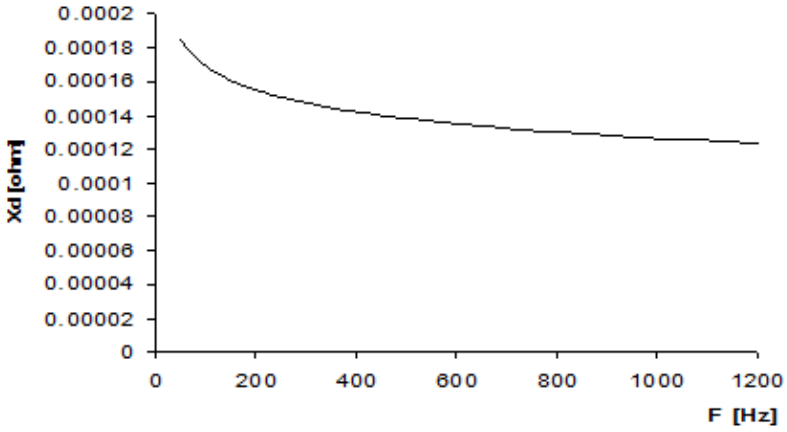

Figure 5.19: Reactance variation with frequency

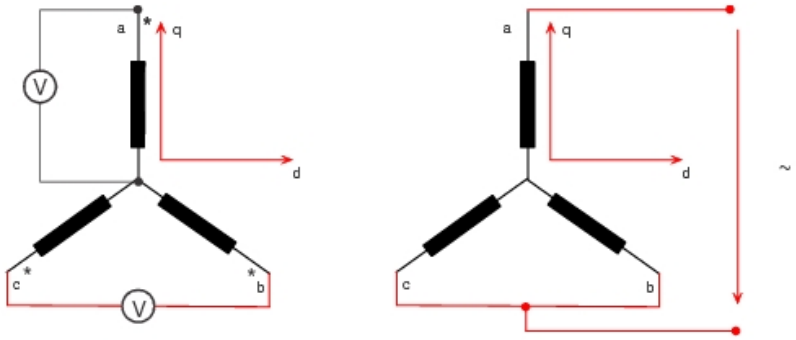

Figure 5.20: Alignment for inductance measurement for axial flux nonoverlapping PMSM

5.3.4 No load tests

In no load mode the back emf of the generator was recorded at various speeds. From these tests the permanent magnet fundamental flux was found:

$$\psi_{PM} = \frac{V_0\sqrt{2}}{2\pi p_1 n} = 0.077 Wb \tag{5.29}$$

There is a difference of almost 12% in PM flux obtained from the measured EMF and the measured torque, which maybe traceable back to measurements errors.

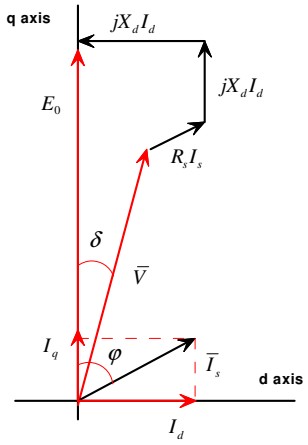

Figure 5.21: Vector diagram for axial flux nonoverlapping PMSM

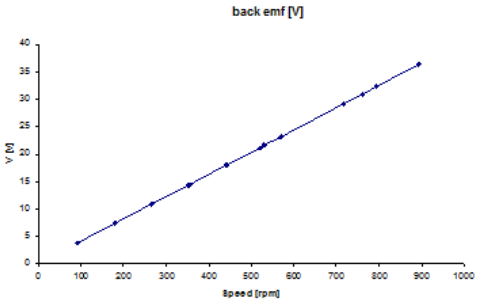

Figure 5.22: No load back EMF

5.4 Control aspects of thefractional nonoverlapping winding 48/40 AFPM Machine

The AFPMM can be controlled by means of the well- known field Oriented Controller (FOC). Due to machine design, the field-weakening operation results unpractical then it is not dealt with in the chapter [35].

Consequently, the FOC just selects a current vector in quadrature with the electrical position of the magnet flux vector. Such current is imposed by means of two PI controllers acting in the rotor frame. The PI controller outputs a reference voltage in the rotor frame that is then traduced into a vector in the stator frame. This voltage vector modulates the Voltage Source Inverter (VSI) trough the Space Vector Modulation (SVM). The main issue is the determination of the electrical angle of the flux to align the current in quadrature to.

The use of a quadrature encoder is unviable in practice because it is costly, noise sensitive and difficult to arrange mechanically in such axial flux direct

drives. Consequently, the paper considers the scheme with encoder just as a tool to evidence what is the optimal performance of this drive.

The technical literature proposes many sensorless control algorithms that can be applied on non-salient AFPMMs. In this case we have considered a method based the Sliding Mode flux Observer is briefly reviewed and applied to illustrate the AFPMMs in sensorless operation mode. This sensorless control algorithm does not work at zero speed [48] because it relies only on the e.m.f estimation. For this reason, an open loop ramp is used to start the motor.

5.4.1 Sliding Mode flux Observer

The actual dynamics of the motor currents expressed in the stator frame $i_{\alpha\beta}$ can be formulated in terms of the nominal value of the parameters as :

$$\dot{i}_{\alpha\beta} = \frac{1}{L_n} u_{\alpha\beta} - \frac{R_n}{L_n} i_{\alpha\beta} - \frac{1}{L_n} i_{\alpha\beta} + \xi_{\alpha\beta} \tag{5.30}$$

where

$\xi_{\alpha\beta}$ is a lumped uncertainty expressing the effects of the parameter detuning,

R_n - is the phase resistance,

L_n - is the phase inductance, and

$e_{\alpha\beta}$ - are the magnet induced e.m.f..

Considering the following current estimator:

$$\dot{\hat{i}}_{\alpha\beta} = \frac{1}{L_n} u_{\alpha\beta} - \frac{R_n}{L_n} \hat{i}_{\alpha\beta} + K_{sl} sgn(i_{\alpha\beta} - \hat{i}_{\alpha\beta}) \tag{5.31}$$

once defined the current estimation error as:

$$\varepsilon_{\alpha\beta} = (i_{\alpha\beta} - \hat{i}_{\alpha\beta}) \tag{5.32}$$

the form of the estimator 5.33 implies the choice of $\dot{\varepsilon}_{\alpha\beta} = \varepsilon_{\alpha\beta} = 0$ as sliding hyperplane. The error dynamics are:

$$\dot{\varepsilon}_{\alpha\beta} = \xi_{\alpha\beta} - \frac{1}{L_n} e_{\alpha\beta} - K_{sl} sgn(_{\alpha\beta}) - \frac{R_n}{L_n} \varepsilon_{\alpha\beta} \tag{5.33}$$

To ensure the convergence of the sliding mode must be [24] [25]:

$$\dot{\varepsilon}_{\alpha\beta} \cdot \varepsilon_{\alpha\beta} < 0 \tag{5.34}$$

if the uncertainty is bounded, i.e. $|\xi_{\alpha\beta}| < Z$, the following condition ensures (5.34) holds:

$$K_{sl} \geq Z + \frac{1}{L_n} e_{\alpha\beta} \tag{5.35}$$

for each component of $e_{\alpha\beta}$.

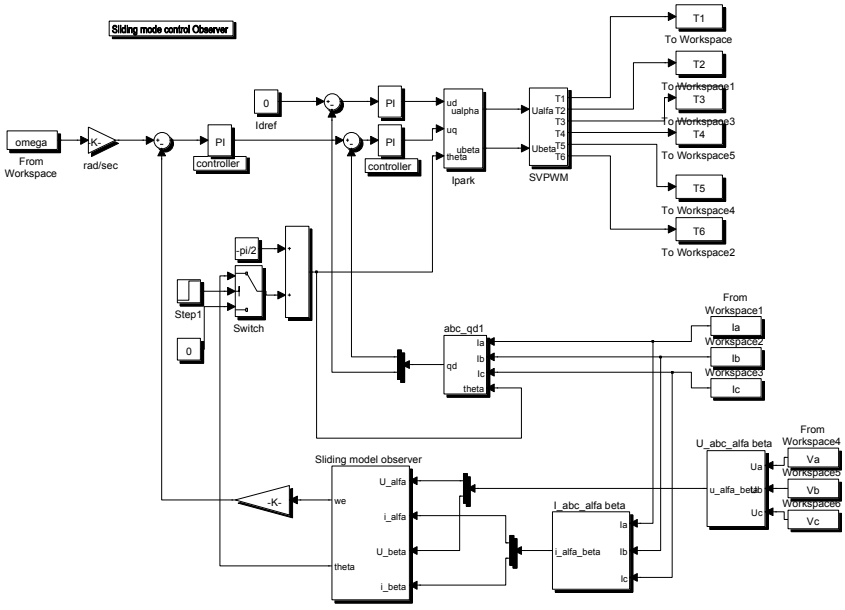

Figure 5.23: Matlab Simulink implementation of vector control with sliding mode observer.

Once the convergence is ensured, the equivalent control method $_{\alpha\beta} = _{\alpha\beta} = 0$ can be used to obtain the motion equation [24]

$$\frac{1}{L_n} e_{\alpha\beta} - \xi_{\alpha\beta} = K_{s/} sgn(i_{\alpha\beta} - \hat{i}_{\alpha\beta}) = z_{\alpha\beta} \tag{5.36}$$

Due to the high-frequency of the signal $z_{\alpha\beta}$, the information $e_{\alpha\beta}$ can be extracted by means of a low pass filter. Considering $e_{\alpha\beta}$ of the sinusoidal form and being θ the angular position of the magnet flux space vector in the stator frame, $e_{\alpha\beta}$ have the form:

$$[e_{\alpha\beta}] = e_M \begin{bmatrix} \cos\theta \\ \sin\theta \end{bmatrix} \tag{5.37}$$

the commutation signals $\sin\theta$, $\cos\theta$ can be obtained as:

$$e_M = \sqrt{e_\alpha + e_\beta} \tag{5.38}$$

5.4.2 Experimental results about the controlled machine

To validate the machine with control the starting process was considered. The machine was started with an inertial load in both encoder and sensorless

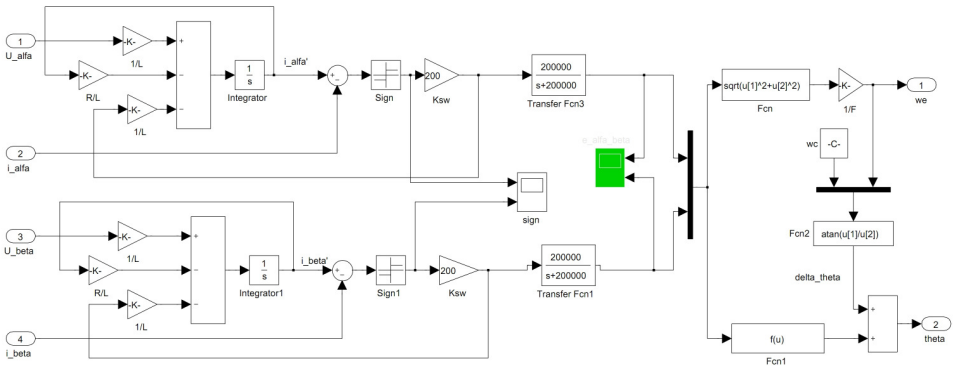

Figure 5.24: Matlab Simulink implementation of sliding mode observer.

configurations.

The test setup consists with PMSG connected to the open architecture inverter the control algorithm beeing implemented by dSpace platform , the AFPM load consists in a PMSM prime mover with SIMOVERT MASTERDRIVE.

The load was actively produced by a PMSM drive in order to emulate various conditions of load, friction and inertia. The presented data relate to an high inertia, no friction condition. Table 5.7 shows the test conditions.

Table 5.7: Test conditions for AFPM 48/40

Parameter	Value Measure Unit
DC-link Voltage	80 V
Emulated Inertia	3 Kgm^2
Switching Frequency	50 kHz
Sampling Frequency	20 kHz
Data Downsampling	5

Figures 5.25 to 5.29 illustrate the encoder operation. The speed trend is reported in Fig. 5.25 while the actual torque is in Fig. 5.26.

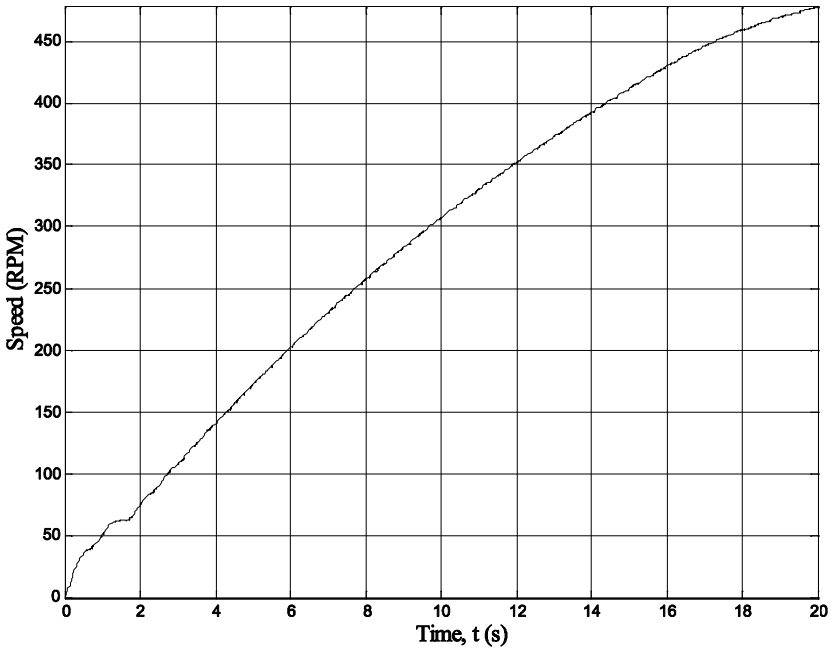

Figure 5.25: Speed in encoder operation

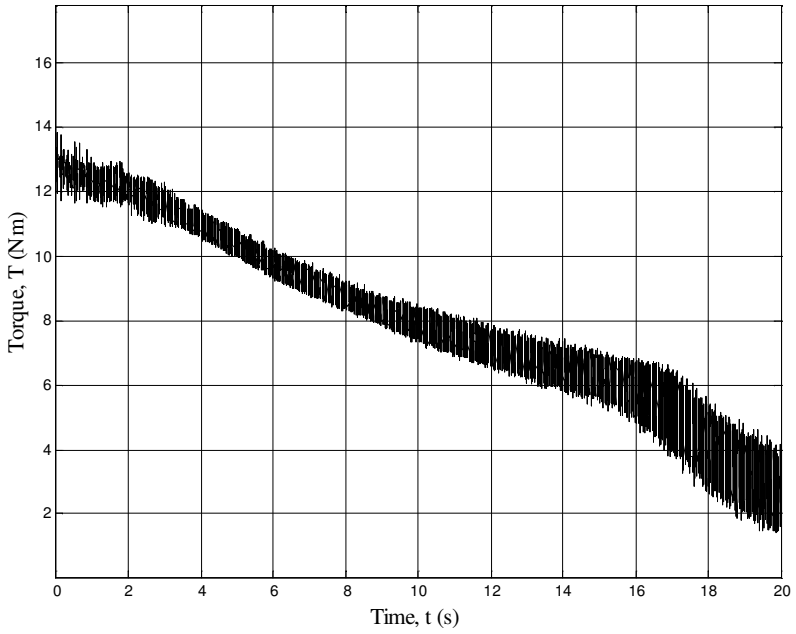

Figure 5.26: Torque in encoder operation

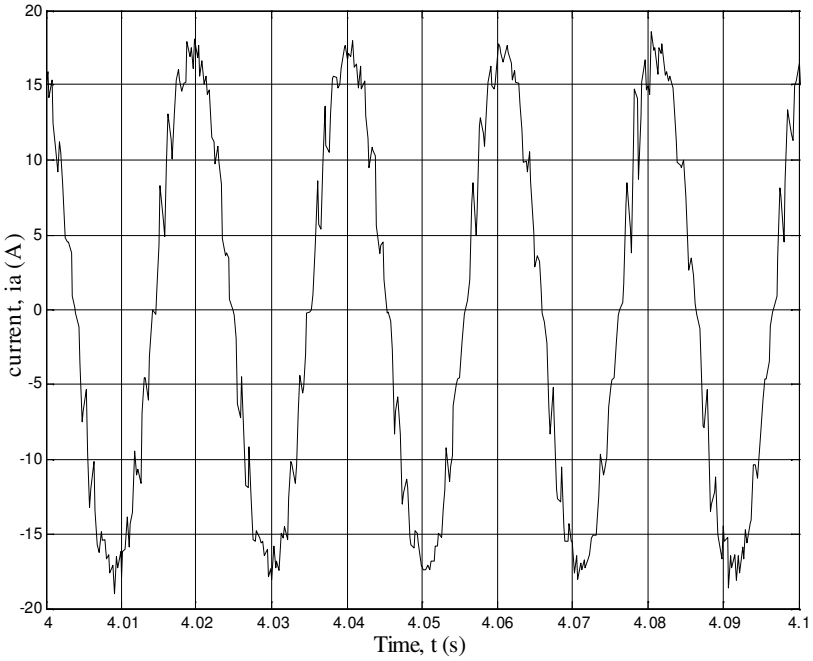

Figure 5.27: Phase current in encoder operation

Figures 5.30-5.34 illustrate the sensorless operation with open loop starting. The speed trend is reported in Fig. 5.30 while the actual torque is in Fig. 5.31.

The instant of the transition between the open loop and the sensorless operation is clearly visible. Figures 5.32-5.34 show three details of the first phase current trend.

Three details of the trend of one of the commutation signal $\cos(\theta)$ are reported in Figs. 5.35 - 5.37 where the estimated signal is compared to the actual one.

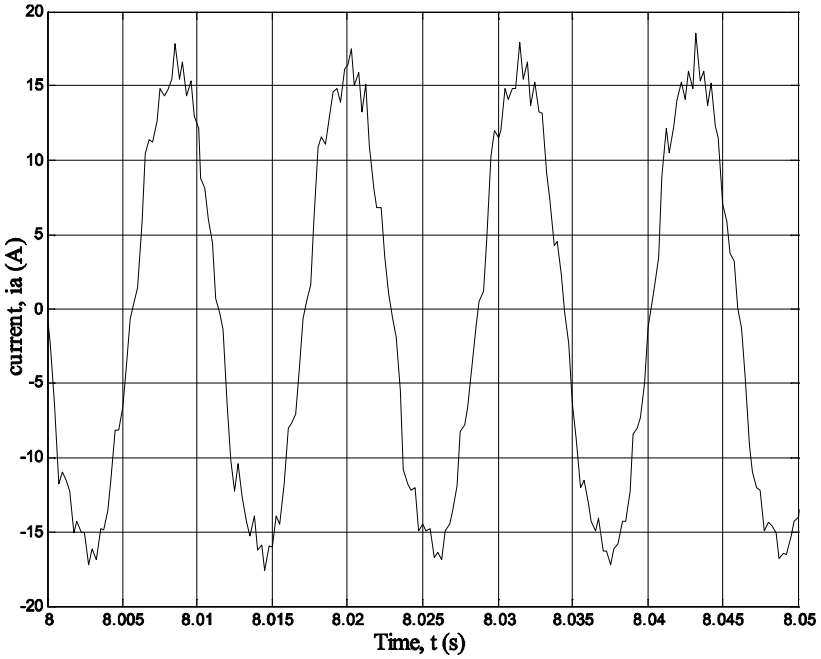

Figure 5.28: Phase current in encoder operation time=T1

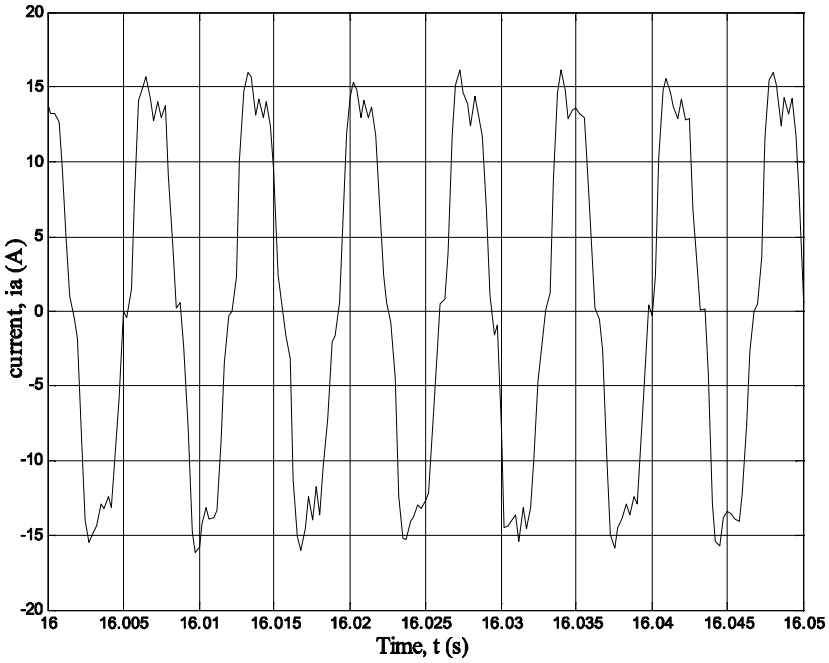

Figure 5.29: Phase current in encoder operation T2

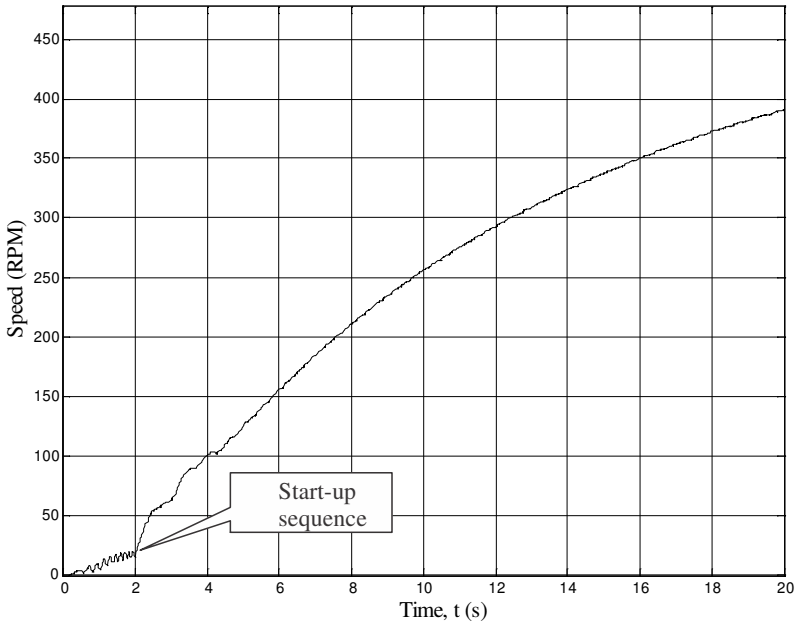

Figure 5.30: Actual speed sensorless operation

5.5 Conclusion

In this chapter we have presented an two applications of specially designed Axial flux PM synchronous motor for fan and for a direct drive of a light electric vehicle.

The main features of this special machines is represented by its winding, of the fractionary slot type. The winding is therefore a concentrated non overlapping one allowing a large number of poles to be achieved in a small diameter. Its end winding connections are short in comparison with traditional windings.

The induced e.m.f. waveform is not distorted, due to the equivalence to a machine with two slots per pole and per phase [15].

Also the chapter presents the performance of the sliding mode flux observer implemented for vector control technique adopted for controlling the motor showing resonable good low speed performance for large number of poles machine.

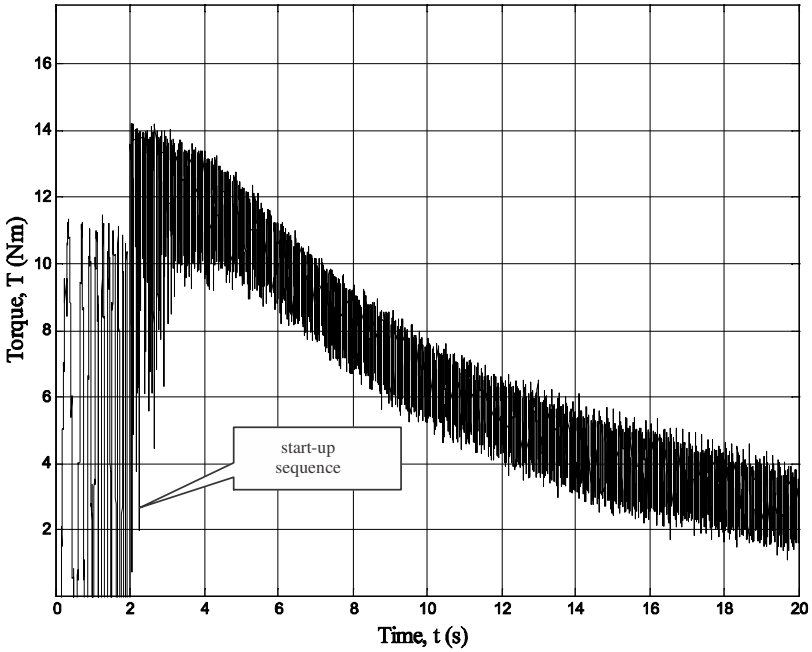

Figure 5.31: Actual torque sensorless operation

Bibliography

[1] P. Campbell, "Principles of a permanent magnet axial-field DC (sensorless operation) machine" Proc. IEE, Dec. 1974 n.121, pp. 1489-1494

[2] P. Campbell, "The magnetic circuit of an axial field DC electrical machine" IEEE Tans.on Mag, vol.11 issue 5 Sept. 1975 pp. 1541-1543

[3] W. Leung, "Sandwich synchronous machines and DC machines" patent specification, London, April 1978 694

[4] EcoSystemO, Kone Corporation www.kone.com

[5] F. Caricchi, F. Crescimbini, O. Honorati, "Modular, axial-flux, permanent-magnet motor for ship propulsion drives" IEEE Trans. on Energy Conv. Vol.14 issue 3, Sept. 1999 pp.673-679

[6] F. Caricchi, F. Crescimbini, E. Santini "Basic principle and design criteria of axial-flux PM machines having counterrotating rotors" IEEE Trans. on Ind. Appl. Vol.31 issue 5, Sept. Oct. 1995 pp. 1062-1068

[7] F. Profumo, Z. Zhang, A. Tenconi, "Axial flux machines drives a new viable solution for electric cars" IEEE Trans on Indl. Electronics vol.44 issue 1, Feb.1997 pp.39-45

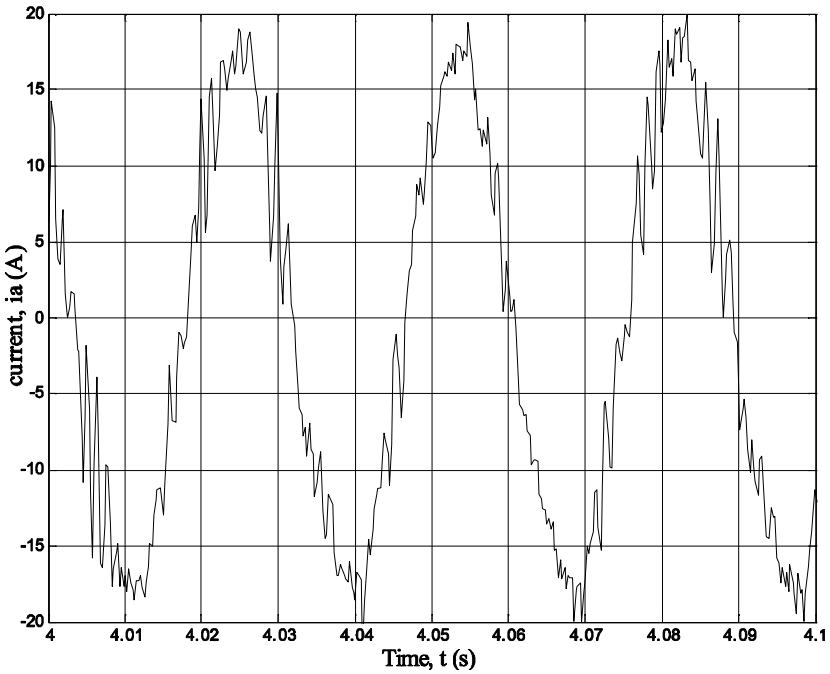

Figure 5.32: Phase current sensorless operation

[8] F. Caricchi, F. Crescimbini, E. Fedeli, G. Noia "Design and construction of a wheel-directly-coupled axial-flux PM motor prototype for EVs" Proc. IEEE Industry Applications Society Annual Meeting, 1994

[9] J.F. Eastham, F Profumo, A.Tenconi, R.J. Hill-Cottmgham, P.C. Coles, G. Gianolio "Axial flux machine for aircraft drive: design and modelling" IEEE Trans. on Mag. Vol.38 issue 5 Sept 2002 pp.3003- 3005

[10] R.J. Hill-Cottmgham, P. C. Coles, J.F. Eastham, F Profumo, A.Tenconi, G. Gianolio "Multi-disc axial flux stratospheric aircraft propeller drive" 36th Proc. IEEE Industry Applications Society Annual Meeting, October 2001

[11] N Brown, J.R. Bumby, L Haydock "A toroidal, axial flux generator for hybrid IC engine/battery electric vehicle applications", SAE 2002, O2P- 308.

[12] The Turbo Genset Company Ltd. Unit 3, Heathrow Summit Centre, Sky-port Drive, Hatch Lane, West Drayton, Middlesex UB7 OL

[13] F Marignetti, M.Scarano "An Axial-flux PM Motor Wheel" Proc. ELECTRO-MOTION'99 July 1999 Patras

[14] Jerome Cros and Philippe Viarouge, " Synthesis of High Performance PM Motors With Concentrated Windings ", IEEE Transactions On Energy Conversion, vol. 17, NO. 2, June 2002

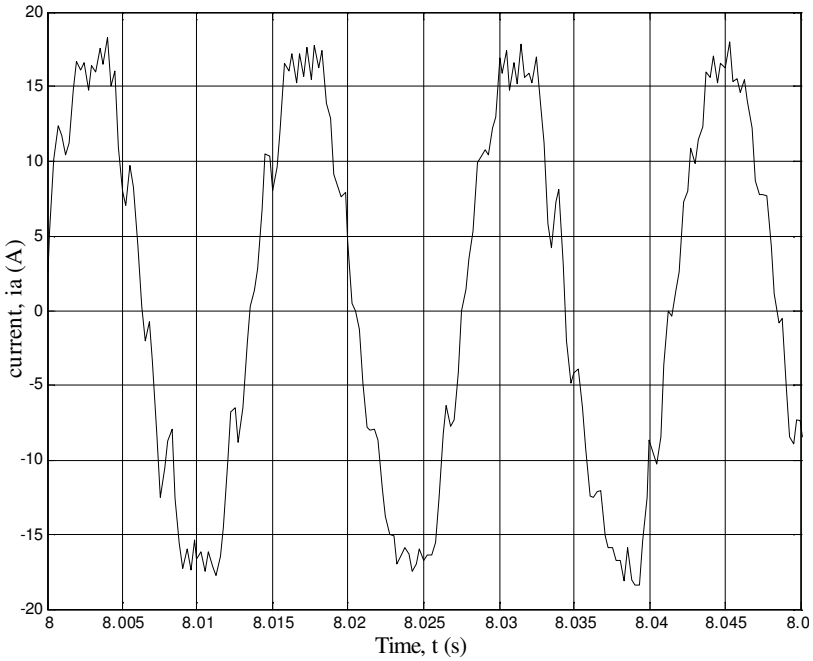

Figure 5.33: Phase current sensorless operation

[15] Azzouzi, J.; Barakat, G.; Dakyo, B. "Quasi-3D analytical modeling of the magnetic field of an axial flux permanent magnet synchronous machine" Electric Machines and Drives Conference, 2003. IEMDC'03. 1-4 June 2003 Pages: 1941- 1947 vol.3

[16] A. Parviainen, M. Niemela, J. Pyrhonen, "Modelmg of Axial flux Permanent-Magnet Machmes" IEEE Trans. on Ind. Appl. Vol. 40 issue 5 Sept.-Oct.2004

[17] F Marignetti, J.R.Bumby, "Electromagnetic modelling of Permanent Magnet Axial flux Motors and Generators" 16th International Conference on Electrical Machmes. 5-8 September Cracow (Poland). vol. 1, pp. 588-594.

[18] V. Utkin, J. Guldner, J. Shi, Sliding Mode Control Electromechanical Systems. London, UK: Taylor& Francis, 1999, Chapters 3 and 8.

[19] I. Boldea, C. A. Nasar "Electric Drives" (Book) CRC Press, 1999 section 7.7 pp. 135-142 695

[20] Saltelli A. Tarantola S., Campolongo, F. and Ratto, M., 2004,"Sensitivity Analysis in Practice. A Guide to Assessing Scientific Models", John Wiley & Sons publishers

[21] http://en.wikipedia.org/wiki/Sensitivity_analysis;

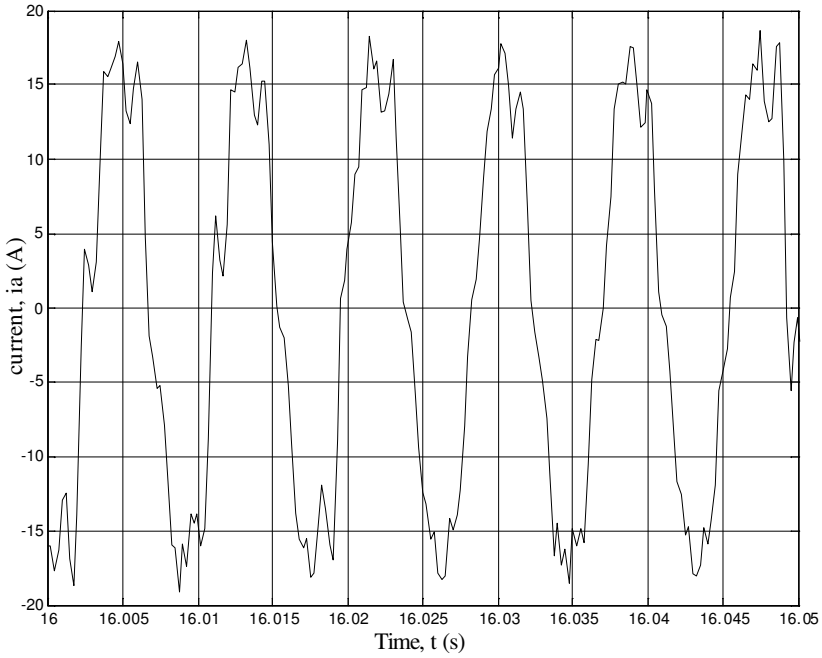

Figure 5.34: Phase current sensorless operation

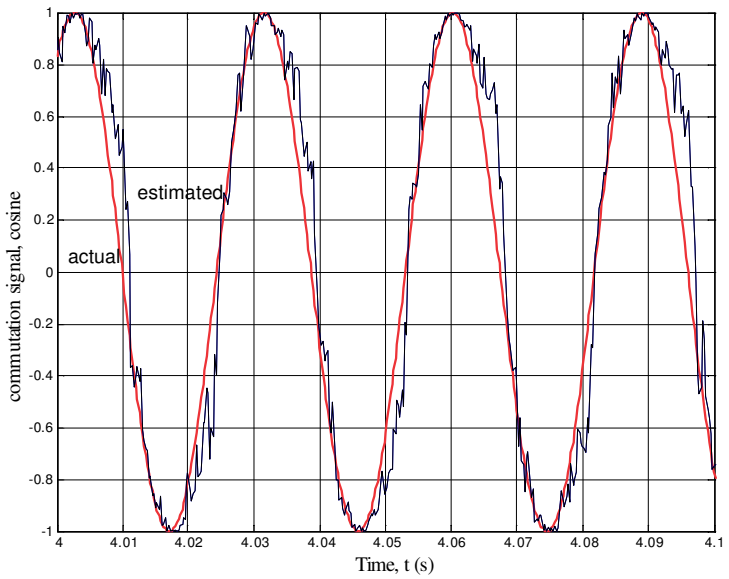

Figure 5.35: Actual and estimated (solid, wider line) commutation signal $\cos(\theta)$ (sensorless operation).

[22] Surong Huang; Jian Luo; Leonardi, F.; Lipo, T.A. ”A comparison of power

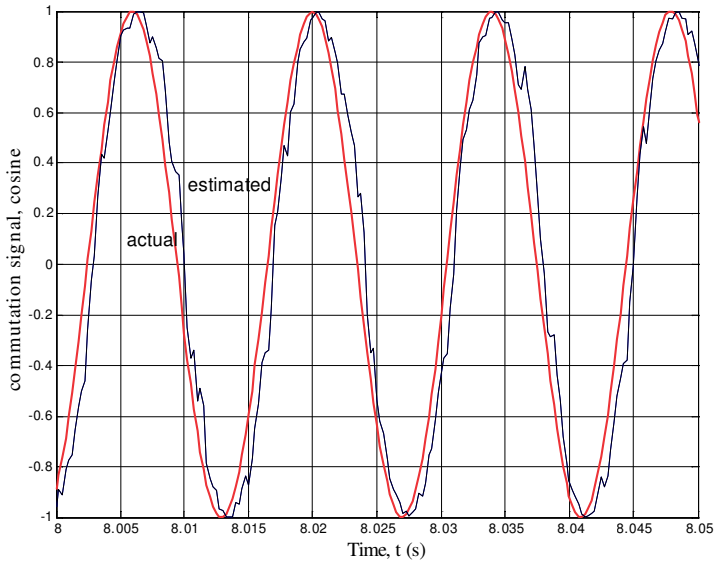

Figure 5.36: Actual and estimated (solid, wider line) commutation signal $\cos(\theta)$ (sensorless operation)

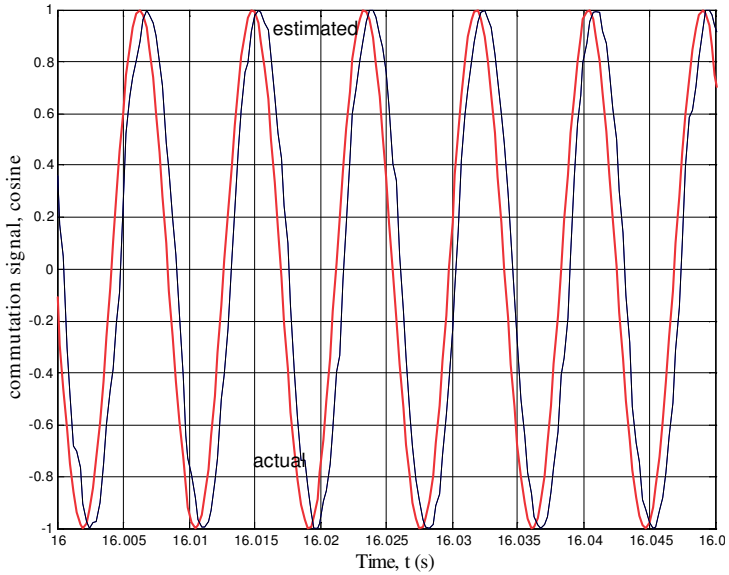

Figure 5.37: Actual and estimated (solid, wider line) commutation signal $\cos(\theta)$ (sensorless operation).

density for axial flux machines based on general purpose sizing equations" IEEE Transactions on Energy Conversion, Volume 14, Issue 2, June 1999 pp. 185 - 192;

[23] Parviainen, A.; Niemela, M.; Pyrhonen, J. ”Modeling of axial flux permanent-magnet machines” IEEE Transactions on Industry Applications, Volume 40, Issue 5, Sept.-Oct. 2004 Page(s):1333 - 1340;

[24] Yee-Pien Yang; Yih-Ping Luh; Cheng-Huei Cheung ”Design and control of axial-flux brushless DC wheel motors for electric Vehicles-part I: multiobjective optimal design and analysis” IEEE Transactions on Magnetics, Volume 40, Issue 4, Part 1, July 2004 Page(s):1873 - 1882;

[25] M. Aydin, S. Husang, and T. A. Lipo, Optimum design and 3D finite element analysis of non-slotted and slotted internal rotor type axial flux PM disc machines, Power Engineering Society Summer Meeting, pp. 1409-1416, 2001.

[26] F. Caricchi, F. Crescimbini, O. Honorati, and E. Santini, Performance evaluation of an axial flux PM generator, Proceedings of International Conference on Electrical Machines (ICEM), pp. 761-765, 1992.

[27] R. J. Hill-Cottingham, P. C. Coles, J. F. Eastham, F. Profumo, A. Tenconi, G. Gianolio, Multi-disc axial flux stratospheric propeller drive, Proc. of IEEE IAS Annual Meeting Confrence Record 2001, vol. 3, pp. 1634-1639, 2001.

[28] F. Caricchi, F. Crescimbini, O. Honorati, Modular, axial-flux permanent magnet motor for ship propulsion drives, IEEE Trans. on Energy Conversion, vol. 14, pp. 673-679, 1999.

[29] M. Aydin, R. Qu and T. A. Lipo, Cogging torque minimizaiton technique for multiple-rotor, axial-flux, surface-mounted-PM motors: alternating magnet pole-arcs in facing rotors, IEEE Industry Applications Society Annual Meeting, Salt Lake City, 2003.

[30] Z. Q. Zhu and D. Howe, Influence of design parameters on cogging torque in permanent magnet motors, IEEE Transactions on Energy Conversion, Vol. 15, No. 4, pp. 2000.

[31] N. Bianchi and S. Bolognani, "Design techniques for reducing the cogging torque in surface-mounted PM motors," *IEEE Trans. Ind. Appl*., vol. 38, no. 5, pp. 1259-1265, Sep. 2002.

[32] C. Studer, A. Keyhani, T. Sebastian, and S. K. Murthy, "Study of cogging torque in permanent magnet machines," in *lAS '97*. *Conf. Rec*. *1997 IEEE Ind. Applicat. Conf. Thirty-Second lAS Annu. Meeting*, New Orleans, LA, 1997, vol. 1, pp. 42-49.

[33] C. Breton, J. Bartolome, J. A. Benito, G. Tassinario, I. flotats, C. W. Lu, and B. J. Chalmers, "Influence of machine symmetry on reduction of cogging torque in permanent-magnet brushless motors," *IEEE Trans. Magn*., vol. 36, no. 5, pp. 3819-3823, Sep. 2000.

[34] C. A. Borghi, D. Casadei, A. Cristofolini, M. Fabbri, and G. Serra, "Application of a multiobjective minimization technique for reducing the torque ripple in permanent-magnet motors," *IEEE Trans. Magn*., vol. 35, no. 5, pp. 4238-4246, Sep. 1999.

[35] S. Skaar, O. K. vel, and R. Nilssen, "Distribution, coil-span and winding factors for AFPM with concentrated windings," in Proc. of Int. Conf. on Electrical Machines, (ICEM), paper no. 346, 2006.

6 A Novel, Single Stator Dual PM Rotor, Synchronous Machine: topology, circuit model and 3D FEM Analysis of Torque Production

This chapter introduces a novel brushless a new application of axial flux permanent magnet synchronous machines featuring fractional tooth concentric winding, single winding and stator, dual PM rotor axial-airgap machine capable to deliverable independently torque at the two rotors by adequate vector control. The proposed topologies, the circuit model and preliminary 3D FEM torque production on a case study constitute the core of the chapter. The proposed dual mechanical port system should capable to be embedded both in parallel(with planetary gears) or series hybrid electric vehicles(HEV) aiming at a more compact and efficient electric power system solution

Vehicles equipped with internal combustion engine (ICE) have been in existence for over a hundred years. Although ICE vehicles (ICEVs) are being improved by modern automotive electronics technology, they need a major change to significantly improve the fuel economy and reduce the emissions [1].

Electric vehicles (EVs) and hybrid EVs (HEVs) have been identified to be the most viable solutions to fundamentally solve the problems associated with ICEVs [2]–[4]. Electric drives are the core technology for EVs and HEVs.

The basic characteristics of an electric drive for EVs are the following [5]–[7]:

1) high torque density and power density;

2) very wide speed range, covering low-speed crawling and high-speed cruising;

3) high efficiency over wide torque and speed ranges;

4) wide constant-power operating capability;

5) high torque capability for electric launch and hill climbing;

6) high intermittent overload capability for overtaking;

7) high reliability and robustness for vehicular environment

8) low acoustic noise;

9) reasonable cost.

On top of the aforementioned characteristics, the electric drive for HEVs needs additional ones as follows [8]–[10]:

1) high-efficiency generation over a wide speed range;

2) good voltage regulation over wide-speed generation.

With the advent of high-energy permanent-magnet (PM) materials, PM motors are becoming more and more attractive. Being continually fueled by new machine topologies and control strategies, PMbrushless (BL) drives have been identified to be the most promising to provide the aforementioned characteristics for modern EVs and HEVs [11].

Hybrid, full electric vehicles (HEV) are considered the way of the future for automobiles [1], to reduce energy consumption and air pollution.

A key problem with HEV is the electric propulsion corroboration with the thermal engine (ICE) such that the latter is allow to operate close to the sweet point (torque and speed for maximum efficiency or minimum emission) indifferent to the vehicle speed [12]. A so called continuously variable transmission (CVT) is to be obtained.

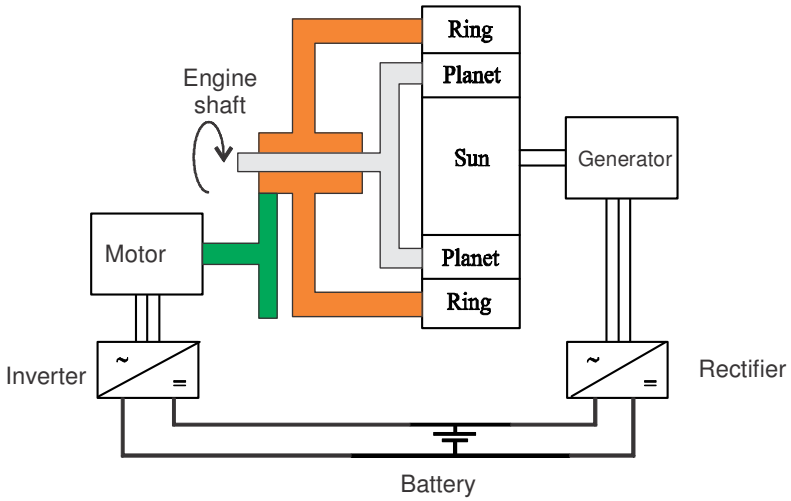

Figure 6.1: E-CVT existing systems with planetary gears (Toyota Prius) for parallel hybrid.

Figure 6.1 and 6.3 identifies two existing e-CVT solutions for parallel HEVs (one commercial and one still a proposition) with two electric machines and two inverters one with planetary gears and one without it but the latter with full power slip-ring brush transfer instead [1].

A distinct electric generator and a propulsion electric motor, both with full power converters are typical for a series HEV (Fig. 6.4).

Internal combustion engines, regardless of fuel type (gasoline, diesel, hydrogen), operate most efficiently at mid-range speeds and high torque levels.

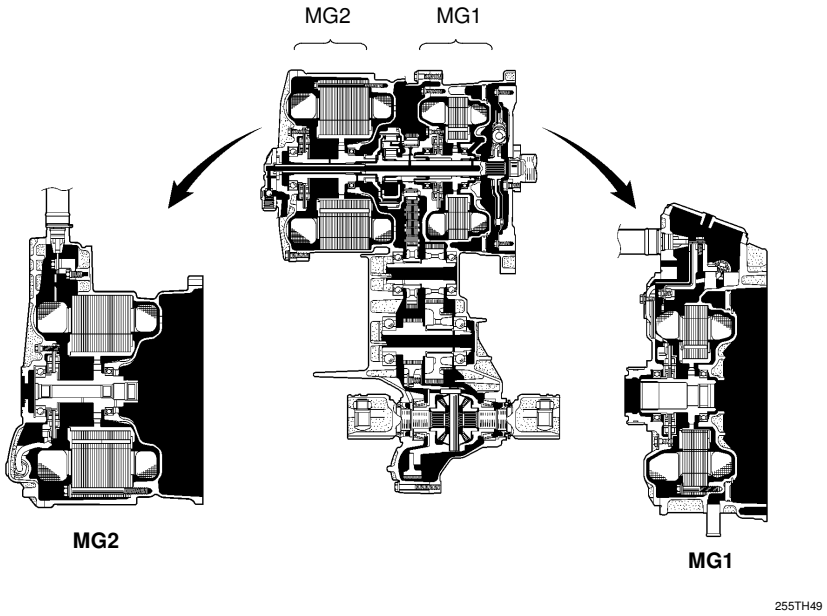

Figure 6.2: Prius 2003 hybrid MG1 (Motor Generator No. 1) and the MG2 (Motor Generator No. 2) embodiments.

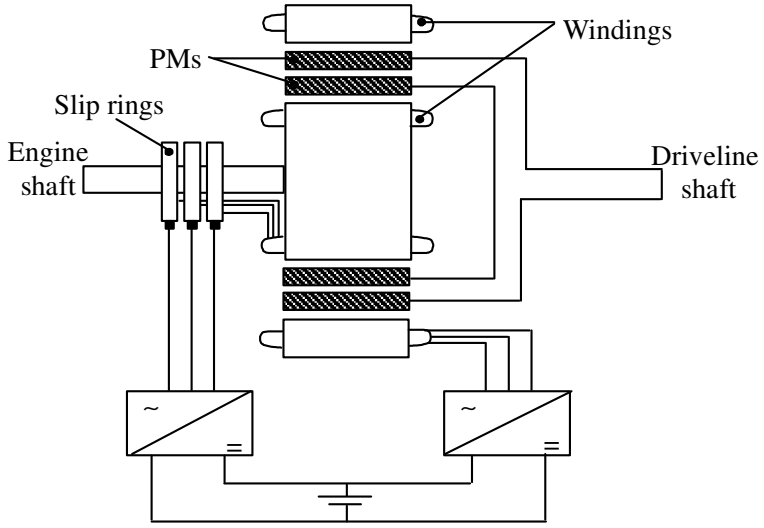

Figure 6.3: Dual radial flux machines for integral-electric (in proposition).

It is one goal of the e-CVT to match the vehicle road load to this engine optimal operating regime [12].

6.1 Constructive elements and topology

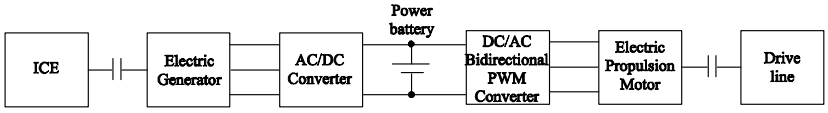

Figure 6.4: Typical series HEV dual electric machines existing system.

In an effort to simplify the planetary-geared e-CVT (Fig. 6.2) for the parallel HEV or the series HEV (Fig. 6.4) we hereby propose to replace the basically two electric machines and their two power converters by a single axial-air-gap electric machine central stator, fed from a single PWM converter with dual frequency voltage output $(V_1(f_1), V_1(f_2))$ and two independent PM rotors with $2p_1$ and $2p_2$ poles placed on the sides of the central stator with Qs slots and a tooth-wound (or Grammee) winding (Fig. 6.7).

The mixture of 2 frequencies in the inverter output voltage (with corresponding phase angles) leads to two different speeds ω_{r1} and ω_{r2} in the two rotors and different positive (or negative) torques as required.

Both frequencies voltages and their currents travel the whole single stator, winding coils sides through only the left side (in Fig. 6.7) produces torque at ωr1 speed and only the right side interacts to produce torque at ω_{r2} speed.

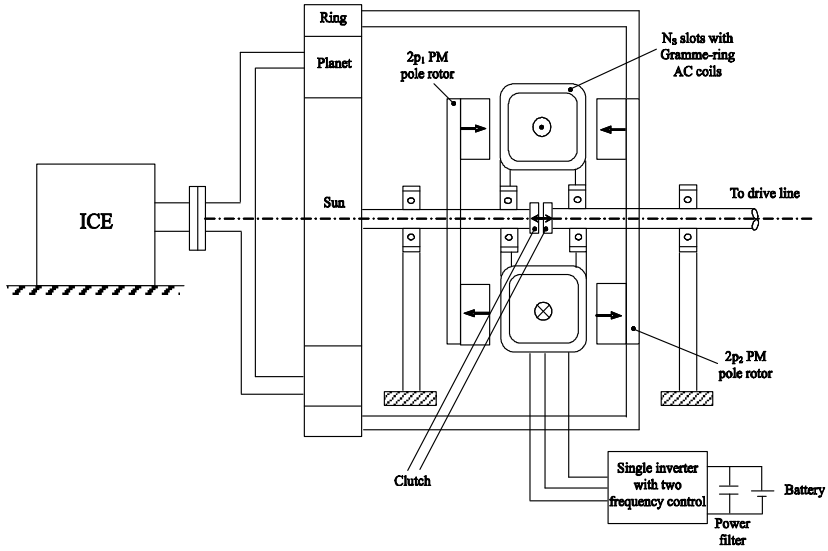

Figure 6.5: Proposed e-CVT with single electric machine stator and inverter for planetary geared parallel HEV.

Winding coils sides through only the left side (in Fig. 6.8) produces torque at ω_{r1} speed and only the right side interacts to produce torque at ω_{r2} speed.

This implies additional copper losses in the stator but if the end connections are kept small part of this inconvenient is removed.

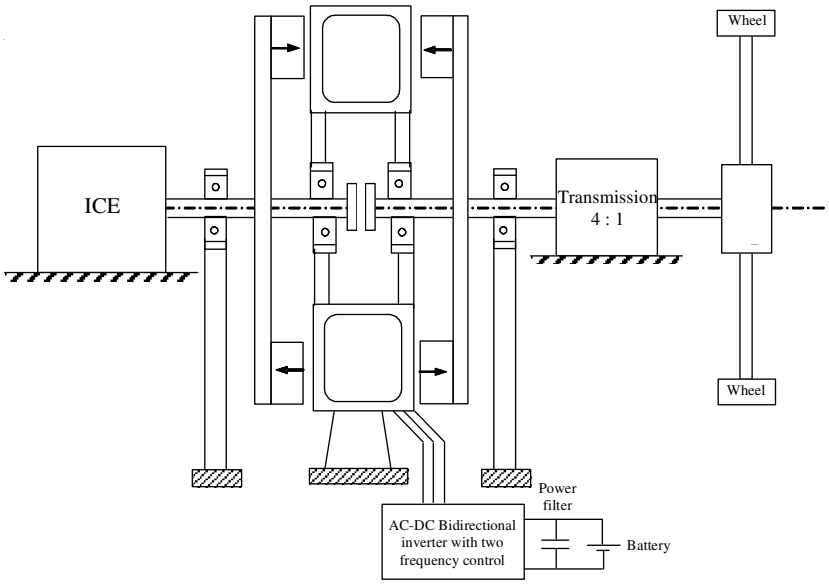

Figure 6.6: Proposed e-CVT with single electric machine stator and inverter for series, HEV.

On the other hand, the single inverter has to handle the entire apparent power related to the interaction of stator magnetic fields with both rotors at different speeds.

Only when the two frequency are equal (and electric rotor speeds related by $\omega_{r1} = \omega_{r2}$ $(n_1 p_1 = n_2 p_2)$ a direct transfer of power directly through the winding for, say, one motoring and one generating operation modes seems to be possible.

Apart from the evident simplification and compactness of the proposed solution attempts to reduce some what the inverter power rating based on motor/generator simultaneity are worth trying.

Through there will be $\omega_2 - \omega_1$ torque pulsations from one frequency (rotor) to the other, the torque stress on the stator will be reduced when one rotor is motoring and one is generating.

Proposed e-CVT topology in detail is presented in Fig. 6.6.

Though Fig. 6.6 is rather self-explanatory, here are few remarks:

"non-through" dual coil unit to build the 3 phase winding with two neighboring poles of same phase opening half of the winding in Fig. 6.8

Through the stator core magnetic circuit SMC material is suggested a rolled-lamination magnetic core is also feasible, especially for the case of "non through" coils; the same rationale is valid for the rotor magnetic core.

Either "through" or "non through" coil shapes way be adapted; it seems that if the number of coil turns is small, "non through" coils may be mounted easily.

It may be, however, possible to adopt double layer coils along tangential

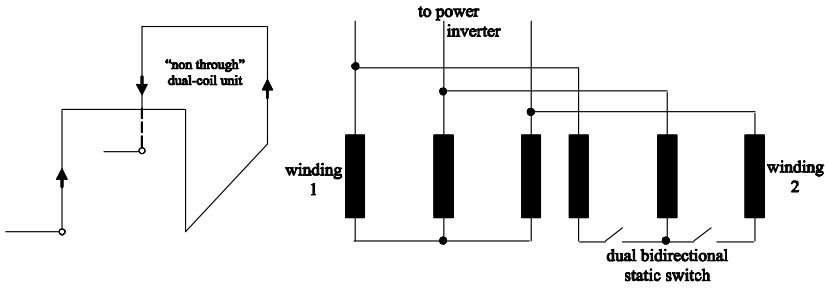

Figure 6.7: Non-through" dual coil unit to build the 3 phase winding with two neighboring poles of same phase opening half of the winding

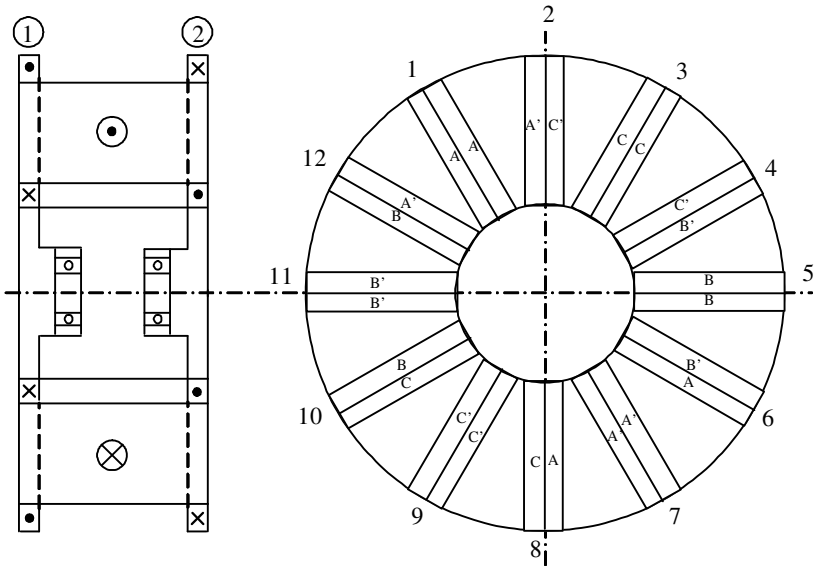

Figure 6.8: Two layers "non-through" coil winding.

direction with opposite polarity on the two stator axial sides (Fig. 6.7). In this case a dual TRIAC switch might be used to disconnect one half winding when only motoring or only generating is needed with one rotor only.

The stator mmf flux in the stator twins circumpherentially in the back iron to avoid severe flux fluctuation in the two rotors besides the PM flux fluctuation effects from one rotor to the other ($2p_1 \neq 2p_2$).

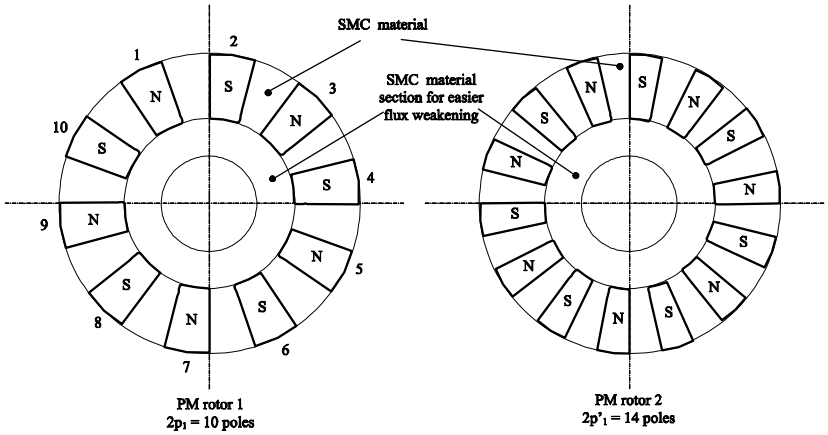

Figure 6.9: Independent rotors configuration.

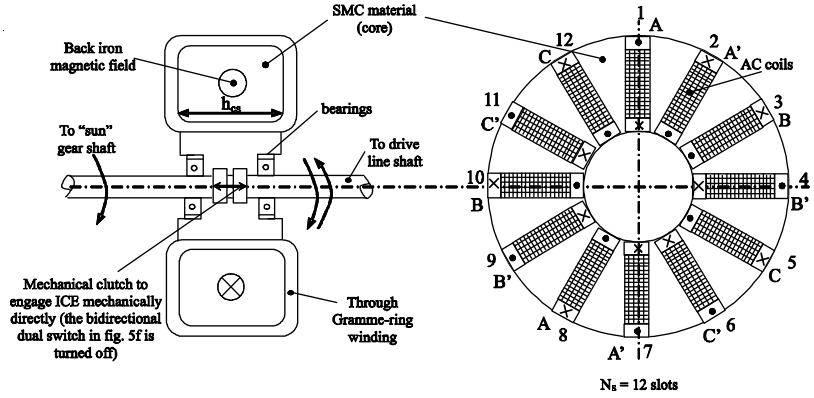

Figure 6.10: SMC build with torus coil configuration.

6.2 The dual PM Rotor Single stator phase coordinate mathematical model

The stator phase supply voltages Vs_{abc} contain 2 frequencies

$$V_{s\,a\,b\,c} = V^*_{s_1}\cos\left(\theta_{er_1} + \gamma_1\right) + V^*_{s_2}\cos\left(\theta_{er_2} + \gamma_2\right) \tag{6.1}$$

$$\frac{d\theta_{er_1}}{dt} = \omega r_1\ , \qquad \frac{d\theta_{er_2}}{dt} = \omega r_2 \tag{6.2}$$

$$\gamma_1 = \frac{\pi}{2} + \delta_{v_1}\ , \quad \gamma_2 = \frac{\pi}{2} + \delta_{v_2} \tag{6.3}$$

where δ_{v1},δ_{v2} are the voltage power angles (positive for motoring, negative for generating); θ_{er1}, θ_{er2} rotors 1 and 2 position (PM rotor axes).

The small SMC rotor pole parts (with some anisotropy) (Fig. 6.10) are used to facilitate PM flux weakening and also to facilitate rotor position estimation in case of sensorless control.

Let us neglecting here the small rotor saliency (left in the rotors SMC pole section there for easier flux weakening) and discuss first the Gramme ring winding case. The total phase inductance L_S (considering both rotors with all phase coils in series) are rather straightforward (as for constant air gap AC machines):

$$L_S \cong 6 \cdot \frac{(N_S \cdot n_c \cdot k_{w1}/3)}{\pi^2 \cdot g_m (1 + k_S) \cdot k_c} \cdot \left[\frac{(1 + k_{diff1})}{p_1} + \frac{(1 + k_{diff2})}{p_2} \right] + L_{ls} + L_{lEC} \tag{6.4}$$

$$R_S = \rho_{co} \cdot \frac{(N_S \cdot n_c/3) \cdot l_{coil}}{I_{rated}} \cdot j_{co\ rated}, \tag{6.5}$$

$$gm = g + hPM \tag{6.6}$$

with

L_{ls} – slot leakage inductance;
L_{lEC}– end connection inductance;
ρ_{co} – copper resistivity;
Q_S – number of stator slots;
nc – number of turns/coils;
l_{coil} – coils length;
g– air gap;
h_{PM} – PM axial thickness;
R_S– stator phase resistance;
j_{co} rated – rated copper current density;
I_{rated} – rated current;
$k_{diff\,1,2}$ – differential leakage inductance coefficients for the rotor with $2p_1$ and respectively $2p_2$ poles (which is know to be large in tooth-wound windings as the stator m.m.f. is reach in space harmonics).

The emf per phase, produced by PM is:

$$E_{1,2abc} = \omega_{r1,2} \cdot \phi_{PM\ 2p_1(2p_2)} \cdot k_{w1} \cdot \frac{N_S}{6} \cdot n_c \cdot \cos\left[\theta_{er\ 1,2} - (i-1)\frac{2\pi}{3} + \frac{\pi}{2} \right] \tag{6.7}$$

With $|L_S|$ a diagonal matrix with constant terms the matrix stator voltage equation are straight forward:

$$|i_{abc} \cdot R_S| - |V_{abc}| = -L_S \frac{d}{dt} |i_{abc}| - |E_{1\ abc} + E_{2\,abc}| \tag{6.8}$$

$$\frac{J}{p_1} \cdot \frac{d\omega_{r1}}{dt} = \frac{p_1}{2} \cdot \frac{(E_{1a} \cdot i_a + E_{1b} \cdot i_b + E_{1c} \cdot i_c)}{\omega_{r1}} - T_{1\ load} \tag{6.9}$$

$$\frac{J}{p_2} \cdot \frac{d\omega_{r2}}{dt} = \frac{p_2}{2} \cdot \frac{(E_{2a} \cdot i_a + E_{2b} \cdot i_b + E_{2c} \cdot i_c)}{\omega_{r2}} - T_{2\ load} \tag{6.10}$$

$$\frac{d\theta_{er1}}{dt} = \omega_{r1}\ ; \qquad \frac{d\theta_{er2}}{dt} = \omega_{r2} \tag{6.11}$$

6.2.1 Dual frequency operating winding

In our case the winding for each side of the stator being a double layer winding $q_c = q = 0.40$ for the 10 poles side, and $q_c = q = 0.29$ for the 14 poles side.

The winding layouts can be represented by means of two matrices as it presented in [15]. first matrix will contain information on the ingoing coil sides of the coils while the second matrix of the outgoing coil sides. The matrices are referred to as M_1 and M_2 for the ingoing and outgoing coil sides respectively. Both matrices have n columns and m rows. In addition, the number of columns equals the number of stator slots and the rows are equal to the number of phases, thus $m = 3$ and $n = Q_s$. The matrices can be expressed as:

$$M_1 = \begin{bmatrix} m_{11} & m_{12} & \cdots & m_{1n} \\ m_{21} & m_{22} & \cdots & m_{2n} \\ \vdots & \vdots & \ddots & \vdots \\ m_{m1} & m_{m2} & \cdots & m_{mn} \end{bmatrix}, \; M_2 = \begin{bmatrix} m_{11} & m_{12} & \cdots & m_{1n} \\ m_{21} & m_{22} & \cdots & m_{2n} \\ \vdots & \vdots & \ddots & \vdots \\ m_{m1} & m_{m2} & \cdots & m_{mm} \end{bmatrix} \tag{6.12}$$

where m_{ij} is the 1 (for the ingoing coils) or -1 (for the outgoing coils) if for the n phase is placed in the m slot otherwise is zero.

The winding in matrix form is very compact and has advantages in machine analysis [16]. The matrix contains all the information of the winding arrangement in the stator slots. This allows the construction of the voltage phasor which is necessary to calculate the winding factor. In addition, the slot mmf can be obtained from the column data. The properties of the matrix are summarized as follows:

- if the winding is symmetrical, the number of assigned elements in all the rows are equal;
- the number of columns is equal to the number of stator slots;
- the number of rows is equal to the number of phases;
- for a single layer winding there is only one nonzero element in a column;
- a double layer winding has two nonzero elements in a row;
- the matrix is valid for both a fixed and variable slot pitch.

The winding matrix is used to calculate the winding factor and the slot mmf.

A vector is assigned to the centre of each stator slot. The exponential representation of a vector is used, i.e.:

$$e^{j\nu\alpha} = \cos(\nu\alpha) + j\cos(\nu\alpha). \tag{6.13}$$

$$v_\nu = \begin{bmatrix} e^{j\nu\alpha_1} & e^{j\nu\alpha_{n2}} & \ldots & e^{j\nu\alpha_{N_S}} \end{bmatrix}^T \quad 1 \le n_2 \le N_S. \tag{6.14}$$

With M_1 and M_2 assigned, the winding factor for any harmonic can be calculated as the product between the matrices and the slot vector as given in [17]. This means that a row of the winding matrix is multiplied by the slot vector column matrix. The matrix product means that all the vectors belonging to the same phase are added where the accounts for both regular and irregular distributed stator slots.

$$(m_{1,i1} + m_{2,i1})\, e^{jp\alpha_1} + (m_{1,i2} + m_{2,i2})\, e^{jp\alpha_2} + (m_{1,iN_s} + m_{2,iN_s})\, e^{jp\alpha_{N_s}} \ . \tag{6.15}$$

The winding factors for the two sides (12- slots 10 poles) and (12 slot -14 poles) windings results as $\xi_1 = 0.966$ for the first and for the second side.

The matrix product means that all the vectors belonging to the same phase arc added and for the case ξ_1 = p equals

$$(m_{1,i1} + m_{2,i1})\, e^{jp\alpha_1} + (m_{1,i2} + m_{2,i2})\, e^{jp\alpha_2} + (m_{1,iN_s} + m_{2,iN_s})\, e^{jp\alpha_{N_s}} \tag{6.16}$$

The prototype stator is built 12 slots with 10 pole pairs for one side and 14 pole pairs on the other side. This is a double layer winding and the number of slots is equal to the number of coils. Both q and qc and the basic winding has 6 slots. The lowest harmonic has 10 pole pairs which is the same as the working harmonic. Therefore, the winding has no sub-harmonics as it is presented in figure 10 and 11. The matrix elements of the basic winding are:

$$\begin{aligned} M_{1,b} &= \begin{pmatrix} 0 & 1 & 0 & 0 & 0 & 0 & 1 & 0 & 0 & 0 & 0 & 0 \\ 0 & 0 & 0 & 0 & 0 & 1 & 0 & 0 & 0 & 0 & 1 & 0 \\ 1 & 0 & 0 & 0 & 0 & 0 & 0 & 0 & 0 & 1 & 0 & 0 \end{pmatrix}, \\ M_{2,b} &= \begin{pmatrix} -1 & 0 & 0 & 0 & 0 & 0 & 0 & -1 & 0 & 0 & 0 & 0 \\ 0 & 0 & 0 & 0 & -1 & 0 & 0 & 0 & 0 & 0 & 0 & -1 \\ 0 & 0 & 0 & -1 & 0 & 0 & 0 & 0 & 0 & 0 & -1 & 0 \end{pmatrix}, \end{aligned} \tag{6.17}$$

the absolute value of the winding factor as a complex number is [17]:

$$\xi_\nu = \frac{3}{2N_c} \left[M_1 v_\nu + M_1 v_\nu \right] \ \in C \tag{6.18}$$

The ampere-turns in each slot can be obtained from the matrix winding columns.

Since the matrices M_1 and M_2 contain the coil side information for the ingoing and outgoing coil sides respectively the total ampere-turns of a coil side is the product of its value in the winding matrix with the number of coil turns nc. For a three-phase winding the slot mmf F_{slot} of the k^{th} slot is calculated as:

$$F_{slot,k} = N_t \sum_{n\,=\,1}^{3} i_n \left(m_{1,1k} + m_{2,1k} \right) \tag{6.19}$$

The windings of the sides are the same since the stator is double sided stator. On each side we have a double layer nonoverlapping winding with tooth concentrated coils as it can be noticed in Fig. 6.13 .

The tooth concentrated coils have the smallest end size and for this reason the leakage inductance is reduced. Because we have a different pole number for each side the resulting winding coefficient will be different as it can be

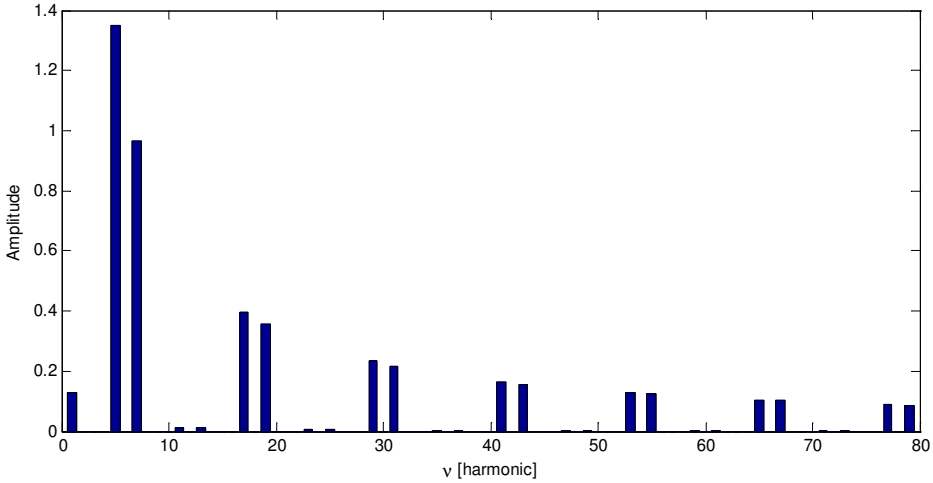

Figure 6.11: Winding harmonics side 1 12 slots /10 poles .

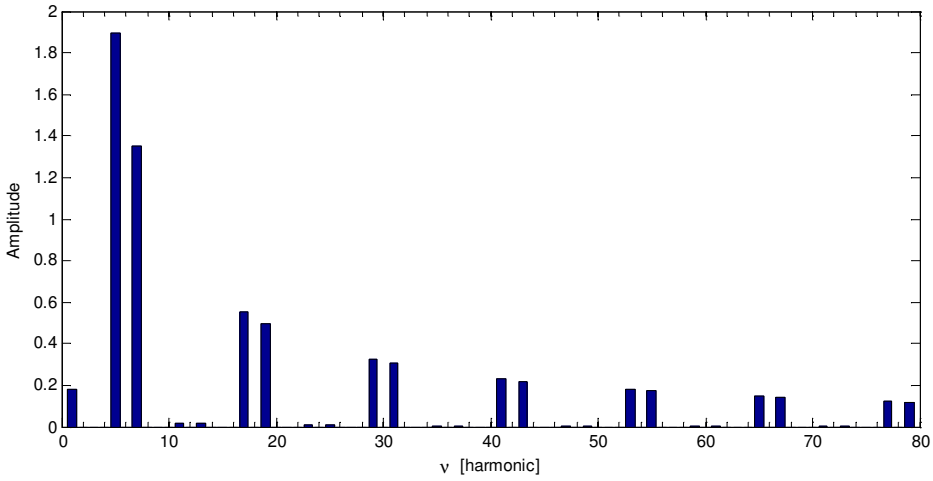

Figure 6.12: Winding harmonics side 2 12 slots /14 poles .

seen from Fig. 6.13 and Fig. 6.14 The 10 pole and 14 pole however have the same winding factor for a 12 slot stator. This fact is present also in several papers both for axial flux and radial flux machines [14].

The two rotor machine is supplied from a single inverter supply. The machine winding is assumed to be star connected with no neutral connection. Therefore the six currents should add up to zero.

6.2.2 Dual rotor AFPM 3D FEM Analysis

A complete 3D FEA model have been developed to yield reasonable predictions of the torque quality and 3D field distribution of flux density for the

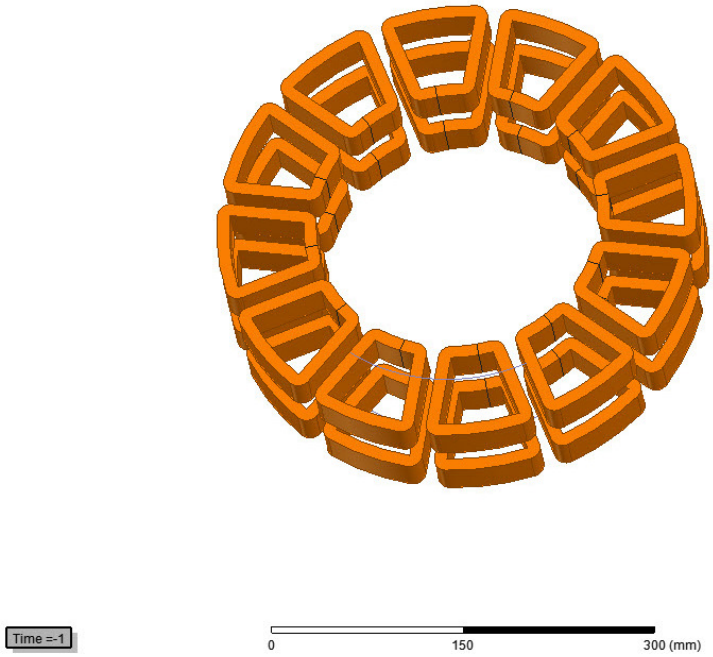

Figure 6.13: Two winding configuration of the prototype.

proposed configuration. Only a full 3D Finite Element Analysis (FEA) can accurately analyze the complex geometry models involving permanent magnets of any shape and material [99]. However this requires a large amount of computation power

There is no need to calculate the reluctances and inductances using circuit type analytical methods since these values can simply be extracted from the finite element analysis. One important advantage of using FEM is the ability to calculate the torque variations such as cogging torque, ripple torque and total torque with changes in rotor position. The main purpose of this analysis is to find out torque in the proposed axial flux machine using 3D field analysis method.

Figure 6.16 shows the airgap flux density vectors of the machine for no load case. It can be seen from the plot that maximum airgap flux density is nearly 0.8T and the average airgap flux density is 0.55 T.

It can also be noted from the airgap flux density plot(Fig.6.16) that the flux density becomes greater at the edges of the magnets because of the fact that the leakage flux between the magnets gains importance and causes high concentration of flux.

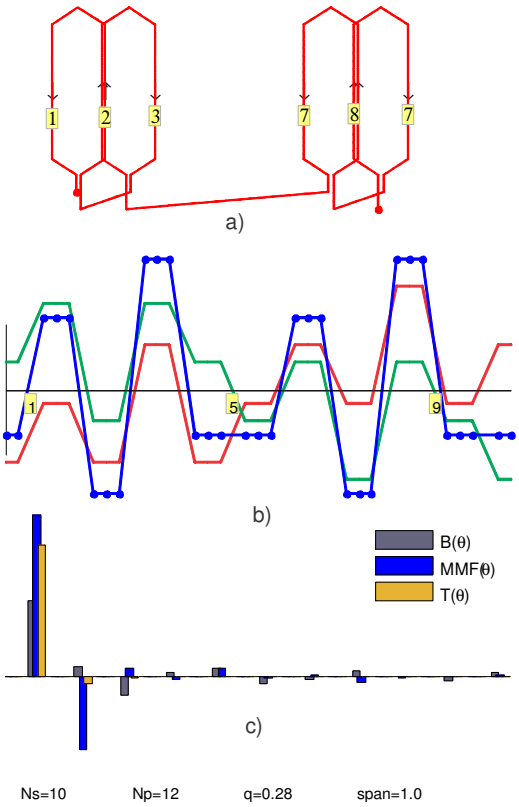

Figure 6.14: a) coil connection b) MMF of the 12/10 winding (blue) c) flux density MMF and torque harmonic

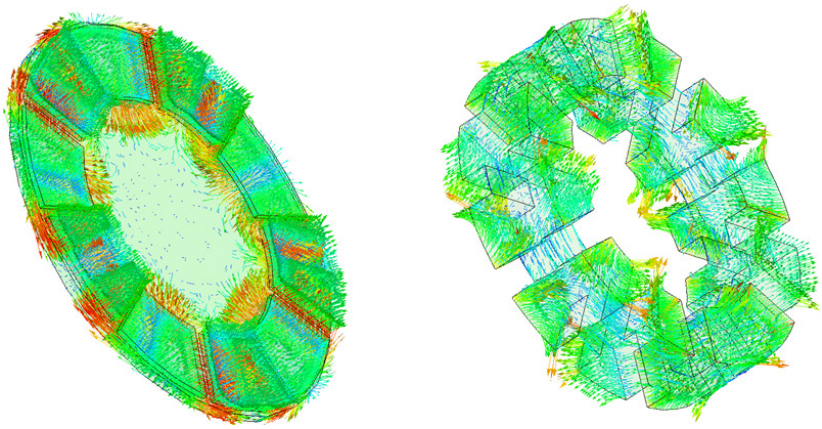

Figure 6.15: The flux density vector in: 10 pole rotor and in central stator

Since the considered prototype has a slotted topology, pulsating torque

Table 6.1: Parameters and machine dimensions

Frequency (f)	50 Hz
Number of poles rotor 1 ($2p$)	10 poles
Number of poles rotor 2 ($2p$)	14 poles
Current density (Js)	4.33 A/mm2
Airgap length (g)	1 mm
Pole-arc-ratio rotor 1 (α_{i1})	0.6944
Pole-arc-ratio rotor 2 (α_{i1})	1
Outer diameter (D_o)	300 mm
Inner diameter (D_i)	180 mm
Slot depth (h_{ss})	30 mm
Axial length of stator core (h_{cs})	90 mm
Axial length of rotor core (h_{cr})	10 mm
Magnet axial length (h_{PM})	5 mm
Permanent magnet material	NeFeBr40

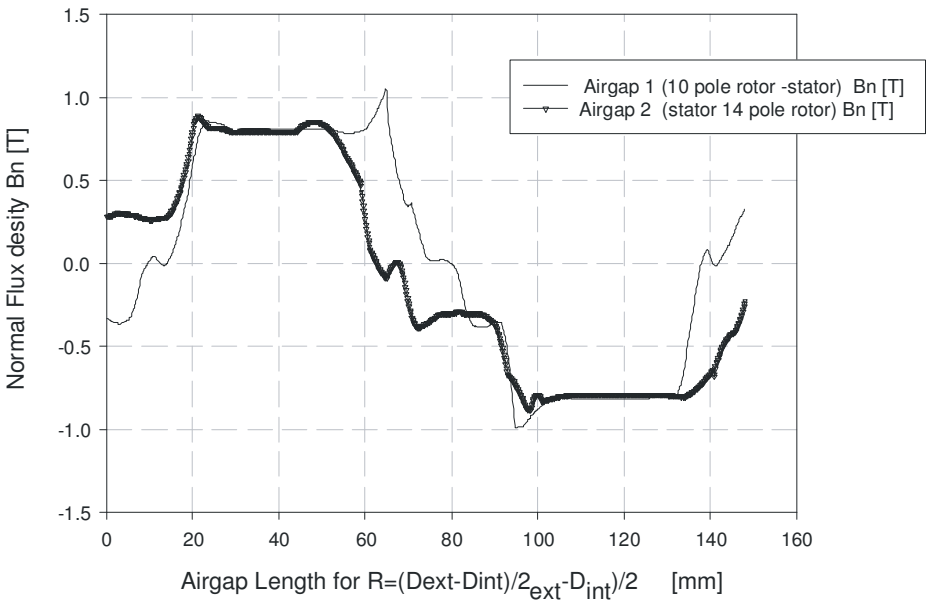

Figure 6.16: No load airgap flux density variation from 3D finite element analysis.

comprises both cogging and ripple torque components.

The two output torques for a fixed dc. current vector(mmf per slot : Aturns) at standstill is presented in Fig. 6.17 The torque for each rotor was computed by means of Maxwell stress tensor for each rotor. The torque pulsations in Fig. 6.18 are mainly due to cogging torque, but they are already reasonable, though they may be reduced by optimal geometrical design, skewing etc.

A ripple torque analysis was accomplished for the synchronous operation

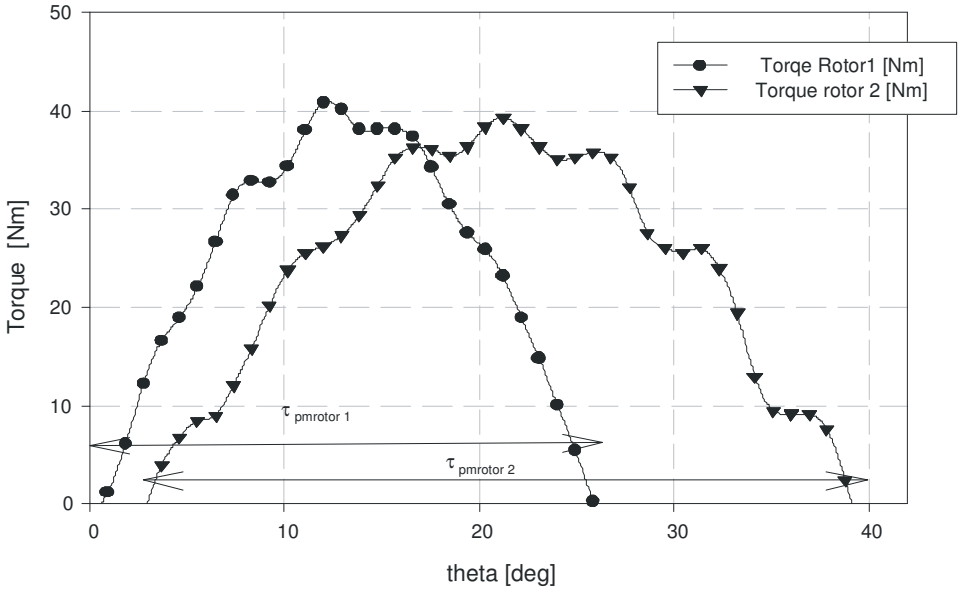

Figure 6.17: 3D Analysis torque for the two rotors.

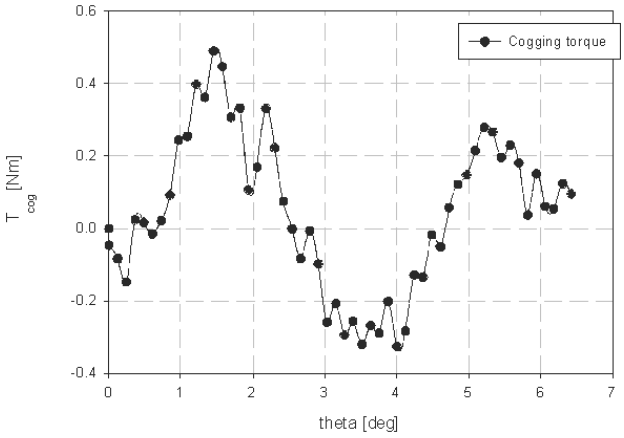

Figure 6.18: Cogging torque from 3D analysis

mode. This means that we have the two rotors running at the same speed. This is a rather particular operation mode. 3D Finite element calculations

were completed in each case for different rotor positions over one pole to investigate the torque quality of the machine (Fig. 6.17).

6.2.3 Conclusions

In this chapter, a system to produce dual, independent, electromechanical torque output using an fractional winding nonoverlapping axial-airgap machine with a single stator & winding and two different PM rotors has been introduced in terms of topologies, circuit model and preliminary 3D-FEM torque production analysis . These preliminary results prove the concept quantitatively but further studies, which are already under way, in relation to dynamic model, control and optimization design are needed to fully prove the practicality of the proposed system.

Bibliography

[1] K.T. Chau, C.C. Chan, C. Liu, "Overview of PM brushless drives for electric and hybrid electric vehicles", IEEE Transactions on IE, vol. 55, no. 6, June 2008, pp. 2246-2257.

[2] C. C. Chan and K. T. Chau, "Modern Electric Vehicle Technology", Oxford, U.K.: Oxford Univ. Press, 2001.

[3] M. Ehsani, K. M. Rahman, and H. A. Toliyat, "Propulsion system design of electric and hybrid vehicles," IEEE Trans. Ind. Electron., vol. 44, no. 1, pp. 19–27, Feb. 1997.

[4] K. T. Chau and C. C. Chan, "Emerging energy-efficient technologies for hybrid electric vehicles," Proc. IEEE, vol. 95, no. 4, pp. 821–835, Apr. 2007.

[5] C. C. Chan and K. T. Chau, "An overview of power electronics in electric vehicles," IEEE Trans. Ind. Electron., vol. 44, no. 1, pp. 3–13, Feb. 1997.

[6] Z. Q. Zhu and D. Howe, "Electrical machines and drives for electric, hybrid and fuel cell vehicles," Proc. IEEE, vol. 95, no. 4, pp. 746–765, Apr. 2007.

[7] M. Terashima, T. Ashikaga, T. Mizuno, K. Natori, N. Fujiwara, and M. Yada, "Novel motors and controllers for high-performance electric vehicle with four in-wheel motors", IEEE Trans. Ind. Electron., vol. 44, no. 1, pp. 28–38, Feb. 1997.

[8] K. T. Chau and Y. S. Wong, "Hybridization of energy sources in electric vehicles," Energy Convers. Manag., vol. 42, no. 9, pp. 1059–1069, Jun. 2001

[9] K. T. Chau and Y. S. Wong, "Overview of power management in hybrid electric vehicles," Energy Convers. Manag., vol. 43, no. 15, pp. 1953–1968, Jun. 2002.

[10] M. Ehsani, Y. Gao, S. E. Gay, and A. Emadi, Modern Electric, Hybrid Electric, and Fuel Cell Vehicles: Fundamentals, Theory, and Design. Boca Raton, fl: CRC Press, 2005.

[11] C. C. Chan, K. T. Chau, J. Z. Jiang,W. Xia, M. Zhu, and R. Zhang, "Novel permanent magnet motor drives for electric vehicles," IEEE Trans. Ind. Electron., vol. 43, no. 2, pp. 331–339, Apr. 1996.

[12] J. M. Miller, "Hybrid electric vehicle propulsion system architectures of the e-CVT type," IEEE Trans. Power Electron., vol. 21, no. 3, pp. 756–767, May 2006.

7 Conclusions

7.1 Thesis summary

First, particular design features of PMSMs with fractional winding with non overlapping coils windings have been presented.

The computation of the magnetic field quantities was performed for the design stage of a 72/68 PSMG using an existing analytical model developed from literature analytical models. The use of the analytical model is important since enable the precise computation of the magnetic field, cogging torque of a large class of PMSMs equipped with fractionary nonoverlapping windings. The use of conformal maps transformations makes possible to take in account the exact geometry influence and particularities of radial flux permanent magnet machines

A full characterisation of new linear flux reversal machine has been presented. In many PMSM it can be noticed the difficulty to perform a real PM – flux concentration due to high fringing. This is the main obstacle to produce higher thrust density but maintain high efficiency and good power factor. In an effort to circumvent this difficult, the present paper introduces a novel configuration of linear flux reversal (LFRM) oscillo-machine with efficient PM flux concentration.

The novel configuration is first introduced and a conceptual design methodology is presented related to a case study. FEA is then used to calculate more exactly the thrust for various current and mover positions. Extensive lab test ware performed in order to characterize the functioning of the LFRM.

Using the same concept of flux concentration applied to flux reversal machine a radial flux FRM was introduced and theoretically characterized.

This choice of a concentrated non-overlapping winding allows a large number of pole pairs to be designed. The present work emphasizes emphasizing the special features of the whole motor drive. from what is noticed the encoder-less operation of the drive is particularly critical when the number of poles is large. Despite this dificulties a vector control schem is presented and a sliding-mode rotor flux estimation scheme is investigated. Its performances are experimentally are comparable d to the encoder operation of standard vector controlled drives.

Based on the special features of the axial flux PMSM it is possible to build a novel brushless, single winding and single stator, dual PM rotor axial-air-gap machine capable to deliver independently torque at the two rotors by adequate vector control. The proposed topology, the circuit model, controlled dynamics simulation and preliminary 3D FEM torque production on a case study constitute a class of electrical machines specially designed for electric traction. The proposed dual mechanical port system should be instrumental in parallel (with planetary gears) or series hybrid electric vehicles (HEV) aiming at a more compact and efficient electric power system solution.

7.2 Contributions

The present thesis includes, from the author point of view, following major original contributions:

- An emphasis of analytical models to be included in the the computation of electromagnetic design of fractionary winding PMSMs chapter 2 with a symbolic computation model implemented as a software application under Wolfram Mathematica;
- Characterization of a PMSG with 72 slots and 68 poles for low speed direct drive applications. In chapter three the design method of PMSM with nonoverlapping windings (integration of Viarouge optimized design of windings);
- The use of capacitor compensated PMSG for increased power extraction from low speed motion offgrid operation;
- Presentation of two new configuration of Flux Reversal Machines with flux concentration effect. One prototype is designed for linear reciprocation motion applications and a second prototype is high torque density PMSM with flux concentration effect which uses conventional laminations capable to compete with transverse flux counterparts (which are mechanically more complex);
- For the linear flux reversal flux concentration machine a dynamic nonlinear model is developed and evaluated (Chapter 4);
- Characterization for the first time of Radial Flux reversal Flux concentration machine (Chapter 4);
- A complete study of Axial Flux nonoverlapping windings consisting in 2D FEM analysis method of torque and performance using multiple planes;
- Investigation of possibilities of reduction of cogging torque up to 2.1% to 1.95% for a 18/16 AFPMSM (Chapter 5);
- An exploratory study of E.M.F. torque for a low speed 48/40 axial type at $P_n = 2000W$ and $\omega_n = 88rad/s$ and possibilities of control of AFPMSM

with nonoverlapping windings both with and without and motion senzor (Chapter 5);

- A 3D field FEM analysis for a special designed AFPMSM for HEV with 12/14 and 12/10 and 12 with one stator and rotor for two independent rotors (Chapter 6);

7.3 Published papers supporting this work

1. Boldea, I., Topor, M., Tutelea, L., Linear flux Reversal PM Oscillo-Machine with Effective flux Concentration, Proceedings of OPTIM 2004, Brasov, Romania, vol 2, pp. 59-64

2. Tutelea, L.N.; Myung Chin Kim; Topor, M.; Ju Lee; Boldea, I.; , "Linear Permanent Magnet Oscillatory Machine: Comprehensive Modeling for Transients With Validation by Experiments," Industrial Electronics, IEEE Transactions on , vol.55, no.2, pp.492-500, Feb. 2008

   doi: 10.1109/TIE.2007.911936

3. G. Tomassi, M. Topor, F. Marignetti, I. Boldea " Characterization of an axial-flux machine with non-overlapping windings as a generator Paper presented at the 6th International Symposium on Advanced Electromechanical Motion Systems – ELECTROMOTION 2005, 27-29 September 2005, Lausanne, Switzerland and selected for publication in 'ELECTROMOTION'.

4. Marignetti, F.; Delli Colli, V.; Cancelliere, P.; Scarano, M.; Boldea, I.; Topor, M.; "A Fractional Slot Axial flux PM Direct Drive," Electric Machines and Drives, 2005 IEEE International Conference on , pp.689-695, 15-15 May 2005
   doi: 10.1109/IEMDC.2005.195798

5. I. Boldea, M. Topor, F. Marignetti, "Characterization of a low speed permanent magnet generator with fractionary nonoverlaping windings", OPTIM 2006, Brasov, Romania, May 2006, Proceedings, ISBN 973-635-703-1 10th International Conference on OPTIMIZATION OF ELECTRICAL AND ELECTRONIC EQUIPMENT OPTIM '06 May 18-19, 2006, Braşov, Romania

6. Boldea, I.; Topor, M.; Marignetti, F.; Deaconu, S.I.; Tutelea, L.N.; , "A novel, single stator dual PM rotor, synchronous machine: Topology, circuit model, controlled dynamics simulation and 3D FEM analysis of torque production," Optimization of Electrical and Electronic Equipment (OPTIM), 2010 12th International Conference on , vol., no., pp.343-351, 20-22 May 2010

   doi: 10.1109/OPTIM.2010.5510568

7. Topor, Marcel; Chun, Yon-Do; Koo, Dae-Hyun; Han, Pil-Wan; Woo, Byung-Chul; Boldea, Ion ”Application of flux reversal principle for axial flux permanent magnet machines

   Journal of Applied Physics, Volume 103, Issue 7, pp. 07F127-07F127-3 (2008).

8. Yon-Do Chun, Marcel, Topor, Dae-Hyun Koo Yun-Hyun Cho Han, Pil-Wan; ”Performance improvement of axial flux permanent magnet motor using 2D analysis model Proceedings of the XIII. International Symposium on Electromagnetic fields in Mechatronics, Electrical and Electronic Engineering (ISEF ’2007), Praga (Rep. Ceha), pp. 175-176, ISBN 978-80-01-03784-3.

A.1 Matlab code for design of Radial Flux Non-Overlapping PMSM

The code was developed by Dr. Ing Dorin Klumpner and was used by author for initial dimensioning the PMSM in chapter 3.

```
%%% copyright Dorin Klumpner 2005 %%%
function output_g_design=g_design(fs_av_N_per_sq_cm,j_A_per_sq_mm,...
lambda_Dro_L,Bg1,Bts,Bys,Byr,algorithm,switch_calculation)
% GENERAL DESIGN
%clear all;
%clc;
format compact;
%algorithm=2;%  hj=1, ga=2, gs=3, direct design(no optimization)=4, calculator+plot=99
switch_plot=0;
if algorithm==99  | algorithm==4;
    switch_plot=1;
end
%
%SPECIFICATION DATA ------------------------------------------------------
%LOAD
T2_peak_n_base=200;         % Nm peak load torque (T2) (without friction)
n_base=88;                  % rpm
%T2_n_max=40;               % Nm
n_max=300;                 % rpm
k_duty_type=0.18;%1         % duty type factor=[(rated torque)^2*S1/(peak torque)^2*Sx];
%                           % example: 0.3Nm possible for S1 0.7Nm possible for S3=>0.18
%INVERTER
ULL_rms_max=8.16;%2.7%      % V line-line voltage of the inverter;
ULL_rms_max=k_inverter*Udc=0.68*12=8.16 V
IL_rms_max=38;%60;          % maximum inverter current
%AMBIENT
Tamb = 40;                  %  C, ambient temperature
Tamb_max=120;               %  C, maximum ambient temperature
%
%experience-based parameters; INPUT values -------------------------------
Tr=0.050;                           % Nm, friction torque (bearing and windage) at rated speed
R_therm_co_amb=4;                   % W/ C  thermal resistance copper-ambient
R_therm_magn_amb=0.8*R_therm_co_amb; % W/ C  thermal resistance magnet-ambient
R_therm_fr_amb=1.0;                 % W/ C  thermal resistance frame-ambient
connect_u=1;          %Uph_rms=connect_u*ULL_rms_max
connect_i=1/sqrt(3);  %Iph_rms=connect_i*IL_rms
connect_R=3/2;        %Rph=connect_R*RLL
a=2;                  %number of pairs of parralel current paths
nb_wind_layers=2;     %number of winding layers per slot
k_u=0.67;%0.95;       %Eph_rms=ku*Uph_rms;   R,X-influence
Tco_max = 150;        % C, maximum copper temperature
%machine topology --------------------------------------
m=3;                % phase number
p=68;                % - number of pole pairs
Ns=72;               % number of slots
q=Ns/(2*m*p);       % number of slots per phase and pole
kw1=0.866;          %winding factor
agap=0.5e-3;        %m airgap
f_LKG=0.8;          %leakage factor (=Fig/FiM)                                    FEM-CORRECTION <<<
kC=1.08;            %Carter factor
%dimensioning factors (experience based)-----------------------------------
%design variables for optimal design

% other dimensioning factors(technological,...)
htt=1e-3;                   % tooth-tip height
hw=1e-3;                    % wedge height
slot_fill=0.278;            % 0.4 slot filling factor, recommended 0.35...0.45
D_shaft=10e-3;              % rotorshaft diameter
betaM=0.97*2*pi/Ns;         % magnet angle (also for low cogging torque)
jpg_gap=0.5e-3;             % rotor airgap extension for sine back-jpg
b_bridge=0.5e-3;            % rotor bridge width
b_web=1e-3;                 % rotor bridge width
wso=2.5e-3;                 % slot opening width
% physical constants ------------------------------------------------------
resco_20= 0.018e-6;     % Ohm m, copper resistivity at 20 C
alpha_resco=0.0037;     %1/ C, temperature coefficient of the resistivity
miu_0 = 4*pi*1e-7;      % air permeability
Br_20=1.15;              % T remanent flux density at 20 C
miu_rec=1.1;            % - recoil permeability of PM
gamFe = 7600;           % kg/m3, iron density
gamco = 8900;           % kg/m3, copper density
gamPM = 6000;           % kg/m3, PM density
p10 = 2;                % W/kg, specific loss (at 50 Hz)
Clam = 2.5;             % $/kg, lamination costs,
Cco = 6;                % $/kg, copper wire costs,
CPM = 100;              % $/kg, PM costs
read_BH;                % read the B-H curve
%
% Preliminary calculations ------------------------------------------------
    Te=T2_peak_n_base+Tr;               % Nm    0.7Nm load torque + 0.05Nm loss torque
    f_base=n_base/60*p;                 % base frequency
```

```
    P2_base=T2_peak_n_base*n_base/9.55; % base shaft power
    fs_av=fs_av_N_per_sq_cm*1e4;        % N/m^2 force density
    j_density=j_A_per_sq_mm*1e6;        % A/m^2 current density
    Uph_rms=connect_u*ULL_rms_max;          % V  phase voltage rms
    %Iph_rms_max=IL_rms_max*connect_i;   % A  IL_rms=Iph_rms_max/connect_i;
% Magnetic circuit sizing _____________________________________________
    Dro=(2*lambda_Dro_L*Te/(pi*fs_av))^(1/3);     % rotor outer diameter
    Dsi=Dro+2*agap;                               % stator inner diameter
    L=Dro/lambda_Dro_L;                           % stack length
    taup=pi*Dsi/(2*p);                            % pole pitch
    Bg_av=2/pi*Bg1;                               % average airgap flux density                FEM-CORRECTION <<<
    Fig=taup*L*Bg_av;                             % airgap pole flux                           FEM-CORRECTION <<<
    Eph_rms=k_u*Uph_rms;                          %
    nt_ph=round(Eph_rms/(2*pi*f_base*kw1*Fig/sqrt(2)));   % number of windings per phase        FEM-CORRECTION <<<
    kE=p*kw1*nt_ph*Fig;                           % back-jpg constant
    kT=sqrt(3)/2*kE;                              % torque constant
    IL_peak=Te/kT;                                % peak line current
    IL_rms=IL_peak/sqrt(2);                       % rms line current
    Iph_rms=IL_rms*connect_i;                     % rms phase current
    A_wire=Iph_rms/(a*j_density);                 % wire area
    d_wire=sqrt(A_wire*4/pi);                     % wire diameter
    A_slot=nt_ph*A_wire/slot_fill*nb_wind_layers; % slot area
    %
    bts=pi*Dsi/(2*p)*Bg_av/Bts;          % tooth width    bts=pi*Dsi/Ns*Bg_av/Bts;              FEM-CORRECTION <<<
    %-----------------------------------------
    ro=Dsi/2+hw+htt;
    rb=bts+ro;
    switch_rb=0;
    count_switch_rb=0;
    %switch_rb_terminate=0;
    while switch_rb==0;
        bs1=ro*sin(pi/6-asin(bts/(2*ro)));
        bs2=rb*sin(pi/6-asin(bts/(2*rb)));
        bs=(bs1+bs2)/2;                   % mean slot width (only for permeance calculation)
        hs=bs2/(tan(asin(bs2/rb)))-bs1/(tan(asin(bs1/ro)));
        A1=(bs1+bs2)/2*hs;
        A2=1/2*rb^2/2*((pi*pi/6-asin(bts/(2*rb)))/pi-sin(pi/6-asin(bts/(2*rb))));
        A_slot_calc=2*(A1+A2);
        if abs(A_slot_calc-A_slot)/A_slot>0.03
            if (A_slot_calc-A_slot) >0;
                count_switch_rb=count_switch_rb+1;
                if count_switch_rb>199
                    %switch_rb_terminate=1;
                    if algorithm==2
                        cd c:\a_iles\r3\pmsm_design\genetic_pmsm
                        stop%pmsm_genetic
                    end
                    %stop
                end
                 rb=rb*0.99;
            else rb=rb*1.01;
            end
        else
            switch_rb=1;
        end
    end
    %-------------------------------------------------------------------
    hts=rb-Dsi/2;                                % tooth height
    hys=pi*Dsi/(2*p)*Bg_av/(2*Bys);              % stator yoke height
    Dso=2*(rb+hys);                              % stator outer diameter
    bM=2*sin(betaM/2)*(Dro/2-jpg_gap-b_bridge); % magnet width
    hmt=Dro/2-(bM/2)/tan(betaM/2);               % heigth magnet top
    hyr=1/2*pi*Dro/(2*p)*Bg_av/Byr;              % rotor yoke heigth; coarse approximation
    lyr=1/2*pi*(Dro-D_shaft)/(2*p);%*0.5..0.7    % rotor yoke length; coarse approximation
    AM=bM*L;                                     % magnet area
    Ag=pi*Dro/(2*p)*L;                           % airgap area
    BM=Bg_av/f_LKG*Ag/AM;                        % magnet flux density                          FEM-CORRECTION <<<
    HM=(BM-Br_20)/(miu_0*miu_rec);               % magnet coercivity
    Hg=Bg_av/miu_0;                              % airgap coercivity
    Hts=spline(B,H,Bts);                         % stator tooth coercivity
    Hys=spline(B,H,Bys);                         % stator yoke coercivity
    Hyr=spline(B,H,Byr);                         % rotor yoke coercivity
    lys = 2/3*pi*(Dso-hys)/(2*p);                % flux path length in stator yoke
    lts=hts;                                     % flux path length in stator teeth
    lg=agap*kC;                                  % flux path length in airgap
    theta_summ_2=(2*Hts*lts+Hys*lys+Hyr*lyr+2*Hg*lg);% total mmf                                 FEM-CORRECTION <<<
    ks=theta_summ_2/(2*Hg*lg);
    hM=-1/2*theta_summ_2/HM;                        % magnet heigth
    % check and correction hM for demagnetization at Tamb_max and IL_max;   TO BE IMPLEMENTED !!!
    if (hM<2e-3) & (hM>0)      %3.5e-3
       hM=2e-3;    %3.5e-3
    end
    l_end_turn=2*pi*bts;                 %coarse approximation(2*pi*bts) of ONE endturn;to be corrected
    lc=2*(L+l_end_turn);                 % coil length
    %
    Rph_20=resco_20*lc*nt_ph/(A_wire*a);
    RLL_20=Rph_20/connect_R;

% Weights/costs of materials _____________________________________________
    wys=gamFe*L*pi*((Dso^2-(Dso-2*hys)^2))/4;            % stator yoke weight
    wts=Ns*gamFe*L*bts*lts;                              % stator teeth weight
    wyr=gamFe*L*(pi*Dro^2/4-2*p*hM*bM);                  % rotor lamination weight
```

```
    wPM = 2*p*gamPM*L*hM*bM;                                % PM weight
    wco = m*a*gamco*lc*nt_ph*A_wire;                        % copper weight
    wmat = wys+wts+wyr+wPM+wco;                             % Total active material weight
    Cmat = (wys+wts+wyr)*Clam+wco*Cco+wPM*CPM;              % Total active material cost
% Losses (rated, at n_base) ____________________________________________
    Rph=Rph_20*(1+(Tco_max-Tamb)*alpha_resco);
    Pco = 3*Rph*Iph_rms^2;    % Copper losses
    Pmec_base =Tr*n_base/9.55;                               % Mechanical rated losses
    Pys = p10*Bys^1.7*wys*((n_base/60*p)/50)^1.7;            % yoke losses
    Pts = p10*Bts^1.7*wts*((n_base/60*p)/50)^1.7;            % stator teeth losses
    PFe=Pys+Pts;                                             % iron losses
    Ploss= Pco+Pmec_base+PFe;                                % total losses
% Efficiency ___________________________________________________________
    EFF=P2_base/(P2_base+Ploss);
    PF =P2_base/(m*Uph_rms*Iph_rms*EFF);
% Temperatures _________________________________________________________
    DTco=k_duty_type*Ploss*R_therm_co_amb;          % K copper Temperature RISE
    DTmagn=k_duty_type*Ploss*R_therm_magn_amb;      % K magnet temperature RISE =factor*DTco
    DTfr=k_duty_type*Ploss*R_therm_fr_amb;          % K frame temperature RISE
    Tco=DTco+Tamb;                                  %  C copper Temperature ABSOLUTE
    Tmagn=DTmagn+Tamb;                              %  C magnet Temperature ABSOLUTE
    Tfr=DTfr+Tamb;                                  %  C frame Temperature ABSOLUTE

% OUTPUT Procedure _____________________________________________________
if switch_plot==1;
    fid=fopen('c:\a_iles\r3\pmsm_design\results.txt','w');
    %algorithm
    t='%                    O U T P U T    F I L E';
    fprintf(fid,t,'char=');
    fprintf(fid,'fs_av_N_per_sq_cm');
    fprintf(fid,'%f\n',fs_av_N_per_sq_cm);
    fprintf(fid,'j_A_per_sq_mm=','char');
    fprintf(fid,'%f\n',j_A_per_sq_mm);
    fprintf(fid,'lambda_Dro_L');
    fprintf(fid,'%f\n',lambda_Dro_L);
    fprintf(fid,'Bg1')
    fprintf(fid,'%f\n',Bg1);
    fprintf(fid,'Bts=');
    fprintf(fid,'%f\n',Bts);
    fprintf(fid,'Bys=');
    fprintf(fid,'%f\n',Bys);
    fprintf(fid,'Byr=');
    fprintf(fid,'%f\n',Byr);
    fprintf(fid,'T2_peak_n_base=');
    fprintf(fid,'%f\n',T2_peak_n_base);
    fprintf(fid,'n_base=');
    fprintf(fid,'%f\n',n_base);
    fprintf(fid,'f_base=')
    fprintf(fid,'%f\n',f_base);
    fprintf(fid,'P2_base=');
    fprintf(fid,'%f\n',P2_base);
    %fprintf(fid,'%f\n',fs_av=fs_av/1e4);
    %fprintf(fid,'%f\n',j_density=j_density/1e6);
    fprintf(fid,'Uph_rms=');
    fprintf(fid,'%f\n',Uph_rms);
    fprintf(fid,'% Magnetic circuit sizing_________________________________');
    fprintf(fid,'Dso=');
    fprintf(fid,'%f\n',Dso);
    fprintf(fid,'Dsi=');
    fprintf(fid,'%f\n',Dsi);
    fprintf(fid,'L=');
    fprintf(fid,'%f\n',L);
    fprintf(fid,'bM=');
    fprintf(fid,'%f\n',bM);
    fprintf(fid,'hM=')
    fprintf(fid,'%f\n',hM);
    fprintf(fid,'hmt=')
    fprintf(fid,'%f\n',hmt);
    fprintf(fid,'hyr=');
    fprintf(fid,'%f\n',hyr);
    fprintf(fid,'Bg_av=');
    fprintf(fid,'%f\n',Bg_av);
    fprintf(fid,'Fig=');
    fprintf(fid,'%f\n',Fig);
    fprintf(fid,'Eph_rms=');
    fprintf(fid,'%f\n',Eph_rms);
    fprintf(fid,'nt_ph');
    fprintf(fid,'%f\n',nt_ph);
    fprintf(fid,'kE=');
    fprintf(fid,'%f\n',kE);
    fprintf(fid,'kT=');
    fprintf(fid,'%f\n',kT);
    fprintf(fid,'IL_peak=');
    fprintf(fid,'%f\n',IL_peak);
    fprintf(fid,'IL_rms=');
    fprintf(fid,'%f\n',IL_rms);
    fprintf(fid,'d_wire=');
    fprintf(fid,'%f\n',d_wire);
    fprintf(fid,'A_slot=');
    fprintf(fid,'%f\n',A_slot);
    fprintf(fid,'bts=')
    fprintf(fid,'%f\n',bts);
```

```
    fprintf(fid,'hts=');
    fprintf(fid,'%f\n',hts);
    fprintf(fid,'hys=');
    fprintf(fid,'%f\n',hys);
    fprintf(fid,'BM=');
    fprintf(fid,'%f\n',BM);
    fprintf(fid,'HM=');
    fprintf(fid,'%f\n',HM);
    fprintf(fid,'Hg=');
    fprintf(fid,'%f\n',Hg);
    fprintf(fid,'Hts=');
    fprintf(fid,'%f\n',Hts);
    fprintf(fid,'Hys=');
    fprintf(fid,'%f\n',Hys);
    fprintf(fid,'Hyr=')
    fprintf(fid,'%f\n',Hyr);
    fprintf(fid,'lys=')
    fprintf(fid,'%f\n',lys);
    fprintf(fid,'lts=')
    fprintf(fid,'%f\n',lts);
    fprintf(fid,'lyr=')
    fprintf(fid,'%f\n',lyr);
    fprintf(fid,'theta_summ_2=');
    fprintf(fid,'%f\n',theta_summ_2);
    fprintf(fid,'ks=')
    fprintf(fid,'%f\n',ks);
    fprintf(fid,'RLL_20=')
    fprintf(fid,'%f\n',RLL_20);
    fprintf(fid,'% Weights/costs of materials_____________________________');
    fprintf(fid,'wmat=');
    fprintf(fid,'%f\n',wmat);
    fprintf(fid,'Cmat');
    fprintf(fid,'%f\n',Cmat);
    fprintf(fid,'% Losses (rated, at n_base) _____________________________');
    fprintf(fid,'Pco=');
    fprintf(fid,'%f\n',Pco);
    fprintf(fid,'Pmec_base=');
    fprintf(fid,'%f\n',Pmec_base);
    %Pys
    %Pts
    fprintf(fid,'PFe')
    fprintf(fid,'%f\n',PFe);
    fprintf(fid,'Ploss')
    fprintf(fid,'%f\n',Ploss);
    fprintf(fid,'% Efficiency_____________________________________________');
    fprintf(fid,'EFF')
    fprintf(fid,'%f\n',EFF);
    fprintf(fid,'PF')
    fprintf(fid,'%f\n',PF);

    fprintf(fid,'% Temperatures_____________________________________________','');
    fprintf(fid,'Tco=');
    fprintf(fid,'%f\n',Tco);
    fclose(fid);

%data for femm design
Ns=Ns;  % number of slots
Nm=p;   % number of magnet poles around air
Lst=L;  % stack length
Rso=Dso/2;      % outside stator radius
Rsi=Dsi/2;      % inside stator radius
Dsh=htt;        % radial shoe depth at gap
Dst=1   % radial shoe taper depth i do notknow  the equivalence of the variables
Wsy=4  % radial width of stator yoke i do notknow  the equivalence of the variables
Wry=4   % radial width of rotor yoke i do notknow  the equivalence of the variables
Wt=4    % width of tooth in slot area i do notknow  the equivalence of the variables
Wso=wso   % width of slot openning at gap
g=agap                  % air gap length


    fid=fopen('c:\a_iles\r3\pmsm_design\sDimm.txt','w');
    fprintf(fid,'%f\n',Ns);
    fprintf(fid,'%f\n',Nm);
    fprintf(fid,'%f\n',Lst);
    fprintf(fid,'%f\n',Rso);
    fprintf(fid,'%f\n',Rsi);
    fprintf(fid,'%f\n',Dsh);
    fprintf(fid,'%f\n',Dst);
    fprintf(fid,'%f\n',Wsy);
    fprintf(fid,'%f\n',Wry);
    fprintf(fid,'%f\n',Wt);
    fprintf(fid,'%f\n',Wso);
    fprintf(fid,'%f\n',g);
    fclose(fid);


    end;% if switch_plot==1       END PLOTS


 ---------------------------------------
output_g_design(1)=EFF;
```

```
output_g_design(2)=hM;
output_g_design(3)=L;
output_g_design(4)=Dso;
output_g_design(5)=bts;
output_g_design(6)=hys;
output_g_design(7)=hyr;
output_g_design(8)=Tco;
output_g_design(9)=d_wire;

% goto par_calc
if switch_calculation==1
    par_calc;
    perf_calc;
end
```

```
\section{LUA for FEMM\ code for design evaluation of  radial flux PMSM\ }
\small
\lstset{frameround=fttt}
\lstset{
language=Matlab,
% general command to set parameter(s)
basicstyle=\ttfamily\color{black}, % print whole listing small
keywordstyle=\small\ttfamily, % underlined bold black keywords
identifierstyle=\ttfamily, % nothing happens
commentstyle=\ttfamily\color{darkgreen}\bfseries\emp, % white comments
stringstyle=\small\ttfamily, % typewriter type for strings
showstringspaces=false} % no special string spaces
\begin{lstlisting}[frame=none]

-- Draw inner rotor PMSM with parallel magnets
-- Duane Hanselman, University of Maine
-- "Brushless Permanent Magnet Motor Design", 2nd ed.
-- 408 pages, see: www.eece.maine.edu/motor
--set up defaults
--mi_openfemmfile("basic.fem")

create(0)
mi_gridsnap("off")
mi_hidegrid()
mi_refreshview()
mi_addboundprop("zero",0,0,0,0,0,0,0,0,0)
-- Motor Input Data
steelmaterial="M-19 Steel"
magnetmaterial="NdFeB 37 MGOe"
Units="millimeters"
mi_addmaterial("steelmaterial",0,0,0,0,0,6.25,0,0,0,0)
mi_addmaterial("magnetmaterial", 1.049, 1.049, 979000,0,0,
0.667,0,0,0,0,0,0)
--mi=addbhpoint("steelmarial",b,h)
--mi_addbhpoint("steelmarial",0,0)
--mi_addbhpoint("steelmarial",0.0046,789.130722)
--mi_addbhpoint("steelmarial",0.006401,10.474786)
--mi_addbhpoint("steelmarial",0.008123,12.016998)
--mi_addbhpoint("steelmarial",0.009845,13.786006)
--mi_addbhpoint("steelmarial",0.014524,15.816824)
--mi_addbhpoint("steelmarial",0.019202,18.147649)
--mi_addbhpoint("steelmarial",0.023880,20.822249)
--mi_addbhpoint("steelmarial",0.031514,23.893940)

handle=openfile("c:\\a_iles\\r3\\pmsm_design\\sDimm.txt","r")

Ns=read(handle,"*n")     -- number of slots
Nm=read(handle,"*n")     -- number of magnet poles around air
Lst=read(handle,"*n")    -- stack length
Rso=read(handle,"*n")    -- outside stator radius
Rsi=read(handle,"*n")    -- inside stator radius
Dsh=read(handle,"*n")    -- radial shoe depth at gap
Dst=read(handle,"*n")    -- radial shoe taper depth
Wsy=read(handle,"*n") -- radial width of stator yoke
Wry=read(handle,"*n") -- radial width of rotor yoke
Wt=read(handle,"*n")     -- width of tooth in slot area
Wso=read(handle,"*n") -- width of slot openning at gap
g=read(handle,"*n")      -- air gap length
closefile(handle)

--Ns=tonumber(prompt("number of slots")) -- number of slots
--Nm=tonumber(prompt("number of magnet poles around air gap")) -- number of magnet poles around r
--Lst=tonumber(prompt("stack length")) -- stack length
--Rso=tonumber(prompt("outside stator radius")) -- outside stator radius
--Rsi=tonumber(prompt("inside stator radius")) -- inside stator radius
--Dsh=tonumber(prompt("radial shoe depth at gap")) -- radial shoe depth at gap
--Dst=tonumber(prompt("radial shoe taper depth")) -- radial shoe taper depth
--Wsy=tonumber(prompt("radial width of stator yoke")) -- radial width of stator yoke
--Wry=tonumber(prompt("radial width of rotor yoke")) -- radial width of rotor yoke
--Wt=tonumber(prompt("width of tooth in slot area")) -- width of tooth in slot area
--Wso=tonumber(prompt("width of slot openning at gap")) -- width of slot openning at gap
--g=tonumber(prompt("air gap length")) -- air gap length
lm=4*g -- magnet length
```

```
Bm=160 -- magnet width in degE

-- Geometry calculations
-- stator
thetas=360/Ns -- angular slot pitch
thetaso=2*asin(Wso/(2*Rsi)) -- angular slot openning
thetat=thetas-thetaso -- angular tooth width

--rotor
thetap=360/Nm -- angular pole pitch
thetam=Bm/180*thetap -- angular magnet width
thetamo=thetap-thetam -- angular magnet spacing
Rro=Rsi-g -- outside rotor radius
Rrm=Rro-lm -- magnet inside radius
Rri=Rrm-Wry -- rotor inside radius
-- Problem Definition
mi_probdef(0,Units,"planar",1e-8,Lst)
-- triangle size specs
maxseggap=1 -- max angular segment length at air gap
maxseg=3 -- max angular segment length elsewhere
esizegap=Rro*2*PI*maxseggap/360 -- max element length at air gap
esize=(Rro+Rso)*PI*maxseg/360 -- max element length elsewhere
-- Now Draw the Crossection
-- Draw Outer Stator Circle
mi_addnode(0,-Rso)
mi_addnode(0,Rso)
mi_addarc(0,-Rso,0,Rso,180,maxseg)
mi_addarc(0,Rso,0,-Rso,180,maxseg)
mi_selectarcsegment(Rso,0)
mi_selectarcsegment(-Rso,0)
mi_setarcsegmentprop(maxseg,"zero",0,0)
-- Draw Stator Teeth
Ra=Rso-Wsy
Ta=-asin(Wt/(2*Ra))
Rb=Rsi+Dsh+Dst
Tb=-asin(Wt/(2*Rb))
Rc=Rsi+Dsh
Tc=-thetat/2
Rd=Rsi
Td=Tc
Re=Rsi
Te=-Td
Rf=Rsi+Dsh
Tf=-Tc
Rg=Rb
Tg=-Tb
Rh=Ra
Th=-Ta
Ri=Ra
Ti=Ta+thetas
Tsb=Ti+Ta -- angular slot bottom width
for n=0,Ns-1,1 do
tos=n*thetas
if n==0 then
xa=Ra*cos(Ta)
ya=Ra*sin(Ta)
mi_addnode(xa,ya)
else
xa=xi
ya=yi
end
xb=Rb*cos(tos+Tb)
yb=Rb*sin(tos+Tb)
mi_addnode(xb,yb)
mi_addsegment(xa,ya,xb,yb)
mi_selectsegment(9*xb/10+xa/10,9*yb/10+ya/10)
mi_setsegmentprop("",esize,0,0,0)
xc=Rc*cos(tos+Tc)
yc=Rc*sin(tos+Tc)
mi_addnode(xc,yc)
mi_addsegment(xb,yb,xc,yc)
mi_selectsegment(9*xc/10+xb/10,9*yc/10+yb/10)
mi_setsegmentprop("",esize,0,0,0)
xd=Rd*cos(tos+Td)
yd=Rd*sin(tos+Td)
mi_addnode(xd,yd)
mi_addsegment(xc,yc,xd,yd)
mi_selectsegment(9*xd/10+xc/10,9*yd/10+yc/10)
mi_setsegmentprop("",esizegap,0,0,0)
xe=Re*cos(tos+Te)
ye=Re*sin(tos+Te)
mi_addnode(xe,ye)
mi_addarc(xd,yd,xe,ye,thetat,maxseggap)
xf=Rf*cos(tos+Tf)
yf=Rf*sin(tos+Tf)
mi_addnode(xf,yf)
mi_addsegment(xe,ye,xf,yf)
mi_selectsegment(9*xf/10+xe/10,9*yf/10+ye/10)
mi_setsegmentprop("",esizegap,0,0,0)
xg=Rg*cos(tos+Tg)
yg=Rg*sin(tos+Tg)
mi_addnode(xg,yg)
```

```
mi_addsegment(xf,yf,xg,yg)
mi_selectsegment(9*xg/10+xf/10,9*yg/10+yf/10)
mi_setsegmentprop("",esize,0,0,0)
xh=Rh*cos(tos+Th)
yh=Rh*sin(tos+Th)
mi_addnode(xh,yh)
mi_addsegment(xg,yg,xh,yh)
mi_selectsegment(9*xh/10+xg/10,9*yh/10+yg/10)
mi_setsegmentprop("",esize,0,0,0)
if n==Ns-1 then
xi=Ra*cos(Ta)
yi=Ra*sin(Ta)
else
xi=Ri*cos(tos+Ti)
yi=Ri*sin(tos+Ti)
mi_addnode(xi,yi)
end
mi_addarc(xh,yh,xi,yi,Tsb,maxseg)
end
-- add material to stator
mi_addblocklabel(0,Rso-Wsy/2)
mi_selectlabel(0,Rso-Wsy/2)
mi_setblockprop(steelmaterial,1,0,"",0,0)
mi_clearselected()

-- Draw Inner Rotor Circle
mi_addnode(0,-Rri)
mi_addnode(0,Rri)
mi_addarc(0,-Rri,0,Rri,180,maxseg)
mi_addarc(0,Rri,0,-Rri,180,maxseg)
mi_selectarcsegment(-Rri,0)
mi_selectarcsegment(Rri,0)
mi_setarcsegmentprop(maxseg,"zero",0,0)
mi_clearselected()

--Draw Rotor Magnets
t2=thetam/2
Ra=Rrm
Ta=-t2
Rb=Rro
Tb=-t2
Rc=Rro
Tc=t2
Rd=Rrm
Td=t2
Te=Ta+thetap
Re=Rrm
alpha=1
for m=0,Nm-1,1 do
tom=m*thetap
if m==0 then
xa=Ra*cos(Ta)
ya=Ra*sin(Ta)
mi_addnode(xa,ya)
else
xa=xe
ya=ye
end
xb=Rb*cos(tom+Tb)
yb=Rb*sin(tom+Tb)
mi_addnode(xb,yb)
mi_addsegment(xa,ya,xb,yb)
mi_selectsegment(9*xb/10+xa/10,9*yb/10+ya/10)
mi_setsegmentprop("",esizegap,0,0,1)
xc=Rc*cos(tom+Tc)
yc=Rc*sin(tom+Tc)
mi_addnode(xc,yc)
mi_addarc(xb,yb,xc,yc,thetam,maxseggap)
mi_selectarcsegment(9*xc/10+xb/10,9*yc/10+yb/10)
mi_setarcsegmentprop(maxseggap,"",0,1)
xd=Rd*cos(tom+Td)
yd=Rd*sin(tom+Td)
mi_addnode(xd,yd)
mi_addsegment(xc,yc,xd,yd)
mi_selectsegment(9*xd/10+xc/10,9*yd/10+yc/10)
mi_setsegmentprop("",esizegap,0,0,1)
mi_addarc(xa,ya,xd,yd,thetam,maxseggap)
mi_selectarcsegment(9*xd/10+xa/10,9*yd/10+ya/10)
mi_setarcsegmentprop(maxseggap,"",0,1)
if m==Nm-1 then
xe=Ra*cos(Ta)
ye=Ra*sin(Ta)
else
xe=Re*cos(tom+Te)
ye=Re*sin(tom+Te)
mi_addnode(xe,ye)
end
mi_addarc(xd,yd,xe,ye,thetamo,maxseggap)
mi_selectarcsegment(9*xe/10+xd/10,9*ye/10+yd/10)
mi_setarcsegmentprop(maxseggap,"",0,1)
xl=(Rro+Rrm)*cos(tom)/2
yl=(Rro+Rrm)*sin(tom)/2
```

```
mdir=alpha*tom + (1-alpha)*(tom-180)
alpha=1-alpha
mi_addblocklabel(xl,yl)
mi_selectlabel(xl,yl)
mi_setblockprop(magnetmaterial,1,0,"",mdir,1)
mi_clearselected()
end
-- add material to rotor
mi_addblocklabel(0,(Rri+Rrm)/2)
mi_selectlabel(0,(Rri+Rrm)/2)
mi_setblockprop(steelmaterial,1,0,"",0,0)
mi_clearselected()
-- add <No Mesh> to inside rotor
mi_addblocklabel(0,Rri/2)
mi_selectlabel(0,Rri/2)
mi_setblockprop("<No Mesh>")
mi_clearselected()
-- add air between rotor and stator
xl=(Rsi+Rso)*cos(thetas/2)/2
yl=(Rsi+Rso)*sin(thetas/2)/2
mi_addblocklabel(xl,yl)
mi_selectlabel(xl,yl)
mi_setblockprop("Air",1,0,"",0,0)
mi_clearselected()
mi_zoom(-Rso,-Rso,Rso,Rso)
--mi_savefemmfile("parallel.fem")
```

A.2 Design of a axial flux PMSM using power density equations Matlab Code

```
function out=design(Nt,eta,speed,Js,A,p,Do,Kfocus,A,g,lambda,Bu)
f=speed*p/(2*60);
%% some contants for the prototype
Ke=pi/4;
Kphi=0;
%% flux leakage factor
Kd=1-p/30;
if f>40
    Bts=5.47*f^(-0.32);
    Bcs=4.38*f^(-0.32);
elseif f<=40
    Bts=1.7;
    Bcs=1.8;
end

Bcr=1.7;
%%airgap flux density is:
%Kfocus=Apm/Ap*Kd
Bg=Kfocus*Bu;
%% the electrical loading is:
Dg=(1+lambda)/2*Do;
As=2*m1*Nt*Irms/(pi*Dg);
A=As*(1+Kphi);
Wcu=pi*Do*lambda/(8*p);
%% the total diameter
Dt=Do+2*Wcu;

%Le=Lr+2*Ls+2*g;
dcs=pi/(16*p)*Do*(1+lambda)*Kfocus*Bu/Bcs;
dss=(A/(2*Js*Kcu))*(1+lambda)/lambda;
Lr=pi/(16*p)*Do*(1+lambda)*Kfocus/Kd;
Ls=dcs+dss;


Le=pi/(16*p)*Do*(1+lambda)*Kfocus*(1/Kd+2*Bu/Bcs)+A/(Js*Kcu)...
*((1+lambda)/lambda)+2*g;
%% KL factor
KL=1/(pi/(16*p)*(1+lambda)*Kfocus*(1/Kd+2*Bu/Bcs)+1/Do*(A/(Js*Kcu)...
*((1+lamnda)/lambda)+2*g));
%% the machine sizing equation is:
Pr=0.11*pi^2*eta*Bg*A*f/p*KL*(1-lambda^2)*(1+lambda)*Do^2*Le;

%% power density

sigma=0.441*pi*eta*Bg*A*f/p*KL*(1-lambda^2)*(1+lambda)*Do^2/Dt^2;
```

```
%% the peak value of the voltage is :
Epk=Ke*Nt*Bg*f/p*(1-lambda^2)*Do^2;

%peak current value is  ;
Ipk=1/(1+Kphi)*Ki*A*pi*Dg/(2*m1*Nt)
%%% now the eficiency the inverse problem
eta=Pr/(0.11*pi^2*eta*Bg*A*f/p*KL*(1-lambda^2)*...
(1+lambda)*Do^2*Le)


%% run the FEM equivalent model
%% we use 4 equivalent models for four radius values
%% the torque is computed at maximum curent value
for i=1:4
Tq(i)=FEM1(Tq);
Bg(i)=FEM1(Bg);
end
%%% input the torque out for the several slice model
Torque=Sum(Tq);
Bg=sum(Bg);

%%read the FEM file for the Bg parameter and A an j
fid = fopen('FEMout.txt');
while 1
    tline = fgetl(fid);
    if ~ischar(tline),   break,   end
    disp(tline)
end
fclose(fid);
Bgfem=tline;
Kfocusfem=Bgfem/Bufem;
Kd=Bgfem/Bpm;
Pr=Torque*speed;
Pcu=3*Irms;
Pfe=0;
Pmec=0;
etaFEM=Pr/(Pcu+Pfe+Pmec+Ps)




out.Ipk=Ipk;
out.Epk=Epk;
out.Pr=Pr;
out.sigma=sigma;
out.Le=Le;
out.Lr=Lr;
out.dcs=dcs;
out.dss=dss;
```

A.3 Analytical model of Fractional Winding PMSM using Wolfram Mathematica Code

Symbolic Solution of Slotless Permanet magnet Synchronous Machine Airgap field model

Clear variables definition

```
Clear[Br, μ0, p, β, α, μr, Rr, Rm, Rs, ωrm, Lu, Nc, Rg, s1, s2, s3, s4, s5, s6, s7, s8, C1, C2, C3,
C4, C5, C6, C7, C8, n, sol, an, bn, r];
```

Definition of necesary set of equations

s1:=(C5 * Rs^(n * p) * n * (p/Rs) + (C6 * n * (p/Rs))/Rs^(n * p))/μ0==0

Symbolic solution for coefficient identification

```
sol = Solve[{s1, s2, s3, s4, s5, s6, s7, s8}, {C1, C2, C3, C4, C5, C6, C7, C8}];
c5 = C5/.sol/.an → 2 * Br * Sin[n * β * p/2]/(μ0 * n * π) * (Cos[n * Pi/2] − Cos[3 * n * Pi/2])/.
bn → 2 * Br * Sin[n * β * p/2]/(μ0 * n * π) * (Sin[n * Pi/2] − Sin[3 * n * Pi/2]);
c6 = C6/.sol/.an → 2 * Br * Sin[n * β * p/2]/(μ0 * n * π) * (Cos[n * Pi/2] − Cos[3 * n * Pi/2])/.
bn → 2 * Br * Sin[n * β * p/2]/(μ0 * n * π) * (Sin[n * Pi/2] − Sin[3 * n * Pi/2]);
c7 = C7/.sol/.an → 2 * Br * Sin[n * β * p/2]/(μ0 * n * π) * (Cos[n * Pi/2] − Cos[3 * n * Pi/2])/.
bn → 2 * Br * Sin[n * β * p/2]/(μ0 * n * π) * (Sin[n * Pi/2] − Sin[3 * n * Pi/2]);
c8 = C8/.sol/.an → 2 * Br * Sin[n * β * p/2]/(μ0 * n * π) * (Cos[n * Pi/2] − Cos[3 * n * Pi/2])/.
bn → 2 * Br * Sin[n * β * p/2]/(μ0 * n * π) * (Sin[n * Pi/2] − Sin[3 * n * Pi/2]);
```

Potential identification using analytical solution { }

```
A1[r_, θ_]:= Σ_{n=1}^{200} ((c5 * r^(n*p) + c6 * r^(−n*p)) * Cos[n * p * θ] + (c7 * r^(n*p) + c8 * r^(−n*p)) * Sin[n * p * θ]);

Bar[r_, θ_] = ∂_θ A1[r, θ]/r;
Bat[r_, θ_] = −∂_r A1[r, θ];
Aairgap = A1[r, θ]/.r → Rg;
Brairgap = Bar[r, θ]/.r → Rg;
```

$$\text{Btairgap} = \text{Bat}[r, \theta]/.r \to \text{Rg};$$

$$\text{Bart} = \text{Bat}[\text{Rg}, \theta - \omega\text{rm} * t];$$

$$\text{Plot3D}\left[\text{Bart}, \left\{\theta, 0, \frac{2\pi}{p}\right\}, \{t, 0, 0.1\}\right]$$

Results

$$\text{Br} = 1.18;$$
$$\mu 0 = 4 * \pi * 10^{-7};$$
$$p = 10;$$
$$\beta = \alpha * (\pi/p);$$
$$\alpha = 2/3;$$
$$\mu\text{r} = 1.05;$$
$$\text{Rr} = 23.97 * 10^{-3};$$
$$\text{Rm} = 27.55 * 10^{-3};$$
$$\text{Rs} = 28.1 * 10^{-3};$$
$$\omega\text{rm} = 100 * \pi;$$
$$\text{Lu} = \frac{50.82}{10^3};$$
$$\text{Nc} = 20;$$
$$\text{Rg} = \frac{(\text{Rs}+\text{Rm})}{2};$$
$$\text{Plot}\left[\text{Aairgap}, \left\{\theta, 0, \frac{2*\pi}{p}\right\}, \text{Filling} \to \text{Axis}\right]$$
$$\text{Plot3D}\left[\text{Bart}, \left\{\theta, 0, \frac{2*\pi}{p}\right\}, \{t, 0, 0.1\}\right]$$

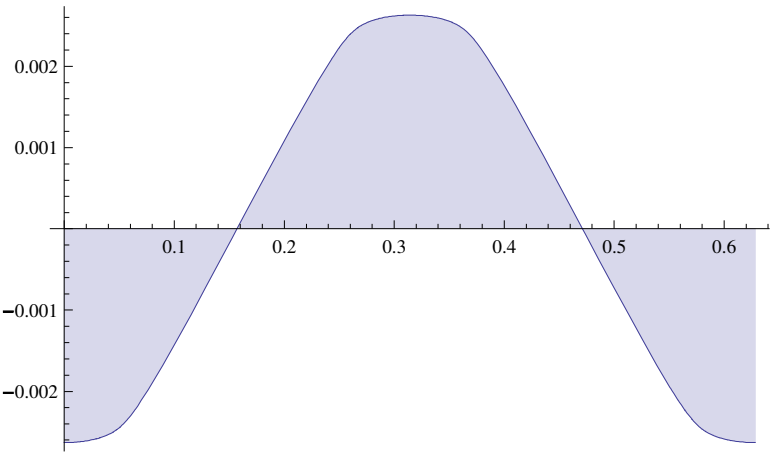

Figure A.1: Airgap potential p=10

$$\text{Plot}\left[\text{Brairgap}, \left\{\theta, 0, \frac{2*\pi}{p}\right\}, \text{Filling} \to \text{Axis}\right]$$
$$\text{Plot}\left[\text{Btairgap}, \left\{\theta, 0, \frac{2*\pi}{p}\right\}, \text{Filling} \to \text{Axis}\right]$$

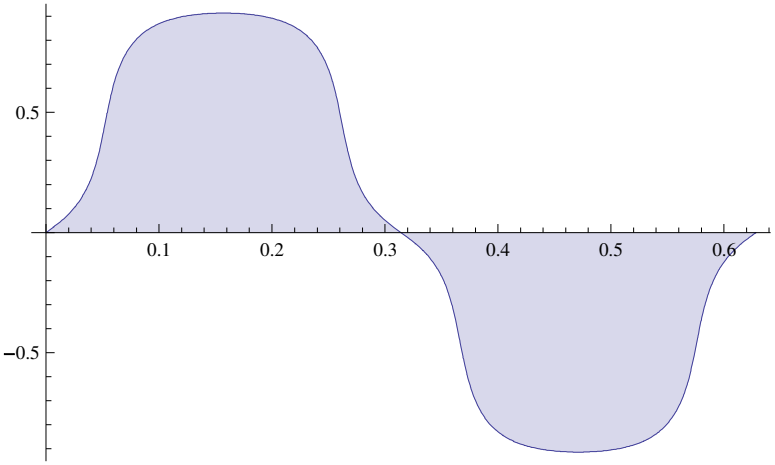

Figure A.2: Radial flux $B_n(\theta)$

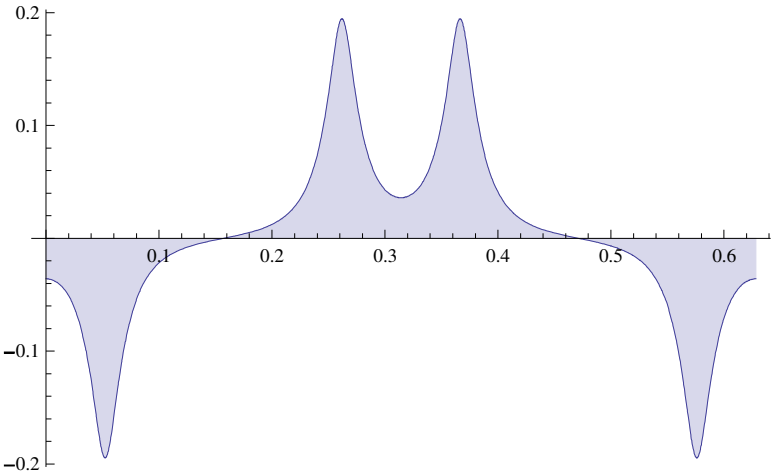

Figure A.3: Tangential flux $B_t(\theta)$

$$\phi[t\_]:=\text{Lu} * \text{Rg} * \int_{-\frac{1}{2}\text{ay}}^{-\frac{1}{2}\text{ay}} \text{Bart}[\text{Rg}, \theta, t]\, d\theta$$

$$\text{Plot}\left[\phi[t], \left\{r, 0, \frac{2*\pi}{p}\right\}, \text{Filling} \to \text{Axis}\right]$$

$$\text{Plot}\left[\phi[t], \left\{r, 0, \frac{2\pi}{p}\right\}, \text{Filling} \to \text{Axis}\right]$$

$$\text{Plot}\left[\text{Bar}[\text{Rg}, 0 - \omega\text{rm} * t], \left\{t, 0, \frac{2*\pi}{p}\right\}\right];$$

Analytical model due to stator currents

$$\text{Qs} = 24;$$

$$p = 2;$$

$$q = \text{Qs}/(2 * p * \text{mp});$$

$$\text{If}[q = 1, y = \text{Qs}/(2 * p)];$$

$$\text{ay} = y * (360/\text{Qs}) * \text{Pi}/180;$$

$$y = 1;$$

$$\text{ay} = y * (360/\text{Qs}) * \text{Pi}/180;$$

$$\text{mp} = 3;$$

$$\text{Qcoil} = \text{Qs}/(6);$$

$$\text{Nc} = 46;$$

$$\text{Ns} = (\text{Nc} * \text{Qcoil});$$

$$q = \text{Qs}/(2 * p * \text{mp});$$

$$\text{tt} = \text{GCD}[\text{Qs}, p];$$

$$\text{If}[\text{OddQ}[\text{Qs}/(\text{tt})], \text{qp} = \text{Qs}/(\text{mp} * \text{tt}), \text{qp} = \text{Qs}/(2 * \text{mp} * \text{tt})];$$

$$\text{Qs} = 24$$

$$p = 2$$

$$\text{Nc} = 46;$$

$$\text{Nc} = 23;$$

$$\text{If}[q == 1,$$

$$\{y = \text{Qs}/p/2;$$

```
ay = 2 * y/Qs * Pi},
If[Mod[q, 1] ≠ 0,
If[(Qs/p/2) < 1,
{y = 1;
ay = 2 * y/Qs * Pi; },
{y = Floor[Qs/p/2];
ay = 2 * y/Qs * Pi; },
{y = Round[0.8 * Qs/(2 * p)];
ay = 2 * y/Qs * Pi}
]
]
];
If[IntegerQ[q],
{Qcoil = Qs/2 * mp; Nc = Nc}
{Qcoil = Qs/mp; Nc = 1/2 * Nc}
]
Ns = Nc * Qcoil/ap

q = Qs/p/mp/2;
tt = GCD[Qs, p];
If[OddQ[Qs/tt],
qp = Qs/mp/tt,
If[EvenQ[Qs/tt],
qp = Qs/mp/tt/2]
];
If[IntegerQ[q],
{alffa = (p * 2 * Pi)/(Qs), kdn = Sin[n * q * alffa/2]/(q * Sin[n * alffa/2])},
{alfap = (180/(mp * qp)) * Pi/180, kdn = Sin[n * qp * alfap/2]/(qp * Sin[n * alfap/2])}];

Ks = Jcn * Cos[ni * θ + xa];
```

```
Bri[r, θ]:=(-(C1 * r^ni + C2/r^ni)) * Sin[ni * θ + xa] * (ni/r);
Hri[r, θ] = (-(C1 * r^ni + C2/r^ni)) * Sin[ni * θ + xa] * (ni/(r * μ0));
Bthetai[r_, θ_]:=(-(C1 * r^ni * (ni/r) - (C2 * (ni/r))/r^ni)) * Cos[ni * θ + xa];
Hthetai[r_, θ_]:=Bthetai[r, θ]/μ0;
sol1 = Solve[Hthetai[Rr, θ]==0, C1];
S1 = Hthetai[Rs, θ]/.sol1;
sol2 = Solve[S1== - Ks, C2];
C2/.sol2;
C1/.sol1;
Xri = (-Jcn) * Rs * μ0 * (r^ni/Rr^(2 * ni) + r^(-ni))*]Sin[(ni * θ + xa)/(r * (Rs^ni/Rr^(2 * ni) -
Rs^(-ni)))];
Xti = (-Jcn) * Rs * μ0 * (r^ni/Rr^(2 * ni) - r^(-ni)) * Cos[(ni * θ + xa)/(r * (Rs^ni/Rr^(2 * ni) -
Rs^(-ni)))];
xx = (-Jcn) * Rs * μ0 * (r^ni/Rr^(2 * ni) + r^(-ni)) * Sin[(ni * θ + xa)/
(r * (Rs^ni/Rr^(2 * ni) - Rs^(-ni)))];
Bxr = (-Jcn) * Rs * μ0 * ((r^ni/Rr^(2 * ni) + r^(-ni))/(r * (Rs^ni/Rr^(2 * ni) - Rs^(-ni))));
```

the three phase currents are defined function of the winding table

```
sgnA = {1, 1, 1, 1};
alphaA = {0, (1/12) * Pi, Pi, 13 * Pi * (1/12)};
sgnC = {-1, -1, -1, -1};
alphaC = {(1/6) * Pi, (1/4) * Pi, 7 * Pi * (1/6), 5 * Pi * (1/4)};
sgnB = {1, 1, 1, 1};
alphaB = {(1/3) * Pi, 5 * Pi * (1/12), 4 * Pi * (1/3), 17 * Pi * (1/12)};
ap = 1;
p = 2;
Qs = 24;
NHI = 100;
NHE = 10;
epa = 0.67 * 10^-2;
```

```
epe = 0.8 * 10^-3;
Rs = 0.7310^-1;
beta = 1;
Imx = 10;
Rm = Rs - epe;
Rr = Rm - epa;
mu1 = 1.0;
μ0 = 4 * Pi * 0.1 * 10^-6;
Br = .8;
M = Br/μ0;
Lu = 40 * 10^(-3);
wrm1 = 275;
r = (Rs + Rm) * (1/2);
wrm = 2 * wrm1 * Pi * (1/60);
t0 = -(1/2) * Pi/(p * wrm);
pe = 4 * Pi * (1/180);
nh = 100;
Jcn:=2 * Nc * Imx * Sin[(1/2) * ni * pe] * Sin[ni * y * Pi/Qs]/(Pi * Rs * ((1/2) * ni * pe));
ang:=ni * θ + Arg[Sin[ni * y * Pi/Qs] + i * Cos[ni * y * Pi/Qs]];
Jc:= ∑_{ni=1}^{nh} Jcn * Cos[ang];
angA:=ang - ni * alphaA[[k]];
angB:=ang - ni * alphaB[[k]];
angC:=ang - ni * alphaC[[k]];
JcA:= ∑_{k=1}^{Qcoil} ∑_{ni=1}^{nh} (sgnA[[k]] * Jcn * Cos[angA]);
JcB:= ∑_{k=1}^{Qcoil} ∑_{ni=1}^{nh} (sgnB[[k]] * Jcn * Cos[angB]);
JcB:= ∑_{k=1}^{Qcoil} ∑_{ni=1}^{nh} (sgnB[[k]] * Jcn * Cos[angB]);

xa = Arg[Sin[ni * y * (Pi/Qs)] + i * Cos[ni * y * (Pi/Qs)]] - ni * alphaA[[k]];
xb = Arg[Sin[ni * y * (Pi/Qs)] + i * Cos[ni * y * (Pi/Qs)]] - ni * alphaB[[k]];
xc = Arg[Sin[ni * y * (Pi/Qs)] + i * Cos[ni * y * (Pi/Qs)]] - ni * alphaC[[k]];
Ik = (4 * Imx * Sin[(Pi * nn)/3])/(Pi * nn);
```

$$i1 = Ik * Cos[nn * p * wrm * (t + t0)];$$

$$i2 = Ik * Cos[nn * p * wrm * ((t + t0) + (2 * Pi)/(3 * (wrm * p)))];$$

$$i3 = Ik * Cos[nn * p * wrm * ((t + t0) + (4 * Pi)/(3 * (wrm * p)))];$$

$$nn = 2 * kx + 1;$$

$$IA = \sum_{kx=0}^{NHI} i1;$$

$$IB = \sum_{kx=0}^{NHI} i2;$$

$$IC = \sum_{kx=0}^{NHI} i3;$$

$$isa = 1;$$

$$isb = 0;$$

$$isc = -1;$$

$$Bri[\theta\_] :=$$

$$\sum_{k=1}^{Qcoil} \sum_{ni=1}^{nh} (Bxr * (isa * sgnA[[k]] * Sin[ni * \theta + xa] + isb * sgnB[[k]] * Sin[ni * \theta + xb] + isc * sgnC[[k]] * Sin[ni * \theta + xc]))$$

$$Bti[\theta\_] :=$$

$$\sum_{k=1}^{Qcoil} \sum_{ni=1}^{nh} (Bxt * (isa * sgnA[[k]] * Cos[ni * \theta + xa] + isb * sgnB[[k]] * Cos[ni * \theta + xb] + isc * sgnC[[k]] * Cos[ni * \theta + xc]))$$

$$Plot[\{IA, IB\}, \{t, 0, 1\}, Filling->Axis]$$

$$Plot\left[Bti[\theta], \left\{\theta, 0, \frac{2*Pi}{p}\right\}, Filling->Axis\right]$$

$$Plot\left[Bri[\theta], \left\{\theta, 0, \frac{2*Pi}{p}\right\}, Filling->Axis\right]$$

```
Conformal transformation
```

$$\theta s = \frac{2*Pi}{Qs}$$

$$s = e^{z};$$

$$p = \sqrt{(((w - b)/(w - a)))}$$

$$z = j * (g1/Pi)[Log[Abs[(1 + p)/(1 - p)]] - Log[Abs[(b + p)/(b - p)] - ((2 * (b - 1))/Sqrt[b]) * ArcTan[p/Sqrt[b]]]];$$

$$t = i\frac{g1}{\pi} Log[w] + Log[Rs] + i((\theta s)/2);$$

$$k = e^{t};$$

```
w = FindMinimum [Re[z - z[w]]^2 + Im[z - z[w]]^2, w] ;
λ[s_]:=[(k/s)(((w - 1))/((w - a)^[(1/2)](w - b)^[(1/2)]))]*;

FourierSeries[λ[s], t, n];
λan = FourierSinCoefficient[λ[s], s, n];
λbn = FourierCosCoefficient[λ[s], s, n];
λ0 = FourierSinCoefficient[λ[s], s, 0];
λa = λ0 + ∑_{n=1}^{Nl} λan * Cos[n * Qs * θ]
λb = ∑_{n=1}^{Nl} λbn * Sin[n * Qs * θ]
```

A.4 Linear Flux Reversall FEMM Lua code

LUA for Femm code for drawing FRM FC prototype 1 using FEMM

```
%% FEMM analysis for  LFRM
%% open  FEMM
clear all;
openfemm
newdocument(0);

%% Definition of the magnetic problem
freq=0; % we define magnetostatic problem
units='millimeters';
type='planar';
precision=1e-8;
depth=1;
minangle=30;
mi_probdef(freq,units,type,precision,depth,minangle);
automesh=1;
meshsize=1;
%% Geometric parameters
taupm=12;
hslot=14;
hopen=12;
hyoke=12;
airgap=0.5;
hmover=18;
hpm=hmover-2;
lpm=3;
%% Definition of materials
materials=struct('permanent_magnets','NdFeB 52 MGOe',...
    'Laminations','US Steel Type 2-S 0.024 inch thickness',...
    'Conductor','2.5mm',...
    'Envirovment','Air');


mi_getmaterial(materials.permanent_magnets);
mi_getmaterial(materials.Laminations);
mi_getmaterial(materials.Conductor);
mi_getmaterial(materials.Envirovment);

%% Definition of circuits
NominalCurrent=10;
circuits=struct('phaseNr',1,'CircuitsName',[],...
'CircuitsCurrent',[],'NrOfTurns',1,'Connection',0);

for i=1:circuits.phaseNr
    mi_addcircprop(strcat('Phase',num2str(i)),...
     NominalCurrent, circuits.Connection);
    circuits.CircuitsName=strcat('Phase',num2str(i));
    mi_addcircprop(strcat('retPhase',num2str(i),''),...
```

```
    -1* NominalCurrent, circuits.Connection);
    circuits.CircuitsName=strcat('RetPhase',num2str(i));
end

%% Definition of objects Regions
object=struct(...
    'Name','',...
    'Material','',...
    'Geometry',[],...
    'automesh',[],...
    'meshsize',[],...
    'Circuit','',...
    'MagnetDir','',...
'Group','',...
'Turns',[],...
'CoordinateLabel',[]);

%% Regions initilize;
PM_N=object;

PM_N.Material=materials.permanent_magnets;
PM_S.MagnetDir=0;
PM_S.Group=111;
PM_N.CoordinateLabel=[];

PM_S=PM_N;
PM_S.MagnetDir=180;
PM_S.Group=110;
PM_S.CoordinateLabel=[];

coil objects
Coil_A1=object;
Coil_A1.Circuit='PhaseA';
Coil_A1.Turns=10;
Coil_A1.CoordinateLabel=[];

Coil_A1_Ret=Coil_A1;
Coil_B1=Coil_A1;
Coil_A2=object;
Coil_B2=object;

Stator1=object;
Stator1.Material=materials.permanent_magnets;
Stator2=Stator1;
Air=object;

%domain={PM_N,PM_S};
 Definition of Stator elements boundaries

geometry=struct();
geometry.Points.x=[
```

```
    0
    0
    (taupm*(-6))
    (taupm*(-6))
    (taupm*(-5))
    (taupm*(-5))
    (taupm*(-4))
    (taupm*(-4))
    (taupm*(-3))
    (taupm*(-3))
    (taupm*(-2))
    (taupm*(-2))
    (taupm*(-1))
    (taupm*(-1))
    ];
geometry.Points.y=[
    hslot
    (hslot+hyoke)
    (hslot+hyoke)
    0
    0
    hopen
    hopen
    0
    0
    hopen
    hopen
    0
    0
    hslot

    ];
Definition of Label center
Stator.Label.Center.x=-6*taupm/2;
Stator.Label.Center.y=(hyoke/2+hslot);
%geometry.y=
nrPoints=(size(geometry.Points.x));
%Point(x1,y1,'None',group);

 Define group Stator
GrStat=10;
firstPoint.x=geometry.Points.x(1);
firstPoint.y=geometry.Points.y(1);
lastPoint.x=geometry.Points.x(nrPoints);
lastPoint.y=geometry.Points.y(nrPoints);
%draw the geometry of the stator
Segments(firstPoint.x,firstPoint.y,lastPoint.x,lastPoint.y,...
1,1,0,0,GrStat);
%Definition of stator Label center
xc=(taupm*(-6))/2;
yc=hslot+hyoke/2;
```

```
for i=1:(nrPoints-1)
    %if i<nrPoints
    x1=geometry.Points.x(i);
    y1=geometry.Points.y(i);
    x2=geometry.Points.x(i+1);
    y2=geometry.Points.y(i+1);
   % else
   % x1=geometry.Points.x(i);
   % y1=geometry.Points.y(i);
   % x2=geometry.Points.x(i);
   % y2=geometry.Points.y(i);
   % end
    %Point(x1,y1,'None',GrStat);
   %mi_addnode(x1,y1);
   Segments(x1,y1,x2,y2,1,1,0,0,GrStat);
end
% Mirror three times the stator geometry

% Add region
Region(xc,yc,'LaminationsS',circuits,materials);
mi_selectgroup(GrStat);
mi_mirror(0,0,0,1);
mi_selectgroup(GrStat);
mi_copyrotate(taupm/4, -(hmover/2+airgap), 180, 1);
%mi_mirror(0,-(hmover/2+airgap),1,-(hmover/2+airgap));
%mi_copyrotate(dx, dy, copies, (editaction))
%pause
% Draw the Coil
GrCoil=11;
[xc1,yc1]=DrawRectangle(-7*taupm,0,taupm,hslot,1,1,0,0,GrCoil);
Region(xc1,yc1,'CoilPhaseA',circuits,materials);
[xc1,yc1]=DrawRectangle(-taupm,0,taupm,hslot,1,1,0,0,GrCoil);
Region(xc1,yc1,'CoilPhaseA',circuits,materials);
[xc1,yc1]=DrawRectangle(0,0,taupm,hslot,1,1,0,0,GrCoil);
Region(xc1,yc1,'CoilPhaseA',circuits,materials);
[xc1,yc1]=DrawRectangle(6*taupm,0,taupm,hslot,1,1,0,0,GrCoil);
Region(xc1,yc1,'CoilPhaseA',circuits,materials);

[xc1,yc1]=DrawRectangle(-7*taupm+taupm/2,-2*airgap-hmover-hslot,...
taupm,hslot,1,1,0,0,GrCoil);
Region(xc1,yc1,'CoilPhaseA',circuits,materials);
[xc1,yc1]=DrawRectangle(-taupm+taupm/2,-2*airgap-hmover-hslot,...
taupm,hslot,1,1,0,0,GrCoil);
Region(xc1,yc1,'CoilPhaseA',circuits,materials);
[xc1,yc1]=DrawRectangle(taupm/2,-2*airgap-hmover-hslot,...
taupm,hslot,1,1,0,0,GrCoil);
Region(xc1,yc1,'CoilPhaseA',circuits,materials);
[xc1,yc1]=DrawRectangle(6*taupm+taupm/2,-2*airgap-hmover-hslot,...
taupm,hslot,1,1,0,0,GrCoil);
Region(xc1,yc1,'CoilPhaseA',circuits,materials);
```

```
% mi_selectgroup(GrCoil);
%
% mi_copytranslate(-6*taupm, 0, 1);
% mi_selectgroup(GrCoil);
% mi_copytranslate(taupm/2, -2*airgap-hmover-hslot, 1);
%
% mi_selectgroup(GrCoil);
% mi_copytranslate(7*taupm, 0, 1);

%% Draw the mover geometry
GrMover=12;
ActualPosition=0;
[xc,yc]=DrawRectangle(-6*taupm-taupm/2+ActualPosition,-airgap,...
14*taupm,-hmover,1,1,0,0,GrMover);
Region(xc,yc,'LaminationsM',circuits,materials);

%DrawRectangle(x0,y0,width,heigth,conditions,elementsize,...
%automesh,hide,group)
%mi_selectgroup(GrStat);
% Draw permanent magnet
% GrMover=11;
% DrawRectangle(-6*taupm-taupm/2,-airgap,...
% 12*taupm,-hmover,1,1,0,0,GrMover);
% %DrawRectangle(x0,y0,width,heigth,conditions,...
% elementsize,automesh,hide,group)

%% Draw permanent magnet geometry north
GrPmsN=13;
GrPmsS=14;
[xc,yc]=DrawRectangle(7*taupm-lpm/2,-airgap-(hmover-hpm)/2,...
lpm,-hpm,1,1,0,0,GrPmsN);
Region(xc,yc,'MagnetN',circuits,materials);
[xc,yc]=DrawRectangle(6*taupm-lpm/2,-airgap-(hmover-hpm)/2,...
lpm,-hpm,1,1,0,0,GrPmsS);
Region(xc,yc,'MagnetS',circuits,materials);

mi_selectgroup(GrPmsN);
mi_copytranslate(-taupm*2, 0, 6);
mi_selectgroup(GrPmsS);
mi_copytranslate(-taupm*2, 0, 6);

%% draw outerregion
GrAir=0;

mi_zoomnatural();
DrawRectangle(-10*taupm,-0.75*(2*airgap+hmover+2*hslot...
+2*hyoke),20*taupm,...
    1.5*(2*airgap+hmover+2*hslot+2*hyoke),1,1,0,0,GrAir);
Region(9.9*taupm,0,'Air',circuits,materials);
mi_zoomnatural();
%% Save files
```

```
mi_saveas('temp.fem')
%% Processing

step=1;
position=0;

mode='Cogging'

switch mode
    case 'Cogging'

        sprintf('position in mm | force in N')
        %open("Roters-Ch9Fig6.fem")
        mi_saveas('temp.fem')
        for n=(0:step:taupm)
            mi_analyze()
            mi_loadsolution()
            mo_groupselectblock(12)
            mo_groupselectblock(13)
            mo_groupselectblock(14)
            force=mo_blockintegral(19)/depth;
            flux=mo_
            Output.Force(n+1)=f;
            Output.Position(n+1)=n;
            Output.Flux(n+1)=
            %    sprintf(0.1*n,f)

           %% Computation of the magnetic quantities
           case 'Noload'

%% initialization of the flux linkages

  fluxA_re=0
  flussoA_im=0

  mo_groupselectblock(1001)
  Sup = mo_blockintegral(5)
  m0_clearblock()

 for q = 1, Qsim ,1
%% slots are groups 1001, 1002, ...
     groupselectblock(1000+q)
     Areal, Aimag = blockintegral(1)
     clearblock()

     Areal = Areal / Sup
     Aimag = Aimag / Sup

     fluxA_re = flussoA_re + Areal * ka[q]
     fluxoB_re = flussoB_re + Areal * kb[q]
     flussoC_re = flussoC_re + Areal * kc[q]
```

```
      flussoA_im = flussoA_im + Aimag * ka[q]
      flussoB_im = flussoB_im + Aimag * kb[q]
      flussoC_im = flussoC_im + Aimag * kc[q]

 end

%% Alternative for the selection:
%% selectblock(Dslot/2*cos(360/24*q+angle),
%Dslot/2*sin(360/24*q+angle))

  flussoA_re = flussoA_re * Lstk * nc * period
  flussoB_re = flussoB_re * Lstk * nc * period
  flussoC_re = flussoC_re * Lstk * nc * period

  flussoA_im = flussoA_im * Lstk * nc * period
  flussoB_im = flussoB_im * Lstk * nc * period
  flussoC_im = flussoC_im * Lstk * nc * period

%% torque and losses

  groupselectblock(10)
  Torque = blockintegral(22) * period
  RotLosses = blockintegral(6) * period
  clearblock()

%% magnetic energy

  groupselectblock()
  Energy = blockintegral(2) * period
  Coenergy = blockintegral(17) * period
  AJintrg = blockintegral(0) * period

%% Append the result in file

   handle=fopen('results.txt','a')
   fprintf(handle,'%6.6f %6.6f %6.6f %6.6f %6.6f...
    %6.6f %6.6f n',...
                flussoA_re,flussoA_im,Force,...
                MoverLosses,Energy,Coenergy,AJintrg);
   fclose(handle)

exitpost()


            mo_close()
            for i=GrMover:GrPmsS
                mi_seteditmode('group')
                mi_selectgroup(i)
                mi_movetranslate(step,0)
            end
```

```
        end
        save
    case 'test'
        for i=1:taupm
            for i=12:14
                mi_seteditmode('group')
                mi_selectgroup(i)
                mi_movetranslate(step,0)
            end

        end
end
```

A.5 Radial Flux Reversal FEMM Lua Code

This code was developed using LUA scripting language for FEMM modeling of the nonoverlapping radial flux reversal PMSM used in chapter 5.

```
%%  RFRM FEM
%% model setup

openfemm;
newdocument(0);
Liron=1;
mi_probdef(0,'millimeters','planar',1E-8,Liron,30);

mi_saveas('NomProblem');

Hide=1;
NoHide=0;

%% Groups
Grp0=0;
GrpSta=1;
GrpEnc=2;
GrpRot=3;

IphaseU=0;
IphaseV=0;
IphaseW=0;

%% Creation des circuits
mi_addcircprop('Phase1',IphaseU,0);
mi_addcircprop('Phase2',IphaseV,0);
mi_addcircprop('Phase3',IphaseW,0);

mi_addcircprop('Phase1',IphaseU,0);
mi_addcircprop('Phase2',IphaseV,0);
mi_addcircprop('Phase3',IphaseW,0);


%% Add materials
mi_getmaterial('NdFeB 40 MGOe')
mi_getmaterial('1010 Steel')
mi_getmaterial('Air')
mi_getmaterial('1mm')

mi_addboundprop('A=0',0,0,0,0,0,0,0,0,0)

GrCoil=130;

Qs=6;
poles=48;
```

```
theta=2*pi/poles;
Rr1=100;
Rr2=90;
Ro=200;
hbridge=0.1;
hpm=19.5;
lpm=5.5;

sSize=3;
%% Second stator design

p1=[sin(theta*8)*Rr1, cos(theta*8)*Rr1];
p2=[sin(theta*15/2)*Rr1, cos(theta*15/2)*Rr1];
p3=[sin(theta*15/2)*Rr2, cos(theta*15/2)*Rr2];
p4=[sin(theta*13/2)*Rr2, cos(theta*13/2)*Rr2];
p5=[sin(theta*13/2)*Rr1, cos(theta*13/2)*Rr1];
p6=[sin(theta*11/2)*Rr1, cos(theta*11/2)*Rr1];
p7=[sin(theta*11/2)*Rr2, cos(theta*11/2)*Rr2];
p8=[sin(theta*9/2)*Rr2, cos(theta*9/2)*Rr2];
p9=[sin(theta*9/2)*Rr1, cos(theta*9/2)*Rr1];
p10=[sin(theta*7/2)*Rr1, cos(theta*7/2)*Rr1];
p11=[sin(theta*7/2)*Rr2, cos(theta*7/2)*Rr2];
p12=[sin(theta*5/2)*Rr2, cos(theta*5/2)*Rr2];
p13=[sin(theta*5/2)*Rr1, cos(theta*5/2)*Rr1];
p14=[sin(theta*3/2)*Rr1, cos(theta*3/2)*Rr1];
p15=[sin(theta*3/2)*Rr2, cos(theta*3/2)*Rr2];
p16=[sin(theta*1/2)*Rr2, cos(theta*1/2)*Rr2];
p17=[sin(theta*1/2)*Rr1, cos(theta*1/2)*Rr1];
p18=[0, Rr1];
p19=[0,0];



mi_addnode(p1);
mi_addnode(p2);
mi_addnode(p3);
mi_addnode(p4);
mi_addnode(p5);
mi_addnode(p6);
mi_addnode(p7);
mi_addnode(p8);
mi_addnode(p9);
mi_addnode(p10);
mi_addnode(p11);
mi_addnode(p12);
mi_addnode(p13);
mi_addnode(p14);
mi_addnode(p15);
mi_addnode(p16);
mi_addnode(p17);
mi_addnode(p18);
```

```
mi_addnode(p19);
% mi_addnode(p20);


%% Add polygon
mi_addsegment(p1,p2);
mi_addsegment(p2,p3);
mi_addsegment(p3,p4);
mi_addsegment(p4,p5);
mi_addsegment(p5,p6);
mi_addsegment(p6,p7);
mi_addsegment(p7,p8);
mi_addsegment(p8,p9);
mi_addsegment(p9,p10);
mi_addsegment(p10,p11);
mi_addsegment(p11,p12);
mi_addsegment(p12,p13);
mi_addsegment(p13,p14);
mi_addsegment(p14,p15);
mi_addsegment(p15,p16);
mi_addsegment(p16,p17);
mi_addsegment(p17,p18);
mi_addsegment(p18,p19);
mi_addsegment(p19,p1);
% mi_addsegment(p20,p1)



%% Design of stator1
Airgap = 0.5;
hslot = 10;
hrotor=20;
Rs = Rr1 + 2*Airgap+hrotor;
Rs2 = Rs + hslot;
Ro = 200;
h1 = 5;
h2 = 40;
b1 = 15;
b2 = 30;


%% Stator design
s1 = [0, Ro];
s2 = [0, (Rs2 + h1 + h2)];
s3 = [((abs(Ro + ((Rs2 + h1 + h2)*(-1))))^((-1))*
(Ro+((Rs2 + h1 + h2)*(-1)))*b2), (Rs2 + h1 + h2)];
s4 = [((abs(Ro + ((Rs2 + h1 + h2)*(-1))))^((-1))*
(Ro+((Rs2 + h1 +h2)*(-1)))*b1), (Rs2 + h1)];
s5 = [sin(theta*1/2)*Rs2, cos(theta*1/2)*Rs2];
s6 = [sin(theta*1/2)*Rs, cos(theta*1/2)*Rs];
s7 = [sin(theta*3/2)*Rs, cos(theta*3/2)*Rs];
```

```
s8 = [sin(theta*3/2)*Rs2,cos(theta*3/2)*Rs2];
s9 = [sin(theta*5/2)*Rs2,cos(theta*5/2)*Rs2];
s10 = [sin(theta*5/2)*Rs,cos(theta*5/2)*Rs];
s11 = [sin(theta*7/2)*Rs,cos(theta*7/2)*Rs];
s12 = [sin(theta*7/2)*Rs2,cos(theta*7/2)*Rs2];
s13 = [sin(theta*4)*Rs2,cos(theta*4)*Rs2];
s14 = [sin(theta*4)*Ro,cos(theta*4)*Ro];



mi_addnode(s1);
mi_addnode(s2);
mi_addnode(s3);
mi_addnode(s4);
mi_addnode(s5);
mi_addnode(s6);
mi_addnode(s7);
mi_addnode(s8);
mi_addnode(s9);
mi_addnode(s10);
mi_addnode(s11);
mi_addnode(s12);
mi_addnode(s13);
mi_addnode(s14);


mi_addsegment(s1,s2);
mi_addsegment(s2,s3);
mi_addsegment(s3,s4);
mi_addsegment(s4,s5);
mi_addsegment(s5,s6);
mi_addsegment(s6,s7);
mi_addsegment(s7,s8);
mi_addsegment(s8,s9);
mi_addsegment(s9,s10);
mi_addsegment(s10,s11);
mi_addsegment(s11,s12);
mi_addsegment(s12,s13);
mi_addsegment(s13,s14);
mi_addarc(s14(1),s14(2),s1(1),s1(2),30,sSize);


Circle(0,0,Rr1+Airgap,110,100,sSize,'None');
Circle(0,0,Rr1+Airgap+hrotor,110,100,sSize,'None');


%% Define permanent magnet
rectangle(lpm,hpm,0,Rr1+Airgap+hrotor/2,poles,120);
```

```
%% Select stator points
GrStat1=90;
nPoints=19;
j=0;
for i=1:nPoints
    if i<nPoints

    j=i+1;
    else
      j=1;
    end
    x1=eval(strcat('p',num2str(i)));
     x2=eval(strcat('p',num2str(j)));
    [xc,yc]=midpoint(x1,x2);
    mi_selectsegment(xc,yc);
   mi_setsegmentprop('None', sSize, 0, 0, GrStat1);
end
mi_seteditmode('segments');
mi_copyrotate(0, 0, -60, 1);
mi_clearselected;
mi_selectnode(0,0);
mi_deleteselectednodes;


%% Select stator2 points
nPoints=14;
j=0;
GrStat2=100;
for i=1:nPoints
    if i<nPoints
    j=i+1;
    else
      j=1;
    end
    x1=eval(strcat('s',num2str(i)));
     x2=eval(strcat('s',num2str(j)));
    [xc,yc]=midpoint(x1,x2);
    mi_selectsegment(xc,yc);
   mi_setsegmentprop('None', sSize, 0, 0,GrStat2);
end




mi_createradius(s3(1),s3(2),10);
mi_selectarcsegment(s3(1),s3(2));
mi_setarcsegmentprop(sSize, 'None',0,GrStat2);

 mi_selectgroup(GrStat2);
 mi_mirror(0,0,Ro*cos(pi/3),Ro*sin(pi/3));
```

```
 mi_selectgroup(GrStat2);
mi_copyrotate(0, 0, 60,5);
mi_selectgroup(GrStat1);
mi_copyrotate(0, 0, 120,2);
GrPm=120;
mi_selectgroup(GrPm);
 mi_copyrotate(0,0,-4*180/poles,24);
mi_clearselected;

%% Adding labels

[c1(1),c1(2)]=midpoint(s3,s4);
c2=[0, c1(2)];
c3=s4;
c4=[0,c3(2)];


mi_addnode(c1);
mi_addnode(c2);
mi_addnode(c4);


mi_addsegment(c1,c2);
mi_addsegment(c3,c4);


[xcoil1,ycoil1]=midpoint(c1,c2)

 mi_selectsegment(xcoil1,ycoil1);
   mi_setsegmentprop('None', sSize, 0, 0,GrStat2);
mi_clearselected();
mi_selectarcsegment(Ro*cos(pi/2-pi/12),Ro*sin(pi/2-pi/12));
mi_setarcsegmentprop(sSize, 'None',0, GrStat2);
% mi_mirror(0,0,0,Ro);

mi_copyrotate(0, 0, 30,11);


mi_clearselected();
%mi_selectarcsegment(Ro*cos(pi/2-pi/12),Ro*sin(pi/2-pi/12));
mi_selectsegment(c1(1)/2,c1(2));
mi_selectsegment(c3(1)/2,c3(2));
mi_mirror(0,0,0,Ro);
mi_copyrotate(0, 0, 60,5);
% mi_selectsegment(c1(1)/2,c1(2));
mi_selectsegment(c3(1)/2,c3(2));
mi_setsegmentprop('None', sSize, 0, 0, GrStat2);
mi_selectsegment(c1(1)/2,c1(2));
mi_selectsegment(c3(2)/2,c3(2));
mi_mirror(0,0,0,Ro);
mi_selectsegment(c1(1)/2,c1(2));
```

```
mi_selectsegment(c3(1)/2,c3(2));
mi_selectsegment(-c1(1)/2,c1(2));
mi_selectsegment(-c1(1)/2,c3(2));
mi_copyrotate(0, 0, 60,5);
%
mi_addblocklabel(s3(1),s3(2));
automesh=0;
 meshsize=3;
 incircuit='';
 magdirection=0;
 group=GrStat2;
 turns=0;

mi_selectlabel(s3(1),s3(2));
mi_setblockprop('1010 Steel', automesh, meshsize, incircuit, ...
magdirection,group, turns);
mi_mirror(0,0,0,Ro);
mi_selectlabel(s3(1),s3(2));
mi_selectlabel(-s3(1),s3(2));
mi_copyrotate(0, 0, 60,5);
mi_clearselected;

%% LayerOne Labels
[xcoil1,ycoil1]=midpoint(c2,s2)
mi_addblocklabel(0,ycoil1);
mi_selectlabel();
%% LayerOne Labels
[xcoil2,ycoil2]=midpoint(c2,s4)
mi_addblocklabel(0,ycoil2);

[xcoil2,ycoil2]=midpoint(c2,s4)
mi_addblocklabel(0,ycoil2);

[xair1,yair1]=midpoint(s4,s5);
mi_addblocklabel(0,yair1);
mi_selectlabel(0,yair1);
mi_setblockprop('Air', automesh, meshsize, incircuit,...
 magdirection,group, turns);
 group=GrCoil;
 mi_clearselected;
mi_selectlabel(0,ycoil1);
mi_setblockprop('1mm', automesh, meshsize, 'Phase1',...
 magdirection,group, turns);
mi_clearselected;
mi_selectlabel(0,ycoil2);

mi_setblockprop('1mm', automesh, meshsize,'Phase1',...
 magdirection,group, turns);
mi_addblocklabel(0,0);
mi_setblockprop('1mm', automesh, meshsize,'Phase1',...
 magdirection,group, turns);
```

```
% mi_selectlabel(0,ycoil1);
% mi_selectlabel(0,ycoil2);
mi_selectlabel(0,ycoil1);
% mi_selectlabel(0,ycoil2);
mi_copyrotate(0, 0, 60,5);

%%  Three layers airgap
Circle(0,0,Rr1/2,110,100,sSize,'None');
Circle(0,0,Rr1/2,110,100,sSize,'None');

mi_addblocklabel(0,3/4*Rr1);
mi_selectlabel(0,3/4*Rr1);
mi_setblockprop('1010 Steel', automesh, meshsize, incircuit, ...
magdirection,group, turns);
mi_clearselected();

mi_addblocklabel(0,Rr1+Airgap+2*hrotor/3);
mi_selectlabel(0,Rr1+Airgap+2*hrotor/3);

mi_setblockprop('1010 Steel', automesh, meshsize, incircuit,...
 magdirection,GrPm, turns);
mi_moverotate(0, 0,7.5/2);
mi_clearselected();



mi_addblocklabel(0,Rr2-0.5*(Rr2-Rr1));
mi_selectlabel(0,Rr2-0.5*(Rr2-Rr1));
mi_setblockprop('Air', automesh, meshsize,incircuit, ...
magdirection,GrStat1, turns);
mi_moverotate(0, 0,7.5);
mi_clearselected();


mi_addblocklabel(0,0);
mi_selectlabel(0,0);
mi_setblockprop('Air', automesh, meshsize,incircuit, ...
magdirection,group, turns);


%% Sorrounding air
Circle(0,0,1.1*Ro,0,100,sSize,'A=0');


mi_addblocklabel(0,1.05*Ro);
mi_selectlabel(0,1.05*Ro);
mi_setblockprop('Air', automesh, meshsize, incircuit, ...
magdirection,group, turns);
mi_clearselected();

%Circle(0,0,Rr1+Airgap/3,110,100,sSize,'None');
```

```
%Circle(0,0,Rr1+2/3*Airgap,110,100,sSize,'None');
%Circle(0,0,Rr1+Airgap+hrotor+Airgap/3,110,100,sSize,'None');
%Circle(0,0,Rr1+Airgap+hrotor+2/3*Airgap,110,100,sSize,'None');
mi_zoomnatural();
```

A.6 18/16 Axial flux FEA Comsol FEMLAB analysis code

This code was developed using LUA scripting language for modeling an slice of the nonoverlapping axial flux PMSM used in chapter 5.

```
% COMSOL Multiphysics Model M-file
% Generated by COMSOL 3 and upgraded by  Marcel Topor



%function axial(D0,Din,g)
clc
clear all
%viarouge method
parameters;

tic

wmech=pi/30*speed;

%call winding design function Viarouge script
sb=viarouge(slots,poles,m);

Din=lambda*Do;
rmin=Din/2;
rmax=Do/2;
tausmin=2*pi*rmin/slots;
lcoil=(tausmin-TW)/2-linsulation;
L=(Do-Din)/2;
ls=L/slices;

%the big loop
for k=0:slices-1
%k=5;
clear fem
%flclear fem

%various parameters and data  updated for
%the design
radius=Do/2-ls*k;
taupm=2*pi*radius/poles;
taus=2*pi*radius/slots;

%coil width is equal to the smallest area

hatx=(taus-TW-b0)/2;
haty=th-(2*ovg+lstack+hcoil+h0);
%coil area
```

```
Acoil=lcoil*hcoil-ovg*ovg;

lpm=taupm-lspacer;


%g1=rect2(th,tw,'base','corner','pos',[0,0]);
% Constants

% Constants
fem.const = {'hback','0.011', ...
  'Imax',num2str(Imax), ...
  'coil_area',num2str(Acoil), ...
  'Nt','47', ...
  'Jin','Nt*Imax*sqrt(2)/coil_area', ...
  'coil_w','0.013', ...
  'coil_h','0.035', ...
  'Br','1.23', ...
  'Jout','-Jin', ...
  'Ja','Jin', ...
  'Jb','-Ja/2', ...
  'Jc','-Ja/2', ...
  'Jb_','-Jb', ...
  'speed','1800', ...
  'poles','16', ...
  'slots','18', ...
  'q','18/(3*16)', ...
  't_','2', ...
  'Jc_','-Jc', ...
  'tau_pole','2*pi/poles*radius', ...
  'Do',num2str(Do), ...
  'Din',num2str(Din), ...
  'L',num2str(L), ...
  'slices','5', ...
  'ls','L/slices', ...
  'radius','Do/2', ...
  'taus','2*pi/slots*radius', ...
  'th','0.049', ...
  'tw','0.02', ...
  'hpm','0.005', ...
  'sigFe','1.03e7', ...
  'sigCu','5.99e7', ...
  'sigNeFeBr','0.694', ...
  'murNeFeBr','1.045', ...
  'murFe','2000', ...
  'vx','1800/60*radius', ...
  'murCu','1'};



clear fcns
fcns{1}.type='interp';
```

```
fcns{1}.name='MUR';
fcns{1}.method='cubic';
fcns{1}.extmethod='extrap';


for i=1:length(MUR)
dd=num2str(MUR(i,1));
ee=num2str(MUR(i,2));
xx(i)={dd};
yy(i)={ee};
end


fcns{1}.x=xx;
fcns{1}.data=yy;
fem.functions = fcns;

% Geometry definition the easy part
% Tooth shape design 1-18

s1x=[0,0];
s2x=[0,tw+ovg];
s3x=[tw+ovg,tw+ovg];
s4x=[tw+ovg,tw];
s5x=[tw,tw];
s6x=[tw,tw+ovg];
s7x=[tw+ovg,tw+ovg];
s8x=[tw+ovg,tw];
s9x=[tw,tw];
s10x=[tw,tw+hatx];
s11x=[tw+hatx,tw+hatx];
s12x=[tw+hatx,0];



s1y=[0,th];
s2y=[th,th];
s3y=[th,th-ovg];
s4y=[th-ovg,th-ovg];
s5y=[th-ovg,th-ovg-lstack];
s6y=[th-ovg-lstack,th-ovg-lstack];
s7y=[th-ovg-lstack,th-2*ovg-lstack];
s8y=[th-2*ovg-lstack,th-2*ovg-lstack];
s9y=[th-2*ovg-lstack,th-2*ovg-lstack-hcoil];
s10y=[th-2*ovg-lstack-hcoil,h0];
s11y=[h0,0];
s12y=[0,0];
%we compute the area of the tooth usign a
%contour technique
SX=[s1x s2x s3x s4x s5x s6x s7x s8x s9x s10x s11x s12x];
SY=[s1y s2y s3y s4y s5y s6y s7y s8y s9y s10y s11y s12y];
```

```
C=[SX;SY];


Atooth(k+1)=2*polygeom(SX,SY);
Vtooth(k+1)=Atooth(k+1)*ls;


carr={curve2(s1x,s1y,[1,1]), ...
  curve2(s2x,s2y,[1,1]), ...
  curve2(s3x,s3y,[1,1]), ...
  curve2(s4x,s4y,[1,1]), ...
  curve2(s5x,s5y,[1,1]), ...
  curve2(s6x,s6y,[1,1]), ...
  curve2(s7x,s7y,[1,1]), ...
  curve2(s8x,s8y,[1,1]), ...
  curve2(s9x,s9y,[1,1]), ...
  curve2(s10x,s10y,[1,1]), ...
  curve2(s11x,s11y,[1,1]), ...
  curve2(s12x,s12y,[1,1])};
g1=geomcoerce('solid',carr);
g2=mirror(g1,[taus/2,0],[1,0]);
garr=geomarrayr(g1,taus,0,slots/2,1);

 [g1,g3,g5,g7,g9,g11,g13,g15,g17]=deal(garr{:});
 garr=geomarrayr(g2,taus,0,slots/2,1);
 [g2,g4,g6,g8,g10,g12,g14,g16,g18]=deal(garr{:});

% we draw the coils 19-36


carr={curve2([tw,tw+lcoil],[h0+haty,h0+haty],[1,1]), ...
  curve2([tw+lcoil,tw+lcoil],[h0+haty,h0+haty+hcoil+ovg],
  [1,1]), ...
  curve2([tw+lcoil,tw+ovg],[h0+haty+hcoil+ovg,...
  h0+haty+hcoil+ovg],
  [1,1]), ...
  curve2([tw+ovg,tw+ovg],[h0+haty+hcoil+ovg,...
  h0+haty+hcoil],
  [1,1]), ...
  curve2([tw+ovg,tw],[h0+haty+hcoil,...
  h0+haty+hcoil],[1,1]), ...
  curve2([tw,tw],[h0+haty+hcoil,h0+haty],[1,1]), ...
  curve2([tw,tw+lcoil],[h0+haty,h0+haty],[1,1])};
g19=geomcoerce('solid',carr);
g20=mirror(g19,[taus/2,0],[1,0]);
garr=geomarrayr(g19,taus,0,slots/2,1);
[g19,g21,g23,g25,g27,g29,g31,g33,g35]=deal(garr{:});

garr=geomarrayr(g20,taus,0,slots/2,1);
```

```
[g20,g22,g24,g26,g28,g30,g32,g34,g36]=deal(garr{:});



% now the PMs
g37=rect2(lpm,2*hpm,'base','corner','pos',[0,-g-2*hpm]);
% we need to multiply the PMs 37-44
garr=geomarrayr(g37,taupm,0,poles/2,1);
[g37,g38,g39,g40,g41,g42,g43,g44]=deal(garr{:});
% the interpms
g45=rect2(taupm-lpm,hpm*2,'base','corner','pos',...
[lpm,-g-2*hpm]);
% we need to multiply the spacers 45-52

garr1=geomarrayr(g45,taupm,0,poles/2,1);
[g45,g46,g47,g48,g49,g50,g51,g52]=deal(garr1{:});

%also the back iron is necesary to be done  53-61
g53=rect2(taus-TW,lstack,'base','corner','pos',...
[tw,th-ovg-lstack]);
garr=geomarrayr(g53,taus,0,slots/2,1);
[g53,g54,g55,g56,g57,g58,g59,g60,g61]=deal(garr{:});

Aback(k+1)=(taus-TW)*lstack;
Vback(k+1)=Aback(k+1)*ls;

%inner air dimension

%stator II 62-79
g62=mirror(g1,[0,-g-hpm],[0,1]);
g63=mirror(g2,[0,-g-hpm],[0,1]);
g64=mirror(g3,[0,-g-hpm],[0,1]);
g65=mirror(g4,[0,-g-hpm],[0,1]);
g66=mirror(g5,[0,-g-hpm],[0,1]);
g67=mirror(g6,[0,-g-hpm],[0,1]);
g68=mirror(g7,[0,-g-hpm],[0,1]);
g69=mirror(g8,[0,-g-hpm],[0,1]);
g70=mirror(g9,[0,-g-hpm],[0,1]);
g71=mirror(g10,[0,-g-hpm],[0,1]);
g72=mirror(g11,[0,-g-hpm],[0,1]);
g73=mirror(g12,[0,-g-hpm],[0,1]);
g74=mirror(g13,[0,-g-hpm],[0,1]);
g75=mirror(g14,[0,-g-hpm],[0,1]);
g76=mirror(g15,[0,-g-hpm],[0,1]);
g77=mirror(g16,[0,-g-hpm],[0,1]);
g78=mirror(g17,[0,-g-hpm],[0,1]);
g79=mirror(g18,[0,-g-hpm],[0,1]);

%Slots II 82-100
g80=mirror(g19,[0,-g-hpm],[0,1]);
```

```
g81=mirror(g20,[0,-g-hpm],[0,1]);
g82=mirror(g21,[0,-g-hpm],[0,1]);
g83=mirror(g22,[0,-g-hpm],[0,1]);
g84=mirror(g23,[0,-g-hpm],[0,1]);
g85=mirror(g24,[0,-g-hpm],[0,1]);
g86=mirror(g25,[0,-g-hpm],[0,1]);
g87=mirror(g26,[0,-g-hpm],[0,1]);
g88=mirror(g27,[0,-g-hpm],[0,1]);
g89=mirror(g28,[0,-g-hpm],[0,1]);
g90=mirror(g29,[0,-g-hpm],[0,1]);
g91=mirror(g30,[0,-g-hpm],[0,1]);
g92=mirror(g31,[0,-g-hpm],[0,1]);
g93=mirror(g32,[0,-g-hpm],[0,1]);
g94=mirror(g33,[0,-g-hpm],[0,1]);
g95=mirror(g34,[0,-g-hpm],[0,1]);
g96=mirror(g35,[0,-g-hpm],[0,1]);
g97=mirror(g36,[0,-g-hpm],[0,1]);


%PMS have no need to be updated
%back iron need too 101-109
g98=mirror(g53,[0,-g-hpm],[0,1]);
g99=mirror(g54,[0,-g-hpm],[0,1]);
g100=mirror(g55,[0,-g-hpm],[0,1]);
g101=mirror(g56,[0,-g-hpm],[0,1]);
g102=mirror(g57,[0,-g-hpm],[0,1]);
g103=mirror(g58,[0,-g-hpm],[0,1]);
g104=mirror(g59,[0,-g-hpm],[0,1]);
g105=mirror(g60,[0,-g-hpm],[0,1]);
g106=mirror(g61,[0,-g-hpm],[0,1]);

%Outer air dimension 62-63
g107=rect2(taupm*8,th*3,'base','corner','pos',[0,-th*1.5]);


clear s
s.objs={g1,g2,g3,g4,g5,g6,g7,g8,g9,g10,g11,g12,...
        g13,g14,g15,g16,g17, ...
  g18,g19,g20,g21,g22,g23,g24,g25,g26,g27,g28,...
  g29,g30,g31,g32,g33,g34, ...
  g35,g36,g37,g38,g39,g40,g41,g42,g43,g44,g45,...
  g46,g47,g48,g49,g50,g51, ...
  g52,g53,g54,g55,g56,g57,g58,g59,g60,g61,g62,...
  g63,g64,g65,g66,g67,g68, ...
  g69,g70,g71,g72,g73,g74,g75,g76,g77,g78,g79,...
  g80,g81,g82,g83,g84,g85, ...
  g86,g87,g88,g89,g90,g91,g92,g93,g94,g95,g96,...
  g97,g98,g99,g100,g101,g102, ...
  g103,g104,g105,g106,g107};

s.name={'g1','g2','g3','g4','g5','g6','g7','g8','g9','g10',
```

```
'g11','g12','g13','g14','g15','g16','g17','g18','g19','g20',
'g21','g22','g23', g24','g25','g26','g27','g28','g29','g30',
'g31','g32','g33','g34','g35', 'g36','g37','g38','g39','g40',
'g41','g42','g43','g44','g45','g46','g47', 'g48','g49','g50',
'g51','g52','g53','g54','g55','g56','g57','g58','g59', 'g60',
'g61','g61','g62','g64','g65','g66','g67','g68','g69','g70',
'g71', 'g72','g73','g74','g75','g76','g77','g78','g79','g80',
'g81','g82','g83', 'g84','g85','g86','g87','g88','g89','g90',
'g91','g92','g93','g94','g95', 'g96','g97','g98','g99','g100'
'g101','g102','g103','g104','g105','g106','g107'};



s.tags={'g1','g2','g3','g4','g5','g6','g7','g8','g9','g10',
  'g11','g12','g13','g14','g15','g16','g17','g18','g19','g20',
  'g21','g22','g23','g24','g25','g26','g27','g28','g29','g30',
  'g31','g32','g33','g34','g35','g36','g37','g38','g39','g40',
  'g41','g42','g43','g44','g45','g46','g47','g48','g49','g50',
  'g51','g52','g53','g54','g55','g56','g57','g58','g59','g60',
  'g61','g62','g63','g64','g65','g66','g67','g68','g69','g70',
  'g71','g72','g73','g74','g75','g76','g77','g78','g79','g80',
  'g81','g82','g83','g84','g85','g86','g87','g88','g89','g90',
  'g91','g92','g93','g94','g95','g96','g97','g98','g99','g100',
  'g101','g102','g103','g104','g105','g106','g107'};
% maybe the geometry needs to be reanalised

  %geomexport(strcat('slice_',num2str(k),'.dxf'),s.objs);
% definition of subdomain numbers
lamination=1;
PhaseA=2;
PhaseAret=3;
PhaseB=4;
PhaseBret=5;
PhaseC=6;
PhaseCret=7;
pmn=8;
pms=9;
spacer=10;



fem.draw=struct('s',s);
fem.geom=geomcsg(fem);
%

[gx,st] = geomcsg(fem);


%the final geometry
subdomains=get(fem.geom,'nmr');
```

```
edges=get(fem.geom,'nbs');

[ix,iy,v]=find(st);
domain=11*ones(1,subdomains);

% we have to solve the winding problem  we over write only
% the non air objects
for i=1:length(ix)
gg=ix(i);
kk=iy(i);
%
        if kk<=18
        domain(gg)=lamination;
        end
% We have to work a little for the coil section &
%  to the PMS tool
if ((kk>18)&(kk<=36))
        %a dirty trick we use interp

        domain(gg)=interp1(sb,kk-18);


end

        if ((kk>36)&(kk<=44))
                if (rem(kk,2)==0)
                domain(gg)=pms;
                else
                domain(gg)=pmn;
                end
        end

        if ((kk>44)&(kk<=52))
                domain(gg)=spacer;
                end

        if ((kk>52)&(kk<=61))
                domain(gg)=lamination;
        end

        if ((kk>61)&(kk<=97))
                domain(gg)=lamination;
        end
        %again the coils
        if ((kk>79)&(kk<=97))
                domain(gg)=interp1(sb,kk-79);
        end

        if ((kk>97)&(kk<=106))
                domain(gg)=lamination;
        end
```

```
end


ind=domain;


% Application mode 1 electromagnetics
clear appl
appl.mode.class = 'PerpendicularCurrents';
appl.module = 'EM';
appl.assignsuffix = '_emqa';
clear bnd
% we have to work here also
%[g,ct] = geomcsg(fem,fem.c.objs);

[fem,assocmap] = geomanalyze(fem);
assocmap{3}

clear bnd
bnd.type = {'cont','A0'};
bnd.ind = [2,2,2,1,2,1,2,1,2,1,2,1,2,1,2,1,1,1,1,1,1,1,1,1,
1,1,1,1,1,1, ...
  1,1,1,1,1,1,1,1,1,1,1,1,1,1,1,1,1,1,1,1,1,1,1,1,1,1,1,1,1,1,1,1
  ,1,1,1,1,1,1, ...
  1,1,1,1,1,1,1,1,1,1,1,1,1,1,1,1,1,1,1,1,1,1,1,1,1,1,1,1,1,1,1,1,
  1,1,1,1,1,1, ...
  1,1,1,1,1,1,1,1,1,1,1,1,1,1,1,1,1,1,1,1,1,1,1,1,1,1,1,1,1,1,1,1,
  1,1,1,1,1,1, ...
  1,1,1,1,1,1,1,1,1,1,1,1,1,1,1,1,1,1,1,1,1,1,1,1,1,1,1,1,1,1,1,1,
  1,1,1,1,1,1, ...
  1,1,1,1,1,1,1,1,1,1,1,1,1,1,1,1,1,1,1,1,1,1,1,1,1,1,1,1,1,1,1,1,
  1,1,1,1,1,1, ...
  1,1,1,1,1,1,1,1,1,1,1,1,1,1,1,1,1,1,1,1,1,1,1,1,1,1,1,1,1,1,1,1,
  1,1,1,1,1,1, ...
  1,1,1,1,1,1,1,1,1,1,1,1,1,1,1,1,1,1,1,1,1,1,1,1,1,1,1,1,1,1,1,1,
  1,1,1,1,1,1, ...
  1,1,1,1,1,1,1,1,1,1,1,1,1,1,1,1,1,1,1,1,1,1,1,1,1,1,1,1,1,1,1,1,
  1,1,1,1,1,1, ...
  1,1,1,1,1,1,1,1,1,1,1,1,1,1,1,1,1,1,1,1,1,1,1,1,1,1,1,1,1,1,1,1,
  1,1,1,1,1,1, ...
  1,1,1,1,1,1,1,1,1,1,1,1,1,1,1,1,1,1,1,1,1,1,1,1,1,1,1,1,1,1,1,1,
  1,1,1,1,1,1, ...
  1,1,1,1,1,1,1,1,1,1,1,1,1,1,1,1,1,1,1,1,1,1,1,1,1,1,1,1,1,1,1,1,
  1,1,1,1,1,1, ...
  1,1,1,1,1,1,1,1,1,1,1,1,1,1,1,1,1,1,1,1,1,1,1,1,1,1,1,1,1,1,1,1,
  1,1,1,1,1,1, ...
  1,1,1,1,1,1,1,1,1,1,1,1,1,1,1,1,1,1,1,1,1,1,1,1,1,1,1,1,1,1,1,1,
  1,1,1,1,1,1, ...
  1,1,1,1,1,1,1,1,1,1,1,1,1,1,1,1,1,1,1,1,1,1,1,1,1,1,1,1,1,1,1,1,
  1,1,1,1,1,1, ...
  1,1,1,1,1,1,1,1,1,1,1,1,1,1,1,1,1,1,1,1,1,1,1,1,1,1,1,1,1,1,1,1,
  1,1,1,1,1,1, ...
  1,1,1,1,1,1,1,1,1,1,1,1,1,1,1,1,1,1,1,1,1,1,1,1,1,1,1,1,1,1,1,1,
```

```
  1,1,1,1,1,1, ...
  1,1,1,1,1,1,1,1,1,1,1,1,1,1,1,1,1,1,1,1,1,1,1,1,1,1,1,1,1,1,1,1,1,1,1,1,1,
  1,1,1,1,1,1, ...
  1,1,1,1,1,1,1,1,1,1,1,1,1,1,1,1,1,1,1,1,1,1,1,1,1,1,1,1,1,1,1,1,1,1,1,1,1,
  1,1,1,1,1,1, ...
  1,1,1,1,1,1,1,1,1,1,1,1,1,1,1,1,1,1,1,1,1,1,1,1,1,1,1,1,1,1,1,1,1,1,1,1,2,2,2,2,2,2,2];
appl.bnd = bnd;
%bnd.type = {'A0','cont'};
%edgeindex=2*ones(1,edges);

%we generate the index of edges automatically and then we modify
% it
%bnd.ind =edgeindex;

appl.bnd = bnd;
clear equ
equ.magconstrel = {'mur','mur','mur','mur','mur','mur','mur',
'Br','Br','mur','mur'};
equ.Br = {{0;0},{0;0},{0;0},{0;0},{0;0},{0;0},{0; ...
  0},{0;'Br'},{0;'-Br'},{0;0},{0;0}};
equ.L = 'ls';
equ.Jez = {0,'Ja','-Ja','Jb','-Jb','Jc','-Jc',0,0,0,0};
equ.sigma = {'sigFe','sigCu','sigCu','sigCu','sigCu','sigCu',
'sigCu','sigNeFeBr', ...
  'sigNeFeBr',0,0};
equ.mur = {'murFe','murCu','murCu','murCu','murCu','murCu','murCu',
'murNeFeBr', ...
  'murNeFeBr',1,1};
equ.name = {'lamination','PhaseA','PhaseB','PhaseC',
'PhaseAret','PhaseBret',...
  'PhaseCret','pmn','pms','spacer','air'};
equ.maxwell = {{},{},{},{},{},{},{},'Axial','Axial','Axial',{}};
%domain assingations
equ.ind = ind;
appl.prop.elemdefault='lag1';

appl.equ = equ;
fem.appl{1} = appl;
fem.border = 1;
fem.units = 'SI';

% Multiphysics
fem=multiphysics(fem);

% % Generate the mesh.
fem.mesh=meshinit(fem);
fem.xmesh=meshextend(fem);
% % Solve problem
%fem.sol=femlin(fem,'solcomp',{'Az'},'outcomp',{'Az'});
fem=adaption(fem,'ngen',1,'report','on');
```

```
% %we save the flux lines
% saveimage(strcat('Flux_lines_slicenr_',num2str(k+1)));

%Interpolate data for B in airgap
%pd=postcrossplot(fem,1,[0 taupm*poles;-g/2 -g/2],'lindata',
%'By_emqa','npoints',1000,'outtype','postdata',...
%                                'title','Airgap flux density  [T]');
%Bg=pd.p(2,:)';
lx=linspace(0,taupm*poles/2,1000);
ly=-g/2*ones(1,1000);
airgapline=[lx;ly];
Bg= postinterp(fem,'By_emqa',airgapline);
Hg= postinterp(fem,'Hy_emqa',airgapline);
%interpolate data in the stack
lx1=linspace(0,taupm*poles/2,1000);
ly1=(th-lstack/2-ovg)*ones(1,1000);
backline=[lx1;ly1];
Bback= postinterp(fem,'normB_emqa',backline);
% the tooth line
lx2=0.1*ones(1,40);
ly2=linspace(0,th,40);
toothline=[lx2;ly2];
Btooth=postinterp(fem,'normB_emqa',toothline);


%flux densities
Btoothav(k+1)=norm(Btooth)/sqrt(length(Btooth));
Bbackav(k+1)=norm(Bback)/sqrt(length(Bback));


%saveimage(strcat('By_slicenr_',num2str(k+1)));

Bgav(k+1) = norm(Bg)/sqrt(length(Bg));


%pd=postcrossplot(fem,1,[0 taupm*poles;-g/2 -g/2],'lindata',
%'By_emqa','npoints',1000,'outtype','postdata',...
%                                'title','Airgap flux density
%                                  [T]');
%a small ffft
a = fft(Bg);
a(1) = [];
b = length(a)/2;
power = 0.00001.*(abs(a(1:b)).^2);
nyq = 1/2;
freq = taupm*(1:b)/b*nyq;
```

```
%plot(freq,power);

%mechanichal parameters
rad(k+1)=radius;
F=cjpgorce(fem,'Wm_emqa','delta',1e-7,'dl',[7 8 9]);
Forcex(k+1)=2*F(1);
%postint(fem,'Axial_forcex_emqa','dl',[5 62 64 118 120 182 192
% 246 256 314 382 392 446 448],'edim',0);
Forcey(k+1)=2*F(2);
%postint(fem,'Axial_forcey_emqa','dl',
%[5 62 64 118 120 182 192 246
%256 314 382 392 446 448],'edim',0);
%We add some sorcery to the script to save
% the useful data for post process
Torque(k+1)=Forcex(k+1)*rad(k+1);



flsave(strcat('SLice nr',num2str(k)),fem);
end

%induced voltage
%coilarea
Btoothav=sum(Btoothav)/slices;
Bbackav=sum(Bbackav)/slices;
Bgav=sum(Bgav)/slices;
Acoil=1/2*2*pi/slots*(rmax^2-rmin^2);
kw1=0.866;

psi1=kw1*Bgav*Nt*Acoil/poles;
V=2*stators*speed*psi1/(sqrt(2));




Vtooth=stators*slots*sum(Vtooth);
Vback=stators*slots*sum(Vback);
%plot(rad,Torque);
Torq=sum(Torque);
Fx=sum(Forcex)/slices;
Fy=sum(Forcey)/slices;
%Perf=performance(Btoothav,Bbackav,Vtooth,Vback,Acoil,Torq,
%wmech,Imax,stators,slots,poles,rmin,rmax,L);

%constants
rho=0.0000000168;
kcp=0.6;

% filter out results w over-saturated materials,
```

```
%  non-interleaved faces, or anomalous results
maxLam=2.5;

%material corelos lookup table protolam data
Coreloss=[0.106132075   0.010225957     0.054981543     0.084242864
0.161056742     0.237870619
0.218497305     0.055783224     0.244115467     0.380921929     0.7273416
1.07376127
0.330862534     0.124096527     0.582078678     0.919569825     1.762282496
2.604995167
0.443227763     0.213025873     1.159340831     1.685113094     3.27318184
4.861250586
0.555592992     0.346624308     1.76297155      2.622742465     5.343288777
8.063835089
0.667958221     0.490543484     2.385798038     3.776071221     7.713437926
11.65080463
0.78032345      0.656215907     3.234667725     5.07642382      10.12478254
15.17314126
0.892688679     0.825484107     4.138589992     6.606712408     13.35274241
20.09877241
1.005053908     1.050933529     5.414332461     8.261001633     17.27322724
26.28545285
1.117419137     1.314352926     6.690074931     10.09402123     20.18807144
30.28212166
1.229784367     1.579391749     7.988852543     12.56991023     27.62731193
42.68471364
1.342149596     1.862785854     10.03281703     15.67498339     33.50055484
51.32612628
1.454514825     2.271859645     12.07678151     18.78413898     39.52257201
60.26100504
1.566880054     2.791770819     14.12074599     22.50232934     49.51051906
76.51870878
1.679245283     3.346087311     16.16471047     26.65833272     61.12274041
95.5871481];
%Asign variables
B=Coreloss(:,1);
p50=Coreloss(:,2);
p150=Coreloss(:,3);
p200=Coreloss(:,4);
p300=Coreloss(:,5);
p400=Coreloss(:,6);
%functional test
ploss=interp1(B,p300,1.8,'spline','extrap');
% Slot resistance
alfacp=round(slots/poles)/(slots/poles);
thetap=2*pi/poles;
taupi=rmin*thetap;
taupo=rmax*thetap;
tauci=alfacp*taupi;
tauco=alfacp*taupo;
%resistance computation
```

```
Rs=Nt*rho*slots^2*L/(kcp*Acoil);
Re=Nt*rho*slots^2*pi*(tauco+tauci)/(4*kcp*Acoil);
Rph=stators*slots*(Rs+Re);

%sttel mass density
gammaFe=7850;

pdTooth=interp1(B,p300,Btoothav,'spline','extrap');
% loss dens in back iron (use average flux density)
pdBack=interp1(B,p300,Bbackav,'spline','extrap');
% loss dens in back iron (use average flux density)

% Power calculations ========================
% ==========================
Ptooth=pdTooth*Vtooth*gammaFe;
 % core loss in tooth
Pbackiron=pdBack*Vback*gammaFe;
  % core loss in back iron (half stator)

Pcore=stators*(Ptooth+Pbackiron);
 % total core loss (whole machine)
%mechanichal power
Pmech=stators*max(abs(Torq))*wmech;
 % Mechanical power (whole machine)
Pcu=m*Imax^2*Rph;
              % conduction loss (whole machine)
Ps=0.01*Pmech;
Pout=Pmech-Pcu-Pcore-Ps;
     % Net power (whole machine)
eta=Pout/Pmech;
     % efficiency

Perf.Pmech=Pmech;
Perf.Pcu=Pcu;
Perf.Pcore=Pcore;
Perf.eta=eta;
Perf.Rph=Rph;



% end of work
Time=toc;
res=fopen('Results.txt','w');
fprintf(res,'Result values----------------------
----------------------\n');
fprintf(res,'Step radius  Tensor [Nm] Forcex [N]
 Forcey [N] torque [N*m]\n');
for l=1:slices

fprintf(res,'%f %f      %f      %f\n',rad(l),Forcex(l)
,Forcey(l),Torque(l));
```

```
end
fprintf(res,'Final values  are :\n');
fprintf(res,'Force x=   %f\n',Fx);
fprintf(res,'Force y=   %f\n',Fy);

fprintf(res,'Voltage =%f\n',V);
fprintf(res,'Torque =%f\n',Torq);
fprintf(res,'Pmec =%f\n',Perf.Pmech);
fprintf(res,'Pcu =%f\n',Perf.Pcu);
fprintf(res,'Pcore =%f\n',Perf.Pcore);
fprintf(res,'Efficiency =%f\n',Perf.eta);
fprintf(res,'Final parameters  are :\n');
fprintf(res,'Phase resistance =%f\n',Perf.Rph)
fprintf(res,'total time of computation is %f
seconds',Time);
fclose(res);

ef=fopen('ef.txt','w');
fprintf(ef,'%f',Perf.eta);
fclose(ef);

%experiment end
%exit
```

A.7 48/40 Axial flux FEMM Lua code

This code was developed for using FEMM and LUA scripting language for modeling an slice of the nonoverlapping axial flux PMSM used in chapter 6

```
%-------------------------------------------------------------%
% Axial flux femm 2D  paramateric  model                      %
% Topor Marcel 2011                                           %
%                                                             %
%-------------------------------------------------------------%

function fx=Axial_1(r,n)
openfemm()

newdocument(0)

% Dimensions
Qs=12;
poles=14;
alphapm=360/poles;

% Initial data
%n=2;                           % current slice computed
nmax=10;                        %maximum number of concetric
                                %shells used in computation
Do=305;                         %Outer diameter
lambda=2;                       %Do/Di factor
Di=Do/lambda;                   %inner diameter
hiron=10;                       %back iron axial length
hyoke=10;                       %yoke axial legth
step=4;                         % rotor shift
depth=(Do-Di)/2*1/nmax;         %deph of computed slice
taupm=alphapm*pi/180*r;         %pole chord
alphaqs=360/Qs;                 % slot angle
tauqs=alphaqs*pi/180*r;         % slot chord angle

airgap=1;                       %airgap axial length
hpm=5;                                  %

beta=0.8;

lpm=taupm*beta;

deltax=(taupm-lpm)/2

%  Winding table
wtable=[...
1       0       0       1       0       0
0       -1      0       1       0       0
0       -1      0       0       0       1
-1      0       0       0       0       1
```

```
-1      0       0       -1      0       0
0       1       0       0       1       0
0       0       -1      0       1       0
0       0       -1      1       0       0
0       -1      0       1       0       0
0       -1      0       0       -1      0
0       0       1       0       0       1
-1      0       0       0       0       1
-1      0       0       0       1       0
0       0       -1      0       1       0
0       0       -1      0       0       -1 ...
]

MatCu='1mm';
PhaseNr=3;

CoilTurns=1;
TabPhaseInf=[];
TabPhaseSup=[];

for j=1:PhaseNr
                TabPhaseInf=[TabPhaseInf,wtable(:,j)]
                %layer 1
        end
        for j=1:PhaseNr
                TabPhaseSup=[TabPhaseInf,wtable(:,2*j)]
                %Layer 2
    end

% Add circuit properties
IphaseU=0;
IphaseV=0;
IphaseW=0;


%% Add the thre phase circuits
mi_addcircprop('Phase1',IphaseU,1)
mi_addcircprop('Phase2',IphaseV,1)
mi_addcircprop('Phase3',IphaseW,1)


% Add materials
mi_probdef(0,'millimeters','planar',1E-8,depth,30)

mi_getmaterial('NdFeB 40 MGOe')
mi_modifymaterial('NdFeB 40 MGOe',0,'PmSN')
mi_getmaterial('NdFeB 40 MGOe')
mi_modifymaterial('NdFeB 40 MGOe',0,'PmNS')
mi_getmaterial('1010 Steel')
mi_getmaterial('Air')
mi_getmaterial('1mm')
```

```
% Boundary properties

mi_addboundprop('A=0',0,0,0,0,0,0,0,0,0)
mi_addboundprop('one', 0, 0, 0, 0, 0, 0, 0, 0, 4);
mi_addboundprop('two', 0, 0, 0, 0, 0, 0, 0, 0, 4);
mi_addboundprop('three', 0, 0, 0, 0, 0, 0, 0, 0, 4);
mi_addboundprop('four', 0, 0, 0, 0, 0, 0, 0, 0, 4);
mi_addboundprop('five', 0, 0, 0, 0, 0, 0, 0, 0, 4);
mi_addboundprop('six', 0, 0, 0, 0, 0, 0, 0, 0, 4);
mi_addboundprop('seven', 0, 0, 0, 0, 0, 0, 0, 0, 4);
mi_addboundprop('eight', 0, 0, 0, 0, 0, 0, 0, 0, 4);
mi_addboundprop('nine', 0, 0, 0, 0, 0, 0, 0, 0, 4);

% group definitions
GrStator=110;
GrStator1=111;
GrMover=90;



% slot profile
b1=1;
b2=10;

if b2>0.6*tauqs
    disp('wrong dimensions')
end

h1=3;
h2=20;
% slot points
c0=[tauqs/2 0];
c1=[b1/2 0];
c2=[b1/2 h1];
c3=[b2/2 h1];
c4=[b2/2 h2];
c5=[0 h2];
c6=[0 h1];

%

mi_drawpolyline([c0(1),c0(2);...
c1(1),c1(2);...
c2(1),c2(2);...
c3(1),c3(2);...
c4(1),c4(2);...
c5(1),c5(2);
c6(1),c6(2);
c2(1),c2(2)]);
```

```
% mi_selectnode(c3)
elementsize=0;
automesh=1;
hide=0;
group=GrStator;


mi_seteditmode('segments');
[xs0,ys0]=midpoint(c0,c1)
mi_selectsegment(xs0,ys0);
[xs,ys]=midpoint(c1,c2)
mi_selectsegment(xs,ys);
 [xs1,ys1]=midpoint(c2,c3);
 mi_setsegmentprop('None', elementsize, automesh,...
  hide, group);
 mi_selectsegment(xs1,ys1);
 [xs2,ys2]=midpoint(c3,c4);
 mi_selectsegment(xs2,ys2);
  [xs3,ys3]=midpoint(c4,c5);

 mi_selectsegment(xs3,ys3);
  [xs4,ys4]=midpoint(c5,c6);
 mi_selectsegment(xs4,ys4);
   [xs5,ys5]=midpoint(c6,c2);
  mi_selectsegment(xs5,ys5);
     [xs6,ys6]=midpoint(c6,c1);
  mi_selectsegment(xs6,ys6);

  mi_setsegmentprop('None', elementsize, automesh,...
   hide, group);

 mi_selectgroup(GrStator)
mi_mirror(tauqs/2,0,tauqs/2,1);

radius=0.9*(b2-b1)/2;
 mi_createradius(tauqs-c3(1),c3(2),radius);
%
 mi_createradius(tauqs-c4(1),c4(2),radius);
 mi_createradius(c3(1),c3(2),radius);
%
 mi_createradius(c4(1),c4(2),radius);



%  select stator

  mi_selectgroup(GrStator)
mi_copytranslate(tauqs,0,Qs-1);


% mi_selectgroup(GrStator1)
```

```
% draw Stator yoke
mi_drawrectangle(0,-airgap/2,Qs*tauqs,h2+hyoke);

mi_drawrectangle(0,-airgap/2,Qs*tauqs,h2+1.5*hyoke);

% draw backIron

mi_drawrectangle(0,-airgap-hpm-hiron,poles*taupm,...
-airgap-hpm);
%draw magnets and coils

for i=0:poles-1
    mi_drawrectangle(deltax+taupm*i,-airgap-hpm,...
    deltax+lpm+taupm*i,-airgap);
    mi_selectsegment(deltax+taupm*i,-airgap-hpm/2);
    mi_selectsegment(deltax+taupm*i+lpm/2,-airgap);
    mi_selectsegment(deltax+taupm*i+lpm,-airgap-hpm/2);
    mi_selectsegment(deltax+taupm*i++lpm/2,-airgap-hpm);
    mi_setsegmentprop('None', elementsize, automesh,...
     hide, GrMover);

        mi_addblocklabel(deltax+lpm/2+taupm*i,-airgap-hpm/2);
        mi_selectlabel(deltax+lpm/2+taupm*i,-airgap-hpm/2);
    if mod(i,2)==0
        blockname='PmSN'
        automesh=0
        meshsize=0;
        incircuit='';
        magdirection=90;
        group=GrMover;
        turns=0;
mi_setblockprop(blockname, automesh, meshsize, ...
incircuit,....
    magdirection,group, turns)


    else
        blockname='PmNS'
        automesh=0;
        meshsize=0;
        incircuit='';
        magdirection=-90;
        group=GrMover;
        turns=0;

       mi_setblockprop(blockname, automesh, meshsize,...
       incircuit, ...
             magdirection,group, turns)
    end
```

```
end
mi_clearselected();
%add  Coil label
mi_seteditmode('blocks');
for i=0:Qs-1

    mi_addblocklabel(b2/4+tauqs*i,h2/2);

    mi_addblocklabel(tauqs*(i+1)-b2/4,h2/2);

    blockname='1mm'
        automesh=0;
        meshsize=0;

        magdirection='';
        group=GrStator;

        coil=i+1;

     if TabPhaseInf(coil,1)~=0
         incircuit=strcat('Phase',num2str(1));
         turns=TabPhaseInf(coil,1)*CoilTurns;
     elseif TabPhaseInf(coil,2)~=0
         incircuit=strcat('Phase',num2str(2));
         turns=TabPhaseInf(coil,2)*CoilTurns;
     elseif TabPhaseInf(coil,3)~=0

         incircuit=strcat('Phase',num2str(2));
         turns=TabPhaseInf(coil,3)*CoilTurns;
     end

         mi_selectlabel(b2/4+tauqs*i,h2/2)
         mi_setblockprop(blockname, automesh, meshsize,...
          incircuit,...
             magdirection,group, turns)
         mi_clearselected

     if TabPhaseSup(coil,1)~=0
         incircuit2=strcat('Phase',num2str(1));
         turns=TabPhaseSup(coil,1)*CoilTurns;
     elseif TabPhaseSup(coil,2)~=0
         incircuit2=strcat('Phase',num2str(2));
         turns=TabPhaseSup(coil,2)*CoilTurns;
     elseif TabPhaseSup(coil,3)~=0
         incircuit2=strcat('Phase',num2str(2));
         turns=TabPhaseSup(coil,3)*CoilTurns;
     end


         mi_selectlabel(tauqs*(i+1)-b2/4,h2/2);
         mi_setblockprop(blockname, automesh, meshsize,...
```

```
          incircuit2, ...
             magdirection,group, turns)
         mi_clearselected


end

mi_clearselected();

% add block labels

mi_addblocklabel(tauqs*Qs/2,h2+hyoke/2);

        mi_selectlabel(tauqs*Qs/2,h2+hyoke/2);
         blockname='1010 Steel';
        automesh=0
        meshsize=0;
        incircuit='';
        magdirection=0;
        group=GrStator;
        turns=0;
         mi_setblockprop(blockname, automesh, meshsize,...
          incircuit,...
         magdirection,group, turns)

           mi_clearselected();
         mi_addblocklabel(tauqs*Qs/2,h2+hyoke+hyoke*0.25);
        mi_selectlabel(tauqs*Qs/2,h2+hyoke+hyoke*0.25);

   blockname='Air';
        automesh=0
        meshsize=0;
        incircuit='';
        magdirection=0;
        group=GrStator;
        turns=0;
        mi_setblockprop(blockname, automesh,...
         meshsize,...
         incircuit,...
            magdirection,group, turns)
mi_clearselected();



mi_selectsegment(0,-airgap+h1/2);
mi_setsegmentprop('one', elementsize,...
 automesh, hide, GrStator);
mi_clearselected
mi_selectsegment(Qs*tauqs,-airgap+h1/2);
mi_setsegmentprop('one', elementsize,...
 automesh, hide, GrStator);
```

```
mi_clearselected

mi_selectsegment(0,(h1+h2/2));
mi_setsegmentprop('two', elementsize,...
 automesh, hide, GrStator);
mi_clearselected
mi_selectsegment(Qs*tauqs,(h1+h2/2));
mi_setsegmentprop('two', elementsize, ...
automesh, hide, GrStator);
mi_clearselected


mi_selectsegment(0,h2+hyoke/2);
mi_setsegmentprop('three', elementsize,...
 automesh, hide, GrStator);
mi_clearselected
mi_selectsegment(Qs*tauqs,h2+hyoke/2);
mi_setsegmentprop('three', elementsize, ...
automesh, hide, GrStator);
mi_clearselected



mi_selectsegment(0,h2+hyoke+0.25*hyoke);
mi_setsegmentprop('four', elementsize, ...
automesh, hide, GrStator);
mi_clearselected
mi_selectsegment(Qs*tauqs,h2+hyoke+0.25*hyoke);
mi_setsegmentprop('four', elementsize,...
 automesh, hide, GrStator);
mi_clearselected



mi_selectsegment(0,-airgap-hpm/2);
mi_setsegmentprop('six', elementsize, ...
automesh, hide, GrMover);
mi_clearselected();
mi_selectsegment(poles*taupm,-airgap-hpm/2);
mi_setsegmentprop('six', elementsize,...
 automesh, hide, GrMover);

mi_clearselected();


% mi_selectsegment(Qs*tauqs/2,-airgap);
% mi_setsegmentprop('five', elementsize,...
%  automesh, hide, GrStator);
% mi_clearselected
% mi_selectsegment(Qs*tauqs/2,h2+hyoke);
% mi_setsegmentprop('six', elementsize,...
```

```
%  automesh, hide, GrStator);
% mi_clearselected

mi_selectsegment(Qs*tauqs/2,h2+hyoke);
mi_setsegmentprop('None', elementsize, ...
automesh, hide, GrStator);
mi_clearselected

mi_selectsegment(Qs*tauqs/2,h2+hyoke+0.5*hyoke);
mi_setsegmentprop('A=0', elementsize,...
 automesh, hide, GrStator);
mi_clearselected



mi_selectsegment(0,-airgap-hpm-hiron/2);
mi_setsegmentprop('nine', elementsize,...
 automesh, hide, GrMover);

mi_clearselected();

mi_selectsegment(poles*taupm,-airgap-hpm-hiron/2);
mi_setsegmentprop('nine', elementsize, ...
automesh, hide, GrMover);
mi_clearselected();

mi_selectsegment(poles*taupm*1/2,-airgap-hpm-hiron);
mi_setsegmentprop('A=0', elementsize,...
 automesh, hide, GrMover);

mi_clearselected();
mi_addblocklabel(poles*taupm*1/2,-airgap-hpm-hiron/2);
mi_selectlabel(poles*taupm*1/2,-airgap-hpm-hiron/2);


blockname='1010 Steel';
automesh=0;
meshsize=0;
incircuit='';
magdirection=0;
group=GrMover;
turns=0;

mi_setblockprop(blockname, automesh, meshsize,...
 incircuit, ...
    magdirection,group, turns)
mi_clearselected();

mi_addblocklabel(poles*taupm*1/2,-airgap-hpm/2);
mi_selectlabel(poles*taupm*1/2,-airgap-hpm/2);
```

```
blockname='Air';
automesh=0
meshsize=0;
incircuit='';
magdirection=0;
group=GrMover;
turns=0;

mi_setblockprop(blockname, automesh, meshsize, ...
incircuit,...
    magdirection,group, turns)
mi_clearselected();



% draw pmsm
mi_selectgroup(GrMover);
mi_movetranslate(step,0);
mi_drawrectangle(0+step,-airgap/2,poles*taupm+step,...
-airgap-hpm-hiron);
mi_selectsegment(Qs*tauqs/2,-airgap/2);
mi_deleteselectedsegments
mi_selectsegment(step/2,-airgap/2);
mi_setsegmentprop('seven', elementsize,...
 automesh, hide, 0);

mi_clearselected();

 mi_clearselected();
mi_selectsegment(poles*taupm+step/2,-airgap/2);
mi_setsegmentprop('seven', elementsize, ...
automesh, hide, 0);
%
mi_clearselected();
%

mi_selectsegment(step,-airgap-hpm/2);
mi_setsegmentprop('eight', elementsize,...
 automesh, hide, GrMover);

  mi_clearselected();

mi_selectsegment(poles*taupm+step,-airgap+hpm/2);
mi_setsegmentprop('eight', elementsize, ...
automesh, hide, GrMover);

mi_clearselected();

mi_zoomnatural();
mi_saveas('temp.fem')
% analysis
```

```
mode='test'

switch  mode
case 'cogging'
    for i=1:taupm

        mi_analyze(1);
        mi_loadsolution()
        mo_groupselectblock(GrMover)
        mo_selectblock(taupm*poles/2+step+i,...
        -airgap/2)
        fx(i)=mo_blockintegral(18);

        mo_close()
        mi_selectgroup(GrMover)

        mi_movetranslate(1,0);


    plot(fx);
    end

    case 'test'
    mi_analyze(1);
    mi_loadsolution()
    mo_groupselectblock(GrMover)
    mo_selectblock(taupm*poles/2+step+i,...
    -airgap/2)
    fx(i)=mo_blockintegral(18);

    mo_addcontour(0,-airgap/2);
    mo_addcontour(taupm*poles,-airgap/2);
    mo_makeplot(2,1000);
    mo_makeplot(2,1000,'c:\\temp\Bn.txt',0)
     mo_makeplot(3,1000,'c:\\temp\Bt.txt',0)
     mo_makeplot(0,1000,'c:\\temp\A.txt',0)

     mo_getcircuitproperties('Phase1');
mo_getcircuitproperties('Phase2');
mo_getcircuitproperties('Phase3');

     mo_close()
    plot(fx);
end
```

A.8 AFPM 16/18 test data

Table A.1: Test data AFPMSM 16/18

NO	Voltage			Current			$cos(\phi)$	Input	Speed	Torque	Output	EFF
	V1	V2	V3	U	V	W		W	rpm	N.m	W	%
	110.2	113.2	112.3	1.08	1.10	1.08	0.996	210	298.8	4.56	142.7	67.9
	144.9	148.8	147.8	1.41	1.45	1.42	0.999	363	397.2	5.7	237.1	65.3
	178.2	183.1	182.0	1.73	1.78	1.75	0.998	549	498.2	6.81	355.3	64.7
	210.6	215.9	214.8	2.04	2.09	2.06	0.999	763	598.3	7.79	488.1	64.0
	240.4	247.0	246.0	2.34	2.40	2.35	1.000	1000	698.3	8.69	635.4	63.5
	269.1	276.6	275.7	2.62	2.68	2.63	1.000	1253	798.4	9.48	792.6	63.3
	296.3	304.4	303.8	2.88	2.95	2.89	1.000	1517	898.4	10.18	957.7	63.1
	321.9	330.5	330.2	3.13	3.20	3.14	0.999	1788	997.3	10.79	1126.8	63.0

A.9 Simulation model for 48/40 APFPM

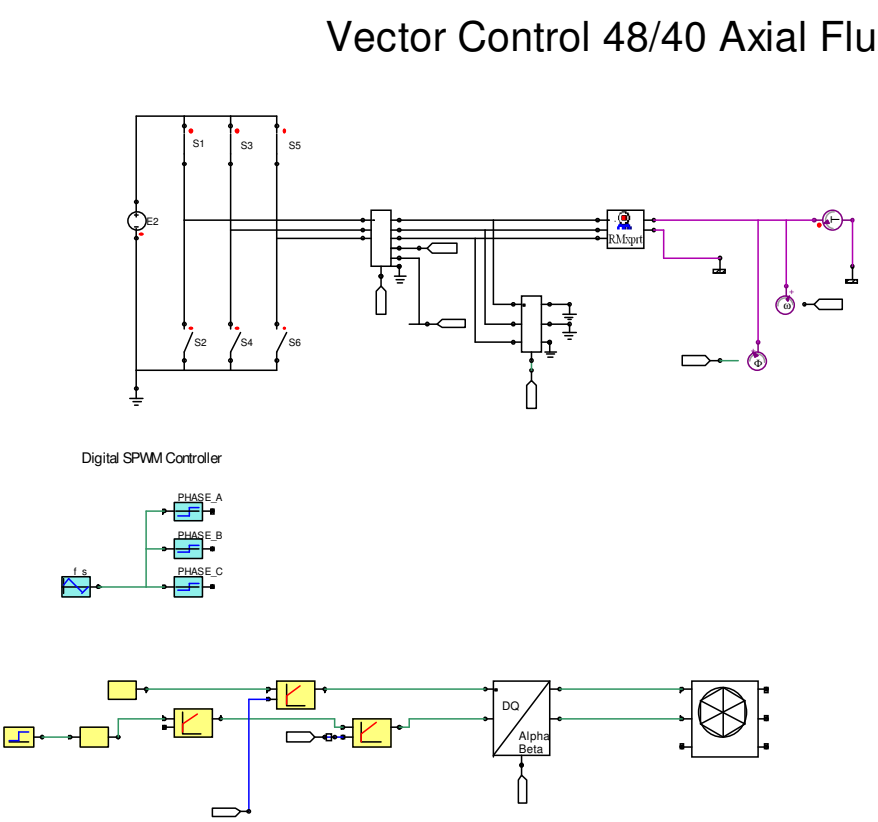

Figure A.4: Ansoft Simplorer model of AFPM sensored SVPWM vector control

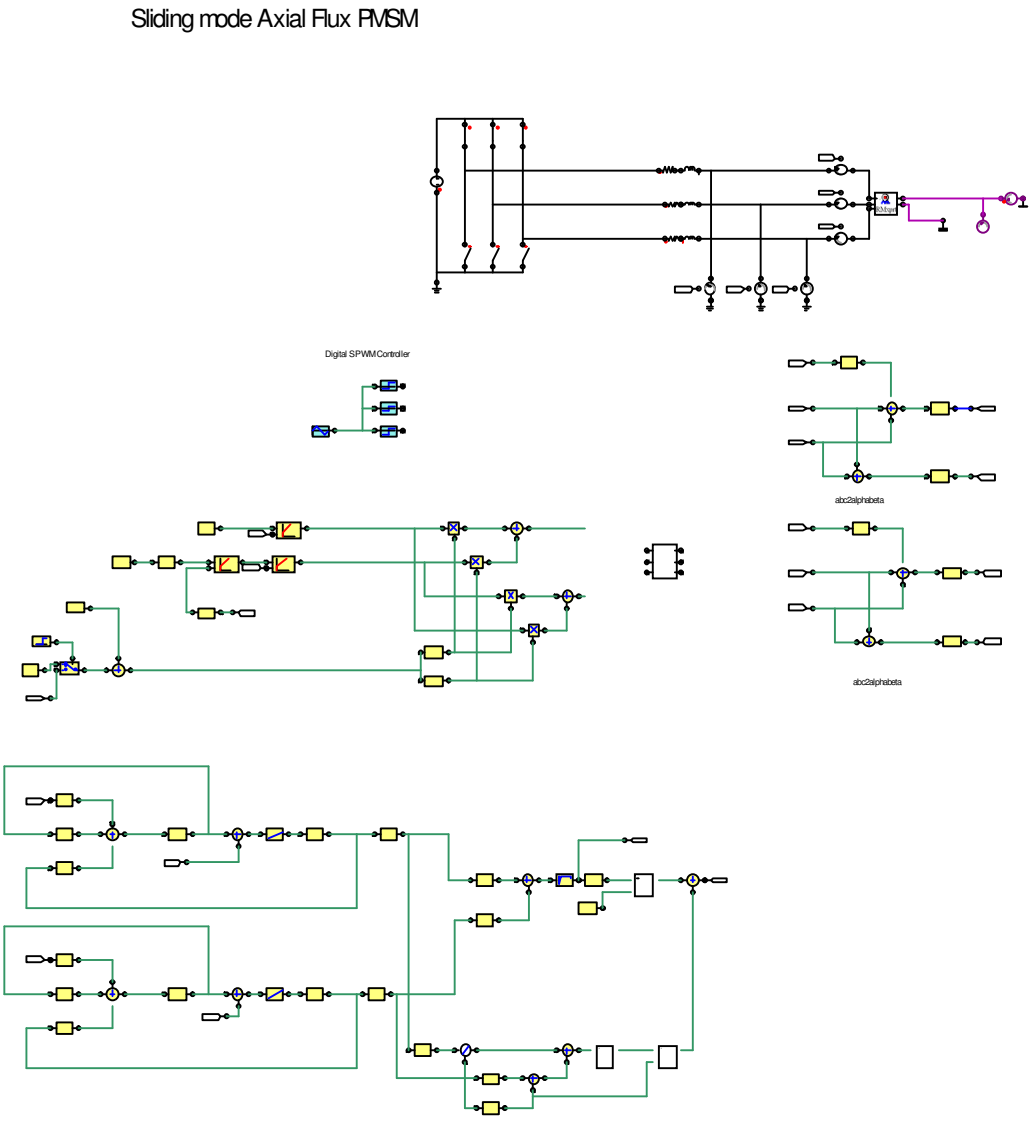

Figure A.5: Ansoft Simplorer model of AFPM sensorless SVPWM vector control

A.10 VHDL code for SVPWM implemented in Simplorer

```
library ieee;
use ieee.math_real.all;

entity sv_pwm is
  generic(clark_k : real := sqrt(2.0/3.0));
   -- Clark Transform Constant used for Voltage Reference --
```

```
  port (quantity Ualpha : in real := 0.0;
  -- Voltage Reference in alpha-beta coordinates --
quantity Ubeta  : in real := 0.0;
 -- Voltage Reference in alpha-beta coordinates --
quantity Ud : in real := 1.35*400.0;
 -- DC bus voltage --
          quantity sector : out real := 1.0;
          -- Sector Number --
          quantity DA, DB, DC : out real := 0.0);
          -- Duty Cycles for phase A, B & C --
end entity sv_pwm;
```

```
architecture default of sv_pwm is
begin
  procedural is
    constant sin60 : real := sin(math_deg_to_rad*60.0);
    -- sin(60^deg) constant --
    constant tan60 : real := tan(math_deg_to_rad*60.0);
    -- tan(60^deg) constant --
    variable d0, d1, d2, d3, d4, d5, d6 : real := 0.0;
     -- For clarity, only a dx, dx+1 and a d0 is necessary --
  begin
  -- see "AN OVERVIEW OF SPACE VECTOR PWM" --
    if Ubeta > 0.0 then
      if Ubeta > abs(Ualpha)*tan60 then
        -- Sector II --
        sector := 2.0;
        d2:=(Ubeta/(2.0*sin60)+Ualpha)/(clark_k*Ud);
        d3:=(Ubeta/(2.0*sin60)-Ualpha)/(clark_k*Ud);
        d0:=d2+d3;     -- d0 used for temp storage
         to check for an to big a reference --
        if d0 > 1.0 then
          report "Reference to big in Sector II,
           d2+d3=" & real'image(d0)
          severity note;
          d2:=d2/d0;
          d3:=d3/d0;
        end if;
        d0:=1.0-d2-d3;
        DB:=d3+d2+d0/2.0;
        DA:=d2+d0/2.0;
        DC:=d0/2.0;
      elsif Ualpha > 0.0 then
        -- Sector I --
        sector := 1.0;
        d1:=(Ualpha-Ubeta/tan60)/(clark_k*Ud);
        d2:=Ubeta/(sin60*clark_k*Ud);
        d0:=d1+d2;
        -- d0 used for temp storage to check for
        an to big a reference --
        if d0 > 1.0 then
          report "Reference to big in Sector I,
           d1+d2=" & real'image(d0)
          severity note;
          d1:=d1/d0;
          d2:=d2/d0;
        end if;
        d0:=1.0-d1-d2;
```

```
      DA:=d1+d2+d0/2.0;
      DB:=d2+d0/2.0;
      DC:=d0/2.0;
    else
      -- Sector III --
      sector := 3.0;
      d3:=Ubeta/(sin60*clark_k*Ud);
      d4:=(-Ualpha-Ubeta/tan60)/(clark_k*Ud);
      d0:=d3+d4;
      -- d0 used for temp storage to check for
       an to big a reference --
      if d0 > 1.0 then
        report "Reference to big in Sector III,
         d3+d4=" & real'image(d0)
        severity note;
        d3:=d3/d0;
        d4:=d4/d0;
      end if;
      d0:=1.0-d3-d4;
      DB:=d3+d4+d0/2.0;
      DC:=d4+d0/2.0;
      DA:=d0/2.0;
    end if;
  elsif Ubeta < -abs(Ualpha)*tan60 then
    -- Sector V --
    sector := 5.0;
    d5:=(-Ubeta/(2.0*sin60)-Ualpha)/(clark_k*Ud);
    d6:=(-Ubeta/(2.0*sin60)+Ualpha)/(clark_k*Ud);
    d0:=d5+d6;
    -- d0 used for temp storage to check for
     an to big a reference --
    if d0 > 1.0 then
      report "Reference to big in Sector V, d5+d6=" &
      real'image(d0)
      severity note;
      d5:=d5/d0;
      d6:=d6/d0;
    end if;
    d0:=1.0-d5-d6;
          DC:=d5+d6+d0/2.0;
    DA:=d6+d0/2.0;
    DB:=d0/2.0;
  elsif Ualpha > 0.0 then
    -- Sector VI --
    sector := 6.0;
    d6:=-Ubeta/(sin60*clark_k*Ud);
    d1:=(Ualpha+Ubeta/tan60)/(clark_k*Ud);
    d0:=d6+d1;
     -- d0 used for temp storage to check
      for an to big a reference --
    if d0 > 1.0 then
      report "Reference to big in Sector VI, d6+d1=" &
       real'image(d0)
      severity note;
      d6:=d6/d0;
      d1:=d1/d0;
    end if;
    d0:=1.0-d6-d1;
```

```
      DA:=d1+d6+d0/2.0;
      DC:=d6+d0/2.0;
      DB:=d0/2.0;
    else
      -- Sector IV --
      sector := 4.0;
      d4:=(-Ualpha+Ubeta/tan60)/(clark_k*Ud);
      d5:=-Ubeta/(sin60*clark_k*Ud);
      d0:=d4+d5;
      -- d0 used for temp storage to check
      for an to big a reference --
      if d0 > 1.0 then
        report "Reference to big in Sector V,
        d4+d5=" & real'image(d0)
        severity note;
        d4:=d4/d0;
        d5:=d5/d0;
      end if;
      d0:=1.0-d4-d5;
      DC:=d5+d4+d0/2.0;
      DB:=d4+d0/2.0;
      DA:=d0/2.0;
    end if;
  end procedural;
end architecture;
```